

NORTHWESTERN UNIVERSITY

The Controlled, Site-Isolated Synthesis of Polyelemental Nanostructures in Polymer  
Nanoreactors

A DISSERTATION

SUBMITTED TO THE GRADUATE SCHOOL  
IN PARTIAL FULFILLMENT OF THE REQUIREMENTS

for the degree

DOCTOR OF PHILOSOPHY

Field of Materials Science and Engineering

By

Pengcheng Chen

EVANSTON, ILLINOIS

December 2018

© Copyright by Pengcheng Chen 2018  
All Rights Reserved

## ABSTRACT

The Controlled, Site-Isolated Synthesis of Polyelemental Nanostructures in Polymer

Nanoreactors

Pengcheng Chen

Polyelemental nanoparticles are an attractive class of materials due to their potential applications, which span the fields of catalysis, plasmonics, electronics, magnetics, targeted drug delivery, and bio-imaging. However, conventional synthetic methods for such structures are limited, especially when the number of elements exceed three. Moreover, the challenge of systematically exploring polyelemental nanoparticles is daunting, due to the vast compositional and structural parameter space that must be examined to adequately elucidate the governing composition and size structure-property relationships. This thesis focuses on the development of methodology for synthesizing polyelemental nanoparticles in a manner that allows for systematic control over structure and composition and is amenable to high throughput screening.

Chapter One begins with an overview of polyelemental nanoparticles and their importance in chemistry and materials science. State-of-the-art synthetic methods for polyelemental nanostructures are reviewed, along with the applications of such materials in the catalysis field.

Chapter Two describes the concept of scanning probe block copolymer lithography (SPBCL), which allows one to generate metal ion-containing polymer nanoreactors in order to synthesize individual nanoparticles. Using five elements (Au, Ag, Co, Cu, and Ni) as a model system, SPBCL was used to synthesize and study all combinations of the five elements at a fixed particle size. This work is important since it sets the stage for using SPBCL as a novel tool for rapidly synthesizing and exploring entire new classes of polyelemental nanoparticles, and points

toward the ability to rapidly define their structures and corresponding physical and chemical properties. Chapter Three further investigates the formation pathway of polyelemental nanoparticles in nanoreactors. A three-stage nucleation and growth process has been identified as central to particle formation.

Chapter Four reports a library of novel SPBCL-synthesized nanoparticles composed of up to seven elements and four phases. Design rules for engineering the configuration of interfaces in polyelemental heterostructured nanoparticles are enumerated. The power of these rules was demonstrated by synthesizing an unprecedented tetra-phase nanoparticle with a six-interface architecture. Given the importance of heterostructured materials in catalysis and energy, these design rules provide a way of engineering polyelemental systems with unprecedented complexity and control.

Chapter Five describes the scale-up synthesis of polyelemental nanoparticles on centimeter-scale substrates with cantilever-free scanning probe techniques. Nanoparticle arrays with a size gradient are used to demonstrate how this technique can be used for particle library generation and high-throughput catalyst screening.

Finally, Chapter Six provides an outlook on polymer nanoreactor-mediated nanoparticle synthesis and highlights several future research directions.

## ACKNOWLEDGEMENTS

First and foremost, I would like to thank my advisor, Professor Chad A. Mirkin, for giving me the opportunity to work in his rewarding group. I have been afforded unexpected freedom and endless support for my PhD research, including the design of experiments, the evaluation of projects, and most importantly, the communication of scientific work both in writing and oral presentations. This thesis would not have been possible without the guidance from Chad. I also feel very fortunate to have gained wonderful experience in the Mirkin group ranging from writing proposals, attending conferences, to leading a subgroup, which not only broadened my horizons but also helped me to grow as a scientist.

I would like to thank my thesis committee, Professor Vinayak P. Dravid, Professor Kenneth R. Shull, and Professor Justin M. Notestein, for their helpful discussions throughout my PhD studies. In particular, I am very grateful to Professor Dravid for his insightful advice and suggestions on electron microscopy characterization. I would also like to thank my former advisor, Professor Zhi-Kang Xu from Zhejiang University, for introducing me into scientific research and for his continuing support throughout my career.

Special thanks to my mentor, Professor Guoliang Liu, for getting me started in the lab, teaching me all the fundamental skills of DPN, and continuously providing guidance on how to be an independent researcher after graduation.

I would like to thank all my collaborators and friends who have provided invaluable suggestions throughout my PhD career and made graduate school experience much more enjoyable: Dr. Brian Meckes, Dr. Zhuang Xie, Dr. Youngeun Kim, Dr. Keith Brown, Dr. Jessie Ku, Dr. Natalia Chernyak, Dr. Yu Zhou, Jingshan Du, Yuan Liu, James Hedrick, Abha Gosavi, Edward

Kluender, Liban Jibril, Dr. Xing Liao, Dr. Liangliang Hao, Dr. Chuan Zhang, Dr. Shu He, Dr. Xiaozhu Zhou, Dr. Maria Cabezas, Dr. Daniel Eichelsdoerfer, Dr. Xiaolong Liu, Prof. Chris Wolverton, Mohan Liu, Dr. Jinsong Wu, Dr. Qingyuan Lin, Shunzhi Wang, Dr. Haixin Lin, Lin Sun, Wenjie Zhou, Jinghan Zhu, Taegon Oh, Dr. Alejo Lifschitz, Dr. Michael Ross, and Dr. Ryan Thaner. I would also like to thank the Mirkin group staff for keeping everything running smoothly, specifically Dr. Sarah Petrosko, Pam Watson, Dr. Sara Rupich, Dr. Tanushri Sengupta, Elizabeth Forest, Dr. Caroline Ko, and Jorge Belmonte.

Lastly, I want to thank my parents for their endless love and encouragement, and for providing me the opportunity to pursue my dream. I want to thank my girlfriend, Shuya, who lights up my life and always wants the best for me. I would not be who I am, without you.

– Pengcheng

October 2018

## TABLE OF CONTENTS

ABSTRACT.....	3
ACKNOWLEDGEMENTS.....	5
TABLE OF CONTENTS.....	7
LIST OF FIGURES .....	10
Chapter One .....	28
1.1 Motivation and Introduction .....	29
1.2 Catalytic Applications of Polyelemental Nanoparticles .....	30
1.3 Synthetic Methods of Polyelemental Nanoparticles .....	35
1.3.1 Wet Chemical Reduction .....	35
1.3.2 Thermal Decomposition.....	41
1.3.3 Molecular Template Mediated Synthesis.....	41
1.3.4 Lithographic Methods .....	42
Chapter Two.....	48
2.1 Introduction.....	49
2.2 Nanoparticles Composed of Miscible Elements .....	50
2.3 Nanoparticles Composed of Immiscible Elements .....	57
2.3 Composition Control of Nanoparticles Synthesized by SPBCL.....	57
2.4 Synthesis of a Polyelemental Nanoparticle Library.....	59
2.5 Materials and Methods.....	82
2.5.1 Materials .....	82
2.5.2 Preparation of Block Copolymer Inks .....	82
2.5.3 SPBCL Patterning Process.....	82
2.5.4 Characterization .....	83
2.6 Conclusions and Outlook .....	84
Chapter Three.....	85
3.1 Introduction.....	86
3.2 Aggregation of a Single Type of Metal in a Polymer Reactor .....	88
3.3 Aggregation of Two Types of Metal in a Polymer Reactor.....	99
3.4 Aggregation of Three Types of Metal in a Polymer Reactor.....	109

3.5 Materials and Methods.....	113
3.5.1 Materials .....	113
3.5.2 Preparation of Block Copolymer Inks .....	113
3.5.3 SPBCL Patterning Process.....	114
3.5.4 Characterization .....	114
3.6 Conclusions and Outlook.....	115
Chapter Four .....	116
4.1 Introduction.....	117
4.2 Number of Possible Interfaces in Multi-Phase Nanoparticles .....	118
4.3 Tri-Phase Nanoparticles with Two or Three Interfaces .....	125
4.4 Interface Engineering in Tetra-Phase Nanoparticles .....	137
4.5 Materials and Methods.....	151
4.5.1 Materials .....	151
4.5.2 Preparation of Block Copolymer Solution.....	151
4.5.3 Nanoparticle (NP) Synthesis.....	151
4.5.4 Density Functional Theory (DFT) Calculations .....	152
4.5.5 Characterization .....	153
4.6 Conclusions and Outlook .....	154
Chapter Five.....	155
5.1 Introduction.....	156
5.2 Scale-up Synthesis of Polyelemental Nanoparticles.....	158
5.3 Catalytic Reduction of 4-Nitrophenol.....	160
5.4 Hydrogenation of Trans-Cinnamaldehyde.....	162
5.5 Size Screening of AuPd Nanoparticle Catalysts.....	164
5.6 Materials and Methods.....	166
5.6.1 Materials .....	166
5.6.2 Preparation of Block Copolymer Inks .....	166
5.6.3 Polymer Pen Lithography (PPL) Patterning Process .....	166
5.6.4 Catalytic Reduction of 4-Nitrophenol.....	167
5.6.5 Hydrogenation of Cinnamaldehyde .....	168
5.6.6 Removal of Carbon Residue on Nanoparticles .....	168

5.6.7 Characterization .....	169
5.7 Conclusions and outlook.....	169
Chapter Six.....	171
6.1 Tip-Directed Synthesis of Polyelemental Nanoparticle Libraries .....	172
6.2 Structural Evolution of Polyelemental Nanoparticles in Polymer Nanoreactors.....	173
6.3 Heterostructure Engineering in Polyelemental Nanoparticles .....	175
6.4 Combinatorial Synthesis of Polyelemental Nanoparticles for Catalyst Screening .....	175
6.5 Summary .....	176
REFERENCES .....	177
CURRICULUM VITAE.....	192

## LIST OF FIGURES

- Figure 1.1** Mechanism of heterogeneous hydrogenation of ethylene. .... 31
- Figure 1.2** Chemo-selective hydrogenation of unsaturated carbonyl compounds. .... 32
- Figure 1.3** Dependence of nanoparticle catalytic activity on exposed facets. (A) TEM image of tetradecyltrimethylammonium bromide (TTAB)-stabilized cubic Pt particles. (B) TEM image of TTAB-stabilized cuboctahedral Pt particles. (C,D) The turnover rates of cyclohexane and cyclohexene in benzene hydrogenation with cubic and cuboctahedral Pt NPs as catalysts. .... 33
- Figure 1.4** NiZn bimetallic catalysts for hydrogenation of acetylene. (A) Measured concentration of ethane (byproduct) at the reactor outlet as a function of acetylene conversion for seven catalysts. (B,C) Modeling of the adsorption of acetylene (B) and ethylene (C) on NiZn catalysts (blue: Ni; gray: Zn; black: C; white: H). .... 34
- Figure 1.5** Uniform bimetallic nanoparticles synthesized by chemical co-reduction method. (A-D) TEM, HRTEM, HAADF-STEM images, and size distribution of (A-D) PtNi<sub>2</sub> octahedrons, (E-H) PtNi<sub>2</sub> truncated octahedrons, and (I-L) PtNi<sub>2</sub> cubes. Element maps show the distribution of Pt in yellow and Ni in red. .... 37
- Figure 1.6** Pt@SiO<sub>2</sub> core-shell nanoparticles synthesized by stepwise method. (A) Schematic representation of the synthesis of Pt@SiO<sub>2</sub> core-shell nanoparticles. (B-D) TEM images of Pt@SiO<sub>2</sub> nanoparticles after calcination at 350°C, 550°C, and 750°C, respectively. .... 39
- Figure 1.7** Non-centrosymmetric heterostructured nanoparticles synthesized by stepwise method. (A-D) Structural model, HRTEM image, and single-point EDS of each type of nanoparticles. In HRTEM images, color-dashed curves outline boundaries of different subunits, and solid color lines highlight lattice orientations of each subunit. (E) Time-dependent normalized optical density of methylene blue molecules (reactant) at 677 nm with different photocatalysts. .... 39
- Figure 1.8** A library of heterostructured nanoparticles synthesized by stepwise cation-exchange. (A) Schematic representation of using cation-exchange reactions to create complex heterostructured nanoparticles with CuS nanosphere, nanorod, and nanodisc as the starting materials. Cu (red), Cd (blue), Zn (green), Ag (pink), Mn (Cyan), Ni (orange), Co (purple). (B-D) Complex nanostructures formed by combining multiple cation exchange steps with regioselective deposition or etching. Cu, Cd, Pt, and Au are shown in red, blue, green, and yellow, respectively. .... 40
- Figure 1.9** Schematic representation of dip-pen nanolithography (DPN). A water meniscus forms between a solid substrate and an AFM tip that is coated with molecule ink. The size of the meniscus, which is controlled by relative humidity, affects the ink transport rate, the effective tip-substrate contact area, and the DPN resolution. .... 43
- Figure 1.10** (A) Schematic illustration of the direct writing of nanoparticles by DPN. (B) AFM topographic image of one patterned dot with multiple nanoparticles inside. .... 44

**Figure 1.11** (A) Schematic illustration of polymer-mediated synthesis of nanoparticles by SPBCL. The method consists of four steps: precursor loading, polymer deposition, precursor aggregation, and particle formation. (B) Heating profile of the annealing process. The two heating cycles ( $\Delta 1$  and  $\Delta 2$ ) correspond to the cycles at  $T_{\text{low}}$  and  $T_{\text{high}}$  in (A). (C) SEM image of Au nanoparticles produced by SPBCL. (Inset) Fourier transform of the SEM image. (D) High-resolution TEM image showing a crystalline Au nanoparticle with a diameter of 8 nm. (Inset) Electron diffraction pattern of the synthesized Au nanoparticle. .... 45

**Figure 1.12** XPS spectra collected before annealing (black), after annealing at  $T_{\text{low}}$  (blue), and after annealing at  $T_{\text{high}}$  (red) for Au (Left), Pt (Center), and Fe (Right) to show the three chemical pathways of forming nanoparticles in SPBCL. .... 46

**Figure 2.1** Representative SPBCL process for preparing an alloy nanoparticle array. (A) SEM image of nanoreactors patterned on a hydrophobic silicon substrate. (B) AFM topographical image of a patterned polymer dot array. The diameter and height of the dots are 300 nm and 80 nm, respectively. (C) Enlarged SEM view of six polymer nanoreactors. (D) After annealing, metal precursors aggregate inside the polymer nanoreactors. (E) Further thermal annealing reduces the precursors and decomposes the polymer to form arrays of single nanoparticles. .... 50

**Figure 2.2** Representative SEM images of arrays of various alloy nanoparticles synthesized by SPBCL. Each image shows a 6-by-4 array of nanoparticles. .... 52

**Figure 2.3** Various 1:1 alloy nanoparticles generated by SPBCL: (A) AuPd, (B) PtNi, (C) PdNi, (D) PtCo, (E) PdCo, (F) CoNi. (First column) HAADF-STEM images of a 2-by-2 nanoparticle array of each system. Dotted circles highlight the position of nanoparticles as a guide to the eye. The insets are zoomed-in images of single alloy nanoparticles. Only one nanoparticle was observed at each site. One scale bar applies to the insets and the other applies to square array STEM images. (Second to fourth columns) EDS elemental mapping of each bimetallic nanoparticle (scale bar: 5 nm). .... 54

**Figure 2.4** EDS spectra of various alloy nanoparticles synthesized by SPBCL. .... 55

**Figure 2.5** HAADF-STEM image of a square array of AuPd nanoparticles. The EDS elemental mapping images corresponding to the nanoparticles at each corner. Color codes: Au (yellow), Pd (red). .... 56

**Figure 2.6** (A) SPBCL pattern of an array of AuAgPd trimetallic nanoparticles imaged by HAADF-STEM and (B) bright-field STEM. (C) EDS elemental mapping of a single AuAgPd nanoparticle. The overlay of Au, Ag, and Pd signals provides evidence for the alloying of these three elements. .... 56

**Figure 2.7** (A) SPBCL pattern of a AuNi nanoparticle array imaged by HAADF-STEM. Dotted circles highlight the position of nanoparticles as a guide to the eye. (B) Enlarged view of a single AuNi nanoparticle. (C) EDS elemental mapping of a single AuNi nanoparticle showing that the nanoparticle is phase-segregated. .... 57

**Figure 2.8** Atomic composition in alloy nanoparticles versus atomic composition in polymer ink. The black dashed line indicates the ideal case. .... 58

**Figure 2.9** The SPBCL-mediated synthesis of multimetallic nanoparticles. (A) Scheme depicting the process: a polymer loaded with metal ion precursor is deposited onto a substrate in the shape of a hemispherical dome *via* dip-pen nanolithography. After two-step thermal annealing, the metal precursors are aggregated and reduced, the polymer is decomposed, and individual nanoparticles result from each dome feature. (B) Unary (top row is a color-coded diagram of the anticipated result; bottom row is each particle, as characterized by EDS Mapping), (C) Binary nanoparticles consisting every two element combination of the five metals; the alloy versus phase-segregated state was consistent with the bulk phase diagrams for each two element combination, (D) Ternary nanoparticles consisting of every three element combination of the five metals; the prediction of alloy versus phase-segregated state was based upon the miscibility of the three components, extracted from the binary data, (E) Quaternary nanoparticles consisting of every four element combination of the five metals; the prediction of alloy versus phase-segregated state was based upon the miscibility of the four components, extracted from the binary and ternary data, and (F) A quinary nanoparticle consisting of a combination of Au, Ag, Cu, Co, and Ni; the prediction of alloy versus phase-segregated state was based upon all of the previous data for the unary through quaternary systems..... 60

**Figure 2.10** HAADF-STEM images and EDS spectra of the unary nanoparticles in Figure 2.9B. (A) Au, (B) Ag, (C) Cu, (D) Co, (E) Ni. Scale bars: 15 nm. .... 61

**Figure 2.11** HAADF-STEM images, EDS spectra, and detailed EDS mapping information of the binary nanoparticles in Figure 2.9C. (A)  $\text{Au}_{0.48}\text{Ag}_{0.52}$ , (B)  $\text{Au}_{0.55}\text{Co}_{0.45}$ , (C)  $\text{Au}_{0.54}\text{Ni}_{0.46}$ , (D)  $\text{Au}_{0.49}\text{Cu}_{0.51}$ , (E)  $\text{Ag}_{0.42}\text{Cu}_{0.58}$ , (F)  $\text{Ag}_{0.57}\text{Ni}_{0.43}$ , (G)  $\text{Ag}_{0.63}\text{Co}_{0.37}$ , (H)  $\text{Cu}_{0.58}\text{Ni}_{0.42}$ , (I)  $\text{Cu}_{0.41}\text{Co}_{0.59}$ , (J)  $\text{Co}_{0.60}\text{Ni}_{0.40}$ . Scale bars: 15 nm. .... 63

**Figure 2.12** HAADF-STEM images, EDS spectra, and detailed EDS mapping information of the ternary nanoparticles in Figure 2.9D. (A)  $\text{Au}_{0.23}\text{Cu}_{0.17}\text{Ni}_{0.60}$ , (B)  $\text{Au}_{0.25}\text{Ag}_{0.19}\text{Co}_{0.56}$ , (C)  $\text{Au}_{0.21}\text{Cu}_{0.35}\text{Co}_{0.44}$ , (D)  $\text{Au}_{0.32}\text{Co}_{0.29}\text{Ni}_{0.39}$ , (E)  $\text{Ag}_{0.48}\text{Co}_{0.28}\text{Ni}_{0.24}$ , (F)  $\text{Ag}_{0.50}\text{Cu}_{0.25}\text{Ni}_{0.25}$ , (G)  $\text{Cu}_{0.33}\text{Co}_{0.52}\text{Ni}_{0.15}$ , (H)  $\text{Au}_{0.24}\text{Ag}_{0.24}\text{Ni}_{0.52}$ , (I)  $\text{Ag}_{0.35}\text{Cu}_{0.38}\text{Co}_{0.27}$ , (J)  $\text{Au}_{0.29}\text{Ag}_{0.37}\text{Cu}_{0.34}$ . Scale bars: 15 nm. The STEM images and EDS mapping information of (H-J) are shown in Figure 2.13 and Figure 2.25. .... 64

**Figure 2.13** AuAgNi and AgCuCo heterostructured nanoparticles generated by SPBCL. (A) HAADF-STEM image and EDS elemental mapping, and (B) schematic illustration of a representative AuAgNi nanoparticle ( $\text{Au}_{0.24}\text{Ag}_{0.24}\text{Ni}_{0.52}$ ). (C) HRTEM image of a AuAgNi nanoparticle. The observed lattice spacings near the interface are 2.36 Å and 2.02 Å, which closely match the AuAg alloy (111) and Ni (111) planes, respectively. (D) A comparison of the nanoparticle composition (20-60nm) with the precursor ink composition. The dashed black line is the ideal 1:1 correlation case. (E) HAADF-STEM image and corresponding EDS mapping of AuAgNi nanoparticles as a function of Ni content. Scale bars: 10 nm. (F) EDS elemental mapping, (G) schematic illustration, and (H) HAADF-STEM image of a representative AgCuCo nanoparticle ( $\text{Ag}_{0.35}\text{Cu}_{0.38}\text{Co}_{0.27}$ ). The Ag, Cu, and Co are immiscible with each other, resulting in a heterotrimer. (I) Dark-field STEM images and EDS elemental mapping of AgCuCo nanoparticles consisting of different compositions. From left to right, the content of Cu is approximately constant at 45% while the content of Ag is 39%, 25%, and 14%, respectively. Scale bars: 15 nm. .... 65

**Figure 2.14** EDS elemental mapping of four neighboring AuAgNi nanoparticles in an array. All four of nanoparticles are heterodimers where one domain is AuAg alloy and the other domain is Ni. Color codes: Au (yellow), Ag (red), Ni (green). Scale bars of insets: 10 nm..... 66

**Figure 2.15** HAADF-STEM images and the corresponding EDS elemental mapping of a AuAgNi nanoparticle. (A) AuAgNi nanoparticle generated by the regular SPBCL process. (B) The same nanoparticle after being thermally annealed at 300 °C in O<sub>2</sub> for 12h. Scale bars: 20 nm. (C) XPS spectra of AuAgNi nanoparticles made by drop-casting polymer ink solution after the thermal annealing process used in SPBCL (black line), and then the same sample after being further thermally annealed at 300 °C in O<sub>2</sub> for 12h (red line). ..... 67

**Figure 2.16** Compositional diagrams assessing the uniformity of SPBCL-generated AuAgNi nanoparticles. The metal loading ratio of the ink solution is: (A) 40% Au, 40% Ag, 20% Ni, (B) 33% Au, 33% Ag, 33% Ni, (C) 25% Au, 25% Ag, 50% Ni, (D) 17% Au, 17% Ag, 66% Ni, and (E) 10% Au, 10% Ag, 80% Ni. (sample size: 50 for each composition). The composition of the nanoparticles follows the composition of the ink solution. .... 68

**Figure 2.17** (A, B) DF-STEM images of AuAgNi nanoparticles synthesized from bulk polymer ink solution with the two-step annealing procedure used in SPBCL. (C) The EDS spectra of the two nanoparticles in B, showing that bulk synthesis results in a mixture of different types of nanoparticles. (D) The compositional uniformity of the AuAgNi nanoparticles synthesized from bulk polymer ink solution (sample size: 50). ..... 69

**Figure 2.18** (A, B) DF-STEM images of AgCuCo nanoparticles synthesized from a bulk polymer ink solution with the two-step annealing procedure used in SPBCL. (C) EDS spectra of the two nanoparticles in B, showing that bulk synthesis results in a mixture of different types of nanoparticles. (D) The compositional uniformity (or lack thereof) of the AgCuCo nanoparticles synthesized from bulk polymer ink solution (sample size: 50). ..... 70

**Figure 2.19** Incomplete coalescing of metal precursors results in multiple nanoparticles forming within a single polymer dome. (A) HAADF-STEM image of multiple AuAgCoNi nanoparticles formed in one large polymer dot. The polymer dot was prepared from an ink solution with a metal loading ratio of 25% Au, 25% Ag, 25% Co, and 25% Ni. The circle highlights the contour of original polymer reactor. (B) Zoomed-in HAADF-STEM image of four representative nanoparticles. (C) EDS elemental mapping of the four nanoparticles. Color codes: Au (yellow), Ag (red), Ni (green), Co (cyan). (D) Overlay of the element maps of Au, Ag, Co, and Ni. .... 70

**Figure 2.20** (A) Compositional uniformity of SPBCL-generated AgCuCo nanoparticles (sample size: 50). The metal loading ratio of the ink solution is: 33% Ag, 33% Cu, and 33% Co. (B) EDS elemental mapping of nine neighboring AgCuCo nanoparticles in an array. All nanoparticles are heterotrimers where Ag, Cu, and Co segregate into three segments. Color codes: Ag (red), Cu (purple), Co (cyan). Scale bars in EDS mapping images: 15 nm. .... 71

**Figure 2.21** HAADF-STEM images and EDS elemental mapping of a AgCuCo nanoparticle. (A) AgCuCo nanoparticle generated by annealing at 500 °C in H<sub>2</sub> for 12h. (B) The same nanoparticle after being thermally annealed at 300 °C in O<sub>2</sub> for 12h. Scale bars: 20 nm. (C) XPS spectra of AgCuCo nanoparticles made by drop-casting polymer ink solution followed by the thermal

annealing process used in SPBCL (black line) and the same sample after being further thermally annealed at 300 °C in O<sub>2</sub> for 12h (red line). ..... 72

**Figure 2.22** Nonparallel phase boundaries in AgCuCo nanoparticles generated by SPBCL. (A) Dark-field STEM image and corresponding EDS elemental mapping of a AgCuCo nanoparticle with nonparallel phase boundaries. Dashed lines highlight the position of Ag-Cu phase boundary and Cu-Co phase boundary. The two interfaces are perpendicular with respect to image plane. Inset: scheme depicting the proposed structure of this nanoparticle. (B) Another representative AgCuCo nanoparticle with nonparallel phase boundaries. Here, the Cu-Co interface is perpendicular to the image plane while the Ag-Cu interface is inclined with respect to the image plane. Inset: scheme depicting the proposed structure of this nanoparticle..... 73

**Figure 2.23** (A) HRTEM image of the interface between Ag and Cu in a AgCu nanoparticle. The observed lattice spacings near the interface are 2.34 Å and 2.08 Å (extracted from FFT), which closely match the Ag (111) and Cu (111) planes. The inset shows the particle with the zoomed-in region indicated with a dashed square. (B) HRTEM image of the interface between AuCu and Co in a AuCuCo nanoparticle. Cu and Co have a very close lattice parameter and similar atomic number contrast in HRTEM. It is difficult to directly identify the Cu-Co interface in a CuCo nanoparticle using HRTEM. Here, 15% Au was added into CuCo nanoparticles to increase the contrast between Cu domain and Co domain. The observed lattice spacing around the interface are 2.21 Å and 2.03 Å, which can be assigned to the AuCu (111) and Co (111) planes. The inset shows the particle with the zoomed-in region indicated with a dashed square. .... 73

**Figure 2.24** SPBCL AgCuCo nanoparticle with low Cu content and three phase boundaries. (A) Dark-field STEM image of a AgCuCo nanoparticle (Ag<sub>0.43</sub>Cu<sub>0.19</sub>Co<sub>0.38</sub>). Inset: scheme depicting the structure of this nanoparticle. (B) EDS elemental mapping of the nanoparticle. (C) Overlay of the element maps of Ag, Cu, and Co. (D) Overlay of the element maps of Ag and Co. (E) Overlay of the element maps of Cu and Co. Dotted circles highlight the position of Ag-Co phase boundary. When the content of Cu is less than 20% in AgCuCo nanoparticles, the amount of Cu is not enough to fully block the contact between Ag and Co. Consequently, a AgCuCo nanoparticle with Ag-Cu, Cu-Co, and Ag-Co phase boundaries is observed. .... 74

**Figure 2.25** AuAgCu heterostructured nanoparticles. (A-D) Schematic illustration, HAADF-STEM images and EDS elemental mapping of four representative AuAgCu nanoparticles with different Au content. From A to D, the Ag content and Cu content are equal in each nanoparticle while the Au content is 10%, 30%, 50%, and 70%, respectively. Scale bars: 20 nm. .... 75

**Figure 2.26** (A) Compositional uniformity of SPBCL-generated AuAgCu nanoparticles (sample size: 50). The metal loading ratio of the ink solution is: 20% Au, 40% Ag, and 40% Cu. (B) EDS elemental mapping of nine neighboring AuAgCu nanoparticles in an array. The nanoparticles are heterodimers where one domain is a AuAg alloy and the other domain is a AuCu alloy. Au is mainly concentrated in the AuCu domain. Color codes: Au (yellow), Ag (red), Cu (purple). Scale bars in EDS mapping images: 10 nm..... 76

**Figure 2.27** HAADF-STEM images and corresponding EDS elemental mapping of a AuAgCu nanoparticle. (A) AuAgCu nanoparticle generated by annealing at 500 °C in H<sub>2</sub> for 12 h. (B) The same nanoparticle after being thermally annealed at 300 °C in O<sub>2</sub> for 12 h. Scale bars: 20 nm. (C)

XPS spectra of AuAgCu nanoparticles made by drop-casting a polymer ink solution followed by the thermal annealing process used in SPBCL (black line) and the same sample after being further thermally annealed at 300 °C in O<sub>2</sub> for 12h (red line). ..... 77

**Figure 2.28** HAADF-STEM images, EDS spectra, and detailed EDS mapping information of the quaternary and quinary nanoparticles in Figure 2.9E and 2.9F. (A) Au<sub>0.32</sub>Ag<sub>0.19</sub>Cu<sub>0.27</sub>Ni<sub>0.22</sub>, (B) Ag<sub>0.27</sub>Cu<sub>0.22</sub>Co<sub>0.35</sub>Ni<sub>0.16</sub>, (C) Au<sub>0.26</sub>Ag<sub>0.22</sub>Co<sub>0.16</sub>Ni<sub>0.36</sub>, (D) Au<sub>0.15</sub>Ag<sub>0.29</sub>Cu<sub>0.18</sub>Co<sub>0.38</sub>, (E) Au<sub>0.23</sub>Cu<sub>0.42</sub>Co<sub>0.16</sub>Ni<sub>0.19</sub>, (F) Au<sub>0.19</sub>Ag<sub>0.24</sub>Cu<sub>0.28</sub>Co<sub>0.14</sub>Ni<sub>0.15</sub>. Scale bars: 15 nm. The STEM images and EDS mapping information of (F) are shown in Figure 2.29. .... 78

**Figure 2.29** Quinary heterostructured nanoparticles (A) HAADF-STEM image of a typical AuAgCuCoNi nanoparticle (Au<sub>0.19</sub>Ag<sub>0.24</sub>Cu<sub>0.28</sub>Co<sub>0.14</sub>Ni<sub>0.15</sub>). (B) Schematic illustration of the structure of AuAgCuCoNi nanoparticle in (A). The nanoparticle phase segregates into three domains: AuAg alloy, AuCu alloy, and CoNi alloy. (C-G) EDS elemental mapping of the AuAgCuCoNi nanoparticle in (A). (C) Distribution of each metal inside the nanoparticle. (D) Overlay of the element maps of Au, Ag, and Cu. (E) Overlay of the element maps of Ag, Cu, and Co. (F) Overlay of the element maps of Co and Ni. (G) Overlay of the element maps of all five metals. .... 80

**Figure 2.30** EDS elemental mapping of a AuAgCuCoNi nanoparticle. Scale bar: 15 nm. The phase boundary between AuAg alloy and AuCu alloy is not parallel with the phase boundary between AuCu alloy and CoNi alloy. Dashed lines highlight the position of phase boundaries. .... 81

**Figure 2.31** Compositional uniformity of SPBCL-generated AuAgCuCoNi nanoparticles (sample size: 50). The metal loading ratio of the ink solution is: 20% Au, 20% Ag, 20% Cu, 20% Co, and 20% Ni. Since EDS has an inherent error of less than 5% due to x-ray absorption and fluorescence, only elements with content larger than 5% are considered as an effective component when counting the number of components in particles. .... 81

**Figure 3.1** Nucleation and growth of monometallic nanoparticles in polymer nanoreactors. (A) A scheme of the nucleation and growth process. (B) Ex-situ ADF-STEM images of the aggregation and growth of Au nanoparticles in polymer features annealed at 100 °C. Dashed circles indicate the edge of polymer features. Scale bar: 300 nm. (C,D) The number (C) and average diameter (D) of the nanoparticles formed in polymer features annealed at 100 °C. The assignment of Stage I and II in (C) and (D) applies to the polymer features with diameters of 1500 nm. .... 88

**Figure 3.2** Remaining free Au in polymer features (1.5 μm) annealed at 100 °C over time. The remaining Au content was calculated by comparing the diameters of intermediate particles to the diameters of the final particles (assuming all Au precursors in a reactor aggregated to form the final particle). The molar ratio between HAuCl<sub>4</sub> and PEO-*b*-P2VP in the starting polymer nanoreactors is 1:4.48. .... 89

**Figure 3.3** Ex-situ ADF-STEM images of Au aggregation in polymer features annealed at 100 °C over time. Dashed circles mark the edge of polymer nanoreactors. .... 89

**Figure 3.4** (A) The number of nanoparticles and (B) the average diameter of nanoparticles formed in polymer features annealed at 100 °C over time. Solid curves are guide to the eye. The

assignments of Stage I and II in (A) and (B) apply only to polymer nanoreactors with diameters of 550 nm and 800 nm. For polymer features with a diameter of 300 nm, Stage I is not observed. This observation suggests that the polymer nanoreactor is not large enough for nucleation of more than one particle. .... 90

**Figure 3.5** An ADF-STEM image of an 8-by-6 array of polymer nanoreactors containing Au salt precursor. The polymer nanoreactors were annealed at 100 °C for 1h to form a single Au NP in each nanoreactor. Scale bar: 3 μm. .... 91

**Figure 3.6** (A) An ADF-STEM image of a NaCl/KCl particle formed in a blank polymer nanoreactor annealed at 100 °C for 1h. The dashed circle marks the edge of the polymer nanoreactor. An EDS spectrum of the crystal is shown underneath the STEM image. Al signals are from the TEM sample holder. (B) An ADF-STEM image of a polymer nanoreactor annealed at 100 °C for 1h. The polymer was purified by dialysis with deionized water for 48 h (ThermoFisher dialysis cassettes, 2K MWCO). The dashed circle marks the edge of the polymer nanoreactor. EDS characterization of the polymer reactor shows no observable Na, K, and Cl signals. .... 91

**Figure 3.7** (A) Ex-situ ADF-STEM images of the aggregation of Au in polymer nanoreactors annealed at 100 °C. Dashed circles indicate the edge of the polymer nanoreactors. Scale bar: 400 nm. (B) Ex-situ ADF-STEM images of the aggregation of Au in polymer nanoreactors annealed at 150 °C. Dashed circles indicate the edge of polymer nanoreactor. Scale bar: 400 nm. (C) The average diameter and number of nanoparticles formed in polymer nanoreactors annealed at 100 °C and 150 °C. .... 92

**Figure 3.8** Ex-situ ADF-STEM images of the aggregation process for (A) Au and (B) Ag precursors in polymer nanoreactors annealed at 120 °C. Dashed circles indicate the edge of polymer nanoreactor. Scale bars: 200 nm. (C) Enlarged views of the aggregated particles within the nanoreactors in (B). Scale bar: 50 nm. .... 93

**Figure 3.9** (A) An ADF-STEM image of the particles formed in a single polymer nanoreactor that contains Ag precursor ( $\text{AgNO}_3$ ). The polymer feature was annealed at 120 °C for 30 min. EDS spectra of the particles reveal the presence of a Ag/AgCl/NaCl mixture along with Ag, and NaCl particles. Al signals are from the TEM sample holder. (B) HRTEM images of the AgCl and KCl/NaCl particles formed in polymer nanoreactors that were annealed at 120 °C for 30 min. The observed lattice spacings are 3.17 Å and 3.60 Å, which correspond to AgCl (111) and KCl (111) planes, respectively. .... 94

**Figure 3.10** (A-F) ADF-STEM images of representative polymer nanoreactors that contain  $\text{Cu}(\text{NO}_3)_2$  subjected to thermal treatment. (G) A Cu 2p XPS spectrum of particles formed by thermally annealing a drop-cast polymer ink solution that contains the Cu precursor at 260 °C for 18h. .... 95

**Figure 3.11** Comparison of the aggregation rates during the formation of different monometallic nanoparticles. (A-C) ADF-STEM images showing the aggregation of Au, Ag, or  $\text{Cu}^{\text{II}}$  species in polymer features annealed at 240 °C. Dashed circles indicate the edge of polymer features. Scale

bar: 200 nm. (D-E) The average diameter (D) and number (E) of the nanoparticles formed in polymer features annealed at 240 °C. Dashed curves are guide to the eye. .... 96

**Figure 3.12** (A) The average diameter and (B) number of nanoparticles formed in polymer nanoreactors (diameters ~ 1 μm) using either AgNO<sub>3</sub> or Cu(NO<sub>3</sub>)<sub>2</sub> precursors that were annealed at 240 °C. Dashed curves are guide to the eye..... 96

**Figure 3.13** Remaining free metal species in polymer nanoreactors that contain one type of precursor and are annealed at 240 °C. (A) Amount of free Ag in polymer features (1 μm). (B) Amount of free Cu in polymer features (1 μm). For each monometallic system, the molar ratio between the metal precursor and PEO-*b*-P2VP in the starting polymer nanoreactors is 1:4.48. The remaining Ag or Cu content was calculated by comparing the diameters of intermediate particles to the final particles (assuming all metal precursors in a reactor aggregate to form the final particle). ..... 97

**Figure 3.14** EDS spectra of the initially nucleated nanoparticles in Figure 2. (A) Au and (B) Ag nanoparticles formed in polymer nanoreactors that were annealed at 240 °C for 1 h. (C) Cu<sup>II</sup> nanoparticles formed in a polymer nanoreactor that was annealed at 240 °C for 2 h. The Al signals in the spectra are from the TEM sample holder..... 98

**Figure 3.15** (A) ADF-STEM image of a representative polymer nanoreactor that contains equal amounts of the metal salt precursors, HAuCl<sub>4</sub> and AgNO<sub>3</sub>, annealed at 120 °C for 30 min. The white dashed circle indicates the edge of the polymer nanoreactor. (B) STEM images along with EDS elemental maps are shown for the particles located within the yellow dashed squares in (A). ..... 99

**Figure 3.16** Formation of AuAg nanoparticles in polymer nanoreactors. (A) ADF-STEM images of representative polymer features that contain either equal amounts of HAuCl<sub>4</sub> and AgNO<sub>3</sub>, only HAuCl<sub>4</sub>, or only AgNO<sub>3</sub> metal salt precursors. The features were annealed at 120 °C for 2h. White dotted circles indicate the edge of polymer features. (B) EDS elemental maps of the AuAg particles located inside the yellow dashed squares in (A). (C) An ADF-STEM image of a polymer feature that contains equal amounts of the metal salt precursors, HAuCl<sub>4</sub> and AgNO<sub>3</sub>, annealed at 160 °C for 4h. (D) ADF-STEM images and EDS elemental maps of the AuAg particle (Au<sub>0.51</sub>Ag<sub>0.49</sub>, atomic composition) located inside a yellow dashed square in (C). The particle was stepwise annealed at (i) 160 °C for 4h, (ii) 160 °C for 18h, and (iii) 260 °C for 4h. (E) Schematic of the structural evolution of AuAg nanoparticles in polymer nanoreactors deposited with SPBCL. . 100

**Figure 3.17** An ADF-STEM image of particles formed in a representative polymer nanoreactor that contains equal amounts of the metal salt precursors, HAuCl<sub>4</sub> and Cu(NO<sub>3</sub>)<sub>2</sub>, annealed at 160 °C for 1 h. Inset: An ADF-STEM image of the polymer nanoreactor containing the nanoparticles. The white dashed circle indicates the edge of the polymer nanoreactor. A primary nucleated particle is observed in the polymer nanoreactor along with some small Cu<sup>II</sup> particles that contribute to coarsening as the reactor is heated. EDS elemental mapping of the primary particle is shown in Figure 3.18. .... 103

**Figure 3.18** ADF-STEM images and EDS elemental maps of representative primary particles formed in polymer nanoreactors that contain equal amounts of the metal salt precursors, HAuCl<sub>4</sub>

and  $\text{Cu}(\text{NO}_3)_2$ , annealed in different conditions: (A) 160 °C for 1h, particle contains 72% Au and 28% Cu and (B) 160 °C for 18h, particle contains 54% Au and 46% Cu, (C) 200 °C for 4h, particle contains 50% Au and 50% Cu, (D) 240 °C for 4h, particle contains 50% Au and 50% Cu, (E) 260 °C for 4h, particle contains 53% Au and 47% Cu. Scale bars: 10 nm. The particle obtained after annealing at 160 °C for 1h has more Au content compared to the other conditions, suggesting that Au aggregates at a faster rate than the Cu species. .... 104

**Figure 3.19** Formation of AuCu nanoparticles in polymer nanoreactors. (A-E) ADF-STEM images and EDS elemental maps of a AuCu particle (44% Au, 56% Cu, atomic composition) formed in a representative polymer feature that contains equal amounts of the metal salt precursors,  $\text{HAuCl}_4$  and  $\text{Cu}(\text{NO}_3)_2$ . White dashed circles indicate the edge of polymer features. The polymer feature was stepwise annealed at (A) 160 °C under Ar for 4 h, (B) 240 °C under Ar for 2 h, (C) 240 °C under Ar for 2 h, (D) 260 °C under Ar for 2 h, and (E) 500 °C under  $\text{H}_2$  for 12 h. Scale bars: 10 nm. (F) Au 4f and Cu 2p XPS spectra of particles synthesized by thermally annealing a drop-cast polymer ink solution at 260 °C for 18 h. Red lines correspond to polymer ink containing both Au and Cu precursors. Black lines correspond to polymer inks containing only one type of precursor. (G) HRTEM image of a AuCu nanoparticle in a polymer feature that is formed by being annealed at 260 °C for 18h. The observed lattice spacing is 1.99 Å (extracted from fast Fourier transform), which closely matches the AuCu alloy (200) plane. .... 105

**Figure 3.20** Formation of AgCu nanoparticles in polymer nanoreactors. (A) ADF-STEM images and (B) EDS elemental maps of a particle formed in a representative polymer feature annealed at 160 °C for 4 h that contains equal amounts of the metal salt precursors,  $\text{AgNO}_3$  and  $\text{Cu}(\text{NO}_3)_2$ . White dashed circles indicate the edge of the polymer feature. (C) Ag 3d and Cu 2p XPS spectra of particles synthesized by thermally annealing a drop-cast polymer ink solution at 260 °C for 18h. Red lines correspond to polymer ink containing both Ag and Cu precursors. Black lines correspond to polymer inks that contain only one type of precursor. (D-G) ADF-STEM images and EDS elemental maps of a AgCu particle (55% Ag, 45% Cu, atomic composition) formed in a representative polymer feature that was stepwise annealed at (D) 160 °C under Ar for 18 h, (E) 260 °C under Ar for 2 h, (F) 260 °C under Ar for 4 h, and (G) 500 °C under  $\text{H}_2$  for 12 h. Scale bars: 15 nm. (H) Schematic depicting the structural evolution of AgCu nanoparticles in polymer features during thermal treatment. .... 107

**Figure 3.21** (A,B) EDS spectra of (A) AuCu and (B) AgCu nanoparticles obtained after annealing polymer nanoreactors at 500 °C under  $\text{H}_2$  for 12 h to achieve their final structures. Al signals are from the TEM sample holder. (C,D) Cu 2p XPS spectra of (C) AuCu and (D) AgCu particles formed by thermally annealing a drop-cast polymer ink solution at 500 °C under  $\text{H}_2$  for 12 h. 108

**Figure 3.22** ADF-STEM images and corresponding EDS elemental mapping of representative kinetic AgCu nanoparticles formed in nanoreactors annealed at 160 °C for 18 h and then 260 °C for 2 h. Scale bars: 15nm. Ag aggregates faster and always enriches in the center of the particles while Cu mainly adsorbs on the periphery of the particles. Since the kinetic particles are formed through random aggregation of particles/atoms, the morphology varies from particle to particle. .... 108

**Figure 3.23** (A-C) ADF-STEM images and EDS elemental maps of particles formed in representative polymer nanoreactors that contain equal amounts of  $\text{HAuCl}_4$ ,  $\text{AgNO}_3$ , and  $\text{Cu}(\text{NO}_3)_2$  precursors. (A) A polymer nanoreactor annealed at 260 °C under Ar for 0.5h, resulting in a particle composed of 48% Au, 43% Ag, and 9% Cu. (B) A polymer nanoreactor annealed at 260 °C under Ar for 4h, resulting in a particle composed of 36% Au, 39% Ag, and 25% Cu. (C) The particle in (B) was further annealed at 500 °C under  $\text{H}_2$  for 12h. Scale bars: 20 nm. .... 109

**Figure 3.24** Formation of AuAgCu nanoparticles in polymer nanoreactors. (A-D) ADF-STEM images and EDS elemental maps of a AuAgCu particle (33% Au, 39% Ag, 28% Cu, atomic composition) formed in a representative polymer feature that contains equal amounts of the metal salt precursors,  $\text{HAuCl}_4$ ,  $\text{AgNO}_3$ , and  $\text{Cu}(\text{NO}_3)_2$ . The polymer nanoreactor was stepwise annealed at (A) 260 °C under Ar for 1.5 h, (B) 260 °C under Ar for 2 h, (C) 260 °C under Ar for 3 h, and (D) 500 °C under  $\text{H}_2$  for 12 h. Scale bars: 20 nm. .... 110

**Figure 3.25** ADF-STEM images and corresponding EDS elemental mapping of representative kinetic AuAgCu nanoparticles formed in nanoreactors annealed at 260 °C for 3 h. Scale bars: 15nm. Au and Ag aggregate faster and always enrich in the center of the particles while Cu mainly localizes on the periphery of the particles. .... 111

**Figure 3.26** Au 4f, Ag 3d, and Cu 2p XPS spectra of particles formed by thermally annealing a drop-cast polymer ink solution containing equal molar amounts of  $\text{HAuCl}_4$ ,  $\text{AgNO}_3$ , and  $\text{Cu}(\text{NO}_3)_2$  at 260 °C for 2 h. The Au and Ag components in nanoparticles annealed at 260 °C for 2h are in the metallic state while the Cu component is in the  $\text{Cu}^0$  and  $\text{Cu}^{\text{II}}$  states. .... 111

**Figure 3.27** EDS elemental analysis of the AuAgCu particle shown in Figure 3.24. (A-D) ADF-STEM images and EDS elemental maps. The particle was annealed stepwise at 260 °C under Ar for 1.5 h, 260 °C under Ar for 2 h, 260 °C under Ar for 3 h, and 500 °C under  $\text{H}_2$  for 12 h. White dashed rectangles in the EDS maps enclose the main part of the particle that excludes the  $\text{Cu}^{\text{II}}$  clusters on the fringe. Yellow dashed rectangles enclose the entire particle. Scale bars: 20nm. (E) The composition of the part of the particle within white dashed rectangles. (F) The composition of the entire particle enclosed in the yellow dashed rectangles. From (A) to (D), the content of Cu in the particle (yellow dashed rectangle) changes slightly from 24% to 28%, while the content of Cu in the main portion of the particle (white dashed rectangles) increases from 13% to 28%, suggesting that the  $\text{Cu}^{\text{II}}$  clusters on the fringe diffuse into the main part during thermal annealing. .... 112

**Figure 3.28** ADF-STEM images and EDS elemental maps of a AuAgCu particle (48% Au, 26% Ag, 26% Cu) formed in a polymer nanoreactor that contains the metal salt precursors,  $\text{HAuCl}_4$ ,  $\text{AgNO}_3$ , and  $\text{Cu}(\text{NO}_3)_2$  (molar ratio 50%:25%:25%), that were stepwise annealed under different conditions: (A) 260 °C under Ar for 4h, (B) 260 °C under Ar for 2h, and (C) 500 °C under  $\text{H}_2$  for 12h. Scale bars: 20 nm. .... 113

**Figure 4.1** Configuration of interfaces in multi-phase nanoparticles. (A) Theoretically possible number of interfaces in heterodimer, heterotrimer, and heterotetramer NPs. All of these NP architectures are observed and characterized in this work except for the striped tetra-phase

structure with three interfaces. (B) The relationship between the architecture of bi-, tri-, and tetra-phase NPs..... 119

**Figure 4.2** (A) HRTEM image of a representative  $\text{Pd}_{0.75}\text{Sn}_{0.25}$  nanoparticle synthesized in a polymer nanoreactor (scale bar, 5 nm). (B) Fast Fourier transform (FFT) and (C) EDS spectrum of the nanoparticle in (A) indicate that the nanoparticle possesses a  $\text{Pd}_3\text{Sn}$  intermetallic structure. .... 121

**Figure 4.3** ADF-STEM images, EDS elemental mapping, and EDS spectra of (A) Au-Co ( $\text{Au}_{0.5}\text{Co}_{0.5}$ ), (B) Au-PdSn ( $\text{Au}_{0.57}\text{Pd}_{0.27}\text{Sn}_{0.16}$ ), and (C) Co-PdSn ( $\text{Co}_{0.66}\text{Pd}_{0.17}\text{Sn}_{0.17}$ ) heterostructured nanoparticles synthesized in polymer nanoreactors (Scale bars, 20 nm). The Cu  $K\alpha$  signals at 8.0 keV in the EDS spectra are from the TEM sample holder. .... 121

**Figure 4.4** Stability test of (A,B) Au-PdSn and (C,D) Co-PdSn heterodimers subjected to thermal annealing. The particles were heated under  $\text{H}_2$  at different conditions and quickly cooled down to ambient temperature in 0.5 h. (A) and (C) show schematic illustration, ADF-STEM images, and EDS mapping of a typical Au-PdSn nanoparticle and a typical Co-PdSn nanoparticle after each annealing step. Scale bar, 20 nm. (B) and (D) show the composition variation of each domain in Au-PdSn and Co-PdSn heterodimers after thermal treatment. The results are calculated based on composition tracking of 15 particles for each type of heterodimer. .... 124

**Figure 4.5** ADF-STEM images and corresponding EDS elemental mapping of a Au-PdSn heterodimer thermally annealed at increasing temperatures. Scale bar, 20 nm..... 125

**Figure 4.6** (A,B) ADF-STEM images and corresponding EDS characterization of AuCoPdSn nanoparticles with different molar ratios between Pd and Sn (Pd:Sn = 1:1,  $\text{Au}_{0.24}\text{Co}_{0.27}\text{Pd}_{0.24}\text{Sn}_{0.25}$ ; Pd:Sn = 2:1,  $\text{Au}_{0.30}\text{Co}_{0.26}\text{Pd}_{0.30}\text{Sn}_{0.14}$ ; Pd:Sn = 3:1,  $\text{Au}_{0.30}\text{Co}_{0.29}\text{Pd}_{0.30}\text{Sn}_{0.11}$ ; and Pd:Sn = 4:1,  $\text{Au}_{0.38}\text{Co}_{0.33}\text{Pd}_{0.23}\text{Sn}_{0.06}$ ). The Pd:Sn ratios of each particle are noted above the STEM images. (C) ADF-STEM image and EDS mapping of a AuNiPdSn nanoparticle with Pd:Sn = 20:1 ( $\text{Au}_{0.18}\text{Ni}_{0.38}\text{Pd}_{0.42}\text{Sn}_{0.02}$ ). Scale bars, 20 nm. .... 126

**Figure 4.7** Au-Co-PdSn tri-phase heterostructured nanoparticles with three interconnected interfaces. (A) ADF-STEM image of a representative Au-Co-PdSn NP ( $\text{Au}_{0.30}\text{Co}_{0.37}\text{Pd}_{0.19}\text{Sn}_{0.14}$ , scale bar, 10 nm). (B) Schematic illustration of the miscibility relationship between the Au, Co, and PdSn phases. (C-F) EDS elemental mapping of the NP in (A). Overlay of selected element maps shows the phase boundaries of (D) Au-Co, (E) Au-PdSn, and (F) Co-PdSn. (G) Overlay of all element maps showing the configuration of the three phase boundaries in a Au-Co-PdSn NP. (H) HRTEM image of the tri-phase junction in a Au-Co-PdSn NP ( $\text{Au}_{0.25}\text{Co}_{0.36}\text{Pd}_{0.29}\text{Sn}_{0.10}$ , scale bar, 3nm). Dashed lines highlight the position of the three phase boundaries. Insets are an ADF-STEM image and EDS mapping of the entire NP. (I) left column: FFT of the regions indicated in (H). right column: EDS spectra of the Au, Co, and PdSn domains of the NP in (H). .... 127

**Figure 4.8** EDS characterization of Au-Co-PdSn nanoparticles with different compositions. The molar ratio of Pd:Sn is approximately 1:1 in each nanoparticle. The varying content of Au, Co, and PdSn only changes the size of each domain in the particles. All the particles possess the same architecture with three interconnected phase boundaries. Scale bar: 20 nm. .... 128

**Figure 4.9** ADF-STEM images and EDS elemental mapping of Au-Co-PdSn nanoparticles whose interfaces are not all perpendicular to the image plane. Dashed lines/circles in the overlay of selected element maps highlight the position of interfaces as a guide to the eye. Scale bars, 15 nm. (A)  $\text{Au}_{0.57}\text{Co}_{0.17}\text{Pd}_{0.16}\text{Sn}_{0.10}$ , Au-PdSn and Co-PdSn interfaces are perpendicular to the image plane while Au-Co interface is inclined/parallel with the image plane. Scheme depicts the proposed structure of this particle. (B)  $\text{Au}_{0.33}\text{Co}_{0.34}\text{Pd}_{0.18}\text{Sn}_{0.15}$ , Au-PdSn interface is perpendicular to the image plane while Co-PdSn and Au-Co interfaces are inclined with the image plane. Scheme depicts the proposed structure of this particle..... 128

**Figure 4.10** (A-D) HRTEM and ADF-STEM characterization of Au-Co heterodimers synthesized in polymer nanoreactors. In each panel, the left column shows TEM and STEM images of entire particles; the right column shows a zoomed-in HRTEM image of the interface region between the Au and Co phases. Insets are FFTs of the Au domain or Co domain. (A) Au is oriented along the [011] zone axis. Co is along the [411] zone axis. The Moiré pattern ( $D = 1.02$  nm) at the interface is attributed to periodical lattice matching between the Co {220} and Au {220} planes. (B) Au and Co are epitaxial, both oriented along the [111] zone axis. The two phases share {220} planes at the interface. (C) Au is oriented along the [111] zone axis while Co only shows lattice fringes in one direction that corresponds to one set of {220} planes. (D) Au and Co are epitaxial, both oriented along the [111] zone axis. The two phases share {422} and {220} planes at the interface. .... 129

**Figure 4.11** (A-C) HRTEM and ADF-STEM characterization of Co-Pd<sub>3</sub>Sn heterodimers synthesized in polymer nanoreactors. In each panel, the left column shows TEM and STEM images of entire particles; the right column shows a zoomed-in HRTEM image of the interface region between the Co and Pd<sub>3</sub>Sn phases. Insets are FFTs of the Pd<sub>3</sub>Sn domain or Co domain. (A) The FFT of Co domain indicates that Co is on the [200] zone axis. The FFT of Pd<sub>3</sub>Sn domain only show one pair of reflections corresponding to Pd<sub>3</sub>Sn (210) planes. (B) Co is oriented along the [111] zone axis while no lattice plane is observable at the same direction in the Pd<sub>3</sub>Sn domain. (C) Co and Pd<sub>3</sub>Sn are on the [411] zone axis. The two phases share {311} planes at the interface. 130

**Figure 4.12** (A-C) HRTEM and ADF-STEM characterization of Au-Pd<sub>3</sub>Sn heterodimers synthesized in polymer nanoreactors. In each panel, the left column shows TEM and STEM images of entire particles; the right column shows a zoomed-in HRTEM image of the interface region between the Au and Pd<sub>3</sub>Sn phases. Insets are FFTs of the Pd<sub>3</sub>Sn domain or Au domain. (A) Au is oriented along the [111] zone axis. Pd<sub>3</sub>Sn shows lattice fringes that can be attributed to {220} planes. The two phases share {220} planes at the interface. (B) Au and Pd<sub>3</sub>Sn share {111} planes at the interface. (C) Au and Pd<sub>3</sub>Sn share {111} planes at part of the interface. Stacking faults are present in the Au domain. .... 131

**Figure 4.13** HRTEM and ADF-STEM characterization of Au-Co-Pd<sub>3</sub>Sn heterotrimers synthesized in polymer nanoreactors. In each panel, the left column shows TEM and ADF-STEM images of entire particles. The right column shows a zoomed-in HRTEM image of the tri-phase junction between the Co, Au, and Pd<sub>3</sub>Sn domains. Insets are FFTs of the Co, Pd<sub>3</sub>Sn or Au domains. Dashed lines highlight the position of the three phase boundaries. (A) The FFT of Co is indicative of Co along the [411] zone axis. The FFT of Au and Pd<sub>3</sub>Sn show reflections in the same direction that correspond to {220} planes. (B) Au and Co are both oriented along the [411] zone axis. The two

phases share {311} planes at the interface. Pd<sub>3</sub>Sn domain only shows (224) crystallographic planes. (C) Au is along the [310] zone axis. Pd<sub>3</sub>Sn is along the [110] zone axis. Meanwhile, no lattice plane is observed in the Co domain. The HRTEM images of all the Au-Co-Pd<sub>3</sub>Sn nanoparticles confirm the formation of three solid-state interfaces in one particle. Despite the same domains (Au, Co, and Pd<sub>3</sub>Sn) constituting the nanoparticles in (A-C), the interfacial lattice structure differs between each individual nanoparticle. .... 131

**Figure 4.14** (A) ADF-STEM images and EDS elemental mapping of Au-Co-Pd<sub>3</sub>Sn tri-phase nanoparticles (Pd:Sn = 1:1) with different angles between the three phase boundaries. (B) ADF-STEM images and EDS elemental mapping of Au-Co-Pd<sub>3</sub>Sn tri-phase nanoparticles (Pd:Sn = 2:1) with different angles between the three phase boundaries. Scale bars, 15 nm. While the nanoparticles in (A) or (B) are composed of the same material phases, the angles between the three phase boundaries are different in each particle. This suggests that the interfacial lattice structures in these nanoparticles are different. The nanoparticles all have a pie-shaped architecture. .... 132

**Figure 4.15** (A) DFT-simulated relaxed structures of the (111) interfacial planes between Ag, Cu, and Co. (B) The surface energies of Ag, Cu, and Co (111) planes and the interfacial energies between Ag, Cu, and Co (111) planes. (C) Calculated total surface and interfacial energies of Ag-Cu-Co nanoparticles (diameter 20 nm) with equal volume of each phase. (D) ADF-STEM image and EDS mapping of a Ag-Cu-Co nanoparticle (Ag<sub>0.23</sub>Cu<sub>0.47</sub>Co<sub>0.30</sub>). Scale bar: 15 nm. .... 133

**Figure 4.16** DFT simulation of the architecture of Au-Co-Pd<sub>3</sub>Sn tri-phase nanoparticles. (A) DFT-simulated relaxed structures of the (111) interfacial planes between Au, Co, and Pd<sub>3</sub>Sn. (B) The Surface energies of Au, Co, and Pd<sub>3</sub>Sn (111) planes and the interfacial energies between Au, Co, and Pd<sub>3</sub>Sn (111) planes. (C) Calculated total surface and interfacial energies of Au-Co-Pd<sub>3</sub>Sn nanoparticles with equal volume of each phase (diameter 20 nm). .... 133

**Figure 4.17** 2D projections of spherical nanoparticle models with either (A) three or (B) two interfaces. Both sphere models consist of three different domains (denoted as D1, D2, and D3). The three domains in Type I nanoparticles are interconnected and have identical shape and size. The three domains in Type II nanoparticles form two interfaces where D1 and D3 are not connected. The volume of the three domains in each model are equal, i.e., V(D1) = V(D2) = V(D3). .... 134

**Figure 4.18** (A,B) ADF-STEM images and EDS mapping of representative Au-Co-Pd<sub>3</sub>Sn kinetic structures synthesized in polymer nanoreactors. Dashed circles in the ADF-STEM images outline the position of the Co phase as guides for the eye. Scale bars, 20 nm. During the final annealing step of particle synthesis (500 °C, H<sub>2</sub>), kinetic particles were trapped after 0.5 h, which results in particles containing more than three metal domains. In (A) Au<sub>0.32</sub>Co<sub>0.31</sub>Pd<sub>0.23</sub>Sn<sub>0.14</sub> and (B) Au<sub>0.27</sub>Co<sub>0.34</sub>Pd<sub>0.27</sub>Sn<sub>0.12</sub> nanoparticles, the Co phases are not fully aggregated to form one integral metal domain. Continuous annealing for another 1 h effectively triggers intraparticle coarsening between the discrete Co domains. .... 135

**Figure 4.19** Structural evolution of Au-Co-Pd<sub>3</sub>Sn tri-phase nanoparticles during thermal annealing. (A) ADF-STEM images (top row) and corresponding EDS mapping (bottom row) of a Au-Co-Pd<sub>3</sub>Sn NP (Au<sub>0.33</sub>Co<sub>0.24</sub>Pd<sub>0.26</sub>Sn<sub>0.17</sub>) annealed under flowing H<sub>2</sub> at 500 °C over time. Dashed yellow lines outline the position of phase boundaries. Scale bar, 15 nm. (B) Statistical distributions of NPs (n = 150) with different architectures. .... 136

**Figure 4.20** A seven-element library of multi-phase heterostructured nanoparticles that utilize PdSn as the basic building block. Here one specific composition for each combination of metals is shown. (A) Heterodimers can be synthesized by combining PdSn with any of the other five metals, which lead to Au-PdSn, Ag-PdSn,  $\text{Cu}_{0.92}\text{Pd}_{0.08}\text{-Cu}_{0.2}(\text{PdSn})_{0.8}$ , Co-PdSn, and  $\text{Ni}_{0.6}\text{Sn}_{0.4}\text{-Ni}_{0.08}(\text{PdSn})_{0.92}$ . (B) AuAg-PdSn, AuCu-PdSn, CuNi-PdSn, and CoNi-PdSn are heterodimers. Au-Co-PdSn, Au-NiSn-PdSn, Ag-Cu-PdSn, Ag-NiSn-PdSn, and Ag-Co-PdSn are heterotrimers with three interconnected interfaces. Co-Cu-PdSn is a heterotrimer with two disconnected interfaces. (C) AuAg-AuCu-PdSn, AuCu-CuNi-PdSn, AuAg-Co-PdSn, AuAg-NiSn-PdSn, AuCu-Co-PdSn, Au-CoNi-PdSn, Ag-CuNi-PdSn, Ag-CoNi-PdSn are heterotrimers with three interconnected interfaces. CoNi-CuNi-PdSn is a heterotrimer with two disconnected interfaces. Ag-Cu-Co-PdSn is a heterotetramer with four interfaces. (D) AuAg-CoNi-PdSn and AuCu-CoNi-PdSn are heterotrimers with three interfaces. AuAg-AuCu-NiSn-PdSn and AuAg-AuCu-Co-PdSn are heterotetramers with five interfaces. Ag-Cu-CoNi-PdSn is a heterotetramer with four interfaces. (E) AuAgCu-CoNi-PdSn is a heterotrimer with three interfaces. The number of phases in one particle is highly dependent on particle composition. For example, CoNiPdSn NPs with two different compositions show either a bi-phase structure (Figure 4.20B) or a tri-phase structure (Figure 4.31B), respectively. Detailed information about the nanoparticles shown in this figure can be found in Figure 4.21-4.24..... 139

**Figure 4.21** ADF-STEM images, EDS spectra, and detailed EDS mapping of the ternary nanoparticles in Figure 4.20A. (A)  $\text{Au}_{0.57}\text{Pd}_{0.27}\text{Sn}_{0.16}$ , (B)  $\text{Ag}_{0.55}\text{Pd}_{0.26}\text{Sn}_{0.19}$ , (C)  $\text{Cu}_{0.46}\text{Pd}_{0.39}\text{Sn}_{0.15}$ , (D)  $\text{Co}_{0.50}\text{Pd}_{0.32}\text{Sn}_{0.18}$ , and (E)  $\text{Ni}_{0.32}\text{Pd}_{0.37}\text{Sn}_{0.31}$ . Scale bars, 15 nm. .... 140

**Figure 4.22** ADF-STEM images, EDS spectra, and detailed EDS mapping of the quaternary nanoparticles in Figure 4.20B. (A)  $\text{Au}_{0.21}\text{Ag}_{0.32}\text{Pd}_{0.32}\text{Sn}_{0.15}$ , (B)  $\text{Au}_{0.31}\text{Co}_{0.34}\text{Pd}_{0.21}\text{Sn}_{0.14}$ , (C)  $\text{Au}_{0.25}\text{Ni}_{0.24}\text{Pd}_{0.20}\text{Sn}_{0.31}$ , (D)  $\text{Au}_{0.24}\text{Cu}_{0.38}\text{Pd}_{0.25}\text{Sn}_{0.13}$ , (E)  $\text{Ag}_{0.30}\text{Cu}_{0.30}\text{Pd}_{0.27}\text{Sn}_{0.13}$ , (F)  $\text{Ag}_{0.22}\text{Ni}_{0.24}\text{Pd}_{0.21}\text{Sn}_{0.33}$ , (G)  $\text{Ag}_{0.43}\text{Co}_{0.23}\text{Pd}_{0.23}\text{Sn}_{0.11}$ , (H)  $\text{Cu}_{0.33}\text{Ni}_{0.32}\text{Pd}_{0.16}\text{Sn}_{0.19}$ , (I)  $\text{Cu}_{0.29}\text{Co}_{0.34}\text{Pd}_{0.21}\text{Sn}_{0.16}$ , and (J)  $\text{Co}_{0.38}\text{Ni}_{0.23}\text{Pd}_{0.18}\text{Sn}_{0.21}$ . Scale bars, 15 nm. .... 140

**Figure 4.23** ADF-STEM images, EDS spectra, and detailed EDS mapping of the quinary nanoparticles in Figure 4.20C. (A)  $\text{Au}_{0.12}\text{Ag}_{0.30}\text{Cu}_{0.28}\text{Pd}_{0.20}\text{Sn}_{0.10}$ , (B)  $\text{Au}_{0.12}\text{Cu}_{0.19}\text{Ni}_{0.26}\text{Pd}_{0.23}\text{Sn}_{0.20}$ , (C)  $\text{Au}_{0.06}\text{Ag}_{0.10}\text{Co}_{0.24}\text{Pd}_{0.39}\text{Sn}_{0.21}$ , (D)  $\text{Au}_{0.20}\text{Ag}_{0.16}\text{Ni}_{0.21}\text{Pd}_{0.19}\text{Sn}_{0.24}$ , (E)  $\text{Au}_{0.25}\text{Cu}_{0.25}\text{Co}_{0.18}\text{Pd}_{0.22}\text{Sn}_{0.10}$ , (F)  $\text{Au}_{0.24}\text{Co}_{0.21}\text{Ni}_{0.15}\text{Pd}_{0.17}\text{Sn}_{0.23}$ , (G)  $\text{Ag}_{0.25}\text{Cu}_{0.25}\text{Ni}_{0.20}\text{Pd}_{0.16}\text{Sn}_{0.14}$ , (H)  $\text{Ag}_{0.32}\text{Cu}_{0.20}\text{Co}_{0.21}\text{Pd}_{0.15}\text{Sn}_{0.12}$ , (I)  $\text{Cu}_{0.38}\text{Co}_{0.15}\text{Ni}_{0.12}\text{Pd}_{0.20}\text{Sn}_{0.15}$ , and (J)  $\text{Ag}_{0.31}\text{Co}_{0.18}\text{Ni}_{0.13}\text{Pd}_{0.21}\text{Sn}_{0.17}$ . Scale bars, 15 nm. .... 141

**Figure 4.24** ADF-STEM images, EDS spectra, and detailed EDS mapping of the senary and septenary nanoparticles in Figure 4.20D and 4.20E. (A)  $\text{Au}_{0.16}\text{Ag}_{0.09}\text{Cu}_{0.18}\text{Ni}_{0.15}\text{Pd}_{0.22}\text{Sn}_{0.20}$ , (B)  $\text{Ag}_{0.25}\text{Cu}_{0.16}\text{Co}_{0.16}\text{Ni}_{0.15}\text{Pd}_{0.17}\text{Sn}_{0.11}$ , (C)  $\text{Au}_{0.10}\text{Ag}_{0.19}\text{Co}_{0.19}\text{Ni}_{0.15}\text{Pd}_{0.20}\text{Sn}_{0.17}$ , (D)  $\text{Au}_{0.18}\text{Ag}_{0.16}\text{Cu}_{0.20}\text{Co}_{0.23}\text{Pd}_{0.13}\text{Sn}_{0.10}$ , (E)  $\text{Au}_{0.14}\text{Cu}_{0.18}\text{Co}_{0.22}\text{Ni}_{0.16}\text{Pd}_{0.17}\text{Sn}_{0.13}$ , and (F)  $\text{Au}_{0.16}\text{Ag}_{0.13}\text{Cu}_{0.16}\text{Co}_{0.15}\text{Ni}_{0.15}\text{Pd}_{0.15}\text{Sn}_{0.10}$ . Scale bars, 15 nm. .... 141

**Figure 4.25** Tetra-phase heterostructured nanoparticles with four interfaces. (A) Schematic illustration depicting the architectures of tri- and tetra-phase NPs composed of Ag, Cu, Co, and PdSn phases. Dashed lines outline the position of the phase boundaries. (B) ADF-STEM images (top row) and EDS mapping (bottom row) of representative tri-phase NPs for all phase combinations. The compositions of the four tri-phase NPs are  $\text{Ag}_{0.23}\text{Cu}_{0.47}\text{Co}_{0.30}$ ,

$\text{Co}_{0.34}\text{Cu}_{0.29}\text{Pd}_{0.21}\text{Sn}_{0.16}$ ,  $\text{Ag}_{0.30}\text{Cu}_{0.30}\text{Pd}_{0.27}\text{Sn}_{0.13}$ , and  $\text{Ag}_{0.33}\text{Co}_{0.23}\text{Pd}_{0.27}\text{Sn}_{0.17}$ . (C) ADF-STEM image (top row) and EDS mapping (bottom row) of a representative tetra-phase NP composed of Ag, Cu, Co, and PdSn phases ( $\text{Ag}_{0.32}\text{Cu}_{0.20}\text{Co}_{0.21}\text{Pd}_{0.15}\text{Sn}_{0.12}$ ). Overlay of selected element maps (middle row) reveals the relative position of the four phases in the NP. Scale bars, 15nm. .... 142

**Figure 4.26** ADF-STEM images and detailed EDS elemental mapping of the tri-phase nanoparticles in Figure 4.25B ( $\text{Ag}_{0.23}\text{Cu}_{0.47}\text{Co}_{0.30}$ ,  $\text{Co}_{0.34}\text{Cu}_{0.29}\text{Pd}_{0.21}\text{Sn}_{0.16}$ ,  $\text{Ag}_{0.30}\text{Cu}_{0.30}\text{Pd}_{0.27}\text{Sn}_{0.13}$ , and  $\text{Ag}_{0.33}\text{Co}_{0.23}\text{Pd}_{0.27}\text{Sn}_{0.17}$ ). Scale bars, 15 nm. Overlay of all element maps (second column) and selected element maps (third to fifth columns) show the relative position of the three phases in each particle. .... 143

**Figure 4.27** ADF-STEM images and EDS elemental mapping of three representative Ag-Cu-Co-PdSn tetra-phase nanoparticles ( $\text{Ag}_{0.28}\text{Cu}_{0.23}\text{Co}_{0.23}\text{Pd}_{0.16}\text{Sn}_{0.10}$ ,  $\text{Ag}_{0.31}\text{Cu}_{0.19}\text{Co}_{0.21}\text{Pd}_{0.17}\text{Sn}_{0.12}$ , and  $\text{Ag}_{0.29}\text{Cu}_{0.21}\text{Co}_{0.22}\text{Pd}_{0.17}\text{Sn}_{0.11}$ ). Scale bars, 15 nm. Overlay of all element maps (middle column) and selected element maps (right column) reveal the configuration of the four phases in Ag-Cu-Co-PdSn particles..... 144

**Figure 4.28** Tetra-phase heterostructured nanoparticles with five interfaces. (A) Schematic illustration depicting the architectures of tri- and tetra-phase NPs composed of AuAg, AuCu, Co, and PdSn phases. Dashed lines outline the position of phase boundaries. (B) ADF-STEM images (top row) and EDS mapping (bottom row) of representative tri-phase NPs for all phase combinations. The compositions of the four tri-phase NPs are  $\text{Au}_{0.30}\text{Ag}_{0.19}\text{Cu}_{0.29}\text{Co}_{0.22}$ ,  $\text{Au}_{0.12}\text{Ag}_{0.30}\text{Cu}_{0.28}\text{Pd}_{0.20}\text{Sn}_{0.10}$ ,  $\text{Au}_{0.06}\text{Ag}_{0.10}\text{Co}_{0.24}\text{Pd}_{0.39}\text{Sn}_{0.21}$ , and  $\text{Au}_{0.13}\text{Cu}_{0.27}\text{Co}_{0.30}\text{Pd}_{0.15}\text{Sn}_{0.15}$ . (C) ADF-STEM image (top row) and EDS mapping (bottom row) of a representative tetra-phase NP composed of AuAg, AuCu, Co, and PdSn phases ( $\text{Au}_{0.18}\text{Ag}_{0.16}\text{Cu}_{0.20}\text{Co}_{0.23}\text{Pd}_{0.13}\text{Sn}_{0.10}$ ). Overlay of selected element maps (middle row) shows the relative configuration of the four phases in the NP. Dashed lines highlight the position of the five phase boundaries. Scale bars, 15 nm. .... 145

**Figure 4.29** ADF-STEM images and detailed EDS elemental mapping information of the tri-phase nanoparticles in Figure 4.28B ( $\text{Au}_{0.30}\text{Ag}_{0.19}\text{Cu}_{0.29}\text{Co}_{0.22}$ ,  $\text{Au}_{0.12}\text{Ag}_{0.30}\text{Cu}_{0.28}\text{Pd}_{0.20}\text{Sn}_{0.10}$ ,  $\text{Au}_{0.06}\text{Ag}_{0.10}\text{Co}_{0.24}\text{Pd}_{0.39}\text{Sn}_{0.21}$ , and  $\text{Au}_{0.13}\text{Cu}_{0.27}\text{Co}_{0.30}\text{Pd}_{0.15}\text{Sn}_{0.15}$ ). Scale bars, 15 nm. Overlays of all element maps (second column) and selected element maps (third to fifth columns) show the relative position of the three phases in each particle. .... 146

**Figure 4.30** ADF-STEM images and EDS elemental mapping of representative (A) AuAg-AuCu-Co-PdSn ( $\text{Au}_{0.11}\text{Ag}_{0.15}\text{Cu}_{0.17}\text{Co}_{0.28}\text{Pd}_{0.19}\text{Sn}_{0.10}$  and  $\text{Au}_{0.17}\text{Ag}_{0.15}\text{Cu}_{0.17}\text{Co}_{0.23}\text{Pd}_{0.18}\text{Sn}_{0.10}$ ) and (B) AuAg-AuCu-NiSn-PdSn ( $\text{Au}_{0.17}\text{Ag}_{0.12}\text{Cu}_{0.22}\text{Ni}_{0.14}\text{Pd}_{0.19}\text{Sn}_{0.16}$ ) tetra-phase nanoparticles. Scale bars, 15 nm. Overlays of all element maps (middle column) and selected element maps (right column) reveal the configuration of the four phases in the nanoparticles. Dashed yellow lines indicate the position of the five phase boundaries in each nanoparticle..... 146

**Figure 4.31** Tetra-phase heterostructured nanoparticles with six interfaces. (A) Schematic illustration depicting the architectures of tri- and tetra-phase NPs composed of Au, CoNi, NiSn, and PdSn phases. Dashed lines outline the position of the phase boundaries. (B) ADF-STEM images (top row) and EDS mapping (bottom row) of representative tri-phase NPs for all phase combinations. The compositions of the four tri-phase NPs are  $\text{Co}_{0.13}\text{Ni}_{0.35}\text{Pd}_{0.26}\text{Sn}_{0.26}$ ,  $\text{Au}_{0.37}\text{Co}_{0.18}\text{Ni}_{0.36}\text{Sn}_{0.09}$ ,  $\text{Au}_{0.29}\text{Co}_{0.17}\text{Ni}_{0.19}\text{Pd}_{0.20}\text{Sn}_{0.15}$ , and  $\text{Au}_{0.25}\text{Ni}_{0.24}\text{Pd}_{0.20}\text{Sn}_{0.31}$ . (C) ADF-STEM

image (top row) and EDS mapping (bottom row) of a representative tetra-phase NP composed of Au, CoNi, NiSn, and PdSn phases ( $\text{Au}_{0.20}\text{Co}_{0.11}\text{Ni}_{0.30}\text{Pd}_{0.21}\text{Sn}_{0.18}$ ). Overlay of selected elemental maps (two middle rows) show the relative position of any two of the four phases. Dashed lines/circles outline the position of the six phase boundaries in the NP. Scale bars, 15 nm. .... 147

**Figure 4.32** ADF-STEM images and detailed EDS elemental mapping information of the tri-phase nanoparticles in Figure 4.31B ( $\text{Co}_{0.13}\text{Ni}_{0.35}\text{Pd}_{0.26}\text{Sn}_{0.26}$ ,  $\text{Au}_{0.37}\text{Co}_{0.18}\text{Ni}_{0.36}\text{Sn}_{0.09}$ ,  $\text{Au}_{0.29}\text{Co}_{0.17}\text{Ni}_{0.19}\text{Pd}_{0.20}\text{Sn}_{0.15}$ , and  $\text{Au}_{0.25}\text{Ni}_{0.24}\text{Pd}_{0.20}\text{Sn}_{0.31}$ ). Overlays of all element maps (second column) and selected element maps (third to fifth columns) show the relative position of the three phases in each particle. Scale bars, 15 nm. .... 148

**Figure 4.33** (A,B) Additional EDS mapping information of the Au-CoNi-NiSn-PdSn tetra-phase nanoparticle in Figure 4.30C. The overlay of selected element maps clearly indicates that the particle consists of four phases with six phase boundaries. (C) EDS mapping of the same particle after rotating the particle  $60^\circ$ . Dashed circles in the images outline the position of CoNi phase as guides for the eye. The CoNi phase moves from the bottom of the image to the center of the image, indicating that the CoNi domain is on top of the particle. Scale bar, 15 nm. .... 149

**Figure 4.34** (A) ADF-STEM image and EDS mapping of a Au-CoNi-NiSn-PdSn tetra-phase nanoparticle with six phase boundaries ( $\text{Au}_{0.18}\text{Co}_{0.14}\text{Ni}_{0.33}\text{Pd}_{0.18}\text{Sn}_{0.17}$ ). (B) ADF-STEM image and EDS mapping of the same particle after rotating the particle  $60^\circ$ . Scale bars, 20 nm. Dashed circles in first and second columns of the images outline the position of the CoNi phase as guides for the eye. After rotating the nanoparticle, the CoNi phase moves from the center of the image to the bottom of the image, indicating that the CoNi domain is on top of the particle. .... 149

**Figure 4.35** (A) ADF-STEM images and EDS elemental mapping of two representative Au-CoNi-NiSn-PdSn tetra-phase nanoparticles ( $\text{Au}_{0.17}\text{Co}_{0.11}\text{Ni}_{0.33}\text{Pd}_{0.24}\text{Sn}_{0.15}$  and  $\text{Au}_{0.18}\text{Co}_{0.09}\text{Ni}_{0.33}\text{Pd}_{0.25}\text{Sn}_{0.15}$ ). Overlays of all element maps (middle column) and selected element maps (right column) indicates that the CoNi phases are either on top of the particle or at the bottom the of particle. (B) ADF-STEM images and EDS elemental mapping of a Au-CoNi-NiSn-PdSn tetra-phase nanoparticle ( $\text{Au}_{0.20}\text{Co}_{0.12}\text{Ni}_{0.32}\text{Pd}_{0.20}\text{Sn}_{0.16}$ ) with the CoNi phase located on the edge. Dashed circle outlines the position of the CoNi phase as a guide. Scale bars, 20 nm. .... 150

**Figure 4.36** Distributions of Au-CoNi-PdSn-NiSn heterotetramers with different architectures (calculated based on 30 particles). .... 150

**Figure 5.1** Schematic illustration of the screening of nanostructures for a wide variety of properties with a substrate containing particles spatially-encoded with respect to size and composition. . 157

**Figure 5.2** Schematic illustration of polymer pen lithography (PPL) for centimeter area molecular printing. .... 159

**Figure 5.3** PPL patterning of centimeter-scale AuPd nanoparticle arrays. (A) Dark-field optical microscopy image of a large-scale pattern of polymer dots. (B) Magnified dark-field image shows a 25-by-25 dot array with  $3\ \mu\text{m}$  dot spacing. (C) SEM image of the polymer dot arrays printed by PPL. (D) SEM image of corresponding AuPd alloy nanoparticles formed after thermally annealing the polymer dots. .... 159

**Figure 5.4** Centimeter-scale AuAgNi nanoparticle arrays generated by a combination of SPBCL and Polymer Pen Lithography (PPL). (A) Dark-field optical microscopy image of a section of the centimeter-scale pattern of polymer features. (B) SEM image of the polymer features printed by PPL. (C) SEM image of the arrays of AuAgNi nanoparticles synthesized from the polymer nanoreactors that were printed by PPL. .... 160

**Figure 5.5** Centimeter-scale AuPd nanoparticle arrays generated on TiO<sub>2</sub> support. (A-C) SEM images of (A) a pristine TiO<sub>2</sub> substrate, (B) polymer features printed on TiO<sub>2</sub>, (C) an array of AuPd nanoparticles synthesized from the printed polymer features. Scale bars, 5 μm. .... 160

**Figure 5.6** Reduction of 4-nitrophenol catalyzed by a PPL-patterned nanoparticle array. (A) Scheme of the catalysis process. A 10 μL aqueous droplet containing 4-nitrophenol and NaBH<sub>4</sub> was dispensed onto a nanoparticle array. In the presence of nanoparticles, 4-nitrophenol was converted into 4-aminophenol. (B) The diameters of the contact area between droplets and various substrates were determined by a contact angle goniometer. About 0.7 million nanoparticles were covered by each droplet. Inset is a typical photograph of reactant droplet on PPL-patterned nanoparticle array. (C) UV-Vis absorption spectra of the droplet solution after running catalysis on different substrates with product and reactant peaks at 296 nm and 400 nm, respectively. (D) Conversion percentage and turnover number of the reaction catalyzed by control sample (no particles), AuNP (16 ± 2 nm diameter) arrays, PdNP (16 ± 3 nm diameter) arrays, and AuPdNP (16 ± 2 nm diameter) arrays. .... 161

**Figure 5.7** General pathways for the hydrogenation of trans-cinnamaldehyde. .... 162

**Figure 5.8** Gas chromatograms of the catalytic hydrogenation of cinnamaldehyde mediated by Si (control, black line), PPL-patterned Pd nanoparticles with 1.5 μm pitch (blue line, particle density 0.44 NP/μm<sup>2</sup>), and spin-coated Pd nanoparticles (red line, particle density 40 NP/μm<sup>2</sup>). Reaction conditions: 120 μL 0.5 mM cinnamaldehyde, 0.3 cm<sup>-2</sup> samples, 1 MPa H<sub>2</sub>, R.T., 24 h. .... 163

**Figure 5.9** (A) SEM image of PPL-patterned Pd nanoparticles with 2.5 μm pitch on a Si substrate. (B) Zoom-in SEM image of a single nanoparticle showing carbon residue around the particle. 163

**Figure 5.10** Gas chromatograms of the catalytic hydrogenation of cinnamaldehyde mediated by Si (control, black line), PPL-patterned Pd nanoparticles with 1.5 μm pitch (green line), and PPL-patterned Pd nanoparticles (1.5 μm pitch, red line) annealed at 400 °C in O<sub>2</sub> and H<sub>2</sub> successively to remove carbon residue. Reaction conditions: 120 μL 0.5 mM cinnamaldehyde, 0.3 cm<sup>-2</sup> samples, 1 MPa H<sub>2</sub>, R.T., 24 h. .... 164

**Figure 5.11** Particle size effect on the activity of AuPd catalysts for the reduction of 4-nitrophenol. (A) Scheme of using a tilted polymer pen array to generate polymer dot array and corresponding AuPd nanoalloy array with size gradient. (B) Dark-field optical image of the gradient polymer dot array. (C) SEM images of the polymer dots on left, middle, and right sites of the gradient sample. Insets are SEM images of the resulting AuPd nanoalloys. The scale bars apply to all panels and insets. (D) The dependence of polymer dot size and corresponding alloy nanoparticle size on the distance from the one side of the gradient sample. (E) Conversion and turnover number of the reaction catalyzed by AuPd nanoalloy with various size. To study the size effect, three regions of the gradient sample are used, namely the left side, middle, and right side (corresponding to the

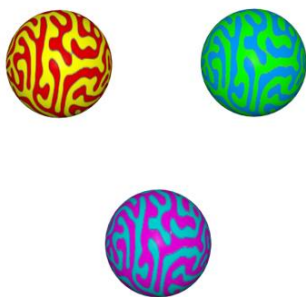
blue, green, and orange sections shown in (D)). The nanoparticle sizes in three regions are  $20 \pm 3$  nm,  $15 \pm 3$  nm, and  $9 \pm 4$  nm, respectively. The activity increases in the sequence of 20, 15, and 9 nm nanoparticles. .... 165

**Figure 6.1** Elements that potentially can be used to synthesize nanoparticles by SPBCL. .... 173

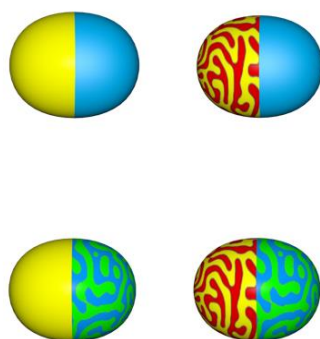
# CHAPTER ONE

## Polyelemental Nanoparticles

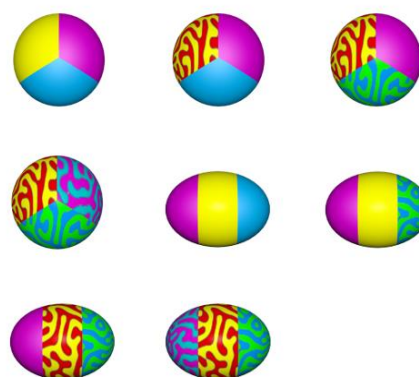
### Alloys



### Heterodimers



### Heterotrimers



## 1.1 Motivation and Introduction

Polyelemental nanoparticles (NPs), commonly referred as multimetallic NPs, are an important frontier of nanomaterials due to their promise in many fields, including catalysis,<sup>1-9</sup> plasmonics,<sup>3,10-13</sup> electronic devices,<sup>14,15</sup> magnetics,<sup>6,16,17</sup> target drug delivery,<sup>18</sup> and bio-imaging.<sup>19-21</sup> On one hand, the high surface-area-to-volume ratio inherent to NPs imparts multimetallic NPs with enhanced surface properties as compared to their bulk counterparts. On the other hand, the incorporation of multiple metals into a single NP enables delicate tuning of the chemical and physical properties of NPs. This property engineering is achieved by the hybrid chemical, electronic, and magnetic interactions between metal components,<sup>3,8,9,12,13,22-33</sup> or by the combination of different properties associated with each pure metal component.<sup>15,18,34-39</sup> For example, in the field of catalysis, first-row transition metals (*e.g.*, Fe, Co, Ni, and Cu) are often doped into a precious metal NP catalyst to adjust the activity of precious metals while lower the overall cost.<sup>3,5,7-9,40</sup> The integration of two catalytic components into one NP have also proven to be useful for enhanced tandem catalysis.<sup>35,41-44</sup>

To date, many methods have been developed to synthesize multimetallic nanomaterials. Nonetheless, control over the size, structural, and compositional homogeneities of multimetallic NPs within a wide range of elemental stoichiometric ratios remains difficult due to the fundamental differences in reduction kinetics of different metal precursors,<sup>2,4</sup> the site-selective nucleation of each metal,<sup>2,45-49</sup> and the phase-separation potentially occurring at the nanoscale.<sup>50-59</sup> Besides, conventional process of optimizing multimetallic NP catalysts usually requires experimentalists to synthesize enormous batches of NPs with specified size and composition in order to comprehensively establish the composition-structure-activity relationship. Indeed, the lack of a

methodology to facilitate obtain polyelemental NPs by design and to efficiently study the enormous parameter space constitutes the major challenge that prohibits the advance of this field. For this reason, numerous research endeavors are continuously put on inventing novel strategies that will enable well-controlled synthesis and facile investigation of multimetallic NPs. This thesis seeks to develop a versatile method for the synthesis of polyelemental NPs with size, composition, and architectures challenging to achieve *via* conventional means. Moreover, the method is intended to be directly amenable to high-efficiency NP catalyst screening, thus avoiding the inefficient process of serially making and characterizing polyelemental catalyst in a stepwise fashion. As such, this thesis contributes to the fields of material science, chemistry, physics, and nanoscience.

## 1.2 Catalytic Applications of Polyelemental Nanoparticles

The use of heterogeneous catalysts is prominent both in scientific research and industrial production of chemicals. It is reported that around 90% of the industrial chemical processes involve some types of heterogeneous catalysts.<sup>60</sup> As an important class of heterogeneous catalysts, NPs (particularly multimetallic ones) have proven to provide chemical reactions with superior reactivity and selectivity, while possessing the inherent advantage of easy handling and recycling.<sup>61-64</sup> Currently, NPs have been widely studied as catalysts for reactions including hydrogenation,<sup>64-67</sup> Suzuki coupling,<sup>68</sup> CO oxidation,<sup>69-72</sup> alcohol oxidation,<sup>73-77</sup> CO<sub>2</sub> reduction,<sup>78,79</sup> *etc.*<sup>40,81-85</sup>

Hydrogenation is one of the major catalytic reactions that are utilized in pharmacy industry for making complex molecules. In addition, hydrogenation is also prevalently used in petroleum refining industry to saturate compounds, crack hydrocarbons, and remove sulfur (hydrodesulfurization), nitrogen (hydrodenitrogenation), and other heterogeneous atoms.<sup>86</sup> Due to

the importance of hydrogenation, the search of high-efficient catalysts has continuous been a major field of research during past few decades. The mechanism of catalytic hydrogenation was first proposed by Horiuti.<sup>87</sup> As shown in Figure 1.1, unsaturated reactants such as ethylene are adsorbed onto catalyst surface while the H-H bond in hydrogen ( $H_2$ ) is cleaved to form metal-hydrogen bond on the catalyst surface. Through this way, the activation energy of reaction is decreased so that hydrogen atoms can be transferred to ethylene to form a new C-H bond.

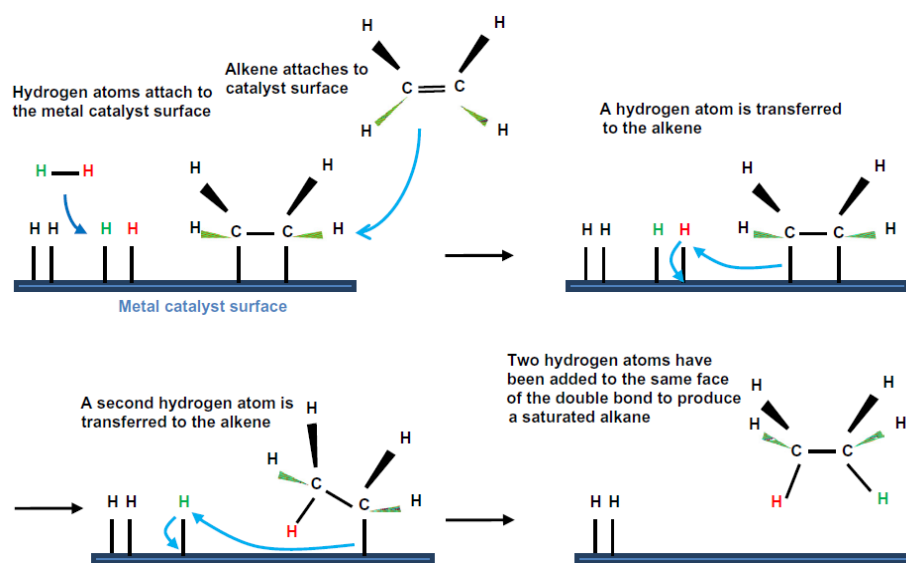


**Figure 1.1** Mechanism of heterogeneous hydrogenation of ethylene.<sup>87</sup>

Currently, both monometallic and multimetallic NPs have been utilized for chemo-selective hydrogenation of compounds that contains multiple functional groups. For example, AuNP is an extensively-studied catalyst for the hydrogenation of  $\alpha,\beta$ -unsaturated ketones and aldehydes (Figure 1.2). In 1999, Hutchings *et al.* reported that the hydrogenation of crotonaldehyde can be catalyzed by AuNPs (2-4 nm) on ZnO supports with an 82% selectivity of crotyl alcohol.<sup>88</sup> The presence of sites at the Au-support interface is considered to be responsible for the preferential activation of the carbonyl group. However, the combination of AuNPs with ZnO supports suffers

from a low reaction conversion (less than 10%). In contrast, when the catalyst support is switched to  $\text{Fe}_2\text{O}_3$ , AuNP promotes the hydrogenation of  $\alpha,\beta$ -unsaturated aldehydes with both high reaction conversion (90%) and high selectivity of unsaturated alcohols (95%).<sup>89</sup> Besides the impact of catalyst supports, other factors including AuNP size, morphology, and synthetic methods are also found to affect catalyst activity considerably. For example, when AuNPs are utilized for the hydrogenation of acrolein, the selectivity of allylic alcohols increases with increasing NP size from 1 to 5 nm.<sup>90</sup> Apart from particle size, the structure of AuNPs, namely the presence of multiply twin defects and the degree of rounding also affect the selectivity.<sup>91</sup> Specifically, AuNPs with higher degree of rounding and a smaller number of twin defects were found to show the highest selectivity towards allylic alcohols.

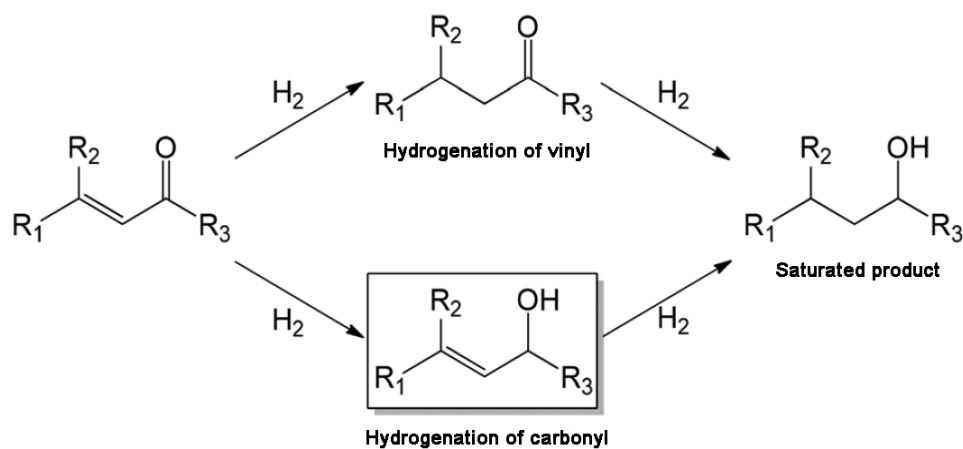


**Figure 1.2** Chemo-selective hydrogenation of unsaturated carbonyl compounds.<sup>90</sup>

In addition to Au, other commonly used monometallic NP catalysts include Pt, Pd, Ru, Rh, *etc.*<sup>86</sup> Likewise, many factors such as NP size, shape, and synthetic method are reported to influence the catalytic activity and selectivity.<sup>86,92,93</sup> Somorjai *et al.* reported that cuboctahedral Pt NPs exhibited superior catalytic activity over cubic Pt NPs when used for benzene hydrogenation (Figure 1.3).<sup>92</sup> The effect of morphology on the catalytic activity is also reported in PdNP system,

where cubic PdNPs are more active than spherical PdNPs for styrene oxide hydrogenation.<sup>93</sup>

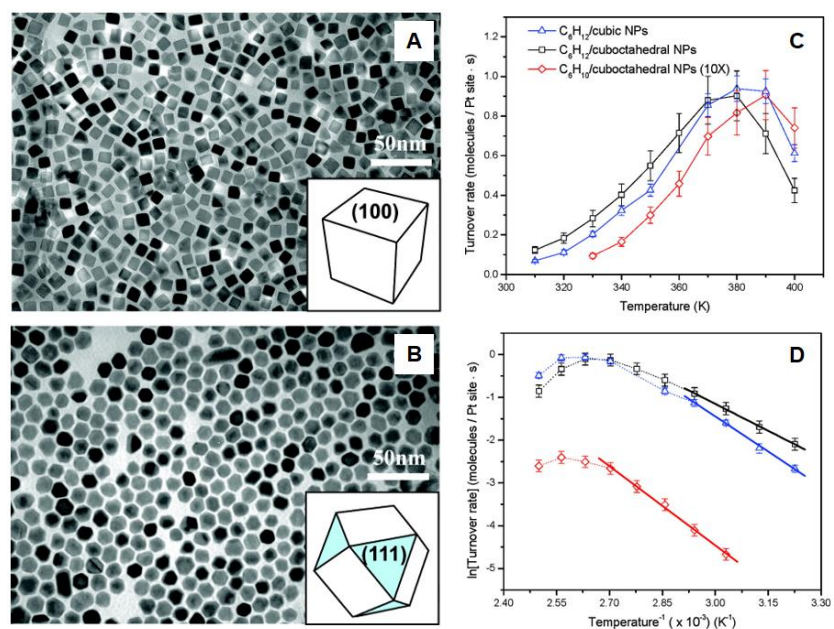


**Figure 1.3** Dependence of nanoparticle catalytic activity on exposed facets. (A) TEM image of tetradecyltrimethylammonium bromide (TTAB)-stabilized cubic Pt particles. (B) TEM image of TTAB-stabilized cuboctahedral Pt particles. (C,D) The turnover rates of cyclohexane and cyclohexene in benzene hydrogenation with cubic and cuboctahedral Pt NPs as catalysts.<sup>92</sup>

Despite the excellent activity of the aforementioned noble metal NPs, they are also limited by the high cost owing to the scarcity of noble metals on earth. As driven by the economic concerns, researches have emphasized the significance of using first row transition metals (Fe, Co, Ni, Cu, *etc.*) to lower catalyst cost.<sup>86</sup> To this end, multimetallic NP catalysts that contains non-noble metals have emerged as an important frontier of NP catalysts. The incorporation of multiple metals into a single catalyst is found to be effective in optimizing the binding strength between reactants and catalysts, which imparts multimetallic nanocatalysts with superior performance as compared with their monometallic analogues. For example, Nørskov *et al.* developed a NiZn nanocatalyst for the selective hydrogenation of acetylene (Figure 1.4).<sup>94</sup> Different compositions were studied to reveal that the selectivity of catalysts increased with increasing Zn content while Ni<sub>0.25</sub>Zn<sub>0.75</sub> possess the

highest selectivity of ethylene. The content of by-product (ethane) was restricted below 0.01% even when the reaction conversion is approaching 100%. Modeling results suggested that both acetylene and ethylene adsorbed onto Ni sites. The change in adsorption properties from Ni catalyst to NiZn catalyst is because Zn changes the electronic properties of Ni rather than Zn increases reactants binding sites. The appropriate binding energy of acetylene with NiZn and low binding energy of ethylene with NiZn contributes to the high selectivity and reactivity. Similar enhancement of reactivity and selectivity of bimetallic NP catalysts were also observed in the hydrogenation of  $\alpha,\beta$ -unsaturated aldehydes<sup>48</sup> and nitrobenzaldehyde.<sup>49</sup> Besides bimetallic NP catalysts, some studies investigated the possibility of using even more complex catalysts (such as trimetallic NPs) for hydrogenation. The introduction of a third component dramatically complicates the catalyst system, increasing the number of parameters need to be thoroughly investigated in order to elucidate the material-structure-activity relationship. Nevertheless, many pioneering works have proven an enhanced activity of trimetallic NPs as compared with either monometallic or bimetallic NPs.<sup>95-97</sup>

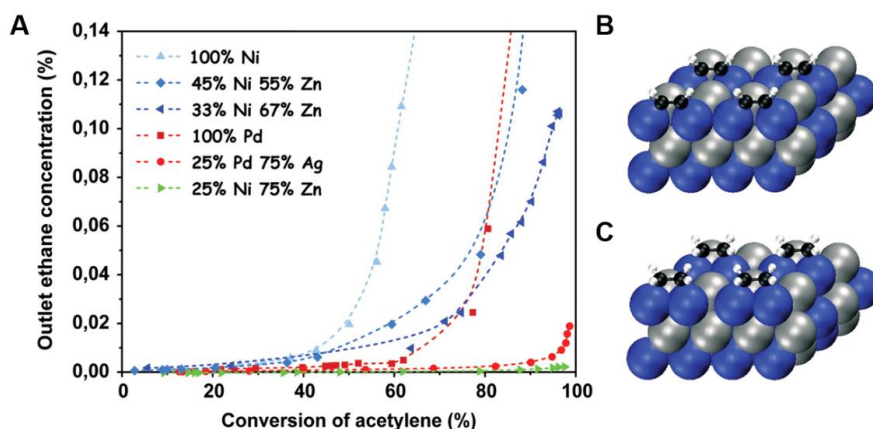


**Figure 1.4** NiZn bimetallic catalysts for hydrogenation of acetylene. (A) Measured concentration of ethane (byproduct) at the reactor outlet as a function of acetylene conversion for seven catalysts. (B,C) Modeling of the adsorption of acetylene (B) and ethylene (C) on NiZn catalysts (blue: Ni; gray: Zn; black: C; white: H).<sup>94</sup>

In general, multimetallic NPs show great potentials for catalytic hydrogenation. The mechanistic understanding is still far behind the advances in experimental discovery, which is due to the difficulty associated with the synthesis covering a vast parameter space, as well as the characterization of catalytic sites at atomic level. Nonetheless, multimetallic NPs will continue to be a promising class of catalytic materials for chemical transformations, if computational and experimental methods can be developed to synthesize and study them more efficiently.

### **1.3 Synthetic Methods of Polyelemental Nanoparticles**

The discovery of new multimetallic NP catalysts that expand the scope and catalytic activity will increase the sustainability and efficiency of chemical processes, which will benefit both industrial and academic communities. To this end, synthetic methods with precise control over NP parameters are highly desired. Currently, many synthetic methods for multimetallic NPs have been explored, including the synthesis in gas-phase, in solution-phase, and on certain substrates. Compared with the synthesis of monometallic NPs, the introduction of more than one metal component dramatically increases the system complexity. Depending on the characteristics of each method, NP structures and properties can be tailored in different manners.

#### *1.3.1 Wet Chemical Reduction*

Since being discovered by Michael Faraday one hundred years ago, wet chemical reduction has become the most commonly used strategy for NP synthesis.<sup>1-3,6,7,98</sup> In a typical synthesis process, metal precursors are mixed with a reducing agent (*e.g.*, NaBH<sub>4</sub>, hydrazine) in the presence of a ligand (stabilizer) such as citrate, alkyl thiol, *etc.* The reducing agent converts metal precursors to metal atoms, which are subsequently aggregated into NPs. During the entire process, the ligand passivates NP surfaces to prevent NPs from agglomeration. To date, wet chemical reduction has

been generalized to NPs composed of materials including Fe, Co, Ni, Cu, Ag, Ru, Rh, Pd, Ir, Pt, Au, *etc.*<sup>1-3,99</sup> The size, shape, and structure of NPs are controlled by synthetic conditions such as temperature, reaction time, and the types of reducing agents, solvents, and capping agents. For example, cubic and cuboctahedral Pt NPs with different facets (Pt (100) and Pt (111)) can be obtained by adjusting the reduction kinetics of Pt precursors (Figure 1.3).<sup>92,100</sup> As for multimetallic NPs, the difficulty in controlling the homogeneity of NPs is increased, which requires more delicate design of the synthesis protocol. Generally, multimetallic NPs can be obtained in three pathways, *i.e.*, 1) one-pot synthesis: mixing metal precursors and reducing them simultaneously; 2) stepwise growth: reducing precursors in a successive manner; 3) post-modification: modifying existing NPs with element-exchange to incorporate more elements.

In the first paradigm, the preparation of uniform NPs is a complex process since more than one metal precursors are existing in the system. Due to the differences in reduction potentials inherent to metals, it is challenging to balance the co-reduction and nucleation of all components over a wide range of stoichiometric ratios.<sup>2,4,45-59</sup> Specifically, one could expect the occurrence of by-products such as monometallic NPs during the synthesis. In order to avoid separate nucleation of two metals, the reducing agent and the reaction system need to be selected carefully. If the reducing agent employed is too strong, the reduction process becomes less controllable. For example, when hydrazine is used as the reducing agent to synthesize NiCo and NiCu NPs, the reduction process was too fast that leads to products far from the intended composition and size distribution.<sup>101</sup> In contrast, higher quality NPs could be achieved using a combination of reducing agent and proper ligand (Figure 1.5).<sup>102-106</sup> For instance, borane-*tert*-butylamine (TBAB) and hexadecanediol were used as reducing agents to synthesize a uniform batch of truncated-octahedral

Pt<sub>3</sub>Ni alloy NPs.<sup>107</sup> During the synthesis process, adamantanecarboxylic acid or adamantaneacetic acid was added as ligands to control the reaction kinetics. In addition to TBAB, other reported mild reducing agents for the preparation of uniform alloy NPs include oleylamine,<sup>108</sup> ethylene glycol,<sup>109</sup> L-ascorbic acid,<sup>1,110</sup> *etc.* Nevertheless, with the wet chemical co-reduction method, it is still time-consuming to figure out an appropriate combination of reducing agent, ligand, and reaction medium for each type of NPs.<sup>111</sup>

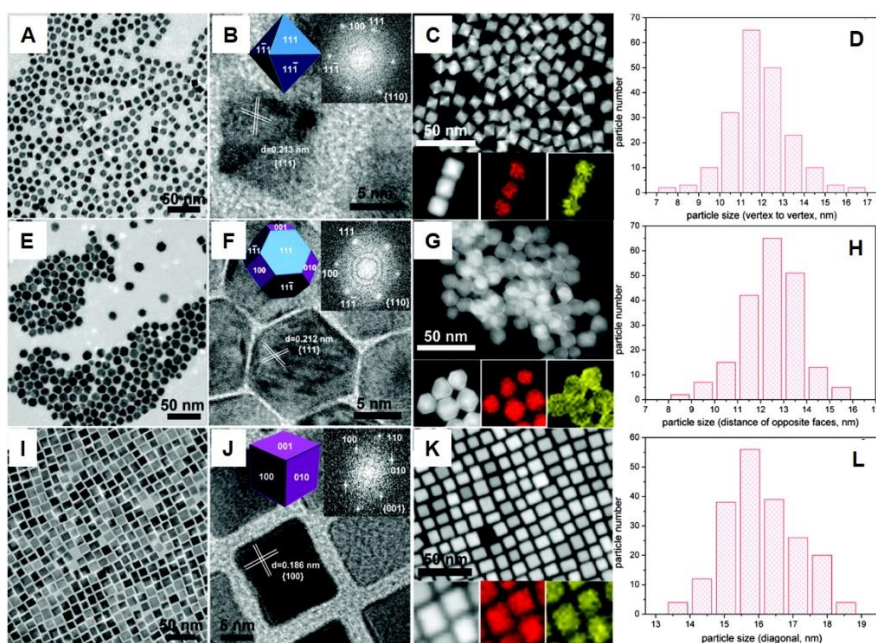


**Figure 1.5** Uniform bimetallic nanoparticles synthesized by chemical co-reduction method. (A-D) TEM, HRTEM, HAADF-STEM images, and size distribution of (A-D) PtNi<sub>2</sub> octahedrons, (E-H) PtNi<sub>2</sub> truncated octahedrons, and (I-L) PtNi<sub>2</sub> cubes. Element maps show the distribution of Pt in yellow and Ni in red.<sup>104</sup>

The second strategy to prepare polyelemental NPs via wet chemical reduction is successive reduction of metal precursors, where one metal is reduced first and then function as a seed to direct the deposition of the second metal. Depending on the affinity of two metals, there are three possible scenarios.<sup>45</sup> If the second metal deposits on the entire surface of the preformed seed of the first metal, core-shell NPs can be synthesized.<sup>112,113</sup> If the deposition only occurs on specific sites of

performed nuclei, then heterostructured NPs will be obtained.<sup>46-48,114-120</sup> If the second metal is able to diffuse into the lattice of preformed nuclei, alloy NPs will be synthesized.<sup>121</sup> Currently, successive reduction is broadly used to prepare core-shell and multi-shell NPs. Sun *et al.* prepared AuPd core-shell NPs by depositing a thin Au shell onto Pd NPs with oleylamine as a reducing agent.<sup>110</sup> Through rationally designing the sequence of metal deposition, multi-shell trimetallic NPs (Au@Pd@PtFe) can be further synthesized.<sup>110</sup> With respect to catalysis, one important design of core-shell NPs is to make the core consisting of transition metal catalysts while the shell consisting of oxide supports (Figure 1.6).<sup>70,112</sup> The oxide shell can potentially prevent NP sintering during catalysis, but it needs to be porous enough so that the reactants can easily diffuse onto and leave the core surface. Another important design of core-shell NPs is to make a core consisting of less-noble metals covered by a thin shell consisting of more-noble metals.<sup>122,123</sup> In this way, the utilization of precious metals can be minimized while the catalytic activity of shell layer can be engineered by tuning the core materials.

In addition to core-shell structures, stepwise growth is also broadly used for the synthesis of heterostructured NPs. By carefully choosing the sequence of metal deposition on a seed particle, heterostructured NPs possessing up to four domains and diverse architectures have been successfully synthesized (Figure 1.7).<sup>32,48</sup> Moreover, studies on heterostructured NPs reveal that the catalytic properties of NPs are highly dependent on particle architectures, *i.e.*, the arrangement of domains/phases within a NP.<sup>29,32</sup>

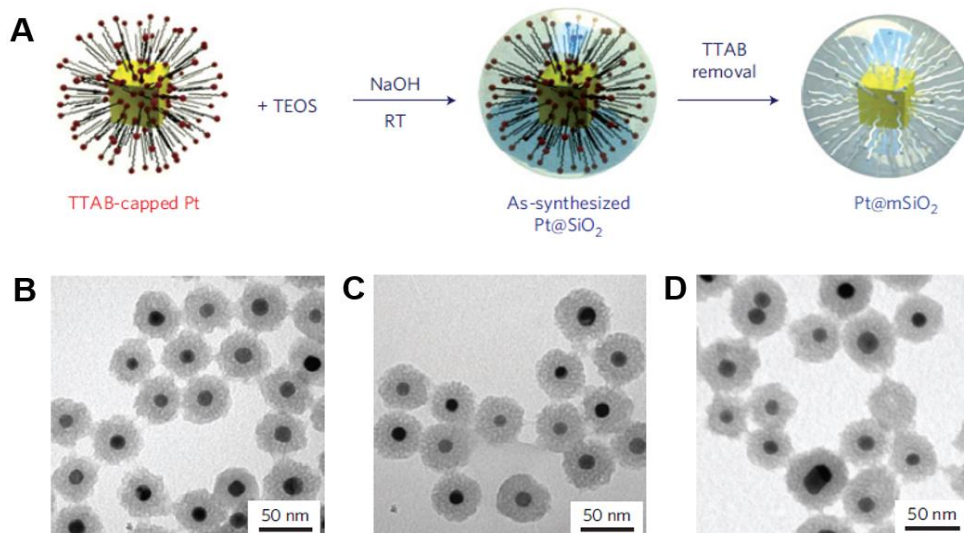


**Figure 1.6** Pt@SiO<sub>2</sub> core-shell nanoparticles synthesized by stepwise method. (A) Schematic representation of the synthesis of Pt@SiO<sub>2</sub> core-shell nanoparticles. (B-D) TEM images of Pt@SiO<sub>2</sub> nanoparticles after calcination at 350°C, 550°C, and 750°C, respectively.<sup>26</sup>

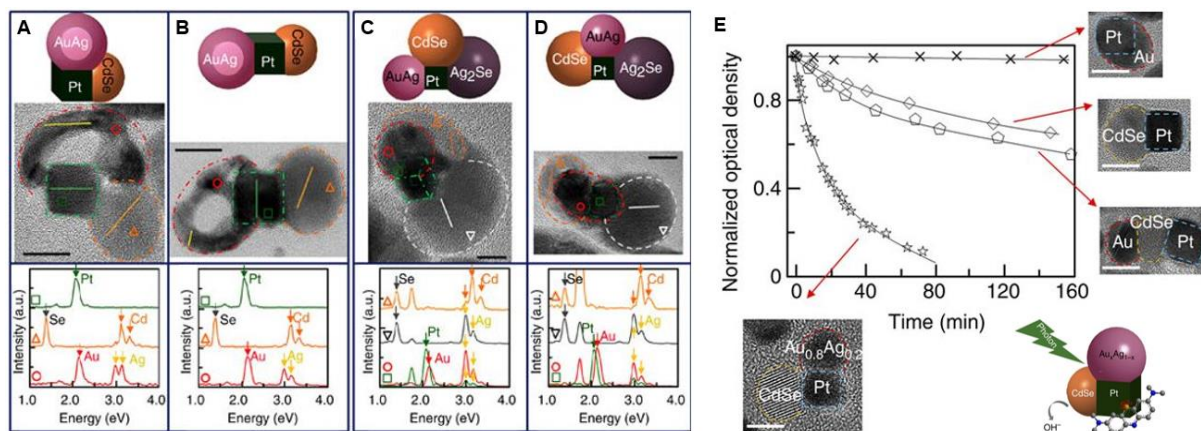


**Figure 1.7** Non-centrosymmetric heterostructured nanoparticles synthesized by stepwise method. (A-D) Structural model, HRTEM image, and single-point EDS of each type of nanoparticles. In HRTEM images, color-dashed curves outline boundaries of different subunits, and solid color lines highlight lattice orientations of each subunit. (E) Time-dependent normalized optical density of methylene blue molecules (reactant) at 677 nm with different photocatalysts.<sup>32</sup>

For the third strategy, post-modification reactions such as oxidation, sulfurization, nitridation, phosphorization, and cation-exchange, can be applied to the preformed NPs to generate higher order of compositional and structural complexity.<sup>2,82,124-126</sup> Recently, Schaak *et al.* reported a library of 47 distinct heterostructured metal sulfide NPs that are made by cation-exchange

reactions.<sup>126</sup> They used CuS nanospheres, nanorods, and nanodiscs as the starting materials (Figure 1.8). Upon manipulating the sequence of cation-exchanges (Ag, Cd, Zn, Co, *etc.*), additional elements were successively introduced into the CuS NPs while novel heterostructures including asymmetric, patchy, porous, and sculpted nanoarchitectures were obtained. This generalizable strategy provides predictable retrosynthetic pathways to complex polyelemental NPs that are otherwise difficult to access. In a contrary vein to adding elements, post-etching has been used to selectively remove metals in polyelemental NPs. This allows the generation of unprotected cavities in a NP, of which the outside surface is protected by ligands. Such materials have the potential to mimic the geometric architecture and property of enzymes.<sup>127</sup>

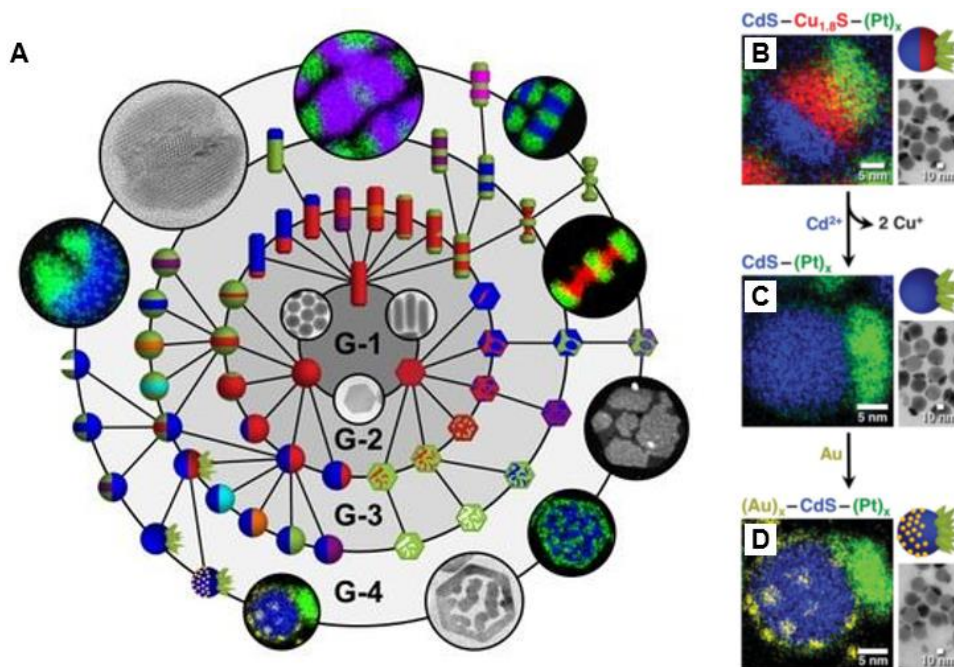


**Figure 1.8** A library of heterostructured nanoparticles synthesized by stepwise cation-exchange. (A) Schematic representation of using cation-exchange reactions to create complex heterostructured nanoparticles with CuS nanosphere, nanorod, and nanodisc as the starting materials. Cu (red), Cd (blue), Zn (green), Ag (pink), Mn (Cyan), Ni (orange), Co (purple). (B-D) Complex nanostructures formed by combining multiple cation exchange steps with regioselective deposition or etching. Cu, Cd, Pt, and Au are shown in red, blue, green, and yellow, respectively.<sup>126</sup>

### 1.3.2 Thermal Decomposition

Thermal decomposition is another commonly used method to synthesize NP catalysts. Through thermolysis of salt precursors or organometallic complexes, monometallic and multimetallic NPs can be generated either in solvent<sup>128-131</sup> or on catalyst supports.<sup>132-135</sup> One unique advantage of NPs synthesized by thermal decomposition is their good stability under harsh reaction conditions, as compared with the analogues synthesized by chemical reduction routes.<sup>132</sup> However, thermal decomposition encounters a similar challenge of the chemical reduction strategy, *i.e.*, the difficulty in controlling the reduction kinetics of different metal precursors. As a result, the product composition is normally inconsistent with the molar ratio of metal precursors. For example, Caps *et al.* studied the synthesis of FeCo NPs *via* thermolysis of  $\text{Fe}(\text{CO})_5$  and  $\text{Co}_2(\text{CO})_8$ .<sup>129</sup> In tetrahydronaphthalene solvent,  $\text{Co}_2(\text{CO})_8$  decomposes at 150 °C while  $\text{Fe}(\text{CO})_5$  decomposes at 200 °C. If the decomposition was carried out at 200 °C, separate phases of Co and Fe could be formed due to the faster decomposition rate of  $\text{Co}_2(\text{CO})_8$ . To solve this problem, one strategy is to use molecular bimetallic compounds (such as  $[\text{FeCo}_3(\text{CO})_{12}]^-$ ,  $[\text{Fe}_3\text{Pt}_3(\text{CO})_{15}]^{2-}$ , and  $[\text{FeNi}_5(\text{CO})_{13}]^{2-}$ ) as the single source of metals.<sup>130</sup> The preformed metal-metal bonds promote the alloying of metals, leading to products with similar composition to precursors. Nonetheless, molecular bimetallic complexes are still limited to some specific systems. To synthesize multimetallic NPs covering broad material library, delicate design of novel metal precursors is requested.

### 1.3.3 Molecular Template Mediated Synthesis

Since the co-nucleation and growth of multiple metals is difficult to manipulate at the bulk scale, one strategy circumventing this problem is to use molecular templates as nanoreactors. Through physically confining precursors into discrete reactors (effectively dividing bulk solution

into many small unit volumes of solution), NP synthesis can be localized at a smaller length scale, thus gaining better control over the co-nucleation and growth process.<sup>136</sup> Particularly, single NPs can be obtained in each reactor if the size of reactors is small enough. In this case, it in principle enables the facile tuning of particle composition if the ratio of metal precursors in templates can be controlled. Furthermore, template-mediated synthesis can also be used to shape the morphology of multimetallic NPs when the nanoreactors possess well-defined shapes.<sup>137,138</sup> Thus far, dendrimers,<sup>136,139-143</sup> microemulsions,<sup>144-146</sup> organic molecular cages,<sup>147</sup> and polymer micelles<sup>137,138,148</sup> have been utilized as nanoreactors to guide the synthesis of multimetallic NPs. The loading of multiple metal precursors in nanoreactors in a uniform and adjustable way remains challenging,<sup>143</sup> which limits the application of this strategy for polyelemental NP synthesis. In addition to chemical/thermal co-reduction and molecular template mediated synthesis, other methods for preparing NPs at a bulk scale include electrochemical deposition,<sup>149</sup> radiolysis,<sup>150</sup> sonochemical reduction,<sup>151</sup> laser ablation,<sup>152</sup> *etc.*

#### 1.3.4 Lithographic Methods

Studies on NPs have revealed that their catalytic properties for each specific reaction are mandated by many factors including size, structure, composition, *etc.* While the aforementioned methods have realized delicate synthesis of complex multimetallic NPs, the serially making and characterizing nature is not inherently amenable to high-efficiency catalyst discovery. Especially for multimetallic NPs with more than three components, the number of parameters needed to be explored separately is vast. To free experimentalists from batches of tedious synthesis, one potential approach is to utilize lithographic techniques to integrate multiplex NP arrays on certain substrate surfaces.<sup>153</sup> In an ideal case, the size, structure, and composition of each NP within the

array can be exclusively defined by local lithographic parameters, thus integrating tremendous amounts of different NPs onto one chip and making high-throughput catalyst screening feasible.

To date, several lithographic methods have been developed to prepare mono- or multimetallic NPs on substrates. These approaches can be generally divided into two categories, *i.e.*, synthesis-then-positioning and positioning-then-synthesis. In the former strategy, NPs are first synthesized by wet chemistry and then organized on surfaces using lithographically defined templates or more-tedious pick-and-place approaches such as microdroplet dewetting,<sup>154</sup> NP sliding,<sup>155,156</sup> and direct writing.<sup>157</sup> In the latter strategy, characterized as precursor-positioning-then-synthesis, metal precursors are physically confined in patterned nanoreactors on substrates and subsequently chemically converted into NP. This strategy uses the advantage of nanoreactor-mediated synthesis (section 1.3.3). Examples of nanoreactors include polymer domains defined by block copolymer lithography,<sup>52,158-163</sup> nanoreactors generated by ink-jet printing,<sup>164,165</sup> and nanocavities prepared by photolithography<sup>166-168</sup> or electron-beam lithography.<sup>169-171</sup> However, none of the methods can control both NP size and composition while guaranteeing the presence of a single multimetallic NP at a precise location, leaving the on-site synthesis of arbitrarily chosen NPs an open challenge.

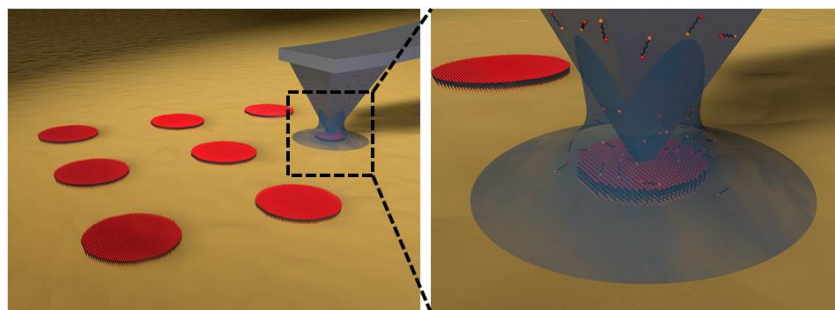


**Figure 1.9** Schematic representation of dip-pen nanolithography (DPN). A water meniscus forms between a solid substrate and an AFM tip that is coated with molecule ink. The size of the meniscus, which is controlled by relative humidity, affects the ink transport rate, the effective tip-substrate

contact area, and the DPN resolution.<sup>172</sup>

Dip-pen nanolithography (DPN) is a molecular printing technique invented in 1999 for preparing nanostructures on surfaces *via* a direct-writing manner.<sup>172-176</sup> In a typical DPN process, an ink-coated atomic force microscopy (AFM) probe is moved to a solid substrate and brought into contact with the substrate surface. During this process, the ink molecules are transferred from the AFM tip to the substrate and a pattern of the ink molecules can be generated through programmed movements of the AFM piezo-scanner (Figure 1.9). Thus far, several groups have attempted to print NPs directly by DPN, but the resulting pattern usually contains multiple NPs in each feature (Figure 1.10).<sup>177-179</sup>

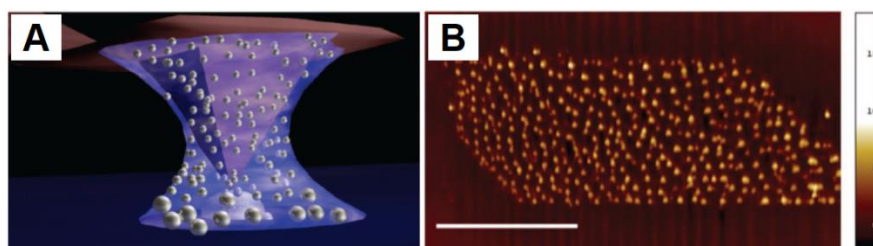


**Figure 1.10** (A) Schematic illustration of the direct writing of nanoparticles by DPN. (B) AFM topographic image of one patterned dot with multiple nanoparticles inside.<sup>177-179</sup>

In 2010, Mirkin *et al.* developed a method, termed scanning probe block copolymer lithography (SPBCL) that integrates polymer-mediated NP synthesis and DPN to synthesize single NPs on surfaces.<sup>9,11</sup> As shown in Figure 1.11, the underlying concept of SPBCL is to first deliver attoliter-scale volume of metal-coordinated block copolymers to a desired location *via* scanning probe lithographic techniques. These polymer features subsequently function as nanoreactors in which single nuclei of metal precursors are formed with thermal annealing. After removing the polymer by thermal decomposition, a single NP is synthesized in each nanoreactor.

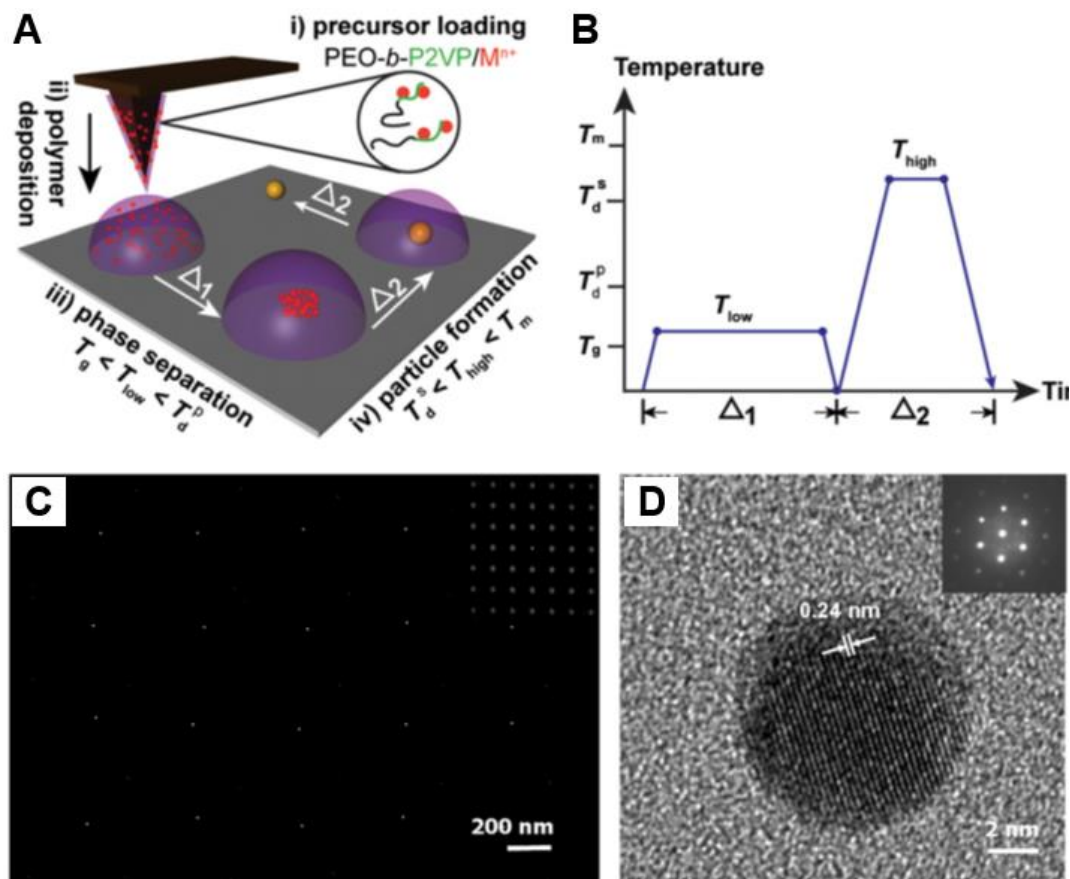


**Figure 1.11** (A) Schematic illustration of polymer-mediated synthesis of nanoparticles by SPBCL. The method consists of four steps: precursor loading, polymer deposition, precursor aggregation, and particle formation. (B) Heating profile of the annealing process. The two heating cycles ( $\Delta_1$  and  $\Delta_2$ ) correspond to the cycles at  $T_{low}$  and  $T_{high}$  in (A). (C) SEM image of Au nanoparticles produced by SPBCL. (Inset) Fourier transform of the SEM image. (D) High-resolution TEM image showing a crystalline Au nanoparticle with a diameter of 8 nm. (Inset) Electron diffraction pattern of the synthesized Au nanoparticle.<sup>180,181</sup>

One major advantage of SPBCL is that it can be used to pattern individual NPs over large areas with the properties of each NP controlled by local lithographic parameters. The tuning of NP size within the range of 3-50 nm is realized by changing polymer feature size, which is controllable by patterning parameters such as humidity, dwell time, tip-withdrawing speed, *etc.*<sup>172,180,181</sup> X-ray photoelectron spectroscopy (XPS) studies have revealed three chemical pathways for synthesizing different NPs by SPBCL (Figure 1.12).<sup>181</sup> Depending on the reduction potential of metal precursors,

metals can be chemically reduced by poly(ethylene oxide) (PEO) when annealed at  $T_{\text{low}}$  (Pathway 1, Au and Ag), thermally reduced when annealed at  $T_{\text{high}}$  (Pathway 2, Pd and Pt), or end up in the same oxidation state as the metal precursors (Pathway 3, Co, Ni, Cu, and Fe). Based on the three pathways, SPBCL has been generalized to include a broad range of materials such as metals (Pd, Ag, Au, Pt),<sup>176,181</sup> metal oxides ( $\text{Fe}_2\text{O}_3$ ,  $\text{Co}_2\text{O}_3$ , NiO, CuO),<sup>181</sup> one semiconductor (CdS),<sup>182</sup> and one metal alloy (AuAg).<sup>181</sup>

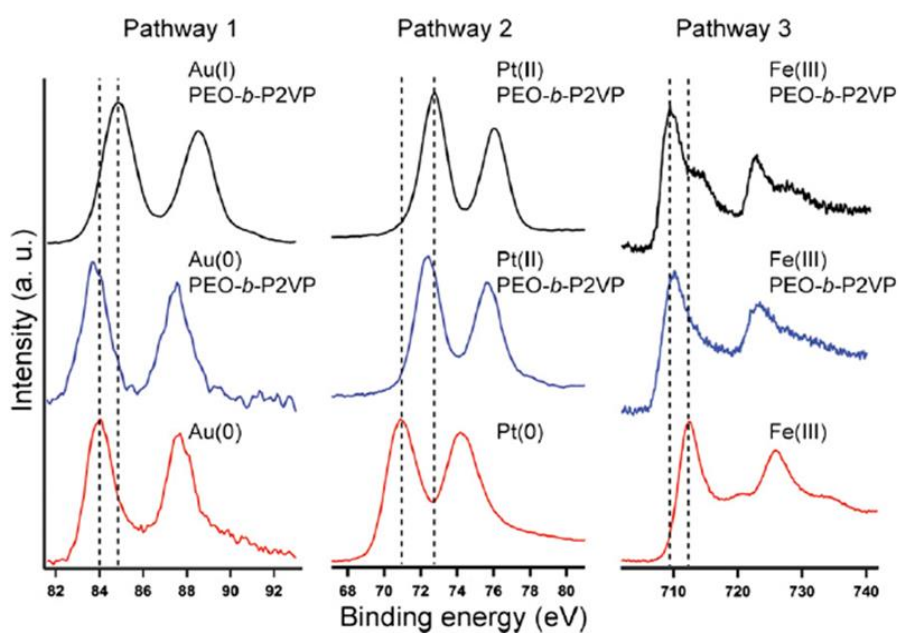


**Figure 1.12** XPS spectra collected before annealing (black), after annealing at  $T_{\text{low}}$  (blue), and after annealing at  $T_{\text{high}}$  (red) for Au (Left), Pt (Center), and Fe (Right) to show the three chemical pathways of forming nanoparticles in SPBCL.<sup>181</sup>

Although SPBCL constitutes a very promising platform to develop multiplex NP arrays for combinatorial catalyst screening. The catalytic activity of synthesized NPs and the generality of SPBCL to polyelemental NPs remains unclear. In the following chapters of this thesis, major breakthroughs in the synthesis of polyelemental NPs and in the control of NP structures are presented. In particular, Chapter Two describes the scope of SPBCL for polyelemental NPs, which

develops SPBCL into a combinatorial synthetic method for polyelemental NPs; Chapter Three details the formation mechanism of polyelemental NPs in polymer nanoreactors, showing unprecedented control over NP structures with SPBCL; Chapter Four presents a set of design rules for polyelemental heterostructures that are distilled based on the architectures of SPBCL-synthesized NPs. The rules guided the synthesis of unprecedented tetra-phase NPs with six phase boundaries; Chapter Five demonstrates the scale-up synthesis of polyelemental NPs with polymer pen lithography (PPL) and investigates the catalytic activity of SPBCL-synthesized NPs.



## 2.1 Introduction

Unary, binary, and even ternary nanostructures can be synthesized by incorporating up to three metals into a single nanoparticle (NP) in an alloyed or phase-segregated state with a variety of synthetic techniques.<sup>2,8,9,47,48,105,144,183</sup> Indeed, the controlled combination of multiple metals at the nanoscale offers an effective way to tune the chemical and physical properties of NPs, either: (i) by facilitating hybrid chemical, electronic, and magnetic interactions between metal components,<sup>8,9,22,23</sup> or (ii) by combining different properties associated with each pure component.<sup>18,36</sup> These properties make multimetallic NPs promising materials for diverse applications, spanning catalysis,<sup>8,9,22,82,122</sup> plasmonics,<sup>10,23</sup> therapy,<sup>18</sup> and biological imaging.<sup>20,36</sup> Moreover, in the context of both catalysis and plasmonics, a multimetallic NP often has properties that exceed the capabilities of unary particles consisting of pure forms of each element.<sup>8-10,82,122</sup> To date, several tools have been developed for screening the composition space of macroscopic multicomponent materials. However, at the nanoscale, controlled synthesis and positioning of multimetallic nanofeatures become increasingly important for systematic study. In NP synthesis, important advances have been made in bulk solution based (either one-pot or stepwise),<sup>47,48,105</sup> microfluidic,<sup>184</sup> and microemulsion methods,<sup>144</sup> but none of these offers the ability to systematically examine compositional diversity in a high throughput manner or beyond three-element particles.

Recently, we reported a method, termed scanning probe block copolymer lithography (SPBCL),<sup>180-182,185</sup> that integrates polymer-mediated particle synthesis and molecular printing techniques such as dip-pen nanolithography (DPN)<sup>172-176</sup> and polymer pen lithography (PPL)<sup>186,187</sup> to pattern single NPs on surfaces. The principle behind SPBCL is to first deliver attoliter-scale

volumes of metal-coordinated block copolymers to a desired location via scanning probe lithography. These polymer features subsequently function as nanoreactors in which single NPs are locally synthesized.<sup>180,181,185</sup> The NP size is controlled by the volume and metal loading of the polymer feature, and in principle, the composition can be controlled by adjusting the types and ratios of metal precursors loaded within the block copolymer nanoreactor.<sup>180-182</sup> Thus far, SPBCL has been generalized to include a broad range of materials such as metals,<sup>181,188</sup> metal oxides<sup>181,187</sup> and one semiconductor.<sup>182</sup> In addition, the synthesis of a AuAg alloy NP was effected by patterning Ag and Au precursors simultaneously,<sup>181</sup> which suggests this may be a general approach for preparing multimetallic NPs, which could be useful for many applications. In this chapter, we study the scope of this approach and evaluate the potential for controlling the composition of the resulting NPs. We show that a library of NPs with controlled composition and structure could be systematically synthesized by SPBCL.

## 2.2 Nanoparticles Composed of Miscible Elements

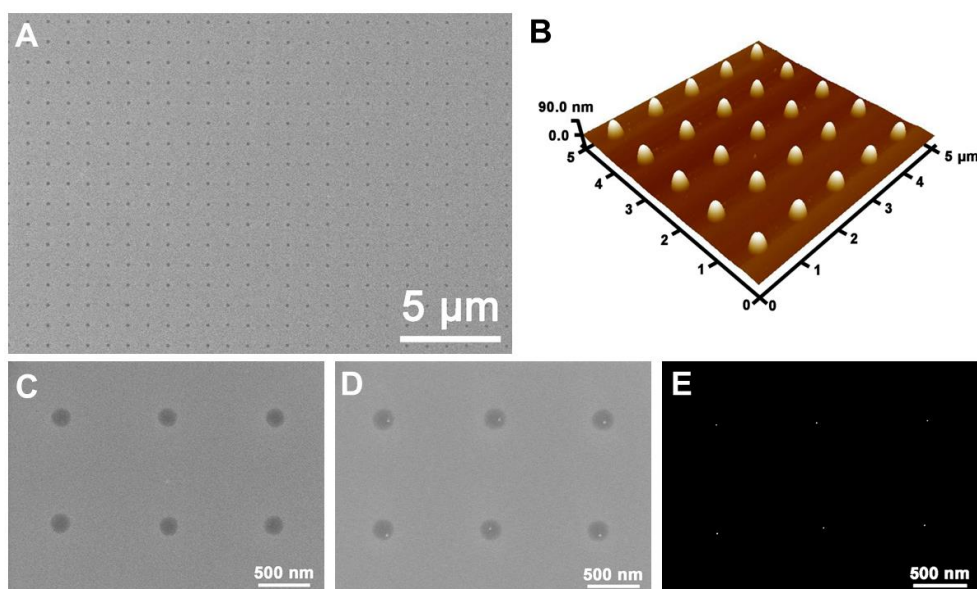


**Figure 2.1** Representative SPBCL process for preparing an alloy nanoparticle array. (A) SEM image of nanoreactors patterned on a hydrophobic silicon substrate. (B) AFM topographical image

of a patterned polymer dot array. The diameter and height of the dots are 300 nm and 80 nm, respectively. (C) Enlarged SEM view of six polymer nanoreactors. (D) After annealing, metal precursors aggregate inside the polymer nanoreactors. (E) Further thermal annealing reduces the precursors and decomposes the polymer to form arrays of single nanoparticles.

Previous studies have shown that SPBCL can be used to control the size of single-component NPs by tuning the volume and metal loading of the polymer feature,<sup>180-182</sup> effectively determining the amount of available precursors for forming NPs. However, when considering the synthesis of multimetallic NPs, it is not obvious that a single NP will be formed. Thus, we initially explore the synthesis of alloy NPs composed of six combinations of transition-metals, *i.e.*, AuPd, PtNi, PdNi, PtCo, PdCo, and CoNi, which are widely used for catalysis.<sup>1,5</sup> In a typical experiment (Figure 2.1), two species of metal precursor (*e.g.*, H<sub>2</sub>AuCl<sub>4</sub> and Na<sub>2</sub>PdCl<sub>4</sub>) were mixed in a solution with a block copolymer, resulting in the metal ions becoming coordinated to the polymer. Here, poly(ethylene oxide)-*b*-poly(2-vinyl pyridine) (PEO-*b*-P2VP) was used as it has been found that the P2VP block coordinates the metal precursors and functions as a carrier to transport metals while the hydrophilic PEO block facilitates the transport of polymer during patterning experiments.<sup>180</sup> Following ink preparation, an array of atomic force microscopy (AFM) probes was coated with the polymer ink and brought in contact with hydrophobic silicon substrates to deposit the metal-coordinated polymers onto the surface. Figure 2.1A-2.1C show typical scanning electron microscopy (SEM) images and an AFM topographical image of the deposited polymer dot arrays. By virtue of performing this patterning with a scanning probe, the pattern of polymer dots can be predefined and controlled through programmed movements of the AFM piezo-scanner, while the size of each polymer dot is controlled by the tip-substrate contact time and tip withdrawal speed.<sup>175,176</sup> Following patterning, the polymer dot-coated substrate was annealed at a temperature (150 °C) higher than the glass transition temperatures of PEO (-76 °C) and P2VP (78 °C), thus

inducing the aggregation of various metal precursors inside each dot. Interestingly, single nuclei were observed to form in each polymer dot (Figure 2.1D). These results suggest that once a nucleus is formed in a polymer nanoreactor, the remaining free metal precursors, regardless of their composition, aggregate onto it due to the lower energy barrier of particle growth than homogenous nucleation of a new particle.<sup>189</sup> This confined nucleation process ensures the formation of one alloy NP in each polymer spot.

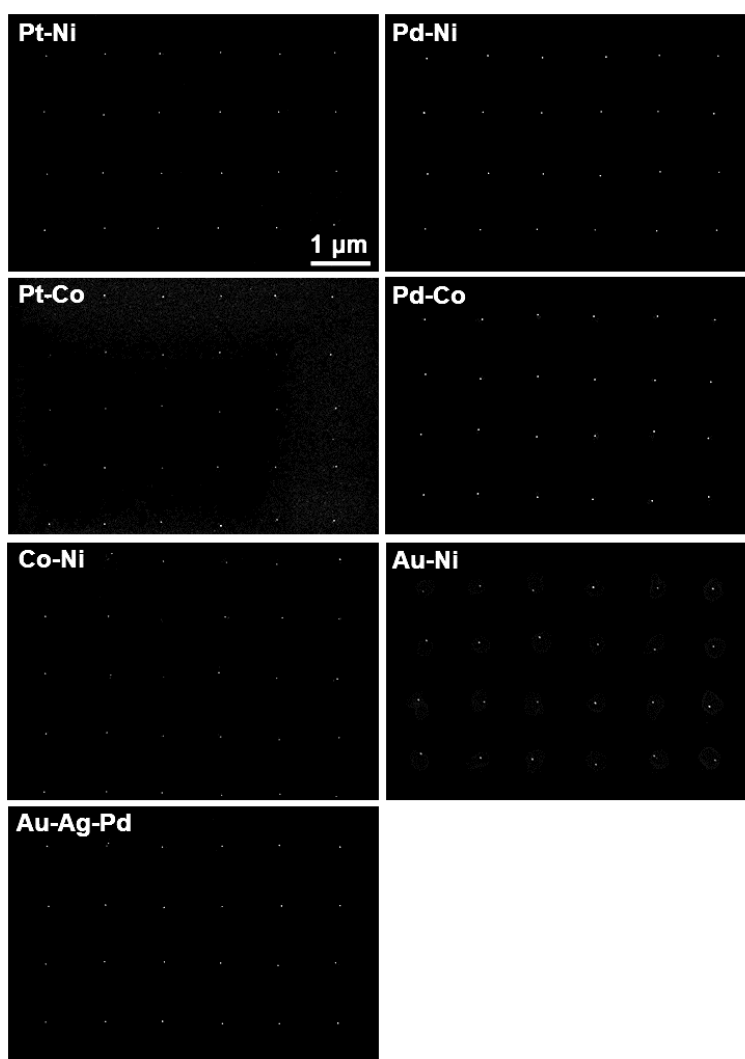


**Figure 2.2** Representative SEM images of arrays of various alloy nanoparticles synthesized by SPBCL. Each image shows a 6-by-4 array of nanoparticles.

It is important to emphasize that the success of this process is based upon the assumption

that homogenous nucleation is less likely than particle growth, a condition that one would expect to be violated as the reactor becomes larger. Experimentally we found that nearly all nanoreactors smaller than 350 nm in diameter formed single NPs, but as nanoreactor diameter was increased to 1  $\mu\text{m}$ , nearly all of the nanoreactors formed multiple nuclei. After the first annealing step, the sample was further annealed at 500  $^{\circ}\text{C}$  to remove the polymer and reduce the metal precursors. Importantly, in all cases studied, the synthesis resulted in the formation of arrays of single alloy NPs, suggesting that the precursors conclude the experiment in the same NP (Figure 2.2).<sup>180,181</sup>

To further confirm the formation of a single alloy NP in each polymer nanoreactor, we carried out scanning transmission electron microscopy (STEM) and high-resolution transmission electron microscopy (HRTEM) characterization of NPs synthesized on TEM grids. As shown in STEM images, only one alloy NP was observed on each site of the square arrays of each bimetallic system (Figure 2.3). The inset high-angle annular dark-field (HAADF) STEM images of individual alloy NPs exhibit even contrast, indicating the uniform alloying of each binary system. The morphology of most alloy NPs is quasi-spherical. Since STEM does not allow for chemical fingerprinting, this characterization was paired with energy dispersive X-ray spectroscopy (EDS) elemental mapping to investigate the compositional distribution within the alloy NPs. Specifically, EDS mapping confirmed that the NPs were homogeneous mixtures of each binary system (Figure 2.3-2.5). This observation can be attributed to the miscibility of these binary metal mixtures.<sup>190</sup> In addition to bimetallic NPs, arrays of single trimetallic NPs were also synthesized by formulating an ink with PEO-*b*-P2VP and three precursors (*i.e.*,  $\text{HAuCl}_4$ ,  $\text{Na}_2\text{PdCl}_4$ , and  $\text{AgNO}_3$ ) for SPBCL (Figure 2.6). The three elements employed here are miscible at arbitrary compositions,<sup>190</sup> which is validated by the EDS elemental mapping of AuAgPd NPs.

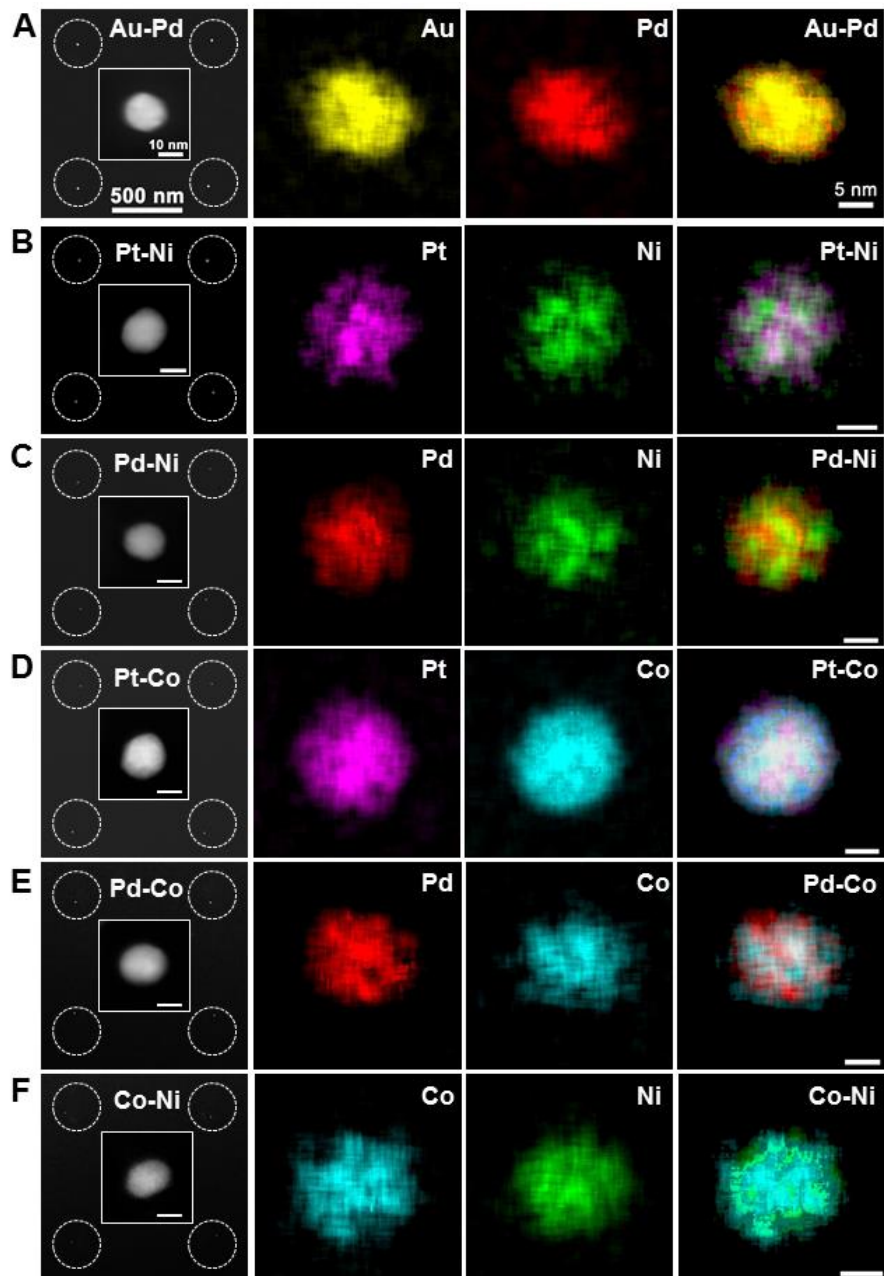


**Figure 2.3** Various 1:1 alloy nanoparticles generated by SPBCL: (A) AuPd, (B) PtNi, (C) PdNi, (D) PtCo, (E) PdCo, (F) CoNi. (First column) HAADF-STEM images of a 2-by-2 nanoparticle array of each system. Dotted circles highlight the position of nanoparticles as a guide to the eye. The insets are zoomed-in images of single alloy nanoparticles. Only one nanoparticle was observed at each site. One scale bar applies to the insets and the other applies to square array STEM images. (Second to fourth columns) EDS elemental mapping of each bimetallic nanoparticle (scale bar: 5 nm).

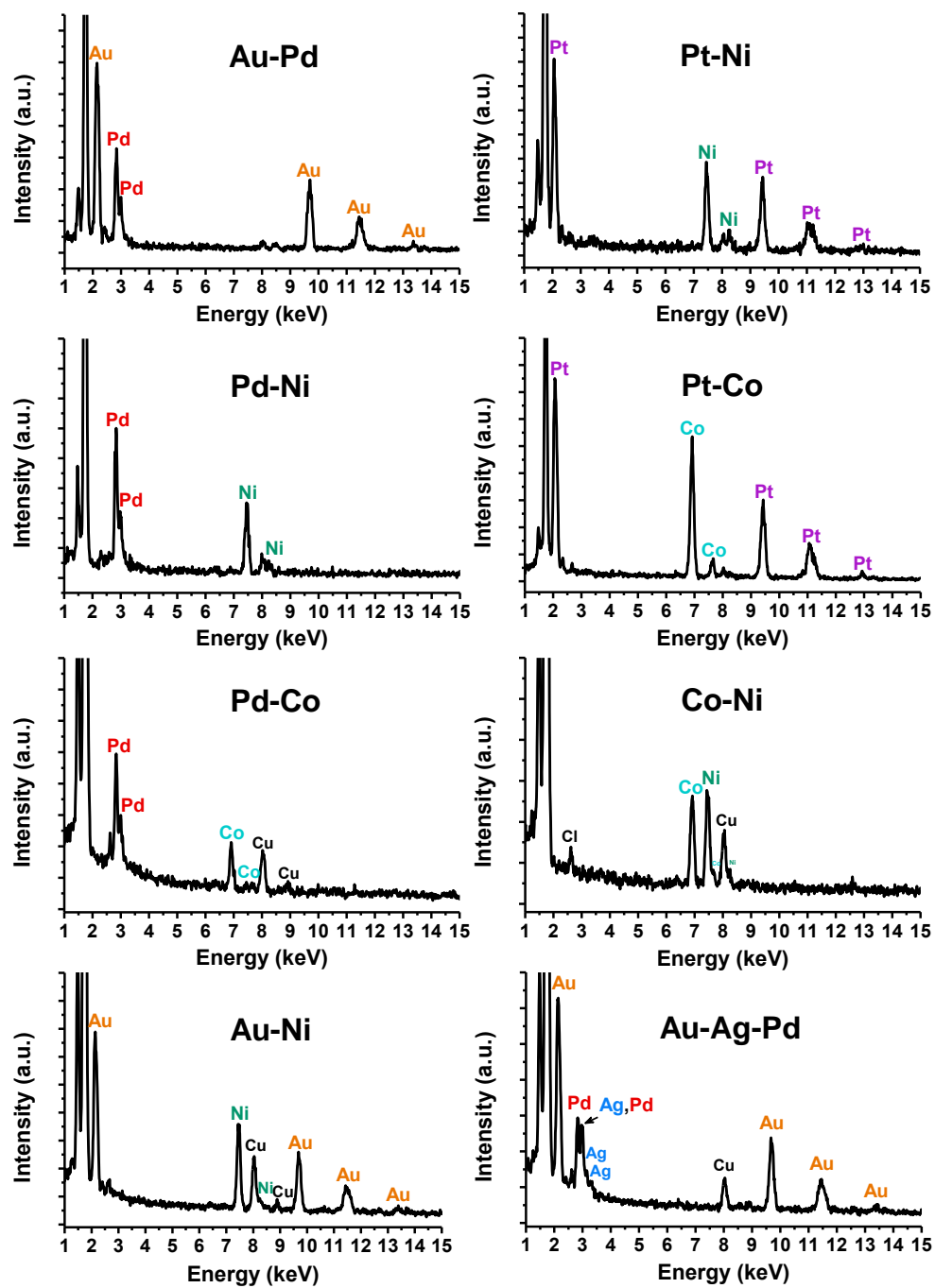


**Figure 2.4** EDS spectra of various alloy nanoparticles synthesized by SPBCL.

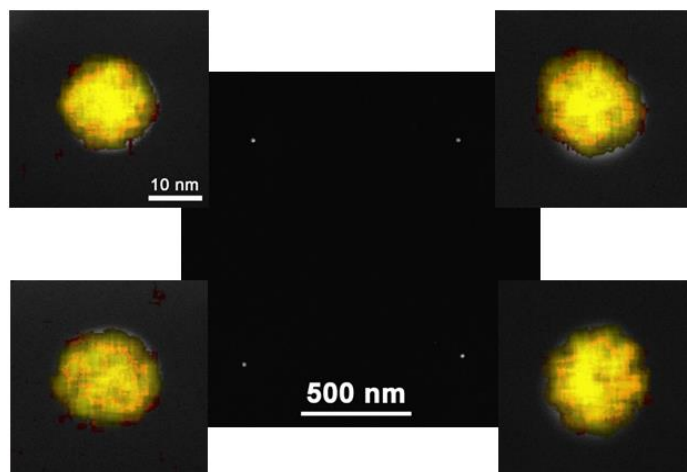


**Figure 2.5** HAADF-STEM image of a square array of AuPd nanoparticles. The EDS elemental mapping images corresponding to the nanoparticles at each corner. Color codes: Au (yellow), Pd (red).

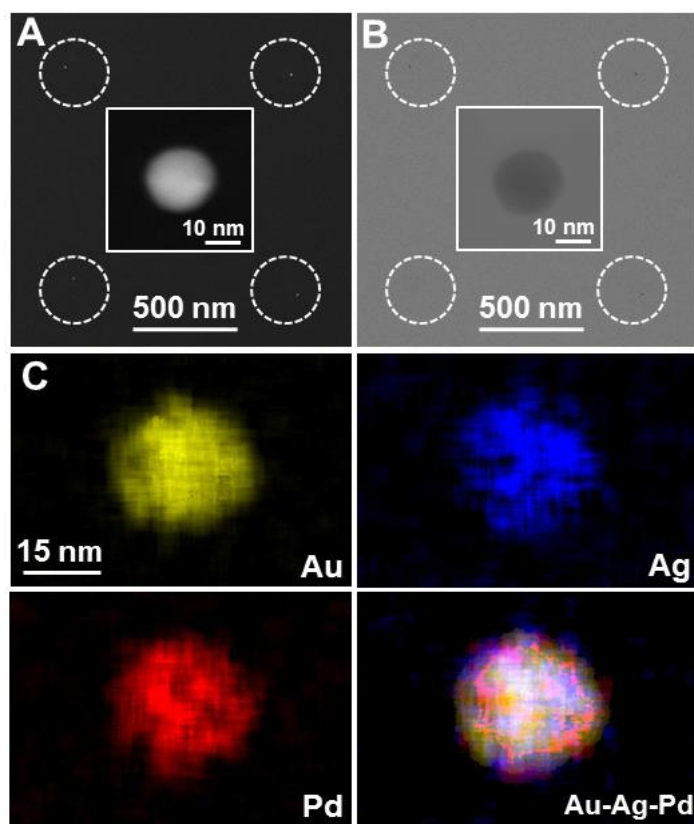


**Figure 2.6** (A) SPBCL pattern of an array of AuAgPd trimetallic nanoparticles imaged by HAADF-STEM and (B) bright-field STEM. (C) EDS elemental mapping of a single AuAgPd nanoparticle. The overlay of Au, Ag, and Pd signals provides evidence for the alloying of these three elements.

### 2.3 Nanoparticles Composed of Immiscible Elements

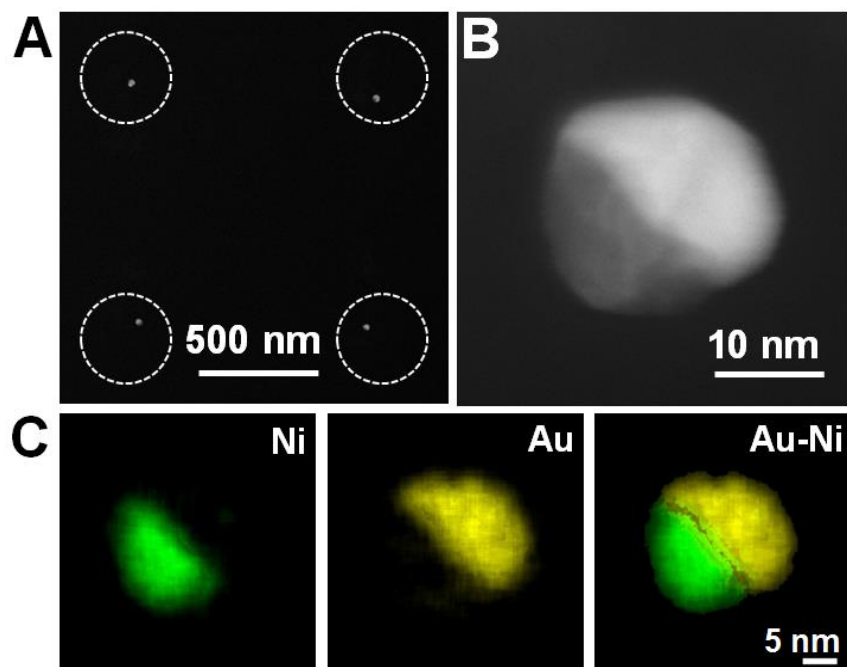


**Figure 2.7** (A) SPBCL pattern of a AuNi nanoparticle array imaged by HAADF-STEM. Dotted circles highlight the position of nanoparticles as a guide to the eye. (B) Enlarged view of a single AuNi nanoparticle. (C) EDS elemental mapping of a single AuNi nanoparticle showing that the nanoparticle is phase-segregated.

In addition to alloy NPs, we also studied NPs comprised of immiscible metals such as Au and Ni. Notably, STEM imaging of AuNi NPs revealed that Au and Ni were heterogeneously structured in the NP (Figure 2.7), with one region being a Ni subcluster and the other part being a Au subcluster. The brightness contrast between Au and Ni in the STEM image is attributed to atomic number contrast. EDS elemental mapping also confirmed the formation of a phase-separated NP. This phenomenon can be understood by considering the immiscibility of Au and Ni, which form two phases at 500 °C.<sup>190</sup>

### 2.3 Composition Control of Nanoparticles Synthesized by SPBCL

The size of SPBCL NPs can be specified by controlling the amount of available precursors for forming NPs.<sup>180-182</sup> In a similar vein, the composition of SPBCL alloy NPs can in principle be

controlled by tuning the amount of each constituent metal precursor. To test this compositional control, AuPd and PtNi alloy NPs were synthesized using nine ink solutions with different metal loading ratios. After patterning these inks and subjecting them to heat treatment, the resulting alloy NPs were examined using EDS. As shown in Figure 2.8, the composition of each alloy NP was within error of the ratio of precursors in the original ink composition with a standard deviation of less than 10%.

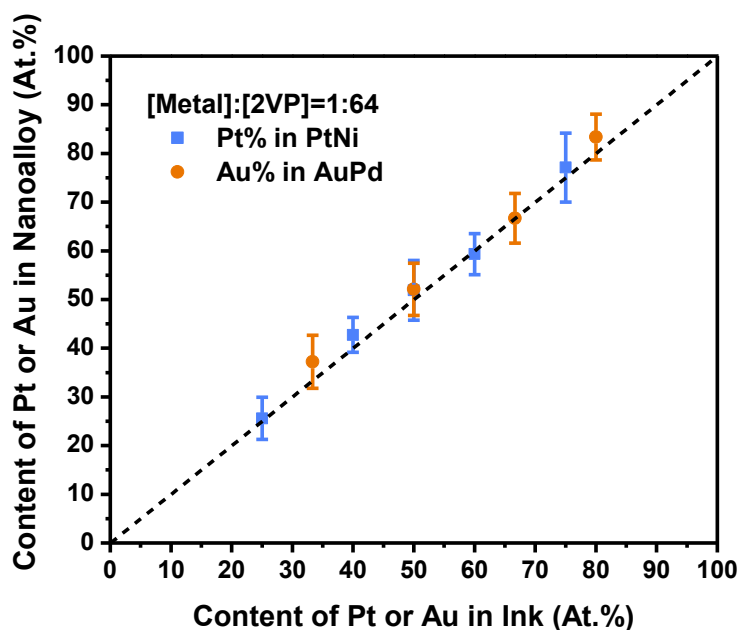


**Figure 2.8** Atomic composition in alloy nanoparticles versus atomic composition in polymer ink. The black dashed line indicates the ideal case.

Importantly, this result is not *a priori* obvious since different metals coordinate to PEO-*b*-P2VP with different affinities. We rationalize that the ink loading composition is reproduced in the NPs due to the fact that the vast majority of coordination sites are not occupied, thus mitigating the effects of competitive binding of metal precursors. As a result, the size and composition of alloy NPs are determined exclusively by the polymer feature and ink formulation. It is important to emphasize that this remarkable compositional uniformity of SPBCL alloy NPs is independent

of the miscibility of elements. Generally, it is difficult to use wet chemistry to synthesize multi-metallic NPs composed of immiscible metals with narrow size and composition distributions.<sup>4,7,103</sup>

## 2.4 Synthesis of a Polyelemental Nanoparticle Library

While the study on bimetallic and trimetallic NPs demonstrates an impressive synthetic capability of SPBCL, such nanostructures could also be made by other methods. Because SPBCL can be potentially used with millions of tips over areas as large as square centimeters to generate nanoscale features consisting of, in principle, a limitless number of polymer types, the technique could become a powerful approach to nanocombinatorics, where new particle compositions, including those not accessible by conventional techniques, can be generated en masse, and characterized and screened in a systematic and site-isolated fashion. To test this hypothesis, we investigate the combinatorial synthesis of particles consisting of five different elements, Au, Ag, Cu, Co, and Ni, *via* SPBCL.

We chose Au, Ag, Cu, Co, and Ni as example elements because they are often components of nanomaterials used in a wide variety of fields, spanning catalysis,<sup>22</sup> plasmonics,<sup>10,23</sup> magnetics,<sup>17</sup> electronics,<sup>14,15</sup> and biology.<sup>18,36</sup> In addition, there are readily available salt precursors that can be easily incorporated into block copolymers such as poly(ethylene oxide)-*b*-poly(2-vinyl pyridine) (PEO-*b*-P2VP). To synthesize NPs composed of these elements, a polymer preloaded with the appropriate metal salt(s) was used as an ink and deposited onto a substrate as hemispherical domes *via* dip-pen nanolithography (DPN) (Figure 2.9A).<sup>172</sup> After deposition, the polymer domes were thermally annealed in a two-step procedure. The first step was carried out in Ar at 120°C for 24 h and induced aggregation of the metal salts within the polymer dome.<sup>181</sup> The second step was carried out under flowing H<sub>2</sub> at 500°C for 12 h, which results in decomposition of the polymer as

well as reduction and coalescence of the aggregate metal ion precursors into a single-metal NP.<sup>181</sup> Moreover, the long-term thermal treatment at relatively high temperature allows the constituent metals to adopt a stable configuration (alloy or phase-separated) based on the compatibility of the elements. This approach allows one to make and study all combinations of the unary, binary, ternary, quaternary, and quinary NPs in a systematic and controlled manner (Figure 2.9B-2.9F).

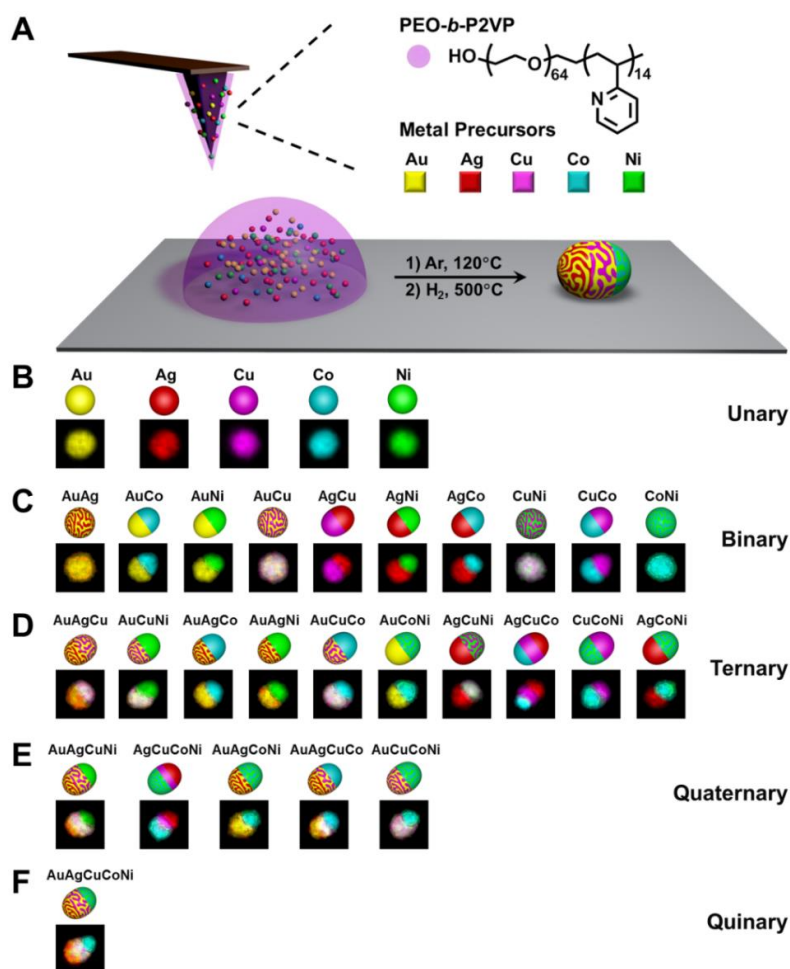


**Figure 2.9** The SPBCL-mediated synthesis of multimetallic nanoparticles. (A) Scheme depicting the process: a polymer loaded with metal ion precursor is deposited onto a substrate in the shape of a hemispherical dome *via* dip-pen nanolithography. After two-step thermal annealing, the metal precursors are aggregated and reduced, the polymer is decomposed, and individual nanoparticles result from each dome feature. (B) Unary (top row is a color-coded diagram of the anticipated result; bottom row is each particle, as characterized by EDS Mapping), (C) Binary nanoparticles consisting every two element combination of the five metals; the alloy versus phase-segregated state was consistent with the bulk phase diagrams for each two element combination, (D) Ternary

nanoparticles consisting of every three element combination of the five metals; the prediction of alloy versus phase-segregated state was based upon the miscibility of the three components, extracted from the binary data, (E) Quaternary nanoparticles consisting of every four element combination of the five metals; the prediction of alloy versus phase-segregated state was based upon the miscibility of the four components, extracted from the binary and ternary data, and (F) A quinary nanoparticle consisting of a combination of Au, Ag, Cu, Co, and Ni; the prediction of alloy versus phase-segregated state was based upon all of the previous data for the unary through quaternary systems.

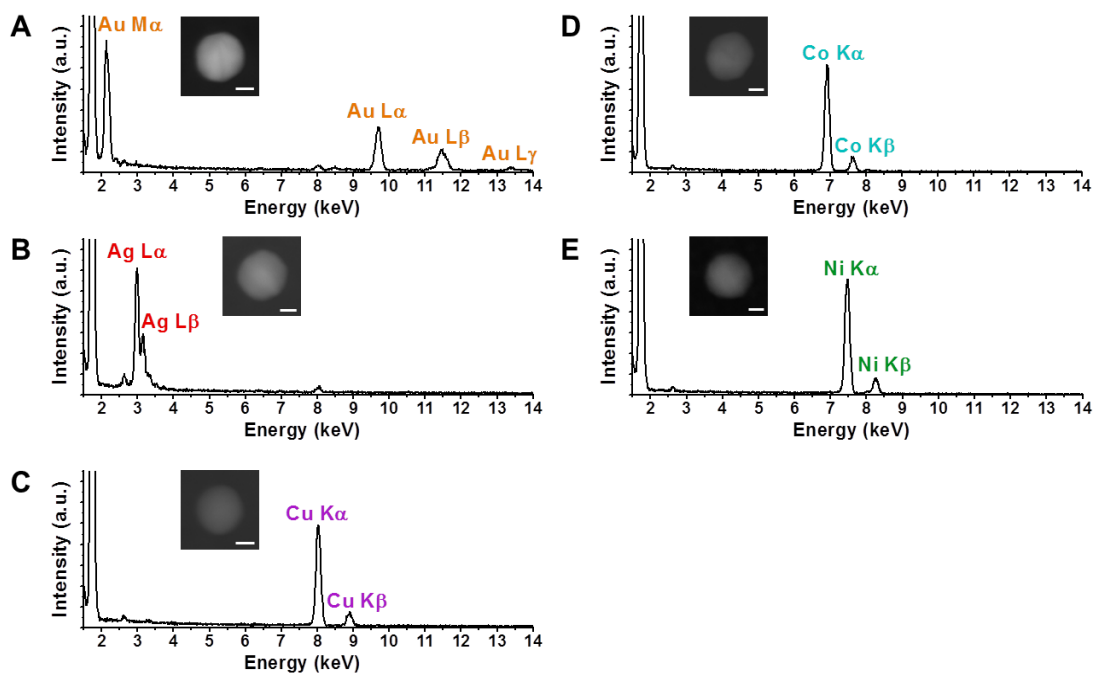
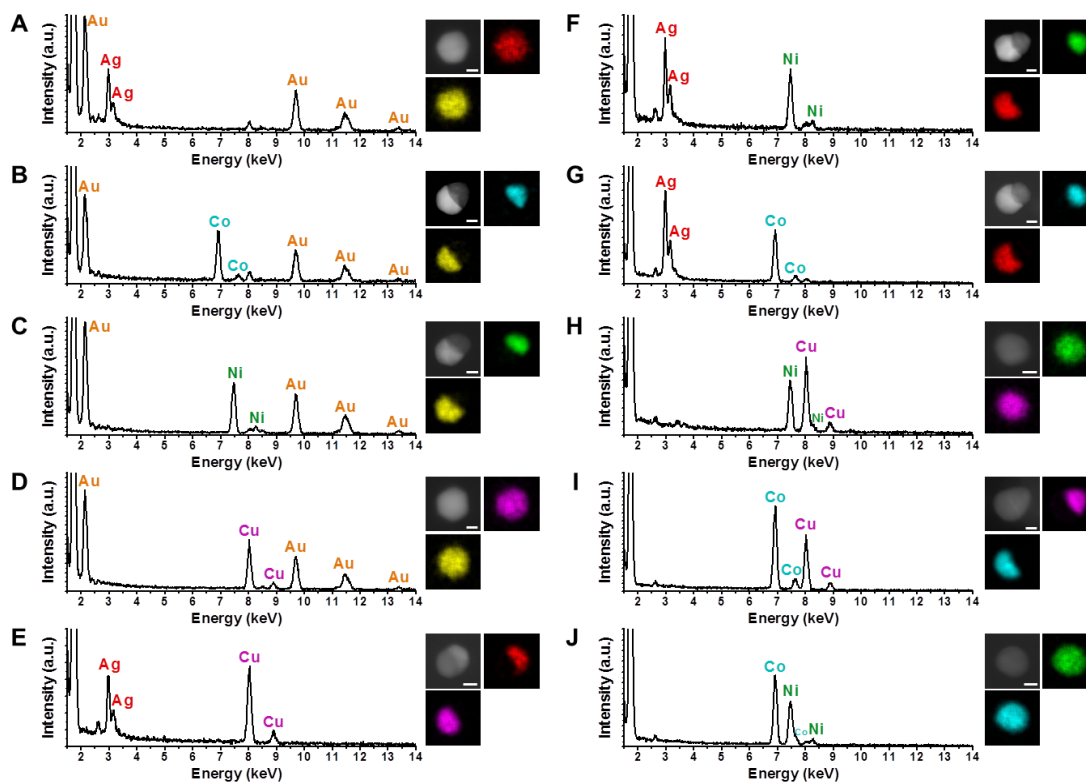


**Figure 2.10** HAADF-STEM images and EDS spectra of the unary nanoparticles in Figure 2.9B. (A) Au, (B) Ag, (C) Cu, (D) Co, (E) Ni. Scale bars: 15 nm.

To evaluate the capability of SPBCL to develop a combinatorial library of NPs, we first prepared the simplest structures, monometallic NPs, on transmission electron microscopy (TEM) grids using ink solutions containing only one type of metal ion precursor. The resulting NPs were characterized by high-angle annular dark-field (HAADF) STEM and EDS. Figure 2.9 shows HAADF-STEM images of SPBCL-prepared Au, Ag, Cu, Co, and Ni NPs with diameters deliberately tailored to ~40 nm. The sizes of NPs were controlled by adjusting the volume and metal loading of the polymer nanoreactors, which dictates the number of metal ions used for forming each NP.<sup>180-182</sup> EDS analysis provides an effective way to reveal the chemical composition

and elemental distribution of each NP product (Figure 2.9B and 2.10).

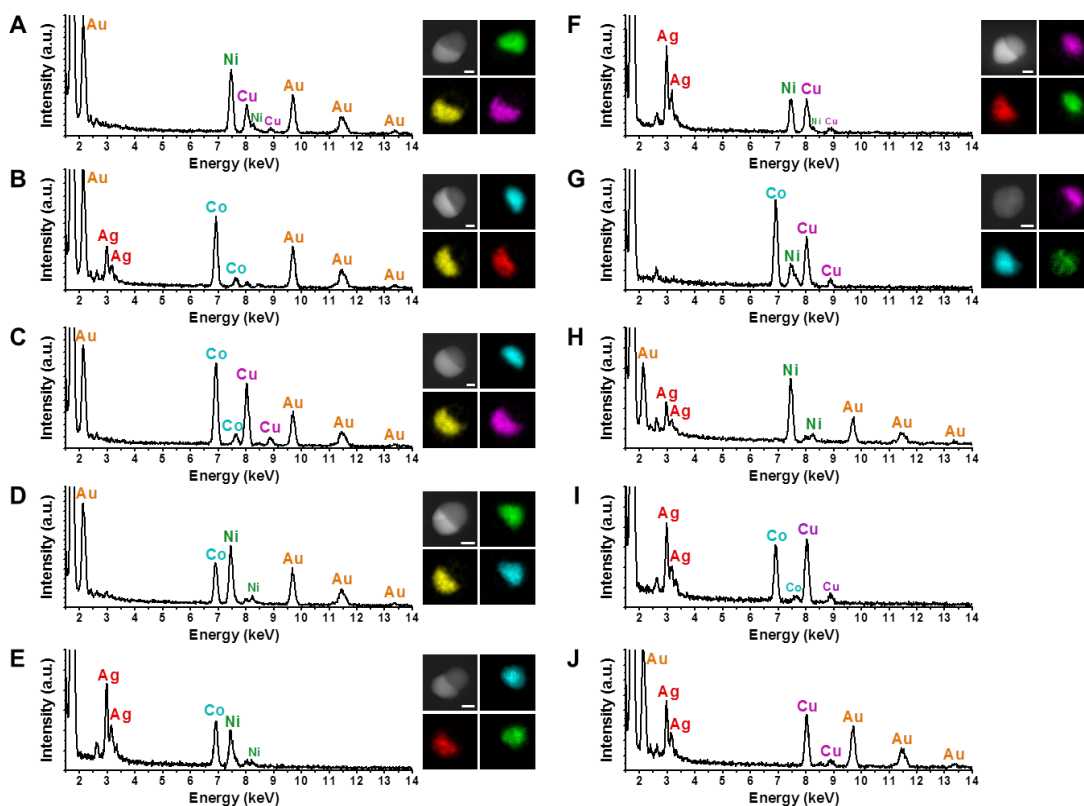
As part of the library, bimetallic NPs were accessed by equally loading two metal ion precursors into the polymer ink (Figure 2.9C and 2.11). Interestingly, among the 10 binary combinations consisting of Au, Ag, Cu, Co, and Ni, four of them (*i.e.*, AuAg, AuCu, CuNi, and CoNi) result in alloy NPs, as validated by the even contrast in HAADF-STEM images of NPs and the overlap of EDS element maps (Figure 2.9C and 2.11). In contrast, the other six combinations result in heterodimers, indicative of phase segregation in each binary mixture. The difference in contrast in the HAADF-STEM images of these heterostructured particles reflects the difference in atomic number between two metal domains, while EDS analysis confirms the separation of the majority of the elements that comprise the NPs. Slight mixing between incompatible metals may still occur, but if so, it is below the detection limit of EDS. The orientation of phase boundaries in heterostructured NPs is random with respect to the substrate (*i.e.*, the image plane). Here, particles with phase boundaries perpendicular to the substrate are used to clearly show the separation of metals. Although there is no reason to believe that nanostructures will necessarily follow the mixing behavior associated with bulk phase diagrams, the binary NPs we explored and prepared herein do.<sup>190</sup> Since no one knows how three, four, and five component particle systems will behave, it is important to build a library of nanostructures in successively more complex fashion, so that each layer of complexity can be used to understand the next series of entries (*e.g.*, ternary structures).



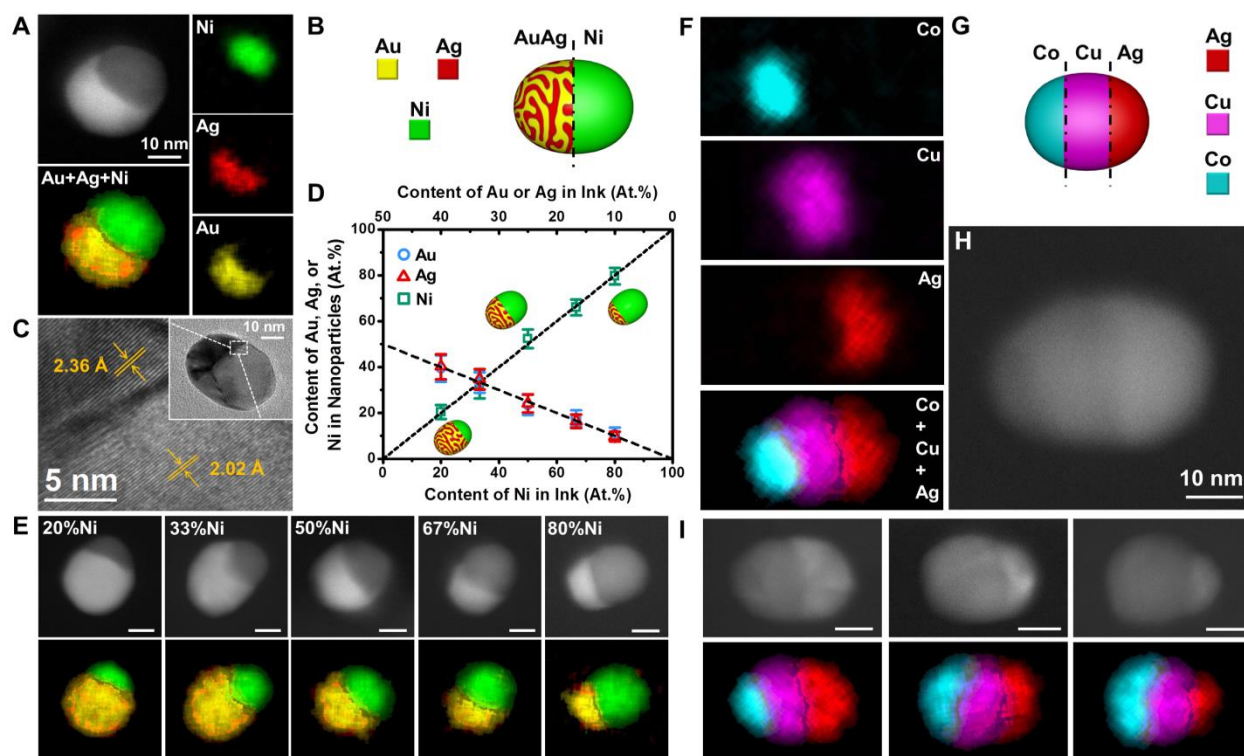
**Figure 2.11** HAADF-STEM images, EDS spectra, and detailed EDS mapping information of the binary nanoparticles in Figure 2.9C. (A)  $\text{Au}_{0.48}\text{Ag}_{0.52}$ , (B)  $\text{Au}_{0.55}\text{Co}_{0.45}$ , (C)  $\text{Au}_{0.54}\text{Ni}_{0.46}$ , (D)  $\text{Au}_{0.49}\text{Cu}_{0.51}$ , (E)  $\text{Ag}_{0.42}\text{Cu}_{0.58}$ , (F)  $\text{Ag}_{0.57}\text{Ni}_{0.43}$ , (G)  $\text{Ag}_{0.63}\text{Co}_{0.37}$ , (H)  $\text{Cu}_{0.58}\text{Ni}_{0.42}$ , (I)  $\text{Cu}_{0.41}\text{Co}_{0.59}$ , (J)  $\text{Co}_{0.60}\text{Ni}_{0.40}$ . Scale bars: 15 nm.

The syntheses of ternary NPs *via* conventional methods are usually constrained by the difficulties in balancing the reduction kinetics of the different metal ion precursors,<sup>2,4</sup> controlling the site-selective nucleation of each metal as opposed to forming multicomponent structures,<sup>47-49</sup> and controlling phase separation at the nanoscale.<sup>57,58</sup> However, trimetallic particles are easily accessible *via* SPBCL because this method pre-confines precursor ions in a single nanoreactor and subsequently transforms them into a single particle, thus bypassing the issues involving precursor reduction potentials and element-specific nucleation. To evaluate the scope of this approach, we synthesized all of the ternary NPs consisting of every combination of Au, Ag, Cu, Co, and Ni (Figure 2.9D and 2.12). While the study of binary particles shows the possibility of controlling particle structure based on metal compatibility, the combination of metal compatibility in ternary

particles is more complicated, which includes four possible combination types. The first combination type (I) occurs when all three components are miscible with each other at any composition, which results in a single alloy particle (Figure 2.6). For the 10 ternary combinations of Au, Ag, Cu, Co, and Ni, the other combination types that occur are ones where: (II) two metals are miscible with each other while the third is not with either, (III) all three metals are immiscible with each other, and (IV) two metals are immiscible while the other is miscible with the other two.



**Figure 2.12** HAADF-STEM images, EDS spectra, and detailed EDS mapping information of the ternary nanoparticles in Figure 2.9D. (A)  $\text{Au}_{0.23}\text{Cu}_{0.17}\text{Ni}_{0.60}$ , (B)  $\text{Au}_{0.25}\text{Ag}_{0.19}\text{Co}_{0.56}$ , (C)  $\text{Au}_{0.21}\text{Cu}_{0.35}\text{Co}_{0.44}$ , (D)  $\text{Au}_{0.32}\text{Co}_{0.29}\text{Ni}_{0.39}$ , (E)  $\text{Ag}_{0.48}\text{Co}_{0.28}\text{Ni}_{0.24}$ , (F)  $\text{Ag}_{0.50}\text{Cu}_{0.25}\text{Ni}_{0.25}$ , (G)  $\text{Cu}_{0.33}\text{Co}_{0.52}\text{Ni}_{0.15}$ , (H)  $\text{Au}_{0.24}\text{Ag}_{0.24}\text{Ni}_{0.52}$ , (I)  $\text{Ag}_{0.35}\text{Cu}_{0.38}\text{Co}_{0.27}$ , (J)  $\text{Au}_{0.29}\text{Ag}_{0.37}\text{Cu}_{0.34}$ . Scale bars: 15 nm. The STEM images and EDS mapping information of (H-J) are shown in Figure 2.13 and Figure 2.25.



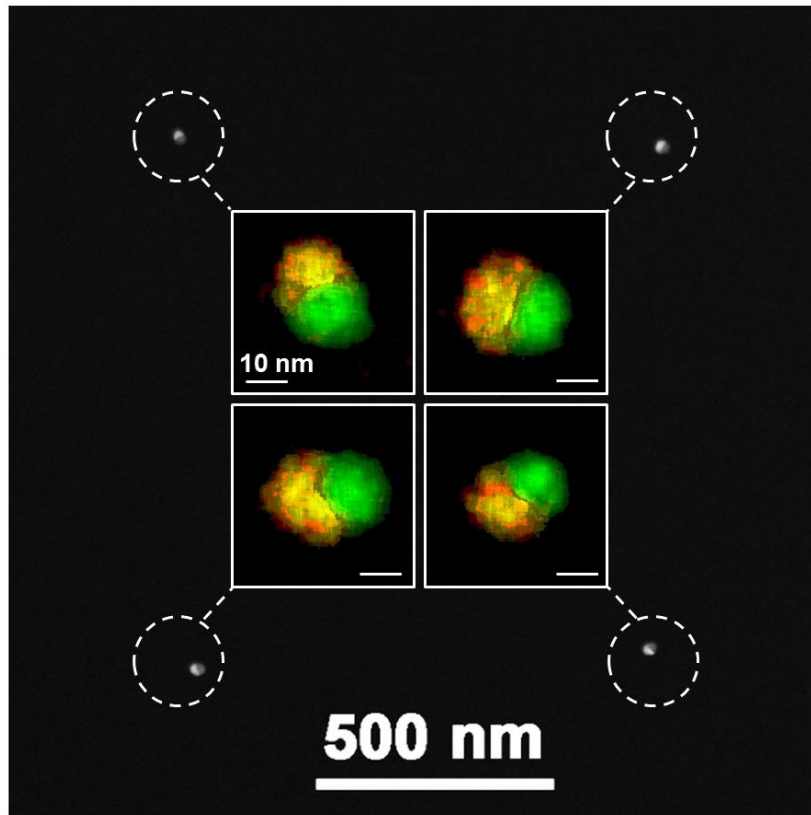


**Figure 2.14** EDS elemental mapping of four neighboring AuAgNi nanoparticles in an array. All four of nanoparticles are heterodimers where one domain is AuAg alloy and the other domain is Ni. Color codes: Au (yellow), Ag (red), Ni (green). Scale bars of insets: 10 nm.

We first explored the combination of Au, Ag, and Ni (Figure 2.13A-2.13E, 2.14, and 2.15), which resulted in type **II** particles, where the first two metals are miscible (Au and Ag), while the third one (Ni) is immiscible with the other two.<sup>190</sup> We synthesized AuAgNi NPs on silicon substrates or on TEM grids using an ink solution with a metal loading ratio of 25% Au, 25% Ag, and 50% Ni. As shown by HAADF-STEM images (Figure 2.14), arrays of AuAgNi NPs could be synthesized, and only one NP was observed in each position within the array. Increasing the magnification reveals that each AuAgNi NP is heterogeneously structured (Figure 2.13A and 2.13B). Each AuAgNi NP was a dimeric heterostructure consisting of a AuAg alloy domain and a Ni domain. The contrast in the HAADF-STEM image arises from the difference in atomic number

between the AuAg alloy and Ni. High-resolution TEM shows that the two domains in the AuAgNi NP are crystalline (Figure 2.13C). Finally, in addition to AuAgNi, the other five ternary combinations that lead to type **II** particles are AuAgCo, AuCuCo, AuCoNi, AgCuNi, and AgCoNi (Figure 2.9D and 2.12).

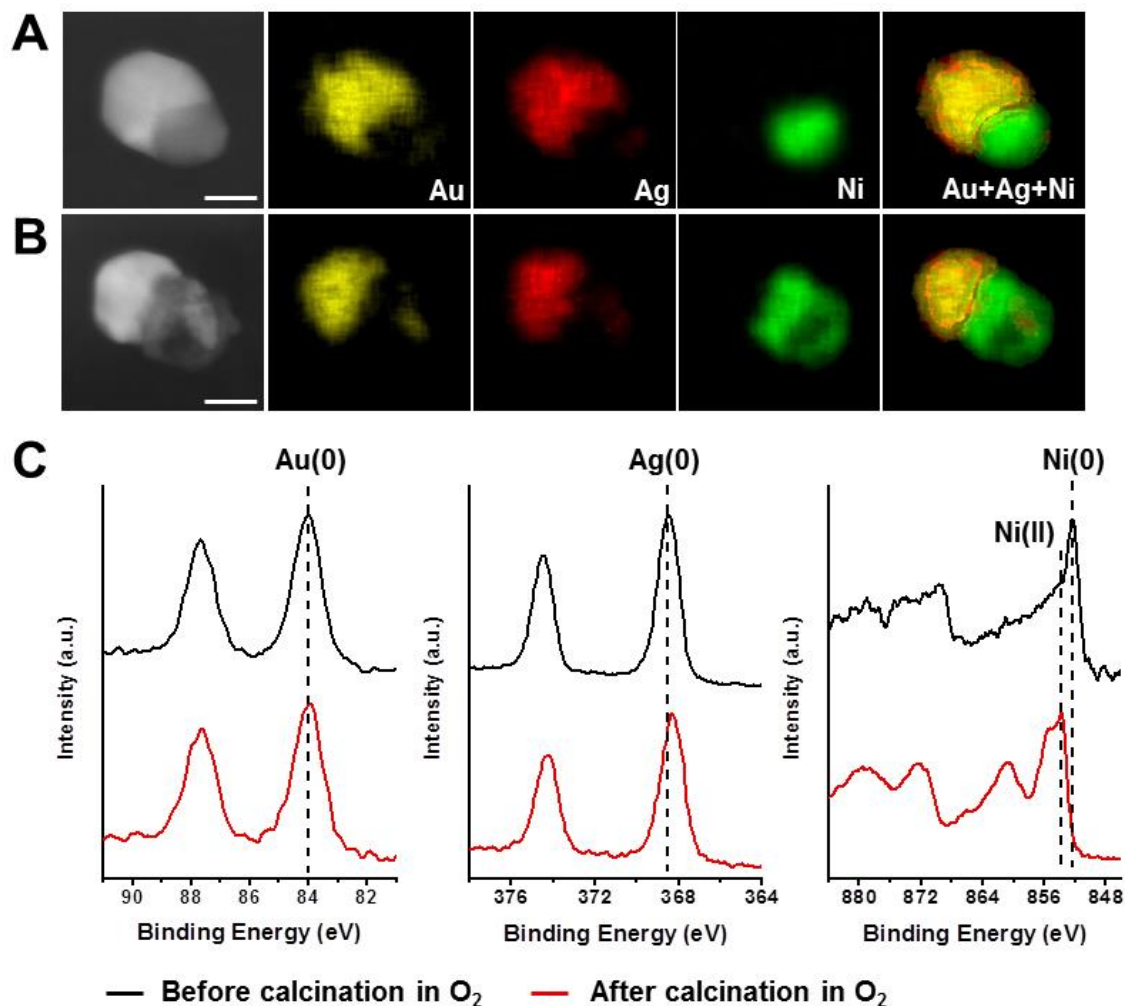


**Figure 2.15** HAADF-STEM images and the corresponding EDS elemental mapping of a AuAgNi nanoparticle. (A) AuAgNi nanoparticle generated by the regular SPBCL process. (B) The same nanoparticle after being thermally annealed at 300 °C in O<sub>2</sub> for 12h. Scale bars: 20 nm. (C) XPS spectra of AuAgNi nanoparticles made by drop-casting polymer ink solution after the thermal annealing process used in SPBCL (black line), and then the same sample after being further thermally annealed at 300 °C in O<sub>2</sub> for 12h (red line).

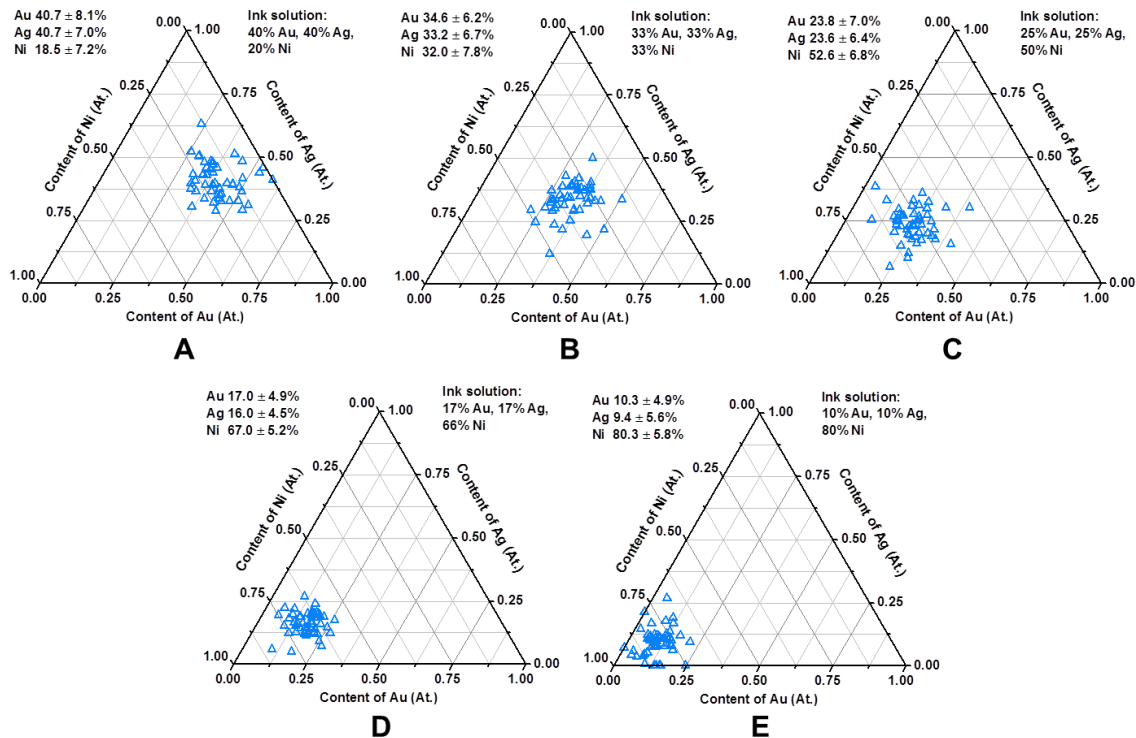


**Figure 2.16** Compositional diagrams assessing the uniformity of SPBCL-generated AuAgNi nanoparticles. The metal loading ratio of the ink solution is: (A) 40% Au, 40% Ag, 20% Ni, (B) 33% Au, 33% Ag, 33% Ni, (C) 25% Au, 25% Ag, 50% Ni, (D) 17% Au, 17% Ag, 66% Ni, and (E) 10% Au, 10% Ag, 80% Ni. (sample size: 50 for each composition). The composition of the nanoparticles follows the composition of the ink solution.

One advantage of using SPBCL for generating NPs is the homogeneity of the patterned nanoreactor, which yields particles that have metallic constituent ratios reflecting those of the ink. This enables straightforward tuning of the particle composition. We used this ability to study the effect of altering metal ratios on the particle structure by examining five ink solutions (Figure 2.13D and 2.13E). The five solutions contained increasing Ni content from 20 to 80% while a 1:1 ratio of Au and Ag was maintained; the NPs were then investigated by EDS to determine elemental distribution and composition. As shown in Figure 2.13E, the varying Ni content in the ink solution effectively changes the relative size of the Ni domains and AuAg alloy domains, respectively, while the dimeric heterostructure of AuAgNi NPs was maintained for all compositions studied. Experimentally, the majority of the AuAgNi NPs (yield = 80%; sample size was 50) match the

composition of ink solutions with a compositional variation of less than 10% (Figure 2.13D and 2.16). The remaining 20% of the NPs exhibit large composition fluctuations and even include bimetallic NPs (*i.e.*, AuAg, AuNi, or AgNi), which is likely caused by the imperfect distribution of precursors in ink solution.

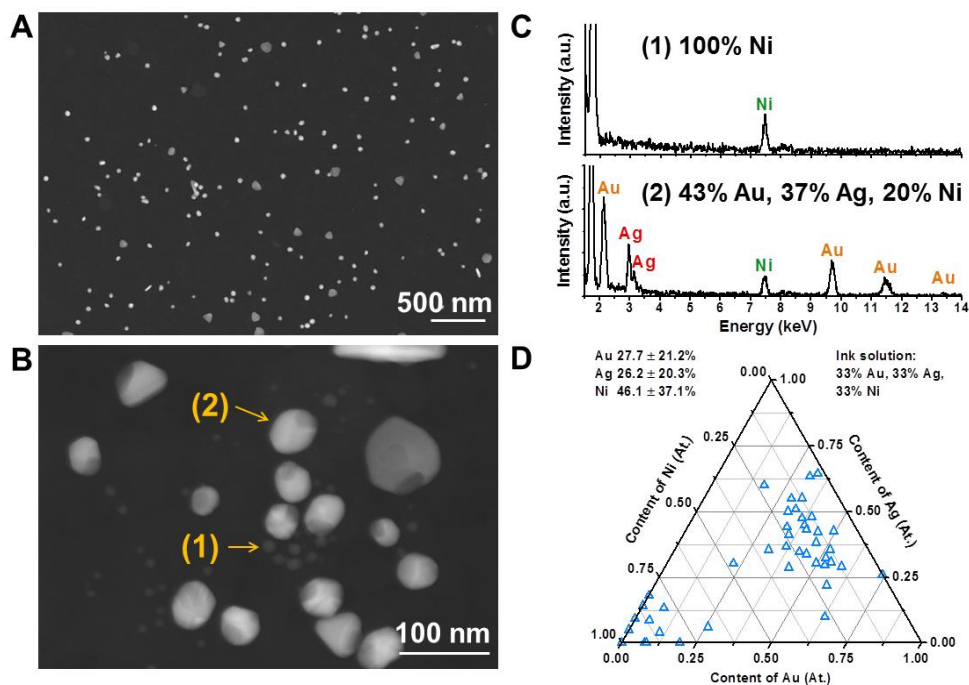


**Figure 2.17** (A, B) DF-STEM images of AuAgNi nanoparticles synthesized from bulk polymer ink solution with the two-step annealing procedure used in SPBCL. (C) The EDS spectra of the two nanoparticles in B, showing that bulk synthesis results in a mixture of different types of nanoparticles. (D) The compositional uniformity of the AuAgNi nanoparticles synthesized from bulk polymer ink solution (sample size: 50).

The formation of one NP per polymer reactor is crucial for this composition control. Indeed, attempts to synthesize NPs in a bulk polymer solution through a similar thermal annealing procedure resulted in heterogeneous mixtures of particles of varying size and composition (Figure 2.17 and 2.18), as is commonly observed in one-pot solution syntheses of multimetallic NPs because different metal precursors exhibit different reduction kinetics and element-specific nucleation.<sup>4,48</sup> In some polymer reactors (ones consisting of a features diameter > 1  $\mu\text{m}$ ), failure of

the atomic precursors to coalesce into a single NP was also observed, which prevented control over NP size and composition because of the formation of multiple particles (Figure 2.19).

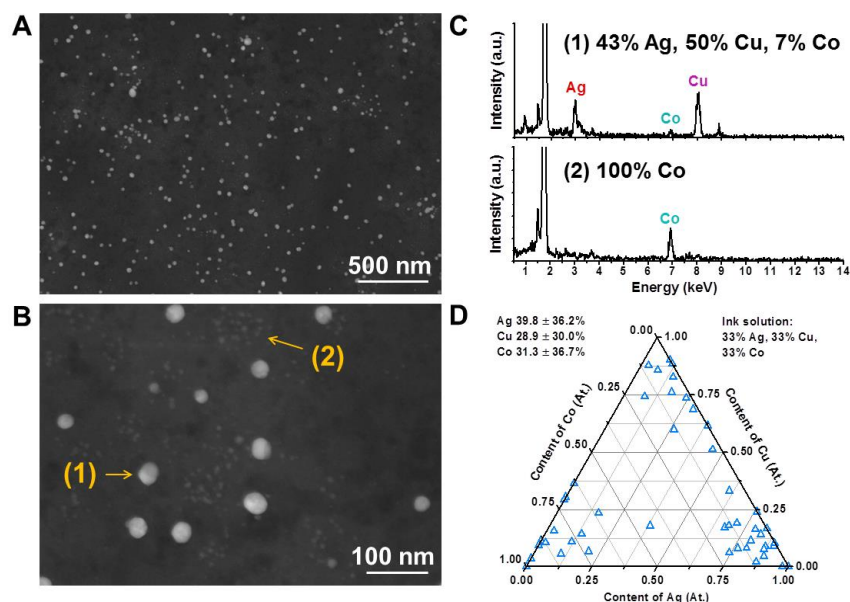


**Figure 2.18** (A, B) DF-STEM images of AgCuCo nanoparticles synthesized from a bulk polymer ink solution with the two-step annealing procedure used in SPBCL. (C) EDS spectra of the two nanoparticles in B, showing that bulk synthesis results in a mixture of different types of nanoparticles. (D) The compositional uniformity (or lack thereof) of the AgCuCo nanoparticles synthesized from bulk polymer ink solution (sample size: 50).

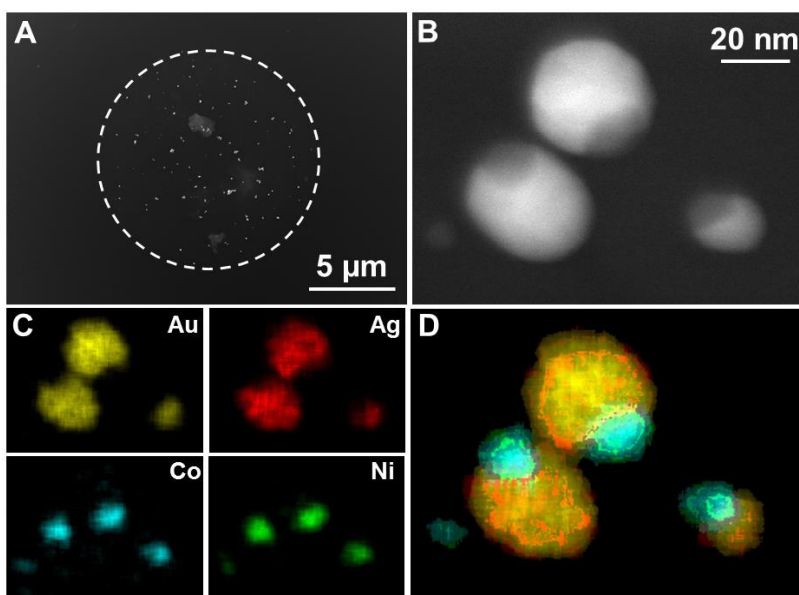


**Figure 2.19** Incomplete coalescing of metal precursors results in multiple nanoparticles forming within a single polymer dome. (A) HAADF-STEM image of multiple AuAgCoNi nanoparticles

formed in one large polymer dot. The polymer dot was prepared from an ink solution with a metal loading ratio of 25% Au, 25% Ag, 25% Co, and 25% Ni. The circle highlights the contour of original polymer reactor. (B) Zoomed-in HAADF-STEM image of four representative nanoparticles. (C) EDS elemental mapping of the four nanoparticles. Color codes: Au (yellow), Ag (red), Ni (green), Co (cyan). (D) Overlay of the element maps of Au, Ag, Co, and Ni.

In the third combination type **III**, the three constituent metals, such as Ag, Cu, and Co, are not miscible with each other, and trimeric heterostructures were expected. As proof-of-concept, we synthesized AgCuCo NPs using an ink solution with a metal loading of 33% for each metal. HAADF-STEM images along with EDS characterization confirm that Ag, Cu, and Co segregate into three segments in a AgCuCo NP (Figure 2.13F-2.13H, 2.20, and 2.21), consistent with the compatibility of these metals.<sup>190</sup>

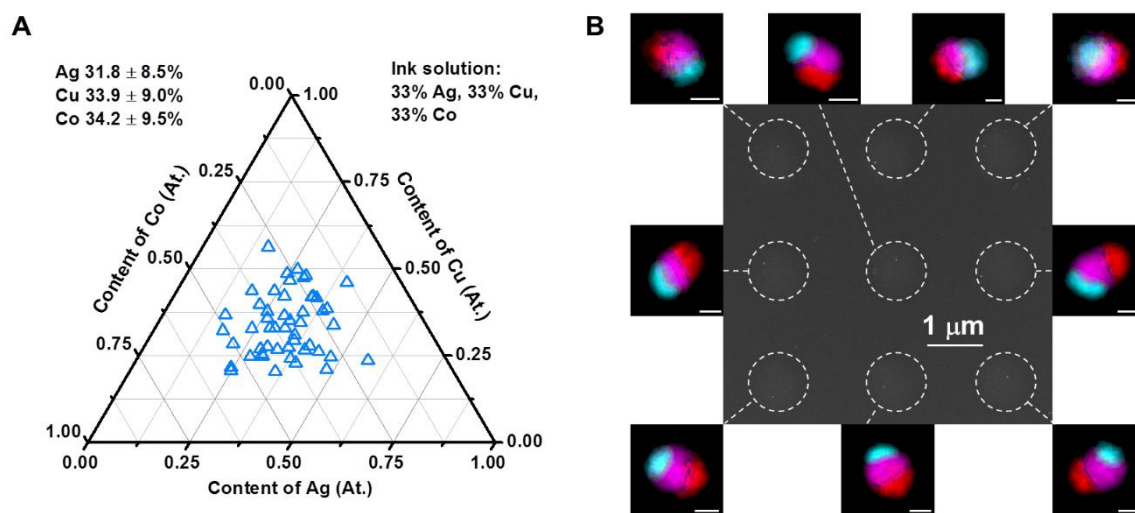


**Figure 2.20** (A) Compositional uniformity of SPBCL-generated AgCuCo nanoparticles (sample size: 50). The metal loading ratio of the ink solution is: 33% Ag, 33% Cu, and 33% Co. (B) EDS elemental mapping of nine neighboring AgCuCo nanoparticles in an array. All nanoparticles are heterotrimers where Ag, Cu, and Co segregate into three segments. Color codes: Ag (red), Cu (purple), Co (cyan). Scale bars in EDS mapping images: 15 nm.

If the Cu content was kept constant while changing the relative loading ratio of Ag and Co in the ink solution, the sizes of the Ag and Co domains, respectively, vary according to the ink formulation, but no apparent alloying of either two metals is observed for all compositions examined (Figure 2.13I). Notably, in the case of all ink compositions studied, the three metal

domains in the NPs shared a common structural feature: a central Cu domain is capped by a Ag or Co domain on each end. The phase boundaries between Ag-Cu and between Cu-Co are not always parallel, as evidenced by STEM and EDS (Figure 2.22 and 2.23). This structural motif for AgCuCo NPs suggests a higher interfacial energy between Ag and Co than the interfacial energy between Ag and Cu or between Cu and Co. Nevertheless, AgCuCo NPs with adjacent Ag-Co domains can be realized when the Cu content is < 20%. Indeed, under these circumstances, the amount of Cu is not sufficient to completely segregate the Ag and Co domains (Figure 2.24).

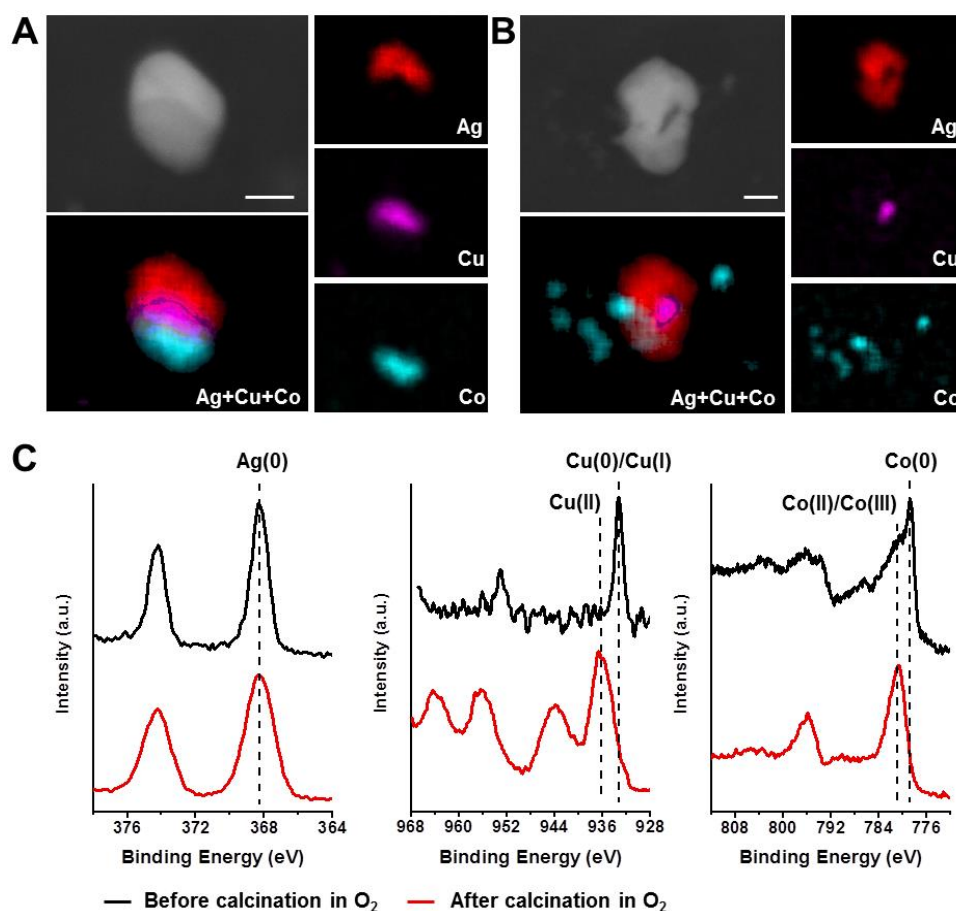


**Figure 2.21** HAADF-STEM images and EDS elemental mapping of a AgCuCo nanoparticle. (A) AgCuCo nanoparticle generated by annealing at 500 °C in H<sub>2</sub> for 12h. (B) The same nanoparticle after being thermally annealed at 300 °C in O<sub>2</sub> for 12h. Scale bars: 20 nm. (C) XPS spectra of AgCuCo nanoparticles made by drop-casting polymer ink solution followed by the thermal annealing process used in SPBCL (black line) and the same sample after being further thermally annealed at 300 °C in O<sub>2</sub> for 12h (red line).

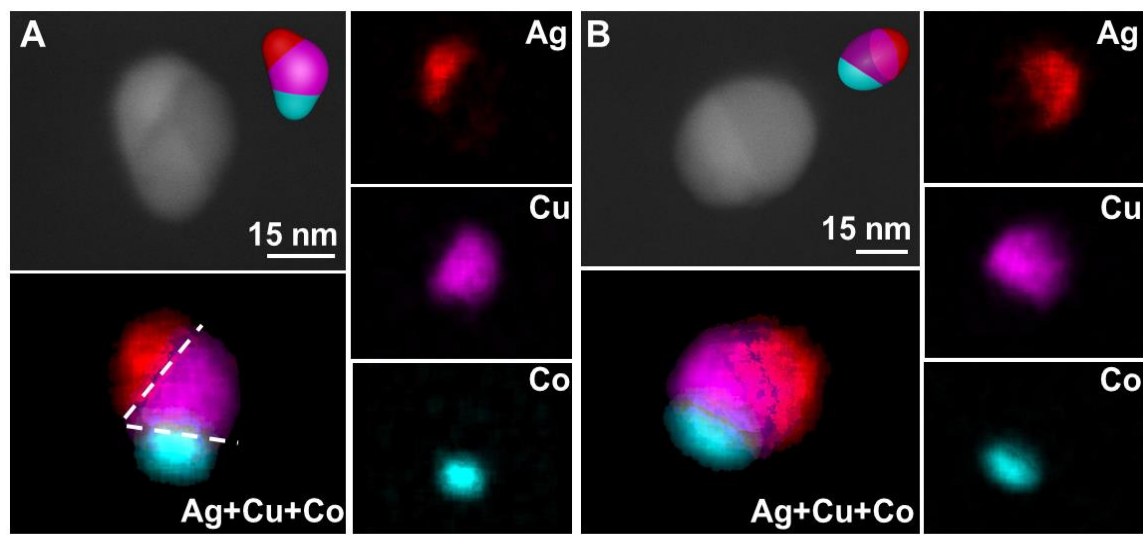


**Figure 2.22** Nonparallel phase boundaries in AgCuCo nanoparticles generated by SPBCL. (A) Dark-field STEM image and corresponding EDS elemental mapping of a AgCuCo nanoparticle with nonparallel phase boundaries. Dashed lines highlight the position of Ag-Cu phase boundary and Cu-Co phase boundary. The two interfaces are perpendicular with respect to image plane. Inset: scheme depicting the proposed structure of this nanoparticle. (B) Another representative AgCuCo nanoparticle with nonparallel phase boundaries. Here, the Cu-Co interface is perpendicular to the image plane while the Ag-Cu interface is inclined with respect to the image plane. Inset: scheme depicting the proposed structure of this nanoparticle.

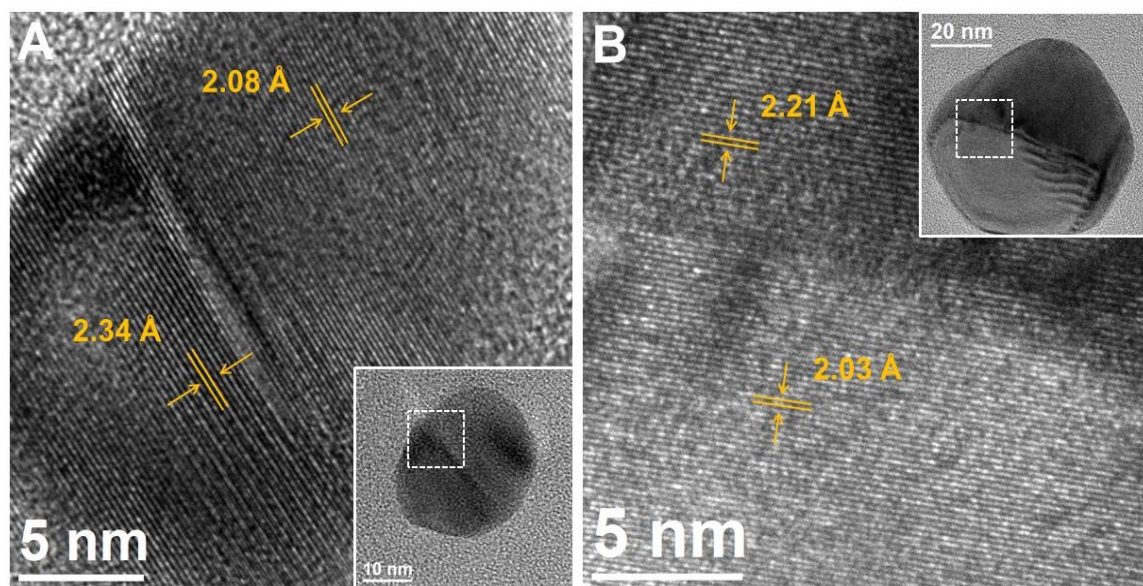


**Figure 2.23** (A) HRTEM image of the interface between Ag and Cu in a AgCu nanoparticle. The observed lattice spacings near the interface are 2.34 Å and 2.08 Å (extracted from FFT), which closely match the Ag (111) and Cu (111) planes. The inset shows the particle with the zoomed-in region indicated with a dashed square. (B) HRTEM image of the interface between AuCu and Co in a AuCuCo nanoparticle. Cu and Co have a very close lattice parameter and similar atomic

number contrast in HRTEM. It is difficult to directly identify the Cu-Co interface in a CuCo nanoparticle using HRTEM. Here, 15% Au was added into CuCo nanoparticles to increase the contrast between Cu domain and Co domain. The observed lattice spacing around the interface are 2.21 Å and 2.03 Å, which can be assigned to the AuCu (111) and Co (111) planes. The inset shows the particle with the zoomed-in region indicated with a dashed square.

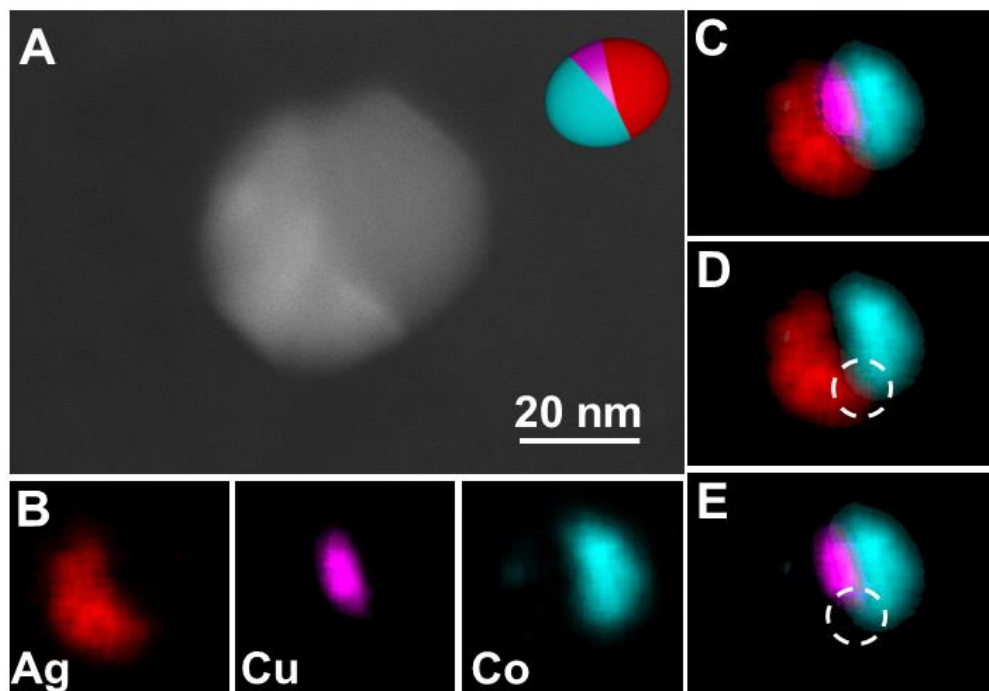


**Figure 2.24** SPBCL AgCuCo nanoparticle with low Cu content and three phase boundaries. (A) Dark-field STEM image of a AgCuCo nanoparticle ( $\text{Ag}_{0.43}\text{Cu}_{0.19}\text{Co}_{0.38}$ ). Inset: scheme depicting the structure of this nanoparticle. (B) EDS elemental mapping of the nanoparticle. (C) Overlay of the element maps of Ag, Cu, and Co. (D) Overlay of the element maps of Ag and Co. (E) Overlay of the element maps of Cu and Co. Dotted circles highlight the position of Ag-Co phase boundary. When the content of Cu is less than 20% in AgCuCo nanoparticles, the amount of Cu is not enough to fully block the contact between Ag and Co. Consequently, a AgCuCo nanoparticle with Ag-Cu, Cu-Co, and Ag-Co phase boundaries is observed.

For the final combination type **IV**, two metals (*e.g.*, Ag and Cu) are not miscible while the third one (*e.g.*, Au) is miscible with the other two. Compared with the previous two types, the particle structure is more dependent on composition because of the increased complexity of interactions between the metals. To further show the advantage of SPBCL in studying composition-dependent phase separation in multimetallic NPs, we synthesized AuAgCu NPs using four ink formulations. The four solutions contained increasing Au content from 10 to 70% while

the Ag and Cu contents were kept equal in each solution. The NPs obtained from these inks are shown in Figure 2.25-2.27.

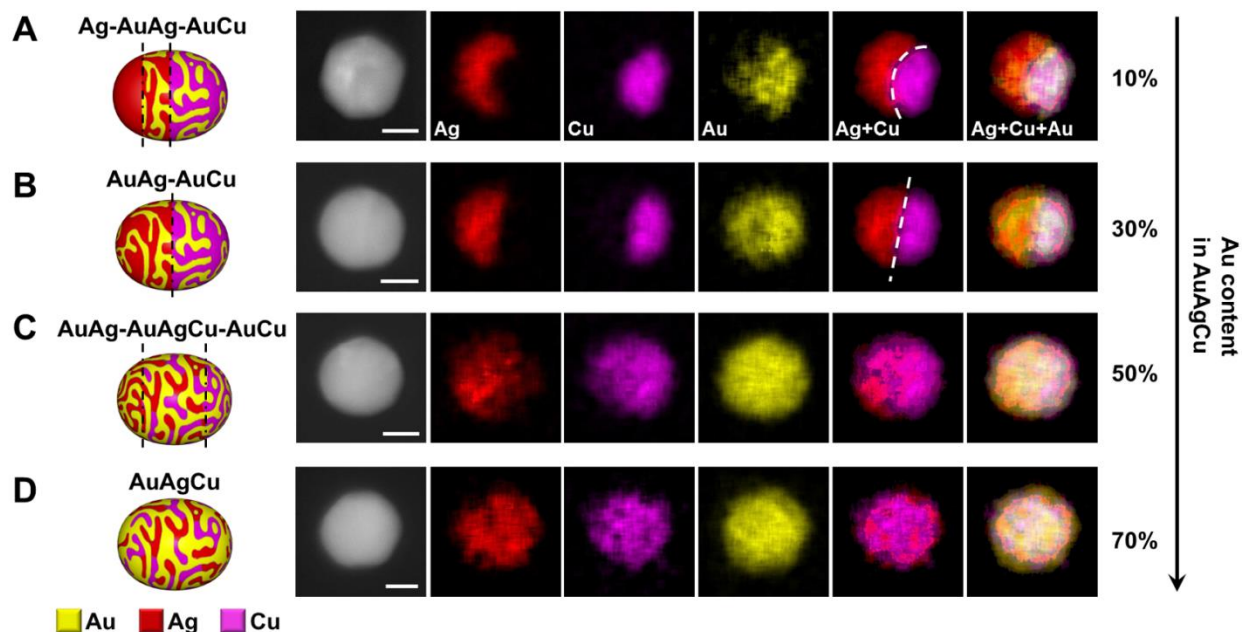


**Figure 2.25** AuAgCu heterostructured nanoparticles. (A-D) Schematic illustration, HAADF-STEM images and EDS elemental mapping of four representative AuAgCu nanoparticles with different Au content. From A to D, the Ag content and Cu content are equal in each nanoparticle while the Au content is 10%, 30%, 50%, and 70%, respectively. Scale bars: 20 nm.

When the Au content in the NPs was only 10%, Ag and Cu phase-segregated into two domains (Figure 2.25A). Experimentally, Au shown a higher affinity for Cu, as indicated by the enrichment of Au in the Cu domain. When the Au content was increased to 30%, Au diffused into the Ag domain, resulting in a Janus NP in which one part is a AuAg alloy and the other part is a AuCu alloy (Figure 2.25B). Further increasing the Au content to 50% resulted in NPs without a distinct boundary between Ag and Cu (Figure 2.25C). Instead, the Ag and Cu started to diffuse into each other's domain, indicating the formation of an intermediate region in the center that consists of a AuAgCu alloy. Finally, when the Au content was increased to 70%, Au was found throughout the entire NP structure and forms an alloy (Figure 2.25D). In addition to AuAgCu, the other two ternary combinations that satisfy type IV are AuCuNi and CuCoNi. Similar to the

AuAgCu system where Au shows preference for Cu over Ag, Cu had a higher affinity for Au than Ni in the AuCuNi system, and Ni has a higher affinity for Co than Cu in the CuCoNi system (Figure 2.9D and 2.12).

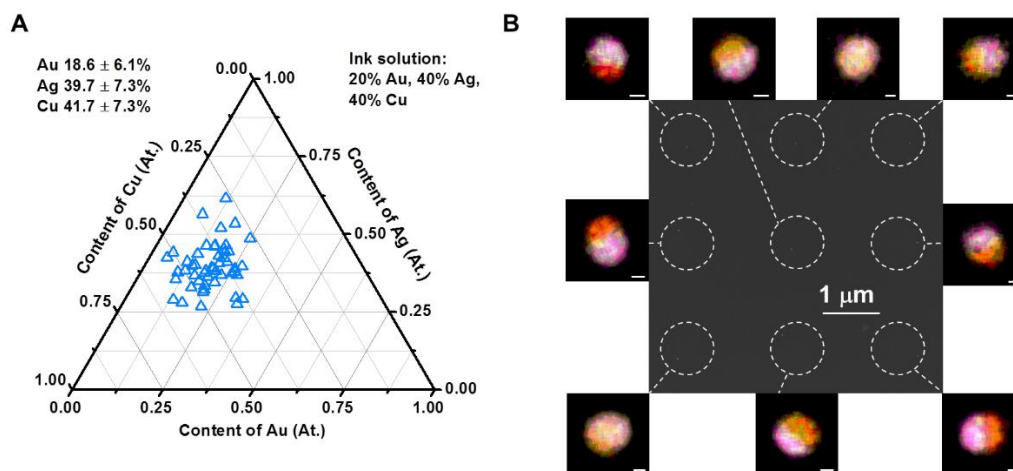


**Figure 2.26** (A) Compositional uniformity of SPBCL-generated AuAgCu nanoparticles (sample size: 50). The metal loading ratio of the ink solution is: 20% Au, 40% Ag, and 40% Cu. (B) EDS elemental mapping of nine neighboring AuAgCu nanoparticles in an array. The nanoparticles are heterodimers where one domain is a AuAg alloy and the other domain is a AuCu alloy. Au is mainly concentrated in the AuCu domain. Color codes: Au (yellow), Ag (red), Cu (purple). Scale bars in EDS mapping images: 10 nm.

To confirm that the NPs are mainly composed of metals after being annealed under  $\text{H}_2$  at 500 °C, we thermally annealed AuAgNi, AuAgCu, and AgCuCo NPs in  $\text{O}_2$  and characterized the morphology change of NPs with STEM-EDS. As shown in Figure 2.15, 2.21 and 2.27, when Cu, Co or Ni are transformed into oxides, they collapse onto the substrate (alumina on a  $\text{Si}_3\text{N}_4$  film is used here) and change the configuration of original NPs. This suggests that particles composed of oxides are not stable enough to maintain their structures when they are subjected to long-term thermal treatment. The oxidation state of the metals that comprise the NPs was further explored by XPS with drop-cast samples (Figure 2.15C, 2.21C, and 2.27C). The Co, Ni, and Cu components in the NPs are in the 0-valent state after being annealed under  $\text{H}_2$  at 500 °C. However, once the particles are exposed to air, the Co, Ni, or Cu components begin to oxidize.

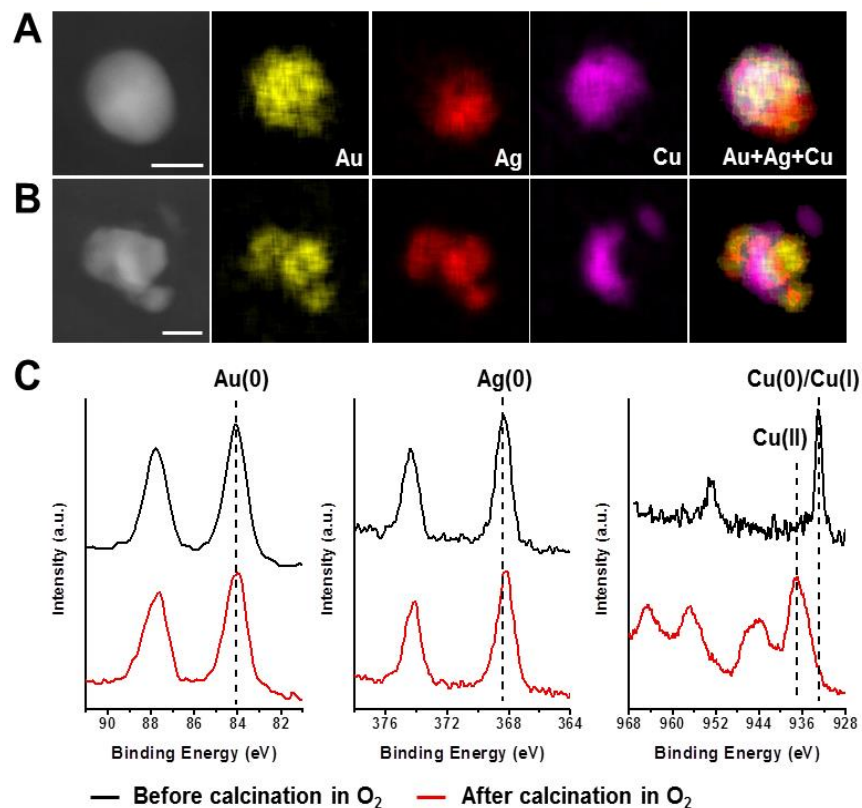


**Figure 2.27** HAADF-STEM images and corresponding EDS elemental mapping of a AuAgCu nanoparticle. (A) AuAgCu nanoparticle generated by annealing at 500 °C in H<sub>2</sub> for 12 h. (B) The same nanoparticle after being thermally annealed at 300 °C in O<sub>2</sub> for 12 h. Scale bars: 20 nm. (C) XPS spectra of AuAgCu nanoparticles made by drop-casting a polymer ink solution followed by the thermal annealing process used in SPBCL (black line) and the same sample after being further thermally annealed at 300 °C in O<sub>2</sub> for 12h (red line).

We further extended the library by synthesizing all quaternary combinations of Au, Ag, Cu, Co, and Ni. The structures of the quaternary NPs were highly dependent on particle composition. Here, we examined one specific ink composition for each combination of metals (Figure 2.9E and 2.28). The aforementioned studies on bimetallic and trimetallic systems are instructive for elucidating and assigning the structure of each quaternary NP. For example, the structure of the AuAgCoNi NP was assigned as a AuAgCo heterodimer primary particle and Ni as the fourth component. The location of the fourth component depends on its miscibility with the three components in the primary particle. Ni is miscible with Co but immiscible with Au and Ag.

Thus, AuAgCoNi NPs still adopt a dimeric structure with one part being a AuAg alloy and the other part a CoNi alloy.

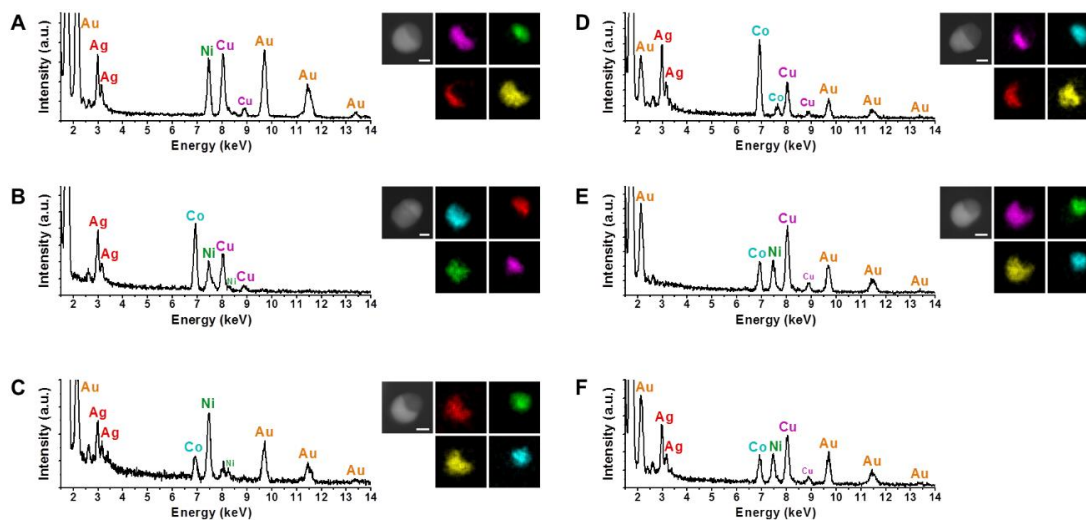


**Figure 2.28** HAADF-STEM images, EDS spectra, and detailed EDS mapping information of the quaternary and quinary nanoparticles in Figure 2.9E and 2.9F. (A)  $\text{Au}_{0.32}\text{Ag}_{0.19}\text{Cu}_{0.27}\text{Ni}_{0.22}$ , (B)  $\text{Ag}_{0.27}\text{Cu}_{0.22}\text{Co}_{0.35}\text{Ni}_{0.16}$ , (C)  $\text{Au}_{0.26}\text{Ag}_{0.22}\text{Co}_{0.16}\text{Ni}_{0.36}$ , (D)  $\text{Au}_{0.15}\text{Ag}_{0.29}\text{Cu}_{0.18}\text{Co}_{0.38}$ , (E)  $\text{Au}_{0.23}\text{Cu}_{0.42}\text{Co}_{0.16}\text{Ni}_{0.19}$ , (F)  $\text{Au}_{0.19}\text{Ag}_{0.24}\text{Cu}_{0.28}\text{Co}_{0.14}\text{Ni}_{0.15}$ . Scale bars: 15 nm. The STEM images and EDS mapping information of (F) are shown in Figure 2.29.

For the other quaternary particles synthesized, the structure can be similarly understood by the miscibility of components. EDS mapping in Figure 2.28A shows the structures of AuAgCuNi. The particle consists of three consecutive domains, *i.e.*, AuAg alloy, AuCu alloy, and Ni. The components of Au, Ag, and Cu in this particle segregate into a AuAg alloy domain and a AuCu alloy domain, which is similar to the structure of AuAgCu particle in Figure 2.25B. The fourth component, Ni, forms an additional domain due to its immiscibility with Au. EDS mapping in Figure 2.28B shows the structures of AgCuCoNi. The particle consists of three consecutive domains, *i.e.*, CoNi alloy, Cu, and Ag. The components of Ag, Cu, and Co in this particle segregate into three domains, which form the primary particle. Ni is mainly present in the Co domain due to its higher affinity for Co than Cu. EDS mapping in Figure 2.28D shows the structures of AuAgCuCo. The particle consists of three consecutive domains, *i.e.*, AuAg alloy, AuCu alloy, and

Co. The components of Ag, Cu, and Co segregate into three domains, which form the primary particle. Au is present in the Ag and Cu domains since it is compatible with Ag and Cu while being immiscible with Co. EDS mapping in Figure 2.28E shows the structures of AuCuCoNi. The particle has a dimer structure with one part being a AuCu alloy and the other a CoNi alloy. AuCoNi segregates into a Au domain and a CoNi domain, which form the primary particle. Cu is only present in the Au domain since it phase-segregates from Co and has a higher affinity for Au than Ni.

The incorporation of four components in one NP *via* SPBCL enables nanostructures with unprecedented compositional and structural complexity. Creating combinatorial libraries with SPBCL even allowed for the synthesis of higher order nanostructures, such as pentametallic NPs consisting of Au, Ag, Cu, Co, and Ni, using an ink solution with an equal loading of the five ion precursors (Figure 2.9F and 2.28-2.31). Composition control was more difficult than with the lower order NPs. Experimentally, we successfully form quinary particles from half of the polymer reactors patterned by SPBCL (yield = 50%; sample size was 50; Figure 2.31). The remaining polymer reactors generate tetrametallic NPs. The AuAgCuCoNi NPs had three distinct structural domains (Figure 2.29B). The overlay of EDS element maps revealed the distribution of metals and their spatial relationship. AgCuCo segregated into three domains, which form the primary NP (Figure 2.29E). Au was present in the Ag and Cu domains because it is only compatible with Ag and Cu but immiscible with Co (Figure 2.29D). Ni is only present in the Co domain because it phase-segregates from Au and has a higher affinity for Co than Cu (Figure 2.29F). Therefore, AuAgCuCoNi NPs composed of three segments, *i.e.*, a AuAg alloy, a AuCu alloy, and a CoNi alloy, were obtained *via* SPBCL (Figure 2.29G). The structure of the AuAgCuCoNi NP was highly

composition dependent. It is important to note that other substrates or annealing conditions may result in different particle structures, providing the potential for additional structure tuning. As such, this result validates SPBCL as a viable platform for synthesizing and studying previously undiscovered multimetallic NPs that are defined by fundamentally interesting and complex heterostructures.

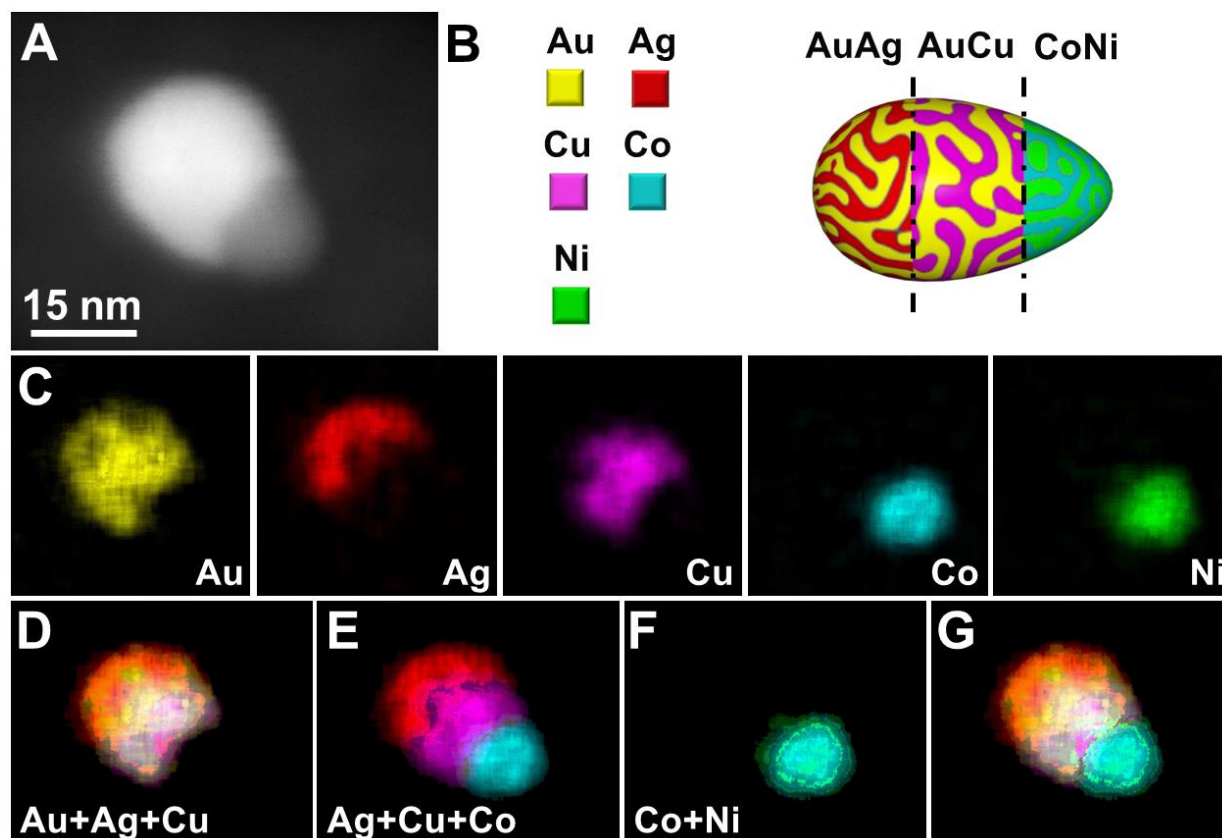


**Figure 2.29** Quinary heterostructured nanoparticles (A) HAADF-STEM image of a typical AuAgCuCoNi nanoparticle ( $\text{Au}_{0.19}\text{Ag}_{0.24}\text{Cu}_{0.28}\text{Co}_{0.14}\text{Ni}_{0.15}$ ). (B) Schematic illustration of the structure of AuAgCuCoNi nanoparticle in (A). The nanoparticle phase segregates into three domains: AuAg alloy, AuCu alloy, and CoNi alloy. (C-G) EDS elemental mapping of the AuAgCuCoNi nanoparticle in (A). (C) Distribution of each metal inside the nanoparticle. (D) Overlay of the element maps of Au, Ag, and Cu. (E) Overlay of the element maps of Ag, Cu, and Co. (F) Overlay of the element maps of Co and Ni. (G) Overlay of the element maps of all five metals.

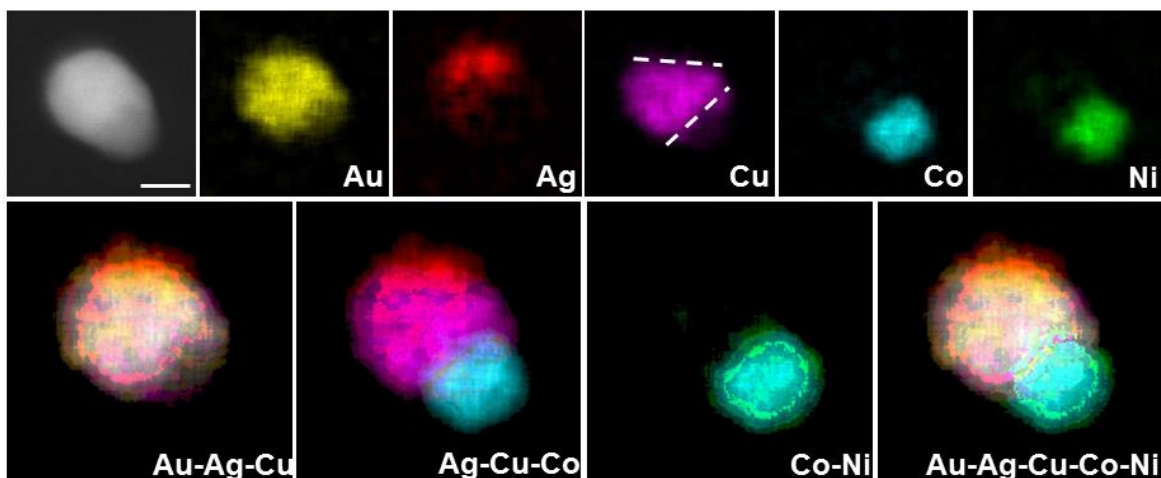


**Figure 2.30** EDS elemental mapping of a AuAgCuCoNi nanoparticle. Scale bar: 15 nm. The phase boundary between AuAg alloy and AuCu alloy is not parallel with the phase boundary between AuCu alloy and CoNi alloy. Dashed lines highlight the position of phase boundaries.

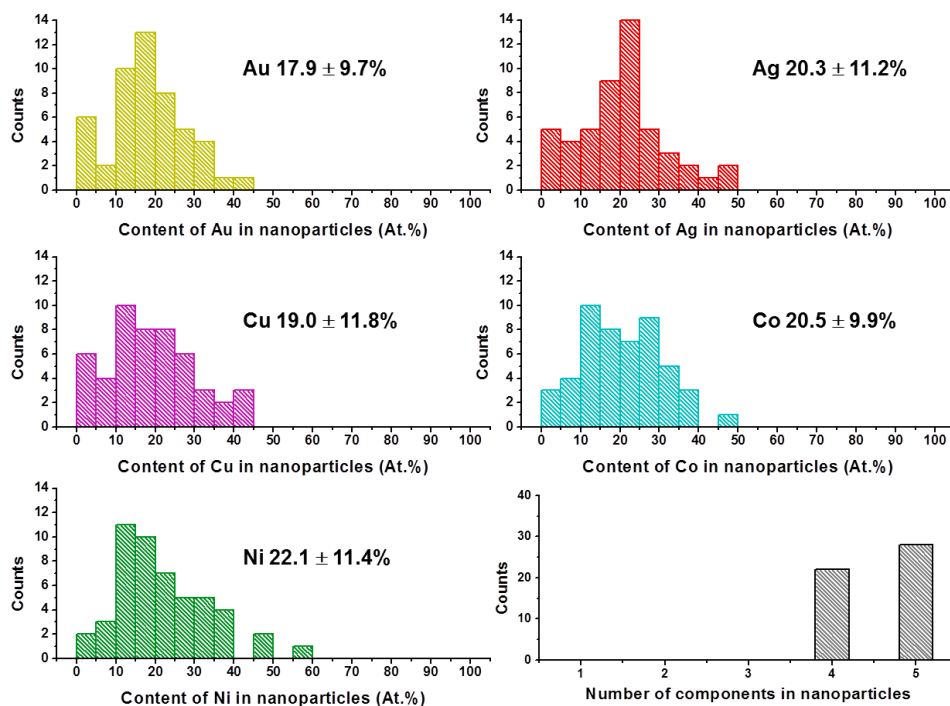


**Figure 2.31** Compositional uniformity of SPBCL-generated AuAgCuCoNi nanoparticles (sample size: 50). The metal loading ratio of the ink solution is: 20% Au, 20% Ag, 20% Cu, 20% Co, and 20% Ni. Since EDS has an inherent error of less than 5% due to x-ray absorption and fluorescence, only elements with content larger than 5% are considered as an effective component when counting the number of components in particles.

## 2.5 Materials and Methods

### 2.5.1 Materials

Poly(ethylene oxide)-*b*-poly(2-vinyl pyridine) (PEO-*b*-P2VP,  $M_n = 2.8$ - $b$ - $1.5$  kg/mol, polydispersity index = 1.11) was purchased from Polymer Source, Inc. Metal compounds,  $\text{HAuCl}_4 \cdot 3\text{H}_2\text{O}$ ,  $\text{AgNO}_3$ ,  $\text{Cu}(\text{NO}_3)_2 \cdot x\text{H}_2\text{O}$ ,  $\text{Co}(\text{NO}_3)_2 \cdot 6\text{H}_2\text{O}$ ,  $\text{Ni}(\text{NO}_3)_2 \cdot 6\text{H}_2\text{O}$ ,  $\text{Na}_2\text{PdCl}_4$ , and  $\text{H}_2\text{PtCl}_6 \cdot 6\text{H}_2\text{O}$  were purchased from Sigma-Aldrich, Inc. and used without further purification. DPN 1D pen arrays (type M, no gold coating) were purchased from Nanoink, Inc. TEM grids with hydrophobic silicon nitride support films ( $\text{SiN}_x$  film thickness = 15 or 50 nm, modified with 2.5 nm atomic layer-deposited alumina and fluoro-methyl-silane) were purchased from Ted Pella, Inc. Silicon wafers were purchased from Nova Electronic Materials.

### 2.5.2 Preparation of Block Copolymer Inks

Polymer inks were prepared by dissolving PEO-*b*-P2VP and different metal compounds in de-ionized water in predetermined molar ratios to achieve inks with specified molar ratios of metal precursors. The ink solution had a polymer concentration of 5 mg/mL and the molar ratio of pyridyl group to total metal precursors was 64:1. We expect that the use of an excess of pyridyl group will lead to a complete complexation of metal ions from the metal precursor salt onto PEO-*b*-P2VP. The pH of the ink solution was adjusted to between 3-4 by addition of  $\text{HNO}_3$ . The ink solution was stirred for 24 h at room temperature prior to use.

### 2.5.3 SPBCL Patterning Process

DPN pen arrays were dip-coated with inks and dried under ambient conditions. Following the inking step, the pen arrays were mounted onto an AFM (XE-150, Park Systems) and brought into contact with a TEM grid to deposit arrays of polymer nanoreactors. The patterning process

was performed in a chamber at a controlled temperature of 25 °C and relative humidity of 90%. The size of the polymer nanoreactors was tuned by adjusting the tip-sample dwell time. In order to convert polymer features into NPs, the TEM grids were put into a tube furnace and thermally annealed. The heating conditions were programmed as follows: ramp to 120 °C under Ar in 1 h, hold at 120 °C for 48 h, cool back to room temperature in 4 h, switch the atmosphere into H<sub>2</sub>, ramp to 500 °C in 2 h, thermally anneal the substrate at 500 °C for 12 h, and cool down to room temperature in 6 h.

#### *2.5.4 Characterization*

SEM images of the NPs synthesized on Si wafers were taken with a Hitachi S-8030 field-emission scanning electron microscope at an acceleration voltage of 5 kV and a current of 20 μA. An in-house designed dual-energy dispersive x-ray spectroscopy (EDS) detectors equipped Hitachi HD-2300 dedicated scanning transmission electron microscope (STEM) was used to image NPs synthesized on TEM grids with 50 nm silicon nitride support films. The bright-field images were recorded using a phase contrast detector, and the dark-field images were taken with a high-angle annular dark-field (HAADF) detector at an electron acceleration voltage of 200 kV. NP composition was studied using the dual EDS detectors equipped on the HD-2300 STEM with a 200 kV acceleration voltage. The L $\alpha$  peaks of Pt, Pd, Ag, and Au, and the K $\alpha$  peaks of Co, Ni, and Cu in the EDS spectra were used for elemental mapping and for composition quantification with standardless Cliff-Lorimer correction method. The atomic composition measured by EDS has an inherent error of less than 5% due to X-ray absorption and fluorescence. Each EDS map is built based on 30 frames with pixel dwell time of 203 μs. Thermo Scientific NSS software was used for EDS data processing. High-resolution TEM (HRTEM) images were taken on a JEOL 2100F

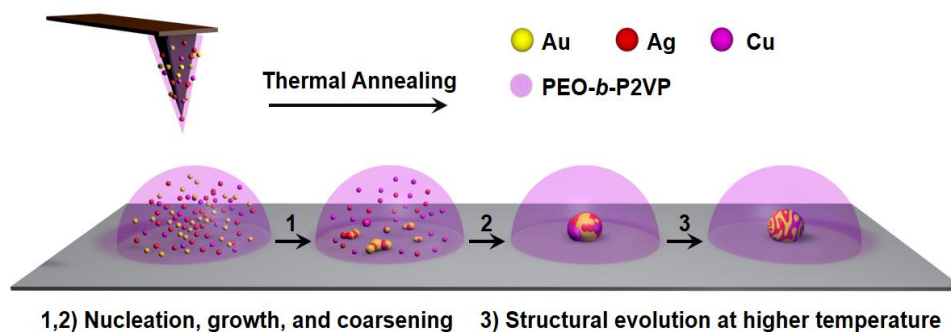
transmission electron microscope at an acceleration voltage of 200 kV with NPs prepared on TEM grids with 15 nm silicon nitride support films. X-ray photoelectron spectroscopy (XPS) spectra were recorded on a Thermo Scientific ESCALAB 250Xi with samples made by drop-casting polymer ink solution, followed by the aforementioned thermal annealing process.

## **2.6 Conclusions and Outlook**

In this chapter, we report that SPBCL can be utilized to synthesize a diverse class of polyelemental NPs (*e.g.*, mixtures of Au, Ag, Cu, Co, Ni, Pd, and Pt) in a site-specific manner. The ability to synthesize and characterize such structures provides an experimental platform to study alloy formation and phase-segregation at the nanoscale, which is important for understanding both structure and function. Given the enormous library of nanostructures that can be tailored based on particle composition and metal compatibility, our work advances the field of multimetallic NPs toward higher compositional diversity and structural complexity, which has the potential to impact a broad range of fields, such as catalysis,<sup>9,22</sup> plasmonics,<sup>10,23</sup> magnetics,<sup>17</sup> electronics,<sup>14,15</sup> biology,<sup>20,36</sup> and medicine.<sup>18</sup>

## CHAPTER THREE

Delineating the Formation Process of a Polyelemental Nanoparticle in a Nanoreactor



Portions of this chapter have been published in: *J. Am. Chem. Soc.*, **2017**, *139*, 9876-9884.

HRTEM characterization of nanoparticles was done in collaboration with Jingshan Du.

### 3.1 Introduction

Multimetallic heterostructured nanoparticles (NPs) that contain well-defined interfaces between inorganic domains have recently attracted extensive interest due to their utility in catalysis,<sup>22,32</sup> plasmonics,<sup>23,27</sup> magnetics,<sup>118</sup> and electronics.<sup>14,15</sup> The chemical, electronic, and magnetic interactions that occur across the interfaces inside heterostructured NPs can be engineered by changing the structure and elemental distribution of each inorganic domain; this allows the chemical and physical properties of NPs to be finely tuned.<sup>23,27,28,32</sup> To achieve this composition-structure-function tuning, wet chemistry approaches, especially stepwise seed-mediated growth processes in solution, have been successfully developed to prepare a wide variety of hetero-nanostructures.<sup>2,24,47,48,53,55,110,124</sup> However, slight changes in synthetic parameters can greatly influence the nucleation and particle growth processes as well as the resulting nanostructures, making targeted synthesis of a specific particle type a complicated and challenging process.<sup>2,45</sup> Consequently, there is a need to develop a fundamental understanding of the growth pathways for multimetallic NPs.<sup>191-27</sup> In this regard, these studies are usually performed either in an *in-situ* manner utilizing TEM<sup>191-195</sup> or X-ray scattering techniques<sup>23,49</sup> with liquid cells, or in an *ex-situ* manner by characterizing the particles in the reaction solution at different time points.<sup>46,183,196</sup> In addition to informing synthetic protocols, mechanistic understanding provides ways of trapping reactive intermediate nanostructures, which can be useful in their own right.<sup>46,183,193,196</sup>

Recently, we reported how scanning probe block copolymer lithography (SPBCL), a technique that delivers attoliter-scale volumes of metal precursor-coordinated polymers to a desired location to form a polymer nanoreactor, could be used to synthesize well-defined

multimetallic NPs in terms of size and composition.<sup>172,180-182,186</sup> This method takes the advantage of polymer nanoreactors to confine metal precursors at the nanoscale.<sup>139,141</sup> Each nanoreactor, when thermally treated, yields an individual NP with a composition that mirrors the stoichiometry defined by the precursors. In Chapter Two, this method has been utilized to construct a combinatorial library of multimetallic NPs consisting of all elemental combinations of Au, Ag, Cu, Co, and Ni at a fixed equal elemental stoichiometry, which includes sets of novel hetero-nanostructures that are composed of miscible and immiscible metals. Since multimetallic NPs have not been synthesized with such precision and complexity before, the process by which the various metals in a polymer reactor aggregate to yield a single NP and then evolve into a final architecture is unclear. Therefore, this study is important for understanding how to control and design nanostructures for catalysis, plasmonics, magnetics, and electronics.

In this chapter, we report an in-depth study on how AuAgCu NPs are formed in polymer nanoreactors. AuAgCu NPs were chosen as a model system because both miscible (Au/Ag and Au/Cu) and immiscible metal pairs (Ag/Cu) are present in this system. The aggregation of different combinations of Au, Ag, and Cu in SPBCL-generated polymer reactors has been studied and characterized by XPS, STEM, and EDS. The study shows that different metal components aggregate at markedly different rates within the polymer nanoreactors, which leads to kinetically trapped states that evolve into either alloy or well-defined, phase-segregated heterostructures. By confining the reagents at a fixed stoichiometry within the polymer nanoreactors, we can systematically study how different metals migrate through a single particle to create alloys or heterostructures. This technique not only is useful for understanding particle formation but can also be used to identify conditions that trap structures in kinetic states, some of which may be

useful in their own right.

### 3.2 Aggregation of a Single Type of Metal in a Polymer Reactor

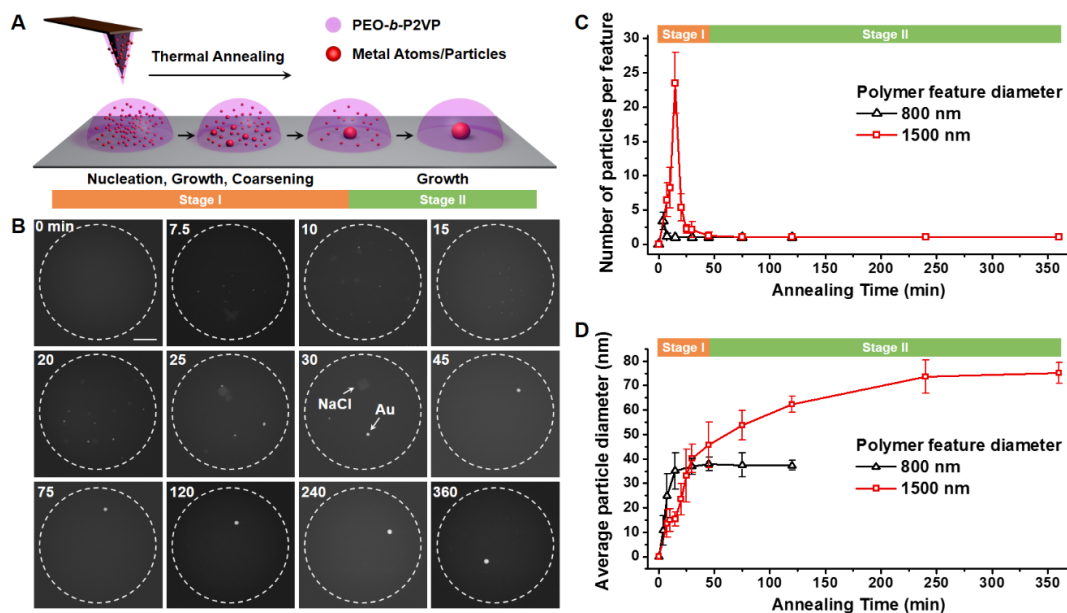


**Figure 3.1** Nucleation and growth of monometallic nanoparticles in polymer nanoreactors. (A) A scheme of the nucleation and growth process. (B) Ex-situ ADF-STEM images of the aggregation and growth of Au nanoparticles in polymer features annealed at 100 °C. Dashed circles indicate the edge of polymer features. Scale bar: 300 nm. (C,D) The number (C) and average diameter (D) of the nanoparticles formed in polymer features annealed at 100 °C. The assignment of Stage I and II in (C) and (D) applies to the polymer features with diameters of 1500 nm.

To investigate the nucleation and growth of metal precursors in polymers, we initially studied the simplest structures, *i.e.*, polymer features that contain only  $\text{HAuCl}_4$ . Previous studies have shown that Au salts, at elevated temperatures, can be reduced by PEO, which results in the subsequent aggregation of the metal atoms and NP nuclei in the polymer reactor.<sup>181,188</sup> Herein, we examined the aggregation of monometallic particles in a quantitative manner. Experimentally, we find that the aggregation process can be divided into two stages (Figure 3.1A and 3.1B, reactor diameters  $\sim 1.5 \mu\text{m}$ , annealed at 100 °C). In the first stage ( $< 45 \text{ min}$ ), many Au particles form in a single polymer nanoreactor with the maximum average number appearing after an annealing time of  $\sim 15 \text{ min}$  (Figure 3.1C). Next, the coarsening (ripening and coalescence) of the particles becomes

the dominant process, overwhelming the rate of new nucleation, resulting in a decrease in the average number of particles per reactor (50 reactors monitored, Figure 3.1C). At the end of Stage I (~ 45 min, Figure 3.1C), only one NP is observed in each reactor, suggesting that the Au concentration in each polymer feature is below the threshold necessary to induce nucleation of new particles (Figure 3.2). During Stage I, the average particle diameter slowly increases until it reaches 46 nm due to the growth and coarsening processes (Figure 3.1D).

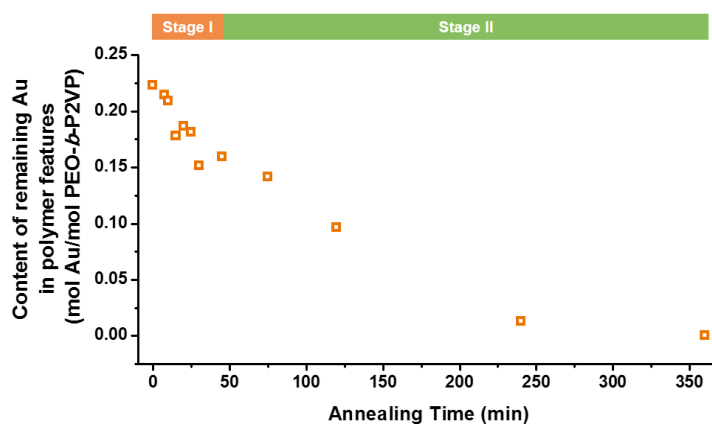


**Figure 3.2** Remaining free Au in polymer features (1.5  $\mu\text{m}$ ) annealed at 100  $^{\circ}\text{C}$  over time. The remaining Au content was calculated by comparing the diameters of intermediate particles to the diameters of the final particles (assuming all Au precursors in a reactor aggregated to form the final particle). The molar ratio between  $\text{HAuCl}_4$  and PEO-*b*-P2VP in the starting polymer nanoreactors is 1:4.48.

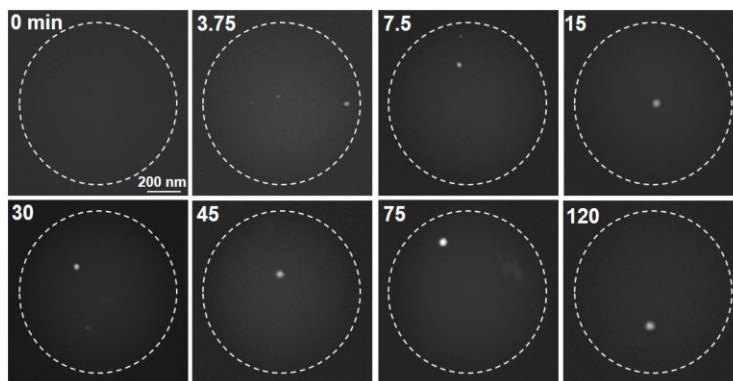


**Figure 3.3** Ex-situ ADF-STEM images of Au aggregation in polymer features annealed at 100  $^{\circ}\text{C}$  over time. Dashed circles mark the edge of polymer nanoreactors.

In Stage II (45 min-360 min), individual particles in each reactor (Figure 3.1C) continue to

grow by depleting the remaining Au in the polymer reactor, and ultimately reaching a final size of about 75 nm after 6 h (Figure 3.1D). This two-stage growth phenomenon was also observed for Au particles formed in smaller reactors (*e.g.*, 550 and 800 nm; Figure 3.1C, 3.1D, and 3.3-3.5). Impurity salt particles (NaCl/KCl) were observed in some polymer reactors (Figure 3.1B and 3.6A), which are a consequence of salt impurities in the commercially available polymer matrix. It is important to note that while both types of particles are present, the Au particles primarily nucleate on the substrate as opposed to salt crystals. In addition, the impurity salts can also be removed from the polymer by dialysis (Figure 3.6B).

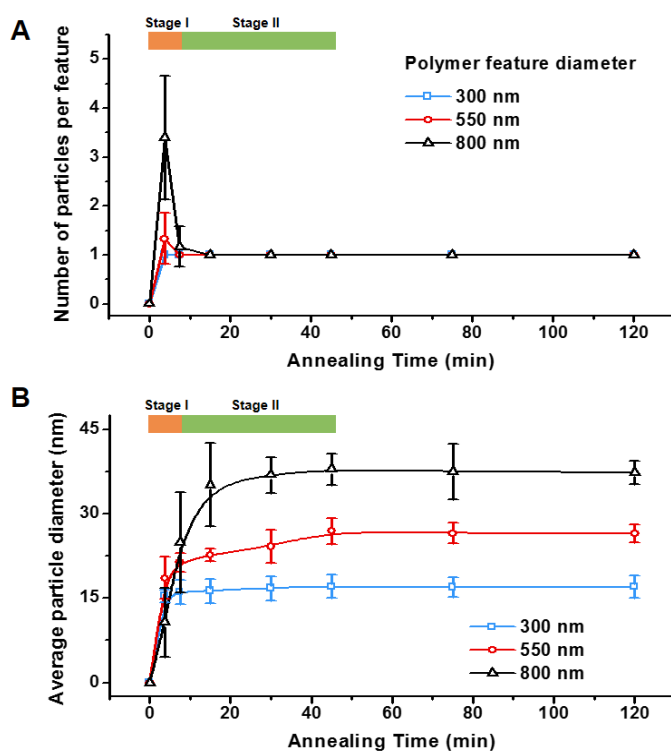


**Figure 3.4** (A) The number of nanoparticles and (B) the average diameter of nanoparticles formed in polymer features annealed at 100 °C over time. Solid curves are guide to the eye. The assignments of Stage I and II in (A) and (B) apply only to polymer nanoreactors with diameters of 550 nm and 800 nm. For polymer features with a diameter of 300 nm, Stage I is not observed. This observation suggests that the polymer nanoreactor is not large enough for nucleation of more than one particle.

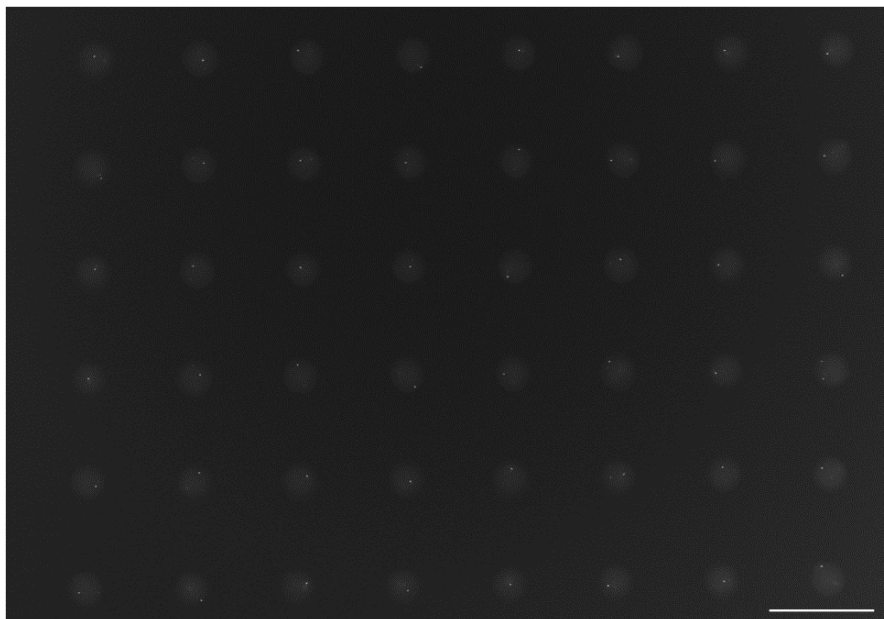


**Figure 3.5** An ADF-STEM image of an 8-by-6 array of polymer nanoreactors containing Au salt precursor. The polymer nanoreactors were annealed at 100 °C for 1h to form a single Au NP in each nanoreactor. Scale bar: 3  $\mu\text{m}$ .

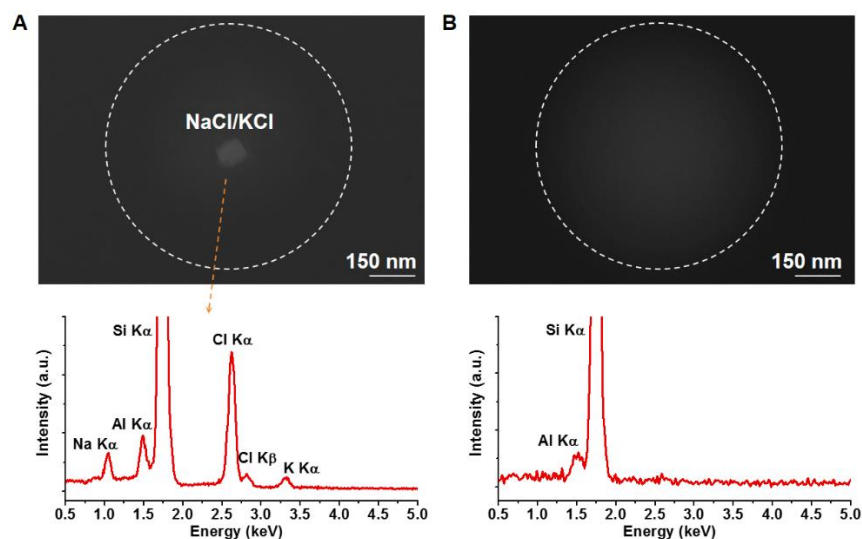


**Figure 3.6** (A) An ADF-STEM image of a NaCl/KCl particle formed in a blank polymer nanoreactor annealed at 100 °C for 1h. The dashed circle marks the edge of the polymer nanoreactor. An EDS spectrum of the crystal is shown underneath the STEM image. Al signals are from the TEM sample holder. (B) An ADF-STEM image of a polymer nanoreactor annealed at 100 °C for 1h. The polymer was purified by dialysis with deionized water for 48 h (ThermoFisher dialysis cassettes, 2K MWCO). The dashed circle marks the edge of the polymer nanoreactor. EDS characterization of the polymer reactor shows no observable Na, K, and Cl signals.

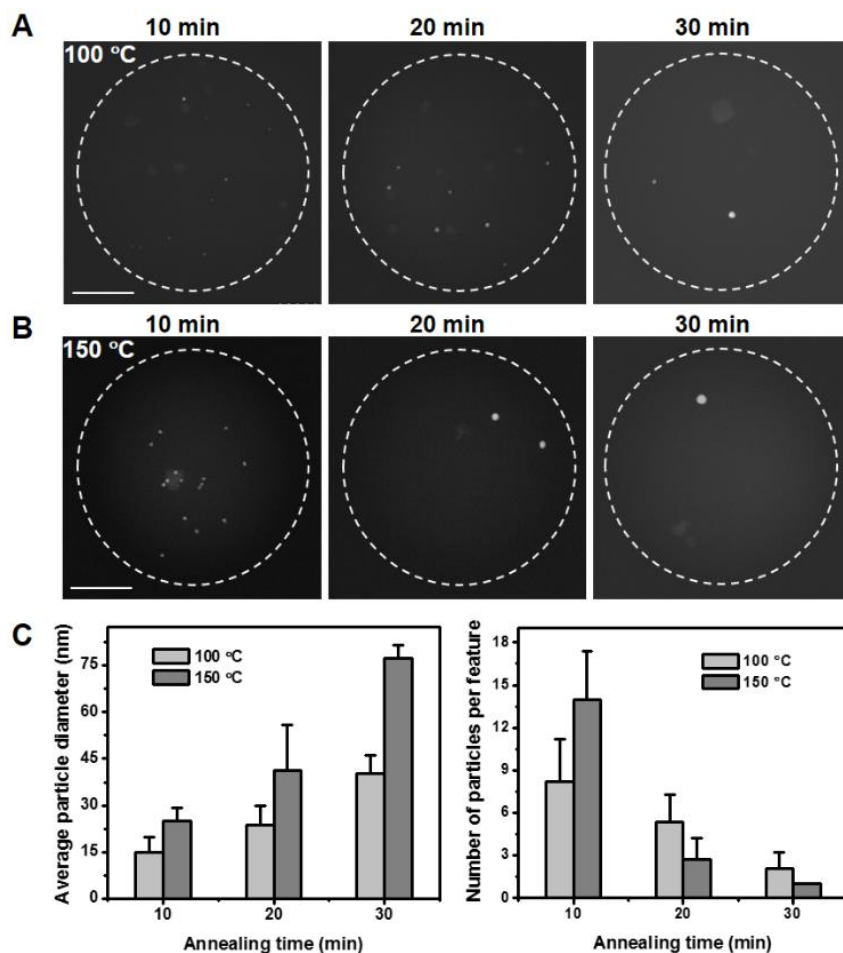


**Figure 3.7** (A) Ex-situ ADF-STEM images of the aggregation of Au in polymer nanoreactors annealed at 100 °C. Dashed circles indicate the edge of the polymer nanoreactors. Scale bar: 400 nm. (B) Ex-situ ADF-STEM images of the aggregation of Au in polymer nanoreactors annealed at 150 °C. Dashed circles indicate the edge of polymer nanoreactor. Scale bar: 400 nm. (C) The average diameter and number of nanoparticles formed in polymer nanoreactors annealed at 100 °C and 150 °C.

Since the mobilities of both Au atoms and particles are accelerated by thermal annealing, temperature plays a key role in tuning the nucleation, growth, and coarsening rates of Au particles. As shown in Figure 3.7, annealing the polymer feature at 150 °C led to a faster aggregation of Au, which requires only 0.5 h to generate NPs that have the same size (75 nm) as those formed in polymer features annealed at 100 °C for 6 h. To evaluate the generality of the aggregation processes, we next investigated polymer features that contain  $\text{AgNO}_3$  or  $\text{Cu}(\text{NO}_3)_2$ . Unlike Au, which

precipitates directly in the form of Au NPs, Ag initially aggregates by forming a mixture of Ag and AgCl particles (annealed at 120 °C for 0.5 h, Figure 3.8 and 3.9). This is likely due to the presence of Cl<sup>-</sup> ions in the reactor that come from the starting polymer matrix. After being annealed at 120 °C for 2 h, all AgCl particles were completely transformed into Ag particles through either thermal decomposition or reduction by PEO,<sup>181</sup> resulting in multiple Ag NPs in each reactor.

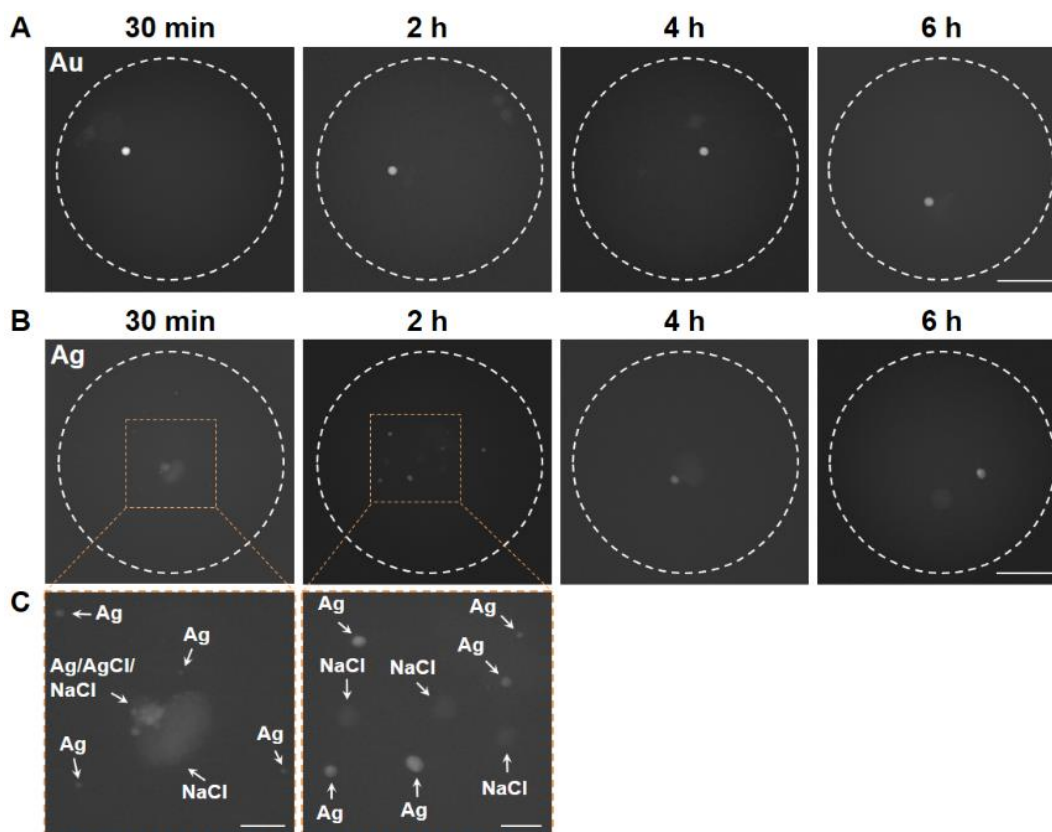


**Figure 3.8** Ex-situ ADF-STEM images of the aggregation process for (A) Au and (B) Ag precursors in polymer nanoreactors annealed at 120 °C. Dashed circles indicate the edge of polymer nanoreactor. Scale bars: 200 nm. (C) Enlarged views of the aggregated particles within the nanoreactors in (B). Scale bar: 50 nm.

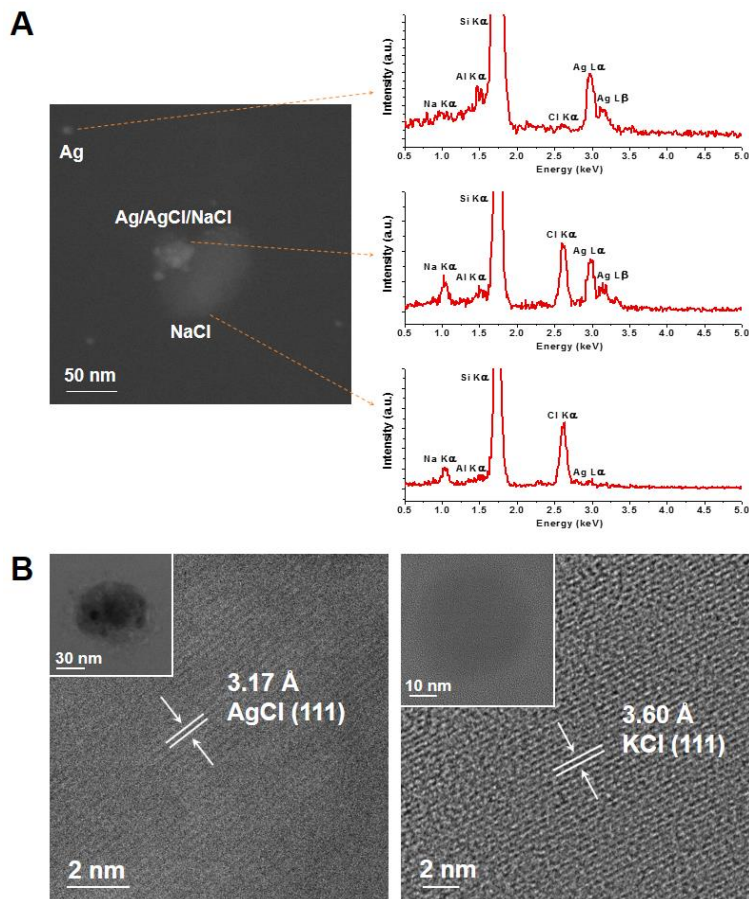


**Figure 3.9** (A) An ADF-STEM image of the particles formed in a single polymer nanoreactor that contains Ag precursor ( $\text{AgNO}_3$ ). The polymer feature was annealed at 120 °C for 30 min. EDS spectra of the particles reveal the presence of a Ag/AgCl/NaCl mixture along with Ag, and NaCl particles. Al signals are from the TEM sample holder. (B) HRTEM images of the AgCl and KCl/NaCl particles formed in polymer nanoreactors that were annealed at 120 °C for 30 min. The observed lattice spacings are 3.17 Å and 3.60 Å, which correspond to AgCl (111) and KCl (111) planes, respectively.

In general, Ag aggregates more slowly than Au when being annealed under identical conditions (Figure 3.8). This rate difference suggests a higher mobility of Au atoms/particles in polymer reactors than that of Ag atoms/particles. In addition, the higher reduction potential of  $\text{AuCl}_4^-/\text{Au}$  ( $E^\circ = 1.002 \text{ V}$ ) than that of  $\text{Ag}^+/\text{Ag}$  ( $E^\circ = 0.7996 \text{ V}$ ) also contributes to faster precipitation of Au. The last element, Cu, requires a longer annealing time or higher annealing temperature for nucleation to occur. As shown in Figure 3.10, particles that contain Cu are only

observable in reactors that are annealed at 160 °C for more than 18 h or at temperatures above 200 °C for 4 h. These Cu-containing particles likely consist of Cu<sup>II</sup> species such as CuO, a decomposition product from thermally annealing the Cu(NO<sub>3</sub>)<sub>2</sub> precursor;<sup>197</sup> the oxidation state of Cu at this stage was confirmed by XPS (Figure 3.10G). The slower nucleation of Cu<sup>II</sup> species can be attributed to the higher thermal stability of the Cu precursor (CuNO<sub>3</sub>), which decomposes at temperature above 180 °C.<sup>197</sup> In contrast, Au<sup>3+</sup> and Ag<sup>+</sup> are reduced to the metallic state by PEO at 120 °C for nucleation (Figure 3.8).

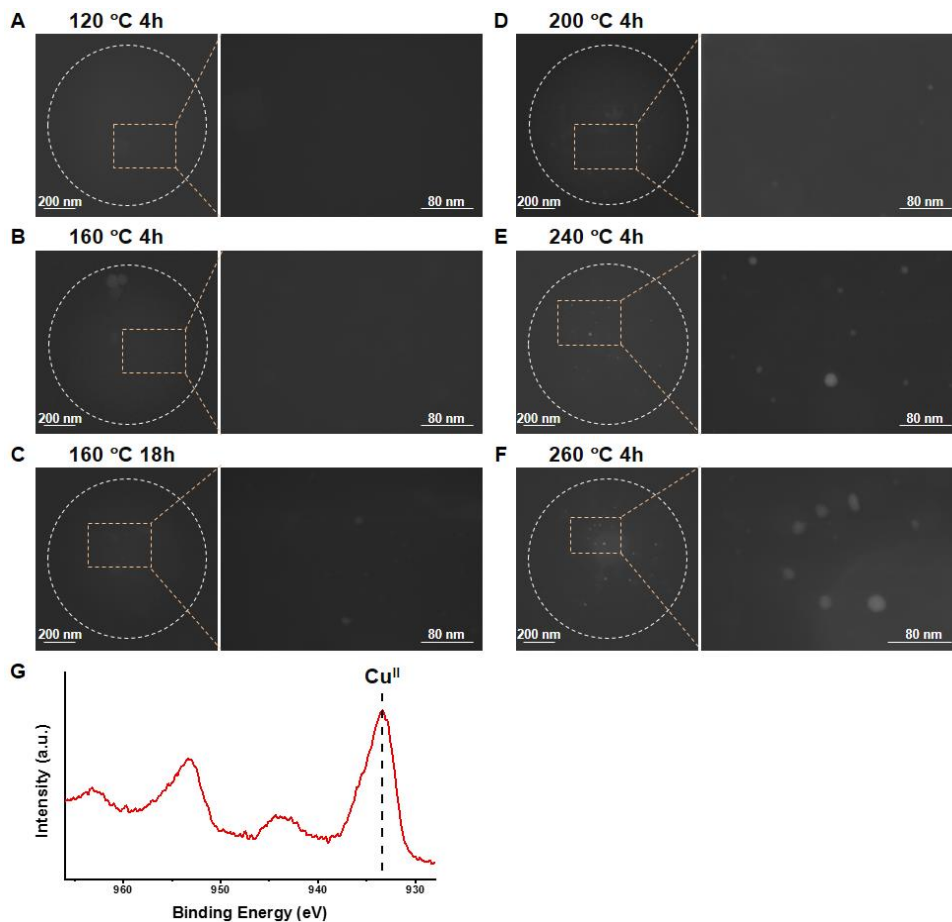


**Figure 3.10** (A-F) ADF-STEM images of representative polymer nanoreactors that contain Cu(NO<sub>3</sub>)<sub>2</sub> subjected to thermal treatment. (G) A Cu 2p XPS spectrum of particles formed by thermally annealing a drop-cast polymer ink solution that contains the Cu precursor at 260 °C for 18h.

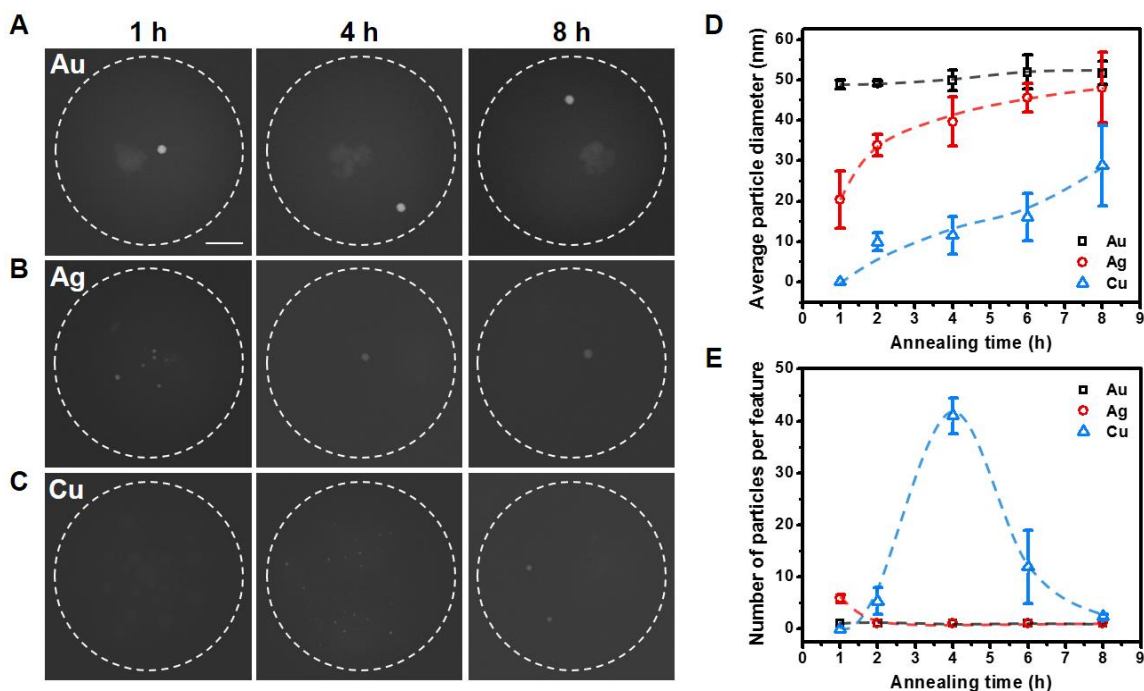


**Figure 3.11** Comparison of the aggregation rates during the formation of different monometallic nanoparticles. (A-C) ADF-STEM images showing the aggregation of Au, Ag, or Cu<sup>II</sup> species in polymer features annealed at 240 °C. Dashed circles indicate the edge of polymer features. Scale bar: 200 nm. (D-E) The average diameter (D) and number (E) of the nanoparticles formed in polymer features annealed at 240 °C. Dashed curves are guide to the eye.

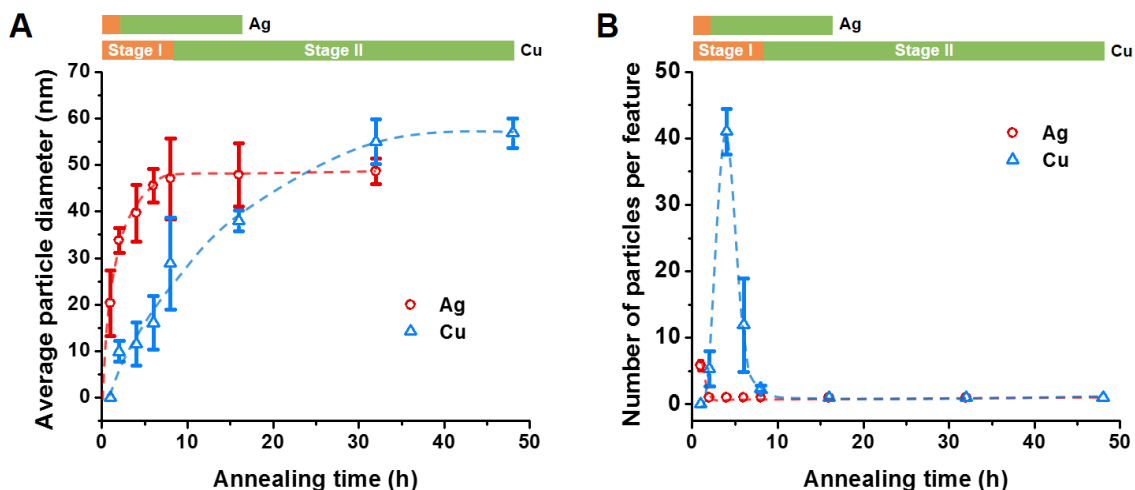


**Figure 3.12** (A) The average diameter and (B) number of nanoparticles formed in polymer nanoreactors (diameters ~ 1  $\mu\text{m}$ ) using either AgNO<sub>3</sub> or Cu(NO<sub>3</sub>)<sub>2</sub> precursors that were annealed at 240 °C. Dashed curves are guide to the eye.

In order to construct a systematic comparison of Au, Ag, and Cu, we annealed polymer reactors that contain each precursor at 240 °C for a predetermined time (Figure 3.11). At this temperature, the Au and Ag salts are reduced quickly and form NPs (Figure 3.11D and 3.11E). Interestingly, while Au undergoes Stage I and II processes in 1 h and forms a single particle per reactor, Ag takes 2 h to finish Stage I and it is not until after 16 h of annealing that Ag reaches the end of Stage II (Figure 3.1A and 3.12).

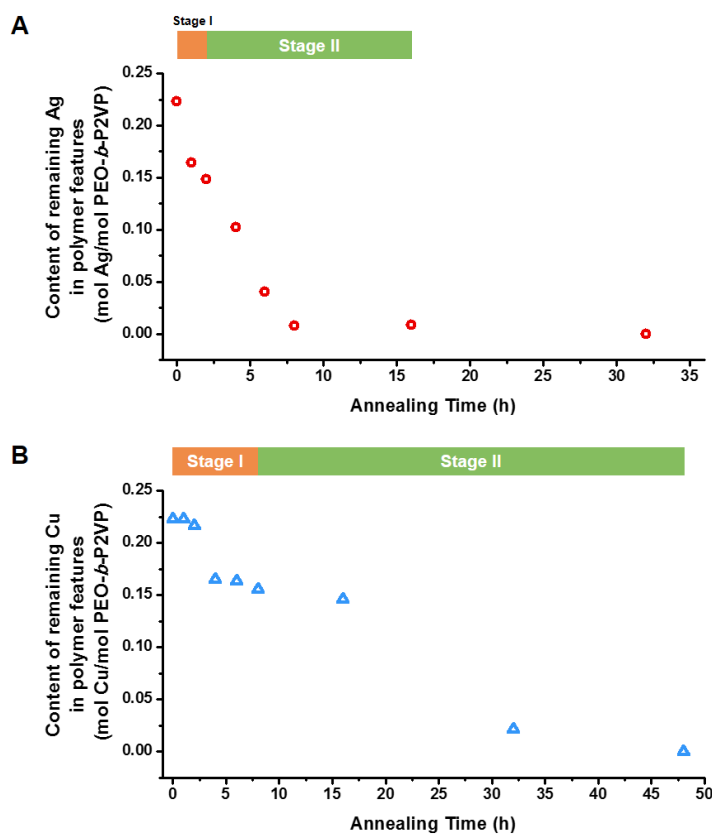


**Figure 3.13** Remaining free metal species in polymer nanoreactors that contain one type of precursor and are annealed at 240 °C. (A) Amount of free Ag in polymer features (1  $\mu\text{m}$ ). (B) Amount of free Cu in polymer features (1  $\mu\text{m}$ ). For each monometallic system, the molar ratio between the metal precursor and PEO-*b*-P2VP in the starting polymer nanoreactors is 1:4.48. The remaining Ag or Cu content was calculated by comparing the diameters of intermediate particles to the final particles (assuming all metal precursors in a reactor aggregate to form the final particle).

By contrast, Cu requires 8 h of annealing to finish Stage I, and it is not until 48 h that Stage

II is completed (Figure 3.12 and 3.13). The slower aggregation of the  $\text{Cu}^{\text{II}}$  species is presumably due to the higher binding strength between  $\text{Cu}^{\text{II}}$  and the substrate ( $\text{SiN}_x$  substrate with a native oxide top layer) than that between the other elements and the substrate. It should be noted that the presence of impurity salts has little effect on the aggregation of Au, Ag, or Cu at 240 °C, since Na, K, and Cl signals are not observed in the EDS spectra of the initially nucleated particles (Figure 3.14). The data for the monometallic systems clearly show that there are markedly different rates of particle formation, an observation that will be used to help understand the multimetallic systems.

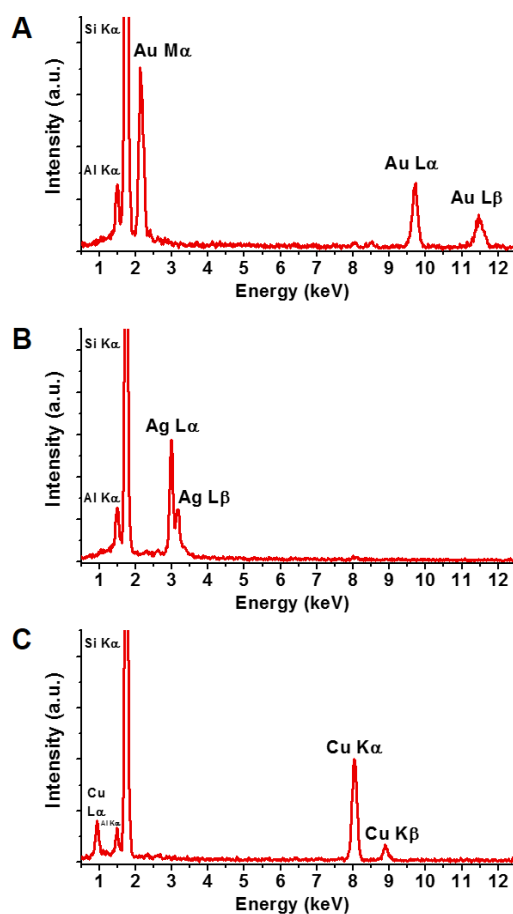


**Figure 3.14** EDS spectra of the initially nucleated nanoparticles in Figure 2. (A) Au and (B) Ag nanoparticles formed in polymer nanoreactors that were annealed at 240 °C for 1 h. (C)  $\text{Cu}^{\text{II}}$  nanoparticles formed in a polymer nanoreactor that was annealed at 240 °C for 2 h. The Al signals in the spectra are from the TEM sample holder.

### 3.3 Aggregation of Two Types of Metal in a Polymer Reactor

With the knowledge gained in the monometallic study, we next examined the co-nucleation/growth process of all bimetallic combinations of Au, Ag, and Cu at fixed 1:1 stoichiometries. For the first binary combination ( $\text{HAuCl}_4/\text{AgNO}_3$ ; reduced metals are miscible), Au, Ag, and AgCl particles initially form and are observable at early time points within the polymer reactors (after being annealed at 120 °C for 30 min, Figure 3.15).

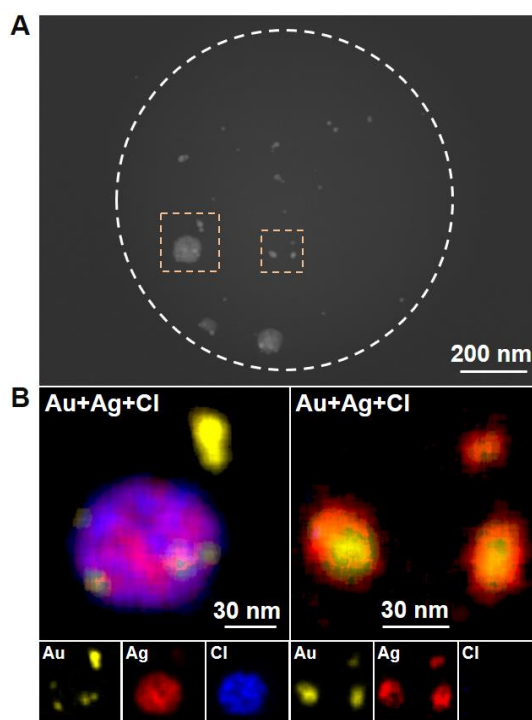


**Figure 3.15** (A) ADF-STEM image of a representative polymer nanoreactor that contains equal amounts of the metal salt precursors,  $\text{HAuCl}_4$  and  $\text{AgNO}_3$ , annealed at 120 °C for 30 min. The white dashed circle indicates the edge of the polymer nanoreactor. (B) STEM images along with EDS elemental maps are shown for the particles located within the yellow dashed squares in (A).

Continuous additional thermal treatment at 120 °C for another 1.5 h completely decomposes the AgCl and results in the formation of multiple irregular-shaped particles in each reactor (Figure 3.16). The irregular-shaped particles are composed of Au and Ag and are structurally inhomogeneous, as evidenced by the Au-enriched and Ag-enriched domains in the

EDS elemental mapping images of the particles (Figure 3.16A and 3.16B). The inhomogeneous structure is caused by the coalescence of the Au and Ag particles early in the particle formation process.

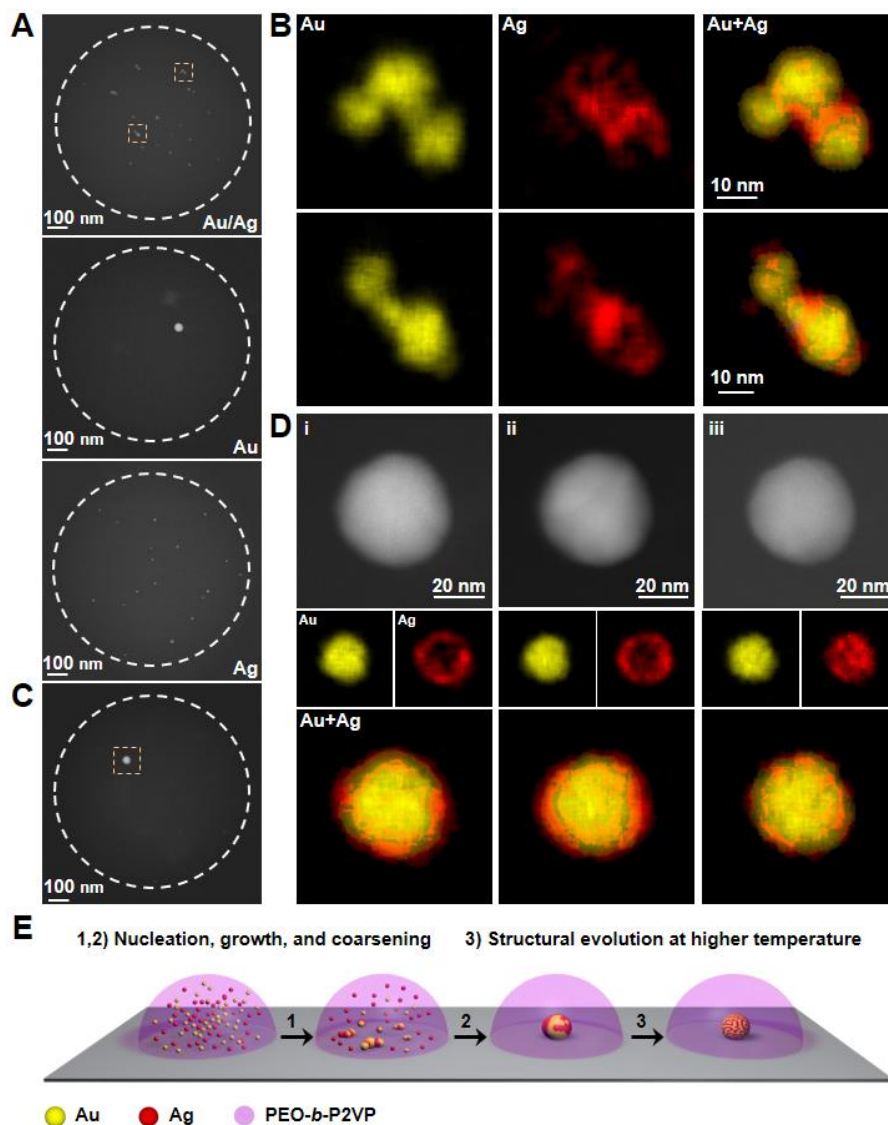


**Figure 3.16** Formation of AuAg nanoparticles in polymer nanoreactors. (A) ADF-STEM images of representative polymer features that contain either equal amounts of  $\text{HAuCl}_4$  and  $\text{AgNO}_3$ , only  $\text{HAuCl}_4$ , or only  $\text{AgNO}_3$  metal salt precursors. The features were annealed at 120 °C for 2h. White dotted circles indicate the edge of polymer features. (B) EDS elemental maps of the AuAg particles located inside the yellow dashed squares in (A). (C) An ADF-STEM image of a polymer feature that contains equal amounts of the metal salt precursors,  $\text{HAuCl}_4$  and  $\text{AgNO}_3$ , annealed at 160 °C for 4h. (D) ADF-STEM images and EDS elemental maps of the AuAg particle ( $\text{Au}_{0.51}\text{Ag}_{0.49}$ ,

atomic composition) located inside a yellow dashed square in (C). The particle was stepwise annealed at (i) 160 °C for 4h, (ii) 160 °C for 18h, and (iii) 260 °C for 4h. (E) Schematic of the structural evolution of AuAg nanoparticles in polymer nanoreactors deposited with SPBCL.

It should be noted that generally, the aggregation of Au is slower for the two-component Au/Ag system when compared to the monometallic system, pure Au system. Indeed, when polymer reactors containing only  $\text{HAuCl}_4$  are heated at 120 °C for 2 h (identical conditions used for the binary system), single well-formed Au NPs form (Figure 3.16A). When one compares the three types of reactors at the same time point (Figure 3.16A), it is clear that the presence of Ag significantly depresses the mobility of Au. In addition, while Au@Ag core-shell nanostructures are observed for some particles, Ag@Au core-shell nanostructures were never found (Figure 3.15 and 3.16B). This is consistent with the conclusion that Au still aggregates at a faster rate than Ag, and can act as a seed for heterogeneous nucleation of a Ag shell. Finally, for the two component system, when it is annealed at 160 °C for 4h, the vast majority of the precursor goes into forming a single primary two-component particle (~50 nm) within each reactor (Figure 3.16C), which is surrounded by much smaller, primarily silver particles (< 3 nm) that continue to contribute to coarsening as the reactor is heated. EDS elemental mapping of the primary particle shows that Au and Ag do not fully alloy even after being heated at 160 °C for 4 h (Figure 3.16D, here a Au@Ag particle is shown). To further explore the temperature-induced structural evolution of the particle, the polymer reactor shown in Figure 3.16D was annealed stepwise at 160 °C for 18 h and at 260 °C for 4 h with EDS mapping carried out after each step. Ag partly diffused into the Au core after being annealed at 160 °C for 18 h, while Au and Ag are fully mixed after being annealed at 260 °C for just 4 h (Figure 3.16D). As such, high temperature and short annealing times exhibit higher efficacy than low temperature and long annealing periods in facilitating the structural evolution of

SPBCL NPs into thermodynamic structures. The entire aggregation process of Au/Ag is summarized in Figure 3.16E. When two metals are present in one reactor, co-nucleation and growth of the two metals result in both monometallic and bimetallic particles in the reactor. Upon particle growth and coarsening of the particles, an individual structurally inhomogeneous particle is obtained. Ultimately, thermal annealing at a relatively high temperature allows the constituent metals to be transformed into a stable configuration.

For the second binary combination (Au/Cu, miscible metals), primary nucleated particles are also formed by a combination of nucleation, growth, and coarsening (Figure 3.17 and 3.18), which is similar to the process observed in the AuAg system. The structure of the primary nucleated particles obtained at low annealing temperature (160 °C for 4 h) is inhomogeneous, as evidenced by the Au-enriched and Cu-enriched domains observed by EDS elemental mapping of the particles (Figure 3.19A). Either longer annealing times (18 h, Figure 3.18) or higher annealing temperatures (240-260 °C, Figure 3.19B-3.19E) increase the alloying of the Au and Cu. The oxidation states of Au and Cu that comprise the nucleated particles were examined by XPS using samples prepared by drop-casting (Figure 3.19F). When Au is present in the reactor, the Cu component is in the 0 valence state after being annealed at 260 °C for 18h, as compared to the formation of particles consisting of Cu<sup>II</sup> species in reactors containing only Cu(NO<sub>3</sub>)<sub>2</sub>. HRTEM characterization of the nucleated particles corroborates the formation of AuCu alloy particles in AuCu reactors (Figure 3.19G). Another distinct difference between the pure Cu and AuCu alloy system is the faster precipitation of Cu observed for the reactors containing Au. The majority of the available Cu accumulates into an alloy particle after being annealed at 160 °C for 4 h (Figure 3.19A), while for the pure Cu system, a higher annealing temperature (240 °C) and a longer

annealing time (48 h) are required (Figure 3.12). Clearly, Au facilitates the reduction and aggregation of Cu. It has been reported that the free electron cloud on the surface of noble metal NPs (*e.g.*, Au) can induce the reduction of non-noble metal ions (*e.g.*,  $\text{Co}^{2+}$ ,  $\text{Cu}^{2+}$ ) that are adsorbed on particle surface, *i.e.*, the noble-metal-induced reduction (NMIR) process.<sup>103,198</sup> In AuCu polymer reactors, the  $\text{Cu}^{\text{II}}$  species presumably adsorbed on the primarily nucleated Au NPs and are then reduced to form AuCu alloy particles. The high mobility of Au atoms/particles expedites the aggregation of AuCu particles, as compared to the slow aggregation of a pure Cu system.

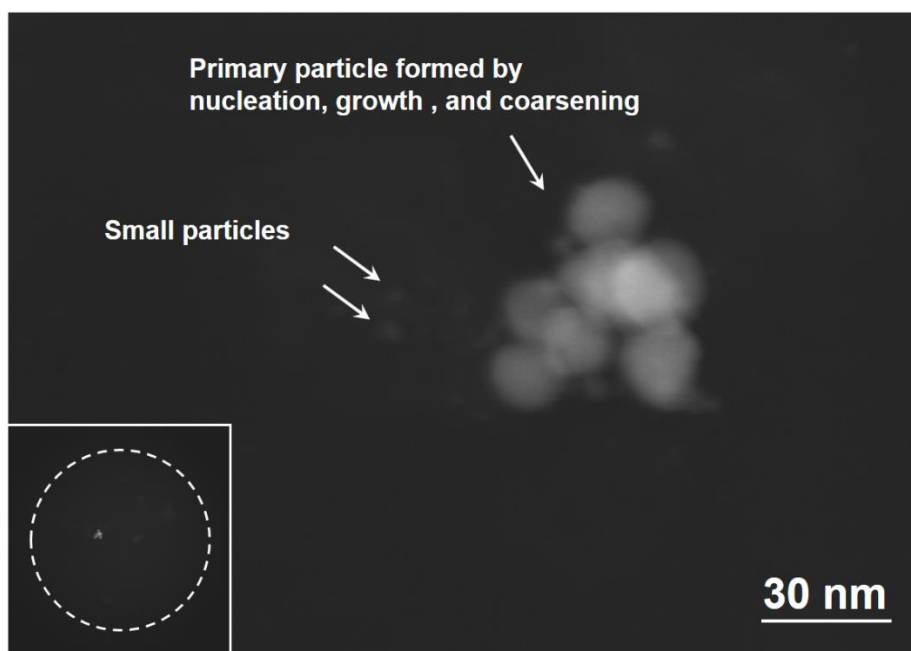


**Figure 3.17** An ADF-STEM image of particles formed in a representative polymer nanoreactor that contains equal amounts of the metal salt precursors,  $\text{HAuCl}_4$  and  $\text{Cu}(\text{NO}_3)_2$ , annealed at  $160^\circ\text{C}$  for 1 h. Inset: An ADF-STEM image of the polymer nanoreactor containing the nanoparticles. The white dashed circle indicates the edge of the polymer nanoreactor. A primary nucleated particle is observed in the polymer nanoreactor along with some small  $\text{Cu}^{\text{II}}$  particles that contribute to coarsening as the reactor is heated. EDS elemental mapping of the primary particle is shown in Figure 3.18.

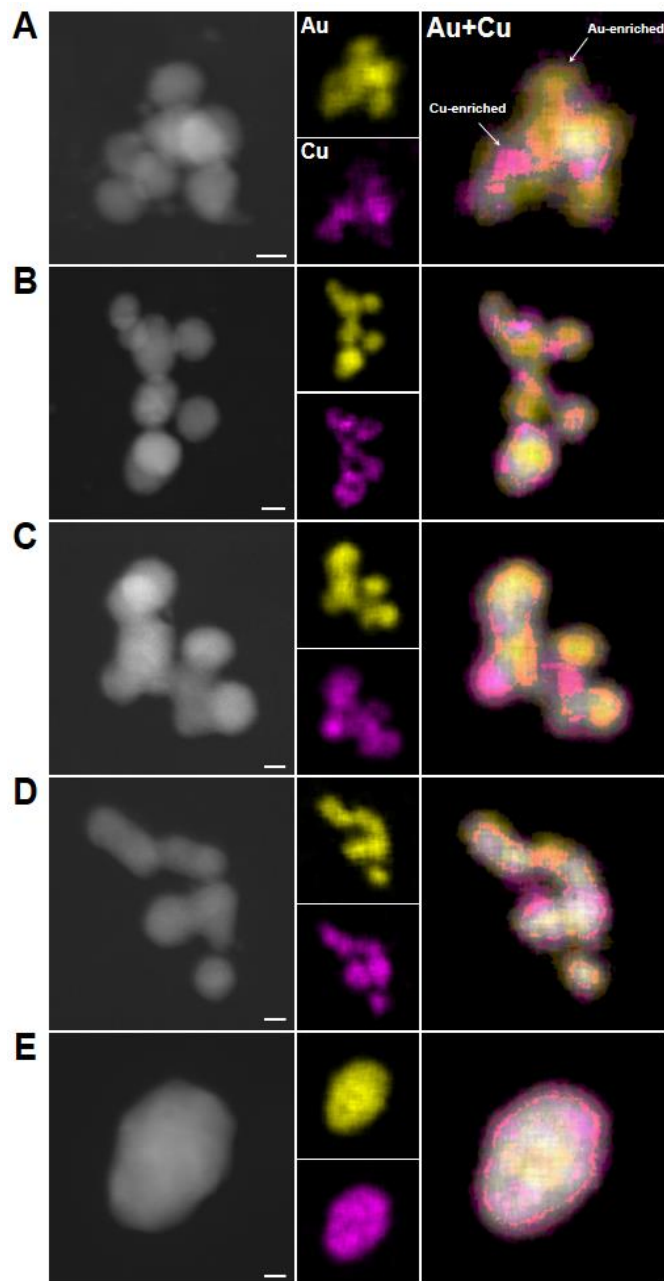


**Figure 3.18** ADF-STEM images and EDS elemental maps of representative primary particles formed in polymer nanoreactors that contain equal amounts of the metal salt precursors,  $\text{HAuCl}_4$  and  $\text{Cu}(\text{NO}_3)_2$ , annealed in different conditions: (A) 160 °C for 1h, particle contains 72% Au and 28% Cu and (B) 160 °C for 18h, particle contains 54% Au and 46% Cu, (C) 200 °C for 4h, particle contains 50% Au and 50% Cu, (D) 240 °C for 4h, particle contains 50% Au and 50% Cu, (E) 260 °C for 4h, particle contains 53% Au and 47% Cu. Scale bars: 10 nm. The particle obtained after annealing at 160 °C for 1h has more Au content compared to the other conditions, suggesting that Au aggregates at a faster rate than the Cu species.

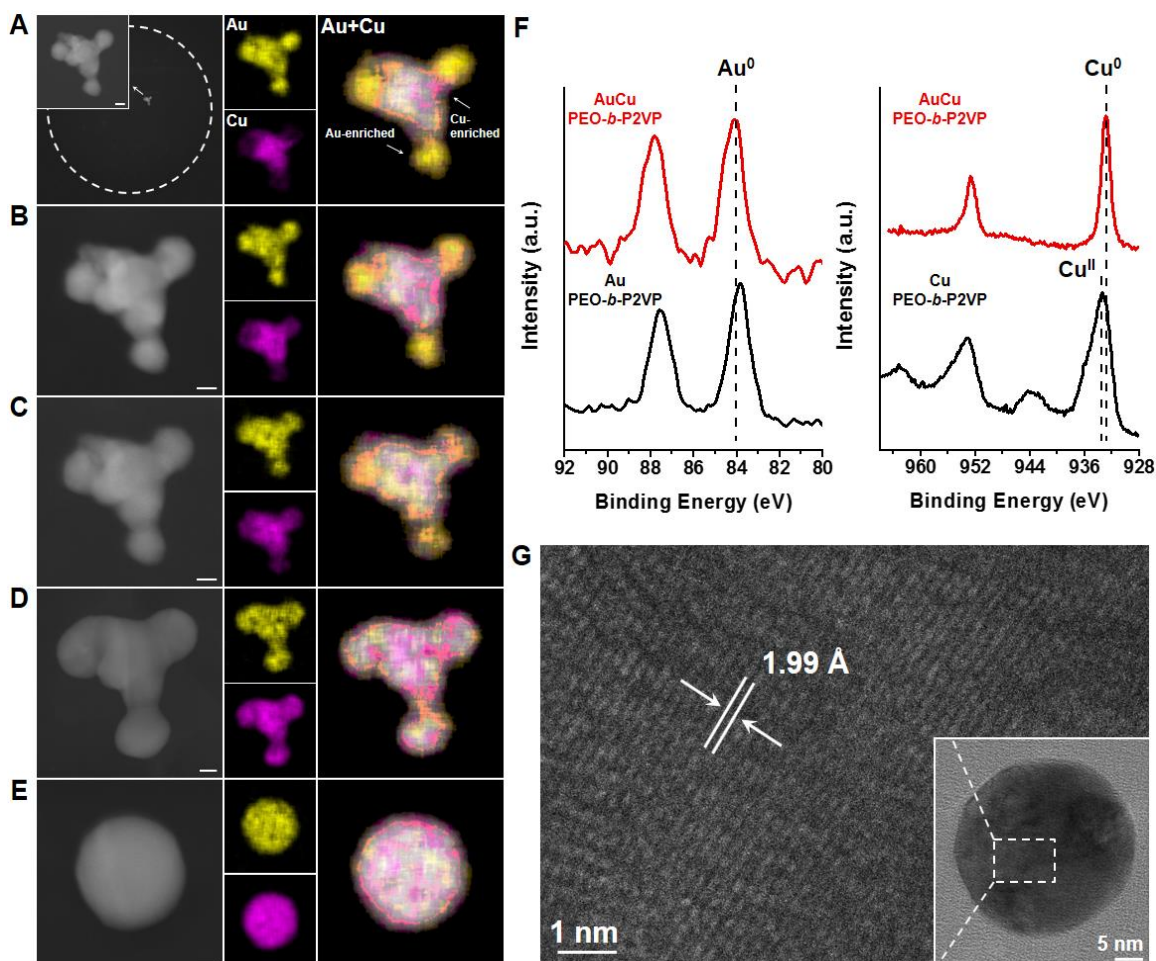


**Figure 3.19** Formation of AuCu nanoparticles in polymer nanoreactors. (A-E) ADF-STEM images and EDS elemental maps of a AuCu particle (44% Au, 56% Cu, atomic composition) formed in a representative polymer feature that contains equal amounts of the metal salt precursors, HAuCl<sub>4</sub> and Cu(NO<sub>3</sub>)<sub>2</sub>. White dashed circles indicate the edge of polymer features. The polymer feature was stepwise annealed at (A) 160 °C under Ar for 4 h, (B) 240 °C under Ar for 2 h, (C) 240 °C under Ar for 2 h, (D) 260 °C under Ar for 2 h, and (E) 500 °C under H<sub>2</sub> for 12 h. Scale bars: 10 nm. (F) Au 4f and Cu 2p XPS spectra of particles synthesized by thermally annealing a drop-cast polymer ink solution at 260 °C for 18 h. Red lines correspond to polymer ink containing both Au and Cu precursors. Black lines correspond to polymer inks containing only one type of precursor. (G) HRTEM image of a AuCu nanoparticle in a polymer feature that is formed by being annealed at 260 °C for 18h. The observed lattice spacing is 1.99 Å (extracted from fast Fourier transform), which closely matches the AuCu alloy (200) plane.

For the final binary combination considered for this study, Ag and Cu are immiscible metals, which results in phase-segregated Ag-Cu heterodimers after high temperature treatment (500 °C). To get a glimpse at how this process works, we initially annealed polymer reactors

containing  $\text{AgNO}_3$  and  $\text{Cu}(\text{NO}_3)_2$  at  $160\text{ }^\circ\text{C}$  for 4 h, the conditions that yielded the AuCu particles in the aforementioned experiment (Figure 3.19A). As evidenced by ADF-STEM images and EDS measurements, only Ag NPs were observed in the reactors (Figures 3.20A and 3.20B). Continuous annealing at  $160\text{ }^\circ\text{C}$  for 18 h results in heterogeneous nucleation or attachment of  $\text{Cu}^{\text{II}}$  clusters onto the Ag cores, as observed by EDS elemental mapping of the particles (Figure 3.20D). The precipitating sequence of Ag followed by Cu is consistent with the monometallic cases (Figure 3.11) because Ag cannot alloy with Cu. XPS characterization validates that Ag cannot facilitate the reduction of  $\text{Cu}^{\text{II}}$  into metallic Cu. The clusters formed around the Ag core particle are composed of  $\text{Cu}^{\text{II}}$  species (Figure 3.20C). Thermal treatment at a higher temperature ( $260\text{ }^\circ\text{C}$ ) is effective in triggering the coarsening (ripening and coalescence) of the  $\text{Cu}^{\text{II}}$  clusters on the surface of the Ag core particle (Figure 3.20E and 3.20F). This intraparticle coarsening process decreases the total surface energy of the  $\text{Cu}^{\text{II}}$  domains as multiple small  $\text{Cu}^{\text{II}}$  clusters are transformed into a single large  $\text{Cu}^{\text{II}}$  cluster on the particle. The resulting Ag- $\text{Cu}^{\text{II}}$  heterodimers can be further transformed into Ag-Cu heterodimers upon subsequent thermal annealing at  $500\text{ }^\circ\text{C}$  under  $\text{H}_2$  (Figure 3.20G, 3.20H, and 3.21). Similar intraparticle coalescence phenomena have been reported in the solution phase synthesis of heterostructured NPs.<sup>199-201</sup> It should be noted that the similarity between nanoreactors made from the same polymer solution ensures that each nanoreactor generates a multimetallic particle through the same process. Due to the different aggregation rates of each element and the random nature of the merging of particles/atoms, kinetic particles made from the same conditions have similar inhomogeneous structures but may vary in morphology (Figure 3.18 and 3.22).

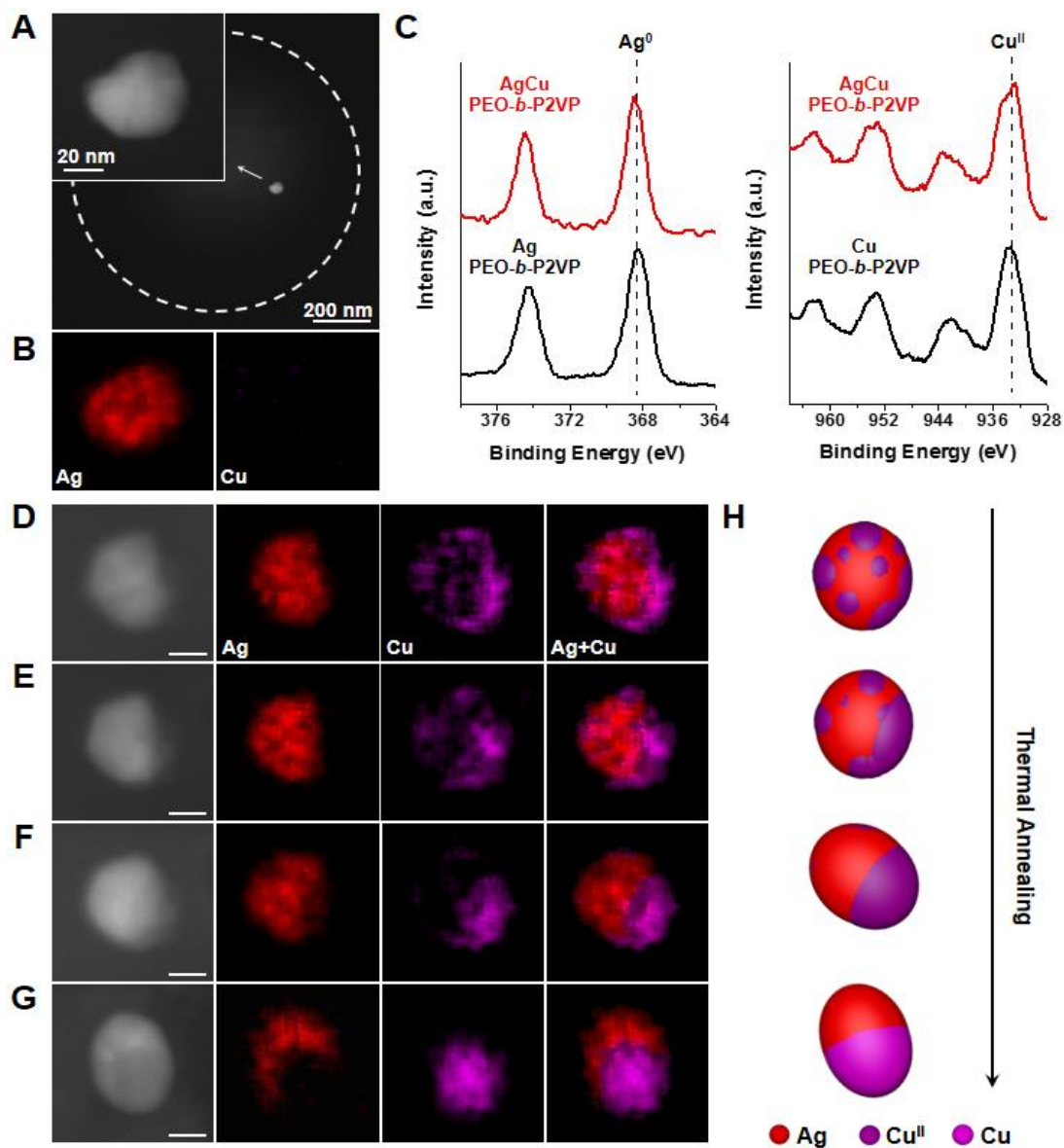


**Figure 3.20** Formation of AgCu nanoparticles in polymer nanoreactors. (A) ADF-STEM images and (B) EDS elemental maps of a particle formed in a representative polymer feature annealed at 160 °C for 4 h that contains equal amounts of the metal salt precursors, AgNO<sub>3</sub> and Cu(NO<sub>3</sub>)<sub>2</sub>. White dashed circles indicate the edge of the polymer feature. (C) Ag 3d and Cu 2p XPS spectra of particles synthesized by thermally annealing a drop-cast polymer ink solution at 260 °C for 18h. Red lines correspond to polymer ink containing both Ag and Cu precursors. Black lines correspond to polymer inks that contain only one type of precursor. (D-G) ADF-STEM images and EDS elemental maps of a AgCu particle (55% Ag, 45% Cu, atomic composition) formed in a representative polymer feature that was stepwise annealed at (D) 160 °C under Ar for 18 h, (E) 260 °C under Ar for 2 h, (F) 260 °C under Ar for 4 h, and (G) 500 °C under H<sub>2</sub> for 12 h. Scale bars: 15 nm. (H) Schematic depicting the structural evolution of AgCu nanoparticles in polymer features during thermal treatment.

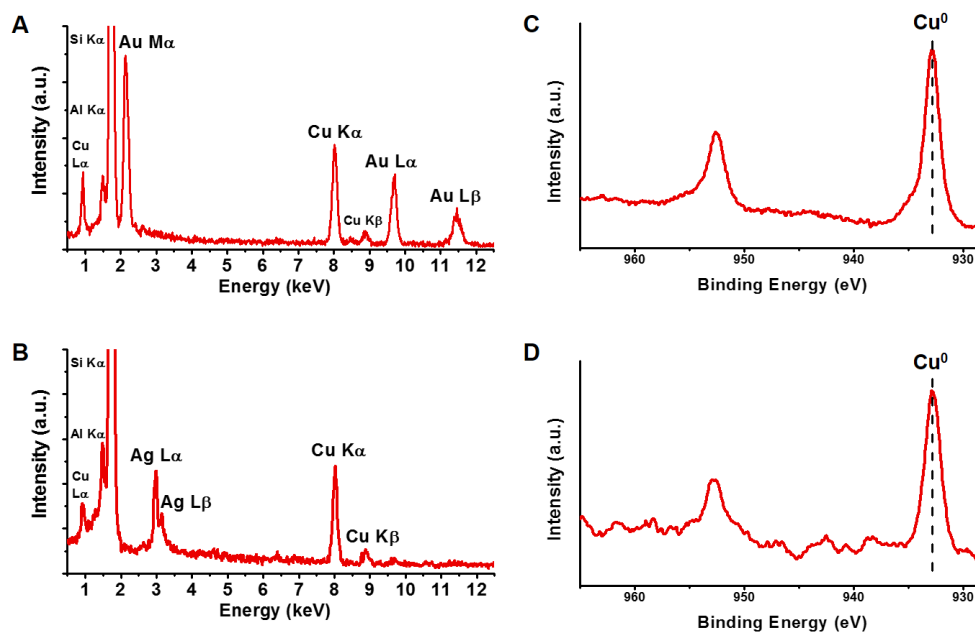


**Figure 3.21** (A,B) EDS spectra of (A) AuCu and (B) AgCu nanoparticles obtained after annealing polymer nanoreactors at 500 °C under H<sub>2</sub> for 12 h to achieve their final structures. Al signals are from the TEM sample holder. (C,D) Cu 2p XPS spectra of (C) AuCu and (D) AgCu particles formed by thermally annealing a drop-cast polymer ink solution at 500 °C under H<sub>2</sub> for 12 h.

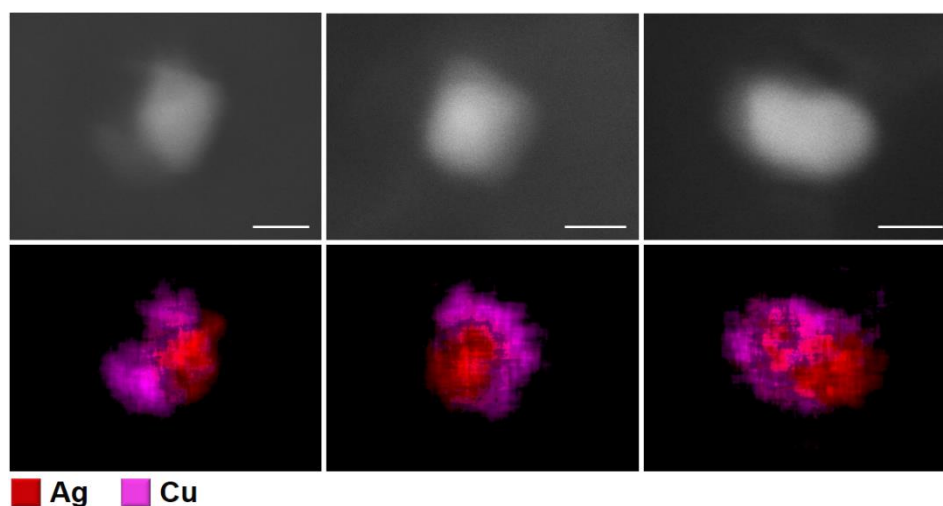


**Figure 3.22** ADF-STEM images and corresponding EDS elemental mapping of representative kinetic AgCu nanoparticles formed in nanoreactors annealed at 160 °C for 18 h and then 260 °C for 2 h. Scale bars: 15nm. Ag aggregates faster and always enriches in the center of the particles while Cu mainly adsorbs on the periphery of the particles. Since the kinetic particles are formed through random aggregation of particles/atoms, the morphology varies from particle to particle.

### 3.4 Aggregation of Three Types of Metal in a Polymer Reactor

The synthesis of multimetallic NPs containing more than two components usually requires delicate control of metal reduction kinetics in order to obtain a desired stoichiometric ratio between constituent metals. By contrast, the composition of SPBCL NP composition is mainly determined by the nanoreactor composition due to the forced aggregation of the metals in the reactor to yield an individual particle. This advantage is particularly useful when studying the formation of trimetallic NPs with target compositions. For example, to reveal the formation mechanism of AuAgCu trimetallic NPs, we annealed polymer reactors containing equal amounts of  $\text{HAuCl}_4$ ,  $\text{AgNO}_3$ , and  $\text{Cu}(\text{NO}_3)_2$  at 260 °C for 0.5h (Figure 3.23).

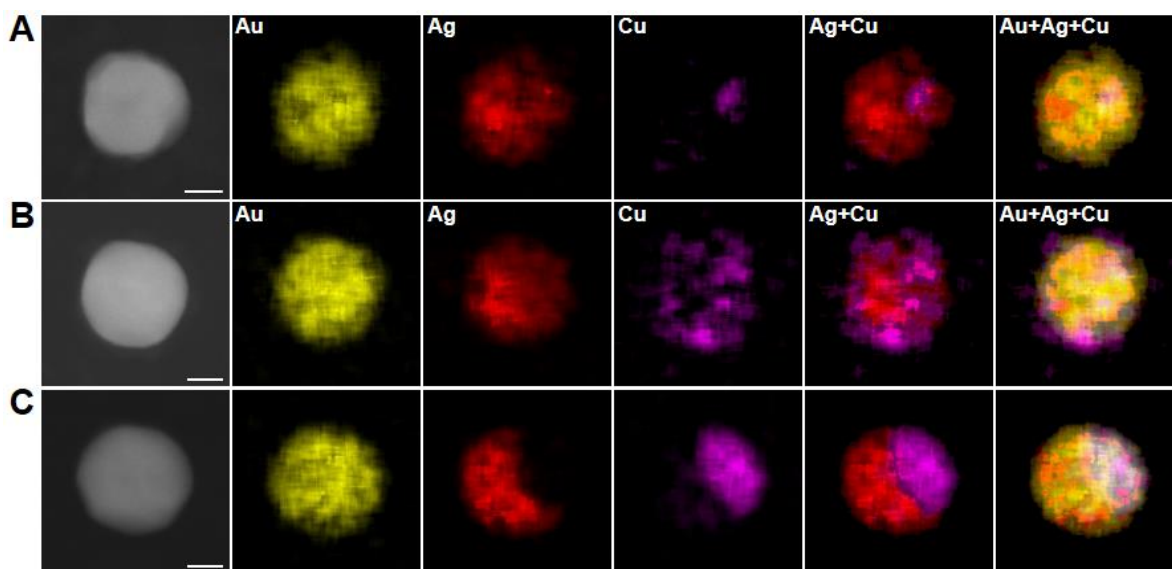


**Figure 3.23** (A-C) ADF-STEM images and EDS elemental maps of particles formed in representative polymer nanoreactors that contain equal amounts of  $\text{HAuCl}_4$ ,  $\text{AgNO}_3$ , and  $\text{Cu}(\text{NO}_3)_2$  precursors. (A) A polymer nanoreactor annealed at 260 °C under Ar for 0.5h, resulting in a particle composed of 48% Au, 43% Ag, and 9% Cu. (B) A polymer nanoreactor annealed at 260 °C under Ar for 4h, resulting in a particle composed of 36% Au, 39% Ag, and 25% Cu. (C) The particle in (B) was further annealed at 500 °C under  $\text{H}_2$  for 12h. Scale bars: 20 nm.

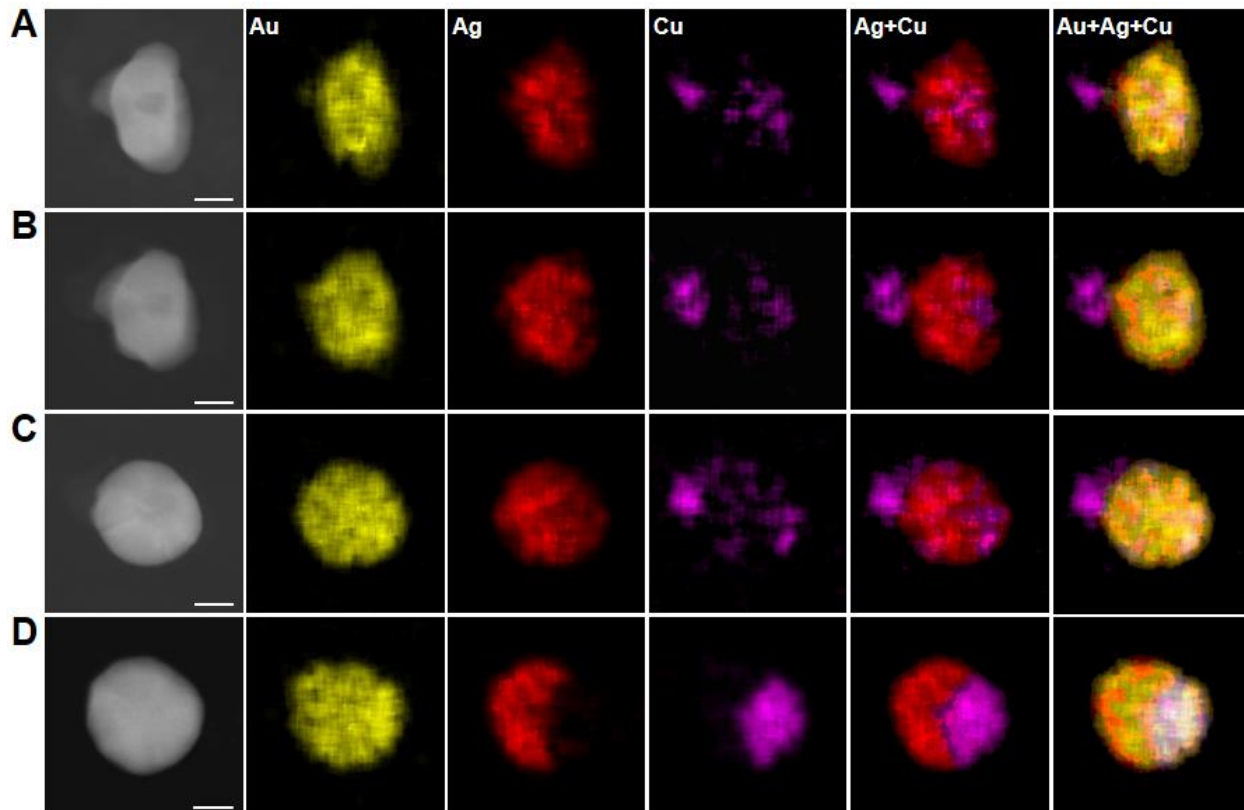


**Figure 3.24** Formation of AuAgCu nanoparticles in polymer nanoreactors. (A-D) ADF-STEM images and EDS elemental maps of a AuAgCu particle (33% Au, 39% Ag, 28% Cu, atomic composition) formed in a representative polymer feature that contains equal amounts of the metal salt precursors,  $\text{HAuCl}_4$ ,  $\text{AgNO}_3$ , and  $\text{Cu}(\text{NO}_3)_2$ . The polymer nanoreactor was stepwise annealed at (A) 260 °C under Ar for 1.5 h, (B) 260 °C under Ar for 2 h, (C) 260 °C under Ar for 3 h, and (D) 500 °C under  $\text{H}_2$  for 12 h. Scale bars: 20 nm.

Through these studies, it is clear that AuAg initially precipitates to form primary particles composed of predominately AuAg alloy and a small amount of AuCu alloy (Figure 3.23). The formation of AuAg primary particles is due to the faster aggregation of Au and Ag than Cu (Figure 3.11). In addition, Ag is not miscible with Cu, which makes the AuAg particle less effective in facilitating the reduction of Cu precursors. With prolonged thermal treatment at 260 °C (1.5 h),  $\text{Cu}^{\text{II}}$  clusters are observed on the fringe of the primary particle through heterogeneous nucleation or attachment of  $\text{Cu}^{\text{II}}$  clusters onto the primary particle (Figure 3.24A, 3.25, and 3.26). After that, the  $\text{Cu}^{\text{II}}$  clusters were reduced and diffuse into the AuAg particle to form a metastable AuAgCu

particle, which contains discrete AuAg grains and AuCu grains, as indicated by EDS measurements (Figure 3.24B, 3.24C, and 3.27).

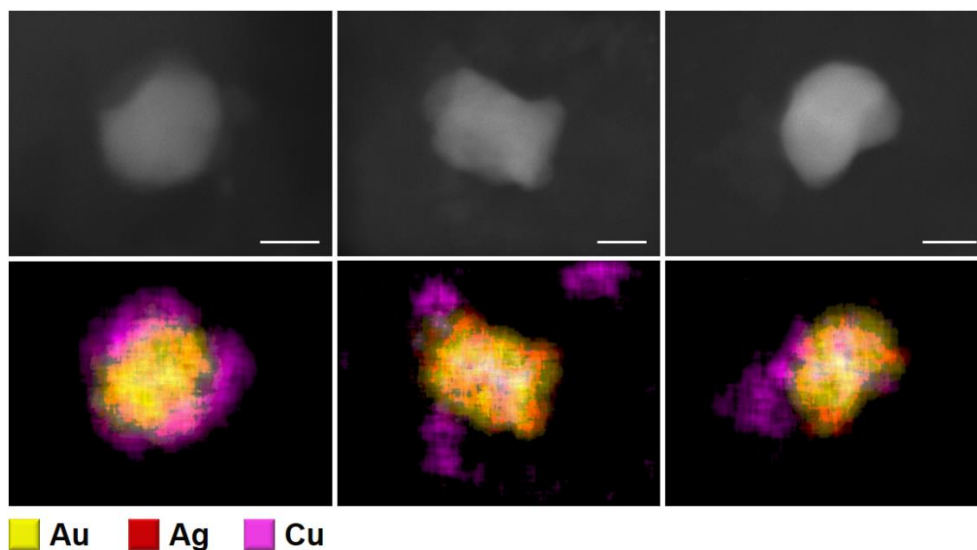


**Figure 3.25** ADF-STEM images and corresponding EDS elemental mapping of representative kinetic AuAgCu nanoparticles formed in nanoreactors annealed at 260 °C for 3 h. Scale bars: 15nm. Au and Ag aggregate faster and always enrich in the center of the particles while Cu mainly localizes on the periphery of the particles.

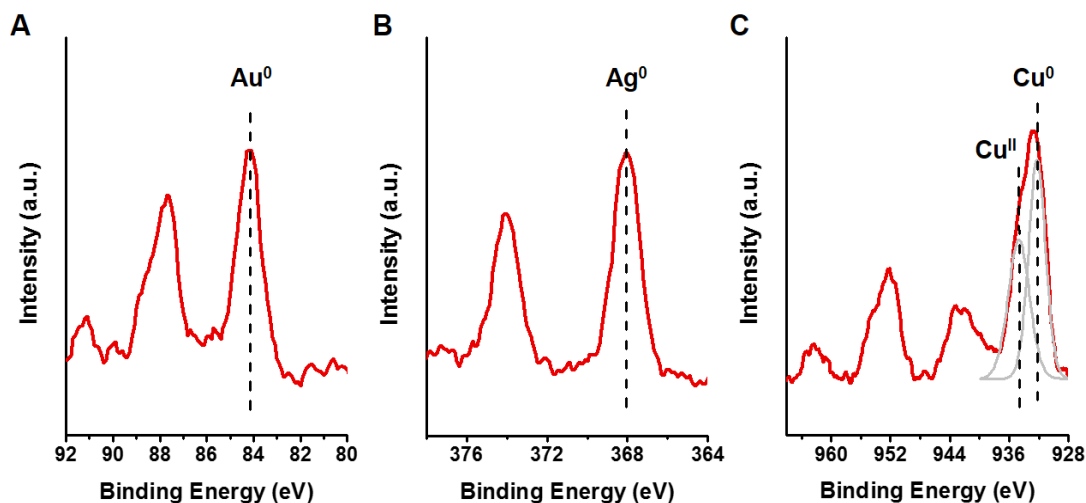


**Figure 3.26** Au 4f, Ag 3d, and Cu 2p XPS spectra of particles formed by thermally annealing a drop-cast polymer ink solution containing equal molar amounts of  $\text{HAuCl}_4$ ,  $\text{AgNO}_3$ , and  $\text{Cu}(\text{NO}_3)_2$  at 260 °C for 2 h. The Au and Ag components in nanoparticles annealed at 260 °C for 2h are in the metallic state while the Cu component is in the  $\text{Cu}^0$  and  $\text{Cu}^{\text{I}}$  states.

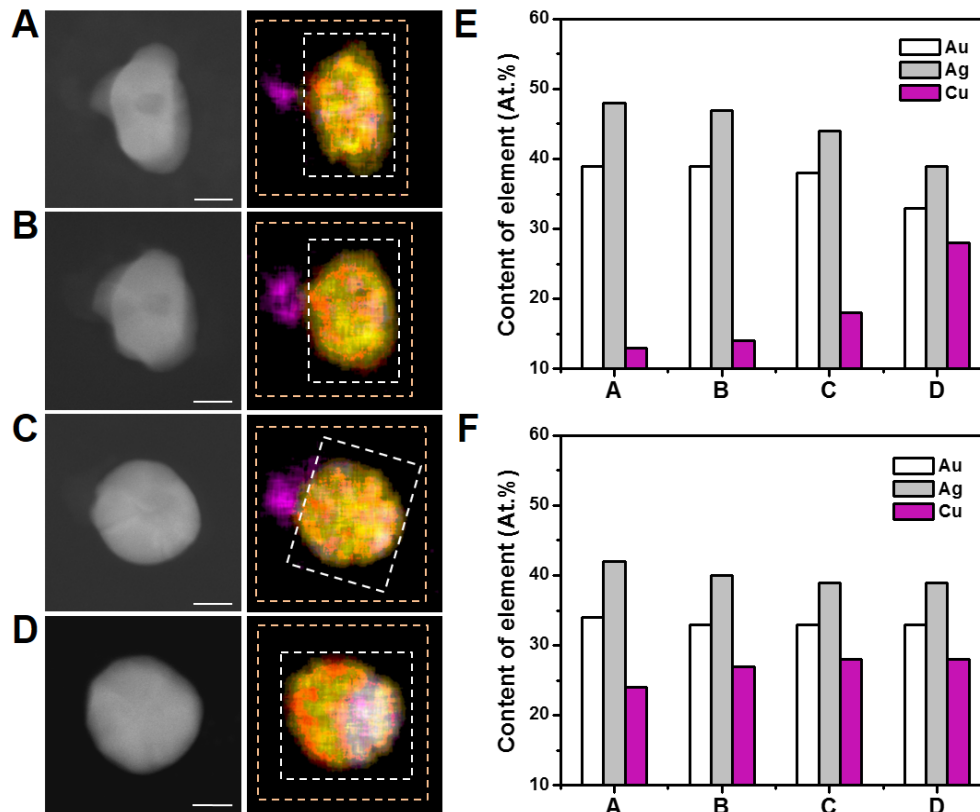


**Figure 3.27** EDS elemental analysis of the AuAgCu particle shown in Figure 3.24. (A-D) ADF-STEM images and EDS elemental maps. The particle was annealed stepwise at 260 °C under Ar for 1.5 h, 260 °C under Ar for 2 h, 260 °C under Ar for 3 h, and 500 °C under H<sub>2</sub> for 12 h. White dashed rectangles in the EDS maps enclose the main part of the particle that excludes the Cu<sup>II</sup> clusters on the fringe. Yellow dashed rectangles enclose the entire particle. Scale bars: 20nm. (E) The composition of the part of the particle within white dashed rectangles. (F) The composition of the entire particle enclosed in the yellow dashed rectangles. From (A) to (D), the content of Cu in the particle (yellow dashed rectangle) changes slightly from 24% to 28%, while the content of Cu in the main portion of the particle (white dashed rectangles) increases from 13% to 28%, suggesting that the Cu<sup>II</sup> clusters on the fringe diffuse into the main part during thermal annealing.

The AuAg grains and AuCu grains are mobile when annealed at 260 °C (Figure 3.24B-3.24D and 3.28), which tend to segregate into a single AuAg domain and a single AuCu domain. Ultimately, when the reactor is annealed at 500 °C under H<sub>2</sub>, the polymer is decomposed and the phase segregation between AuAg and AuCu is completed, generating a AuAgCu heterodimer with one domain being a AuAg alloy and the other one being a AuCu alloy (Figure 3.24D).

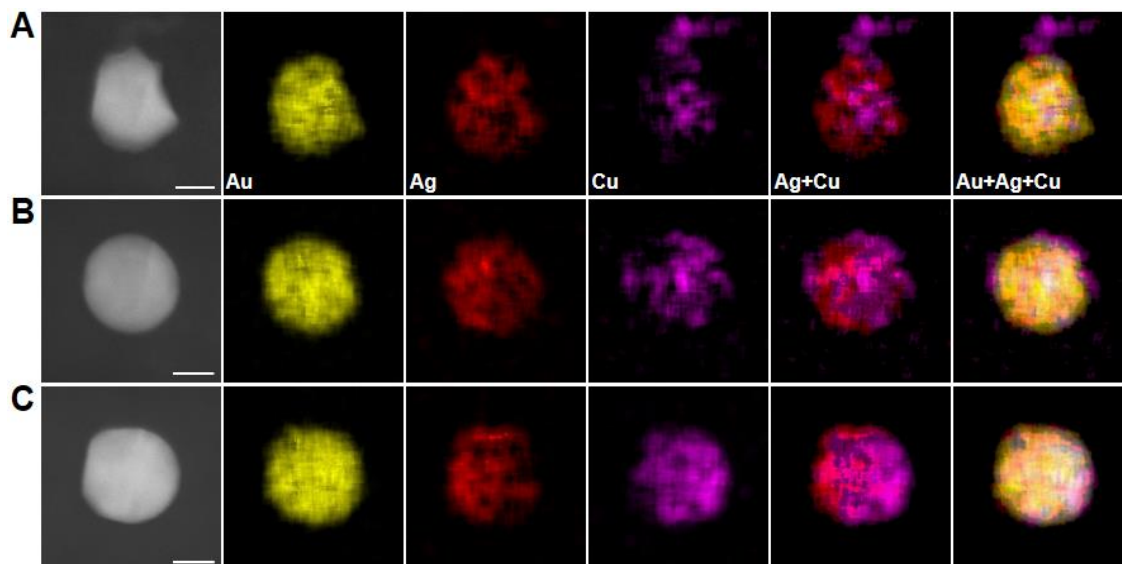


**Figure 3.28** ADF-STEM images and EDS elemental maps of a AuAgCu particle (48% Au, 26% Ag, 26% Cu) formed in a polymer nanoreactor that contains the metal salt precursors,  $\text{HAuCl}_4$ ,  $\text{AgNO}_3$ , and  $\text{Cu}(\text{NO}_3)_2$  (molar ratio 50%:25%:25%), that were stepwise annealed under different conditions: (A) 260 °C under Ar for 4h, (B) 260 °C under Ar for 2h, and (C) 500 °C under  $\text{H}_2$  for 12h. Scale bars: 20 nm.

### 3.5 Materials and Methods

#### 3.5.1 Materials

Poly(ethylene oxide)-*b*-poly(2-vinyl pyridine) (PEO-*b*-P2VP,  $M_n = 2.8$ - $b$ -1.5 kg/mol, polydispersity index = 1.11) was purchased from Polymer Source, Inc. and used as received. Metal compounds,  $\text{HAuCl}_4 \cdot 3\text{H}_2\text{O}$ ,  $\text{AgNO}_3$ , and  $\text{Cu}(\text{NO}_3)_2 \cdot x\text{H}_2\text{O}$  were purchased from Sigma-Aldrich, Inc. and used without further purification. DPN 1D pen arrays (type M, no gold coating) were purchased from Nanoink, Inc. Hexamethyldisilazane (HMDS) was purchased from Sigma-Aldrich. TEM grids with silicon nitride support films ( $\text{Si}_3\text{N}_4$  film thickness = 15 or 50 nm) were purchased from Ted Pella, Inc.

#### 3.5.2 Preparation of Block Copolymer Inks

Polymer inks were prepared by dissolving PEO-*b*-P2VP and different metal compounds in de-ionized water in predetermined molar ratios. The ink solution had a polymer concentration of

5 mg/mL and the molar ratio of pyridyl group to total metal precursors was 64:1. The use of an excess of pyridyl group facilitate a complete complexation of metal ions from the metal precursor salt onto PEO-*b*-P2VP. The pH of the ink solution was adjusted to between 3 and 4 by the addition of HNO<sub>3</sub>. The ink solution was stirred for 24 h at room temperature prior to use.

### *3.5.3 SPBCL Patterning Process*

Hydrophobic TEM grids were obtained by vapor coating the grids with HMDS for 24 h in a desiccator that contained one vial of a HMDS and hexane mixture (1:1, v/v). DPN pen arrays were dip-coated with inks and dried under ambient conditions. Subsequently, the pen arrays were mounted onto an AFM (XE-150, Park Systems) and brought into contact with the hydrophobic TEM grid to deposit arrays of polymer nanoreactors. The patterning process was performed in a chamber at a controlled temperature of 25 °C and relative humidity of 90%. In order to convert polymer features into NPs, the TEM grids were put into a tube furnace and thermally annealed with programmed conditions.

### *3.5.4 Characterization*

Scanning transmission electron microscopy (STEM) characterization of NPs synthesized on TEM grids with 50 nm Si<sub>3</sub>N<sub>4</sub> support films was performed on an in-house designed dual-energy dispersive X-ray spectroscopy (EDS) detector equipped Hitachi HD-2300 dedicated STEM. The dark-field images were taken with an annular dark-field (ADF) detector at an electron acceleration voltage of 200 kV. The detection limit of the size of NPs is around 1 nm. NP composition was studied using the equipped dual EDS detectors (Thermo Scientific) on the HD-2300 STEM with a 200 kV acceleration voltage. The L $\alpha$  peaks of Au and Ag, and the K $\alpha$  peaks of Cu in the EDS spectra were used for elemental mapping and for composition quantification with standardless

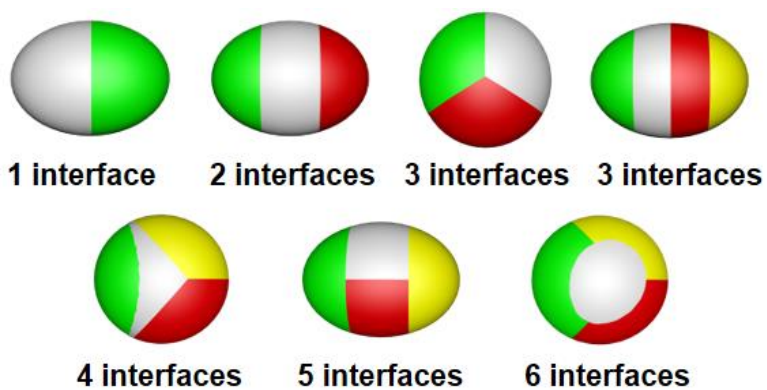
Cliff-Lorimer correction method. The atomic composition measured by EDS has an inherent error of less than 5% due to X-ray absorption and fluorescence. Each EDS map is built based on 30 frames with pixel dimensions of 256×192 and pixel dwell time of 203  $\mu$ s. Thermo Scientific NSS software was used for EDS data processing. High-resolution TEM (HRTEM) images were taken on a JEOL 3200FS transmission electron microscope at an acceleration voltage of 300 kV with NPs prepared on TEM grids with 15 nm Si<sub>3</sub>N<sub>4</sub> support films. X-ray photoelectron spectroscopy (XPS) spectra were recorded on a Thermo Scientific ESCALAB 250Xi with samples made by drop-casting polymer ink solutions, followed by predetermined thermal annealing process.

### **3.6 Conclusions and Outlook**

In summary, the formation processes for multimetallic NPs within PEO-*b*-P2VP polymer nanoreactors were studied with Au, Ag, and Cu salts as model systems. The results contribute to our understanding of NP formation in two important ways. First, it provides insight into the kinetics of NP formation for different metals, and second, it reveals that, for two-component systems in which the metals are miscible (*e.g.*, Au and Cu), the metal that exhibits a faster aggregation rate facilitates the aggregation and reduction of the slower one to form alloy particles; in contrast, immiscible metals (*e.g.*, Ag and Cu) aggregate at rates comparable to those for corresponding single-component systems. Significantly, this understanding of NP formation enables the kinetic trapping of particles with distinct architectures that may otherwise be missed, and such structures may be extremely useful in areas that rely on the emergent properties of NPs, for example, in catalysis, magnetics, plasmonics, and electronics. As this field continues to move towards combinatorial nanoscience, this chapter illustrates that thermal treatment conditions, in addition to particle composition and size, will be an important library parameter.

## CHAPTER FOUR

Heterostructure Engineering in Polyelemental Nanoparticles



DFT calculations were done in collaboration with Mohan Liu and Prof. Chris Wolverton.

## 4.1 Introduction

Phase boundaries or interfaces are important structural features in multi-phase polyelemental nanomaterials.<sup>32,48,202</sup> Indeed, the interfaces in multi-phase nanoparticles (NPs) not only architecturally define them,<sup>15,36</sup> but also introduce structural discontinuity in them,<sup>203</sup> and facilitate electronic interactions between adjacent domains.<sup>27,31</sup> These characteristics make multi-phase NPs useful for applications spanning catalysis,<sup>32,72,202</sup> plasmonics,<sup>12,13</sup> electronic devices,<sup>15</sup> targeted drug delivery,<sup>18</sup> and bio-imaging.<sup>20,36</sup> For example, in the case of plasmonic and catalytic NPs, the charge transfer occurring across an interface can be utilized to tune the properties of one material domain with a neighboring one.<sup>13,22,24</sup> In addition, strain engineering provides a way to modulate the electronic structure of materials when the nearby phases are epitaxial.<sup>204</sup> Such synergistic effects<sup>71,79</sup> are also observed in catalysis where the interface between two domains may be rich in high-energy defects.<sup>202,205</sup> Finally, a single NP with multiple interfaces can exhibit collective properties that are not observed in particles comprised of the individual components (both composition and number and types of interfaces).<sup>38,39</sup> As the field of multi-phase, polyelemental NPs progresses towards higher compositional diversity and structural complexity,<sup>32,48,126,133,164</sup> understanding how specific classes of interfaces can be established in one particle is crucial for designing novel and functional nanostructures. To date, NPs have been synthesized and characterized with up to four phases,<sup>32,46-48,114,117,120,206</sup> and while such studies have identified unique architectures, there is limited general understanding for why specific ones form, and the role of surface/interfacial energy in controlling the architecture of NPs with more than two phases is not fully understood. Indeed, the interfacial energy in multi-phase NPs will be highly dependent on the composition of the domains, the electronic interactions between the

domains, the coherence of the interfacial lattice structure, and the influence of defects such as dislocations, all of which may vary dramatically among different systems.<sup>36,45-48,114,117,120,206,207</sup>

Scanning probe block copolymer lithography (SPBCL), which uses lithographically defined polymer domes as nanoreactors to synthesize multimetallic NPs with broad material choices, allows one to study polyelemental systems of unprecedented complexity. Since the positions of NPs in an SPBCL experiment are spatially controlled, the NPs can be heated to reach thermodynamic architectures while avoiding coarsening between neighboring NPs. Therefore, SPBCL allows one to study multi-phase NPs at the single NP level on substrates that are amenable to thermal annealing and electron microscopy characterization. In this chapter, we utilize SPBCL in combination with density functional theory (DFT) calculations to understand the principles of interface arrangement in multi-phase NPs. From these studies, we identify unexpected miscibility gaps between PdSn alloys and other metals (Au, Ag, Cu, Co, and Ni), that are used to construct a library of compositionally and structurally-related multi-phase NPs. Based on the architecture of the resulting NPs, we establish design rules for synthesizing polyelemental heterostructures with increasing complexity, culminating in an unprecedented tetra-phase NP made from Au, Co, Pd, Sn, and Ni with six phase boundaries.

#### 4.2 Number of Possible Interfaces in Multi-Phase Nanoparticles

*Observation 1: For a polyelemental nanoparticle with  $n$ -phases, the number of possible interfaces*

*is between  $n-1$  and  $\binom{n}{2}$ ;  $\binom{n}{2} = \frac{n(n-1)}{2}$ .*

If one considers kinetic particles, multi-phase NPs have an almost unlimited number of possible architectures, even within particles with a fixed composition and size.<sup>32,45-47,114,126</sup> However, as particles reconfigure to decrease total surface and interfacial energies through the

migration of atoms/domains,<sup>46,47,200,201</sup> kinetically-trapped multi-phase NPs will transform into thermodynamic or close to thermodynamic architectures, once enough energy has been provided to trigger this process. Here, we only consider thermodynamic architectures of heterostructured NPs. Core-shell structures are not considered because they are not experimentally observed.

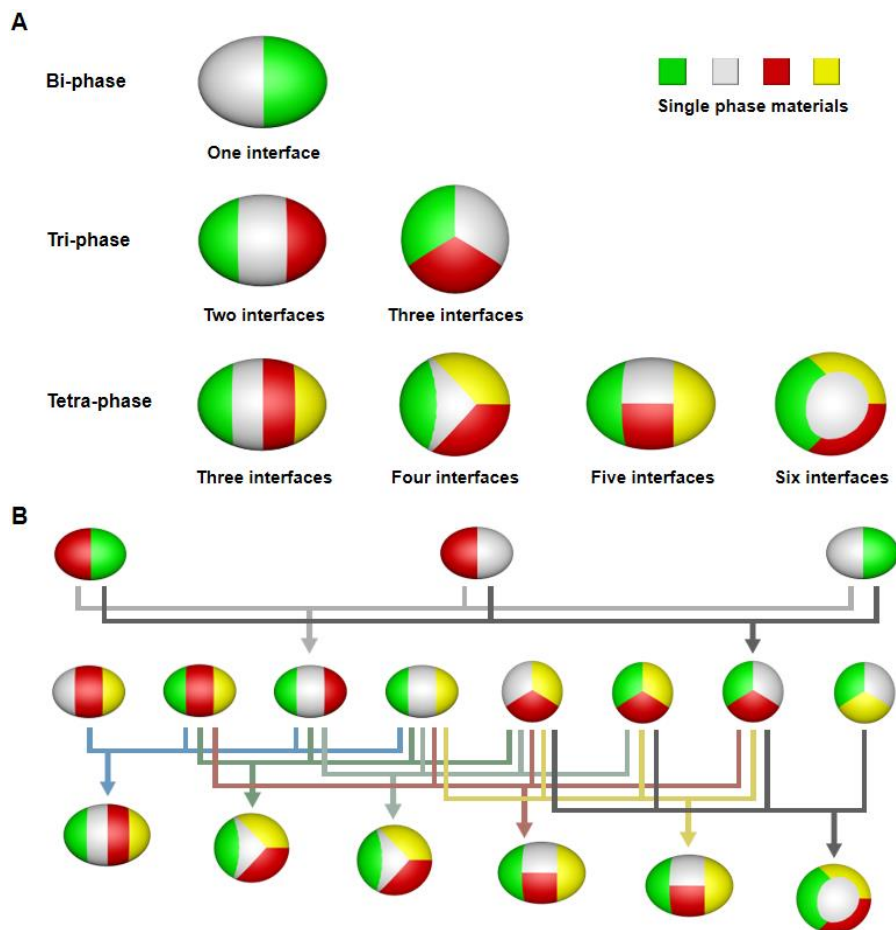


**Figure 4.1** Configuration of interfaces in multi-phase nanoparticles. (A) Theoretically possible number of interfaces in heterodimer, heterotrimer, and heterotetramer NPs. All of these NP architectures are observed and characterized in this work except for the striped tetra-phase structure with three interfaces. (B) The relationship between the architecture of bi-, tri-, and tetra-phase NPs.

For a  $n$ -phase NP, the maximum number of different interfaces is  $\binom{n}{2}$ , which occurs if all phases can be interconnected. Since the  $n$  phases must be part of a single NP, the minimum number of interfaces is  $(n-1)$ , which occurs when the  $n$  phases form a striped layered structure, with each

stripe defining a different phase (Figure 4.1A). Therefore, bi-phase heterostructured NPs have one type of architecture, *i.e.*, a heterodimer with one interface. Tri-phase NPs will have two types of architectures: one is a striped heterotrimer with two interfaces while the other is a pie-shaped structure consisting of three interfaces (Figure 4.1A). For tetra-phase NPs, the number of possible interfaces within a single NP varies from three to six. Based upon this hypothesis and constraint, Figure 4.1 depicts the proposed architecture of all possible bi-phase, tri-phase, and tetra-phase heterostructured NPs, and the proposed relationship between lower and higher order structures.

In order to experimentally validate that these combinations of interfaces exist, it is essential that one create multi-phase NPs that include all possible architectures. Herein we report a systematic study of a septenary system, consisting of particles containing combinations of Au, Ag, Cu, Co, Ni, Pd, and Sn, resulting in a new set of NPs with as many as four phases. According to bulk phase diagrams, Pd and Sn are miscible with the other five elements, forming either solid solutions or intermetallics.<sup>190</sup> However, when we combined three elements consisting of AuPdSn or CoPdSn, respectively, into one NP and annealed under H<sub>2</sub> at 500 °C for 24 h, heterodimers with PdSn domains and Au or Co domains, respectively, were obtained (Figure 4.2 and 4.3). This is a surprising result since any pair of two elements in the combination studied are miscible with one another.<sup>190</sup> Annular dark field scanning transmission electron microscopy (ADF-STEM) images of Au-PdSn and Co-PdSn NPs (here a “-” is used to separate different phases, Table 4.1) clearly show dimeric structures with the contrast mainly from the difference in atomic number between PdSn and Au, or between PdSn and Co. Energy dispersive X-ray spectroscopy (EDS) analysis further verifies the separation of the elements in Au-PdSn and Co-PdSn heterodimers (Figure 4.3).

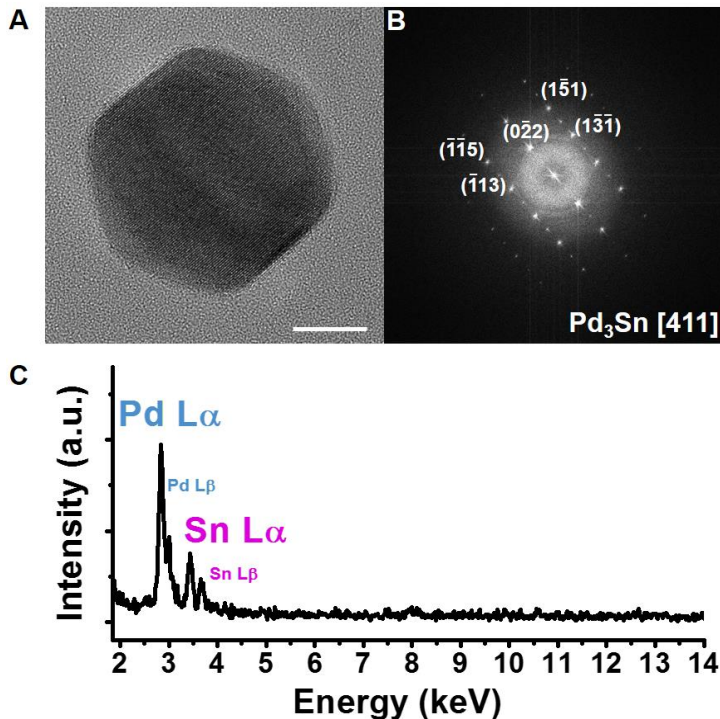


**Figure 4.2** (A) HRTEM image of a representative Pd<sub>0.75</sub>Sn<sub>0.25</sub> nanoparticle synthesized in a polymer nanoreactor (scale bar, 5 nm). (B) Fast Fourier transform (FFT) and (C) EDS spectrum of the nanoparticle in (A) indicate that the nanoparticle possesses a Pd<sub>3</sub>Sn intermetallic structure.

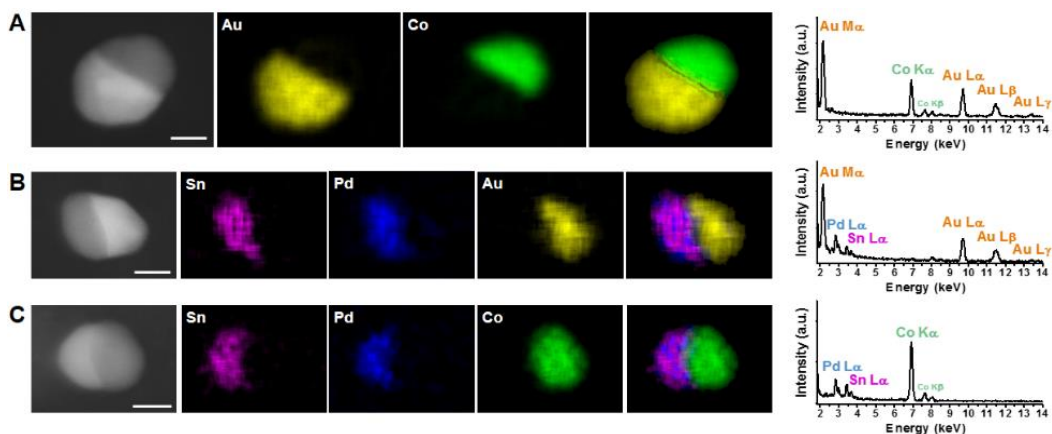


**Figure 4.3** ADF-STEM images, EDS elemental mapping, and EDS spectra of (A) Au-Co (Au<sub>0.5</sub>Co<sub>0.5</sub>), (B) Au-PdSn (Au<sub>0.57</sub>Pd<sub>0.27</sub>Sn<sub>0.16</sub>), and (C) Co-PdSn (Co<sub>0.66</sub>Pd<sub>0.17</sub>Sn<sub>0.17</sub>) heterostructured nanoparticles synthesized in polymer nanoreactors (Scale bars, 20 nm). The Cu K $\alpha$  signals at 8.0 keV in the EDS spectra are from the TEM sample holder.

Denotation	Phases
Au	Au
Ag	Ag
Cu	Cu <sub>0.92</sub> Pd <sub>0.08</sub> (average composition)
Co	Co
NiSn	NiSn alloy
AuAg	AuAg alloy
AuCu	AuCu alloy
CoNi	CoNi alloy
CuNi	CuNi alloy
PdSn (NP does not contain Cu or Ni)	PdSn alloy
PdSn (NP contains Cu)	(PdSn) <sub>0.8</sub> Cu <sub>0.2</sub> (average composition)
PdSn (NP contains Ni)	(PdSn) <sub>0.92</sub> Ni <sub>0.08</sub> (average composition)
PdSn (NP contains Cu and Ni)	(PdSn) <sub>0.8</sub> (CuNi) <sub>0.2</sub> (average composition)

**Table 4.1** Material phases for the nanoparticles. For simplicity, the main elements (content > 80%) of one material phase are used to denote that phase. Different phases in a nanoparticle are separate by “-”. For example, Au-Co-PdSn means a tri-phase nanoparticle with a Au domain, a Co domain, and a PdSn domain.

To understand why this unexpected phase separation was observed, we utilized DFT calculations of the formation energies ( $\Delta H_f$ ) of all known compounds (including unary, binary, and ternary) in the AuPdSn and CoPdSn systems, which are from the Open Quantum Materials Database (OQMD, Table 4.2).<sup>208,209</sup> OQMD is a high-throughput database (oqmd.org) consisting of >500,000 density functional theory (DFT) total energy calculations of compounds from the Inorganic Crystal Structure Database (ICSD) and decorations of commonly occurring crystal structures. Based on the  $\Delta H_f$  of all compounds from OQMD, we computed the energetics of all phases as well as all linear combinations of phases for a given composition, evaluated using the Grand Canonical Linear Programming (GCLP) method.<sup>210</sup> This GCLP calculation allows us to

determine the thermodynamic ground state phase, or collection of phases, stable for a given composition with an arbitrary number of components. In the formalism, the grand potential of a collection of phases is most generally expressed by

$$\Phi(\vec{\mu}, \vec{x}, T, P) = \sum_i x_i G_i(T, P) - \sum_j (\mu_j \sum_i x_i \bar{C}_{i,j})$$

where  $\vec{x}$  is a vector containing the relative amount of each compound,  $G_i(T, P)$  is the Gibbs free energy of compound  $i$  at a given temperature and pressure,  $\vec{\mu}$  is the chemical potential of each element  $j$ , and  $\bar{C}_{i,j}$  is a composition matrix. We find the ground state composition by minimizing  $\Phi$  with respect to  $\vec{x}$ . To determine the stable phases for a certain elemental composition, we apply a constraint such that the amount of each element is equal to that of the initial composition,  $\vec{z}_0$ . The constraint is simply given by:

$$z_j^0 = \sum_i \bar{C}_{i,j} x_i$$

Since the grand potential is linear in  $\vec{x}$  and so is the constraint  $\vec{z}_0$  we can call on highly efficient linear programming techniques to minimize the free energy. Using this GCLP method, we are able to determine stable phases for AuPdSn, CoPdSn, AuCoPdSn, AgPdSn, CuPdSn, and NiPdSn systems. For each system, we have considered formation energies for all compounds in the given phase region from OQMD. The number of compounds we considered for different systems are shown in Table 4.2. In this work, we determined the free energies of formation at 0 K and 0 Pa, *i.e.*,  $G_i(0, 0)$ , which are simply the formation energies of the compounds ( $\Delta H_f$ ). To be consistent with experimental setups, we set the initial composition for each element to be the same. The results of GCLP analysis are tabulated in Table 4.2.

System	Stable phases	$\Delta H_f$ (eV/atom)	Number of compounds evaluated
AuPdSn	33% Au, 67% PdSn	-0.386	25
CoPdSn	33% Co, 67% PdSn	-0.386	24
AuCoPdSn	25% Au, 25% Co, 50% PdSn	-0.289	55
AgPdSn	33% Ag, 67% PdSn	-0.386	20
CuPdSn	33% Cu, 67% PdSn	-0.386	26
NiPdSn	28% Ni <sub>3</sub> Sn <sub>2</sub> , 22% Ni <sub>3</sub> Sn, 50% Pd <sub>2</sub> Sn	-0.424	25

**Table 4.2** Grand canonical linear programming (GCLP) analysis of AuPdSn, CoPdSn, AuCoPdSn, AgPdSn, CuPdSn, and NiPdSn systems with equal content of every element in each system.

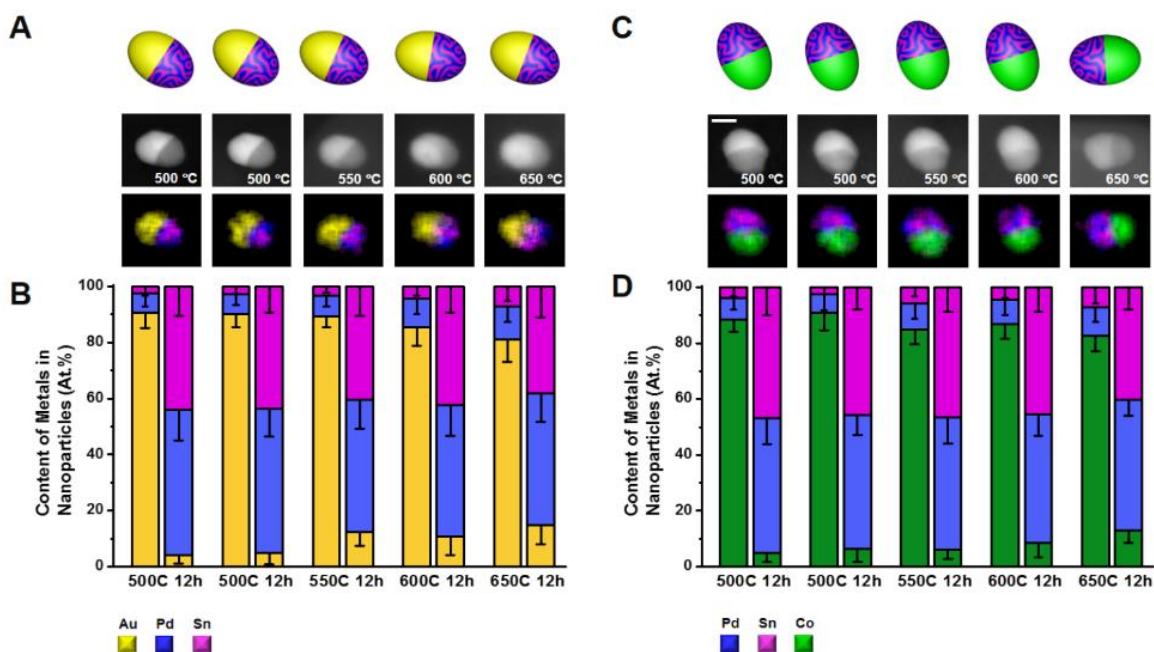


**Figure 4.4** Stability test of (A,B) Au-PdSn and (C,D) Co-PdSn heterodimers subjected to thermal annealing. The particles were heated under H<sub>2</sub> at different conditions and quickly cooled down to ambient temperature in 0.5 h. (A) and (C) show schematic illustration, ADF-STEM images, and EDS mapping of a typical Au-PdSn nanoparticle and a typical Co-PdSn nanoparticle after each annealing step. Scale bar, 20 nm. (B) and (D) show the composition variation of each domain in Au-PdSn and Co-PdSn heterodimers after thermal treatment. The results are calculated based on composition tracking of 15 particles for each type of heterodimer.

For an equal mixture of either Au or Co with Pd and Sn, we identified that the stable phases are PdSn and either Au or Co (*i.e.*, X-PdSn, X = Au or Co). To verify the simulation, we examined

the thermal stability of the Au-PdSn and Co-PdSn heterodimers by heating the NPs to temperatures between 500 and 750 °C (Figure 4.4 and 4.5), with the upper end of the range close to the melting temperature of bulk Au (1064 °C) and far beyond that of bulk Sn (232 °C). Experimentally, the NPs are stable after being heated for more than 2 days. When the annealing temperature is further increased to 800 °C, the morphology of the NPs transforms from an ellipsoid to an irregular shape. Sn-enriched branches were formed on the PdSn semi-ellipsoidal domain (Figure 4.5, 800 °C 12 h). due to the leaching of Sn from the NPs. Nevertheless, we did not observe alloying between Au and PdSn or between Co and PdSn, corroborating the simulation that PdSn phase-segregates with Au or Co. Given the low miscibility between Au and Co (Figure 4.3A), PdSn, Au, and Co constitute a new set of building blocks for constructing higher-order heterostructured NPs.

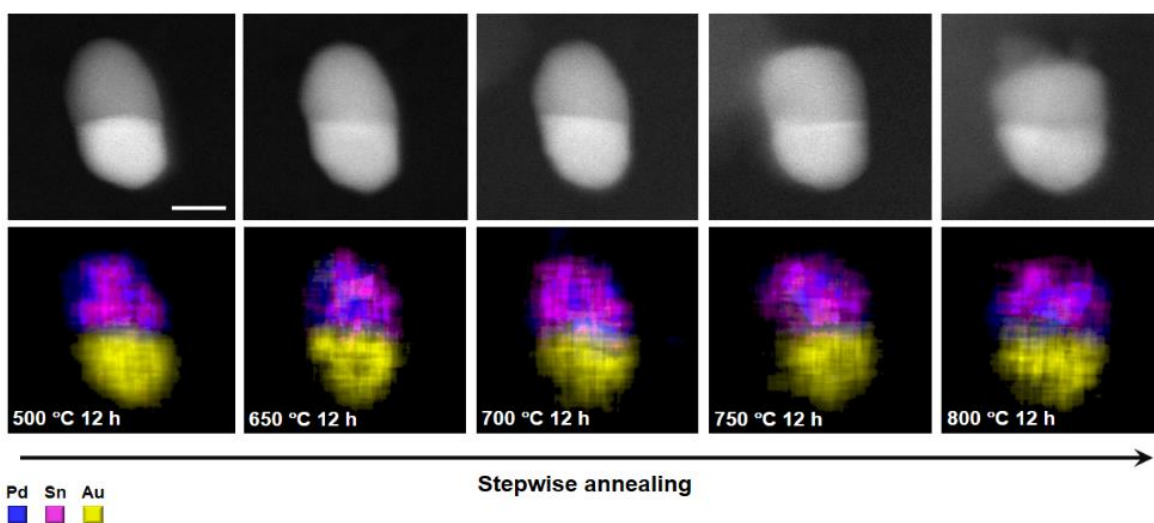


**Figure 4.5** ADF-STEM images and corresponding EDS elemental mapping of a Au-PdSn heterodimer thermally annealed at increasing temperatures. Scale bar, 20 nm.

### 4.3 Tri-Phase Nanoparticles with Two or Three Interfaces

*Observation 2: Bi-phase structures cannot be used to predict the architecture of structures with three or more phases.*

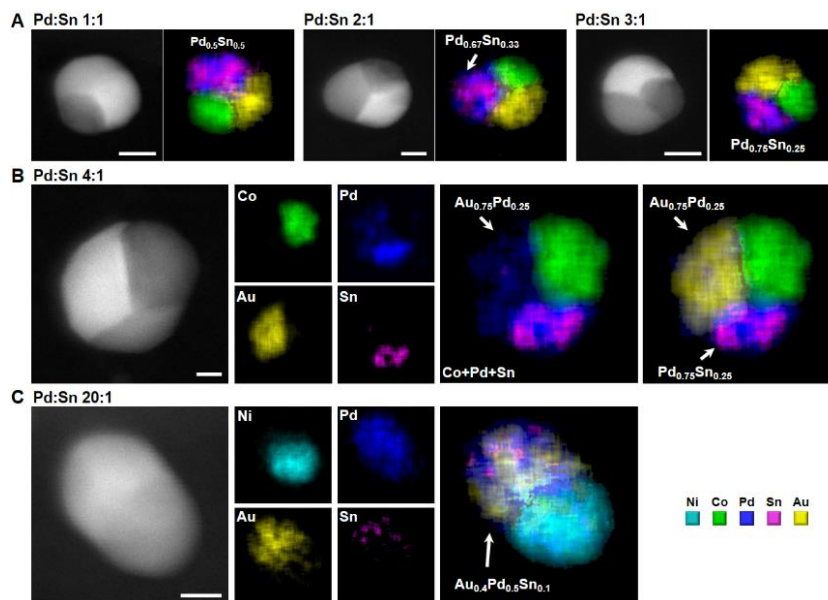


**Figure 4.6** (A,B) ADF-STEM images and corresponding EDS characterization of AuCoPdSn nanoparticles with different molar ratios between Pd and Sn (Pd:Sn = 1:1,  $\text{Au}_{0.24}\text{Co}_{0.27}\text{Pd}_{0.24}\text{Sn}_{0.25}$ ; Pd:Sn = 2:1,  $\text{Au}_{0.30}\text{Co}_{0.26}\text{Pd}_{0.30}\text{Sn}_{0.14}$ ; Pd:Sn = 3:1,  $\text{Au}_{0.30}\text{Co}_{0.29}\text{Pd}_{0.30}\text{Sn}_{0.11}$ ; and Pd:Sn = 4:1,  $\text{Au}_{0.38}\text{Co}_{0.33}\text{Pd}_{0.23}\text{Sn}_{0.06}$ ). The Pd:Sn ratios of each particle are noted above the STEM images. (C) ADF-STEM image and EDS mapping of a AuNiPdSn nanoparticle with Pd:Sn = 20:1 ( $\text{Au}_{0.18}\text{Ni}_{0.38}\text{Pd}_{0.42}\text{Sn}_{0.02}$ ). Scale bars, 20 nm.

For tri-phase NPs, there are two possible types of architectures, *i.e.*, ones with either two or three interfaces (Figure 4.1B). For example, with four element Au-Co-PdSn NPs synthesized by SPBCL, EDS mapping confirms element separation into three interconnected domains, a Au (yellow), Co (green), and PdSn domain (blue/purple, consisting of a compositional variation; *e.g.*,  $\text{Pd}_3\text{Sn}$ ,  $\text{Pd}_2\text{Sn}$ , or  $\text{PdSn}$ , Figure 4.6, 4.7A-4.7G, and 4.8). According to the DFT calculations, all PdSn phases ( $\text{Pd}_3\text{Sn}$ ,  $\text{Pd}_2\text{Sn}$ ,  $\text{PdSn}$ ,  $\text{PdSn}_2$ ,  $\text{PdSn}_3$ , and  $\text{PdSn}_4$ ) should segregate with the other five metals. Experimentally, we found that PdSn domains segregate with other metals when the molar ratio of Pd:Sn is less than or equal to 3:1 (Figure 4.6A), which is consistent with DFT predictions. When the molar ratio of Pd:Sn is increased to 4:1,  $\text{Pd}_3\text{Sn}$  remains an individual domain while the excess amount of Pd diffuses into other metal domains (Figure 4.6B). When the molar ratio of Pd:Sn is further increased to 20:1, phase segregation between PdSn and other metals is no longer

observable (Figure 4.6C). The STEM image contrast between the three domains in a Au-Co-PdSn NP is attributed to differences in atomic number (Figure 4.7A). The orientation of the phase boundaries in the tri-phase NPs is random with respect to the substrate (*i.e.*, the image plane, Figure 4.9). For simplicity, particles with phase boundaries perpendicular to the substrate are used to clearly show the position of different phases.

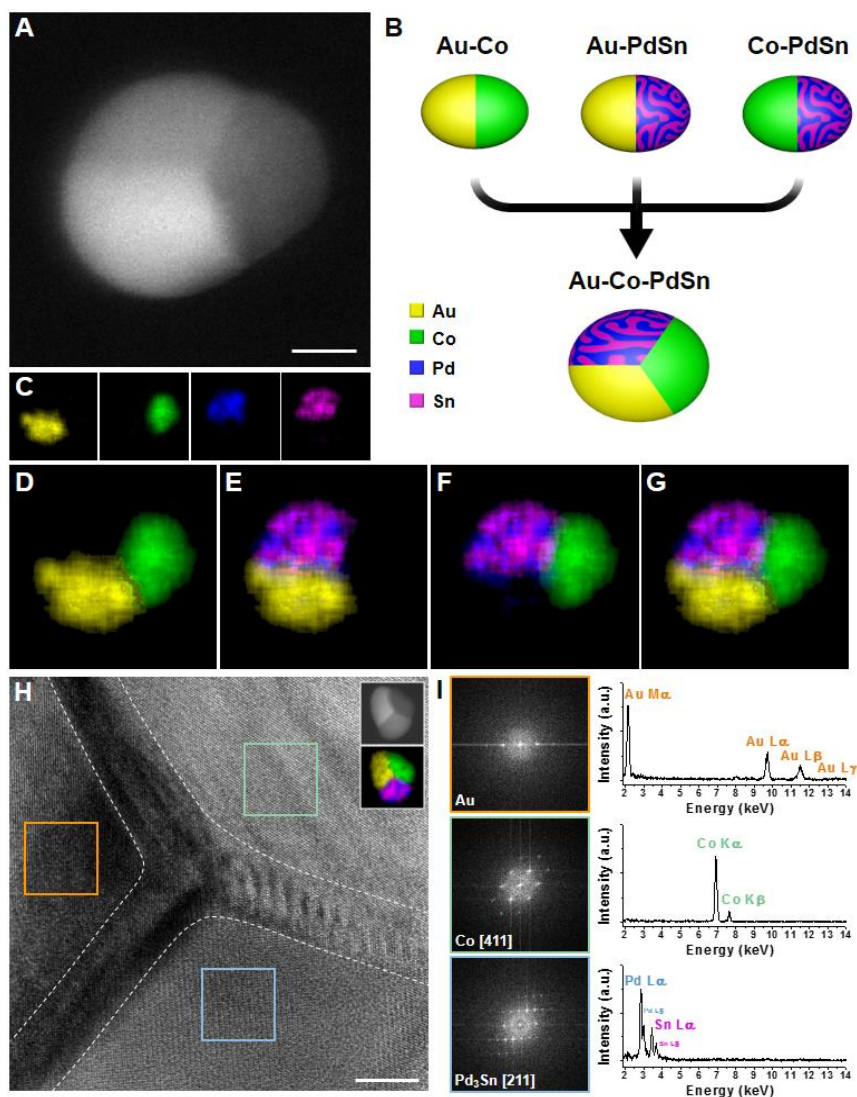


**Figure 4.7** Au-Co-PdSn tri-phase heterostructured nanoparticles with three interconnected interfaces. (A) ADF-STEM image of a representative Au-Co-PdSn NP ( $\text{Au}_{0.30}\text{Co}_{0.37}\text{Pd}_{0.19}\text{Sn}_{0.14}$ , scale bar, 10 nm). (B) Schematic illustration of the miscibility relationship between the Au, Co, and PdSn phases. (C-F) EDS elemental mapping of the NP in (A). Overlay of selected element

maps shows the phase boundaries of (D) Au-Co, (E) Au-PdSn, and (F) Co-PdSn. (G) Overlay of all element maps showing the configuration of the three phase boundaries in a Au-Co-PdSn NP. (H) HRTEM image of the tri-phase junction in a Au-Co-PdSn NP ( $\text{Au}_{0.25}\text{Co}_{0.36}\text{Pd}_{0.29}\text{Sn}_{0.10}$ , scale bar, 3nm). Dashed lines highlight the position of the three phase boundaries. Insets are an ADF-STEM image and EDS mapping of the entire NP. (I) left column: FFT of the regions indicated in (H). right column: EDS spectra of the Au, Co, and PdSn domains of the NP in (H).

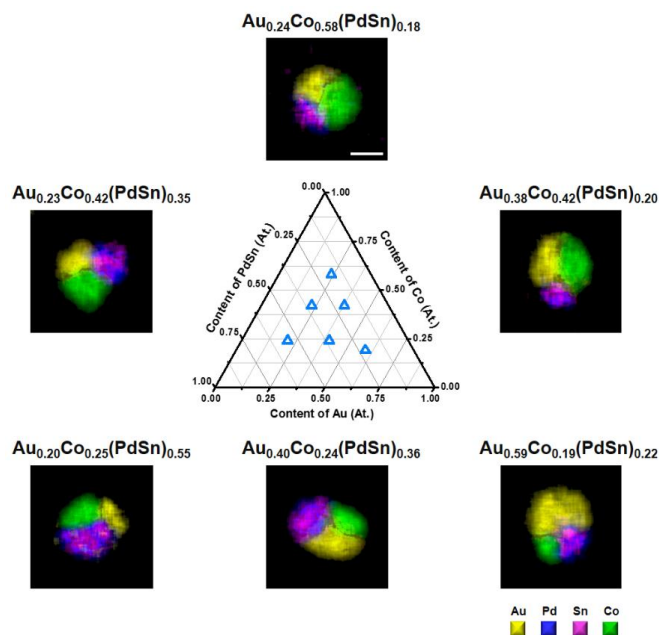


**Figure 4.8** EDS characterization of Au-Co-PdSn nanoparticles with different compositions. The molar ratio of Pd:Sn is approximately 1:1 in each nanoparticle. The varying content of Au, Co, and PdSn only changes the size of each domain in the particles. All the particles possess the same architecture with three interconnected phase boundaries. Scale bar: 20 nm.

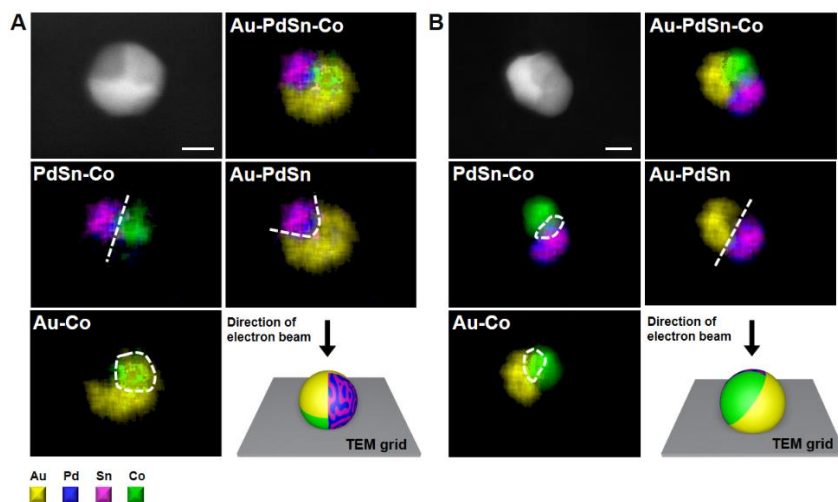


**Figure 4.9** ADF-STEM images and EDS elemental mapping of Au-Co-PdSn nanoparticles whose

interfaces are not all perpendicular to the image plane. Dashed lines/circles in the overlay of selected element maps highlight the position of interfaces as a guide to the eye. Scale bars, 15 nm. (A)  $\text{Au}_{0.57}\text{Co}_{0.17}\text{Pd}_{0.16}\text{Sn}_{0.10}$ , Au-PdSn and Co-PdSn interfaces are perpendicular to the image plane while Au-Co interface is inclined/parallel with the image plane. Scheme depicts the proposed structure of this particle. (B)  $\text{Au}_{0.33}\text{Co}_{0.34}\text{Pd}_{0.18}\text{Sn}_{0.15}$ , Au-PdSn interface is perpendicular to the image plane while Co-PdSn and Au-Co interfaces are inclined with the image plane. Scheme depicts the proposed structure of this particle.

High resolution transmission electron microscopy (HRTEM) characterization of a tri-phase junction in a Au-Co-Pd<sub>3</sub>Sn NP confirms the formation of solid-state interfaces between three domains (Figure 4.7H). Fast Fourier transformations (FFT) of different regions indicate that Co is oriented along the [411] zone axis, and Pd<sub>3</sub>Sn is oriented along the [211] zone axis (Figure 4.7I). The FFT of the Au domain only shows reflections that can be assigned to Au {311} planes. Experimentally, no specific relationship between the lattice structures of the three domains was observed (Figure 4.10-4.14).

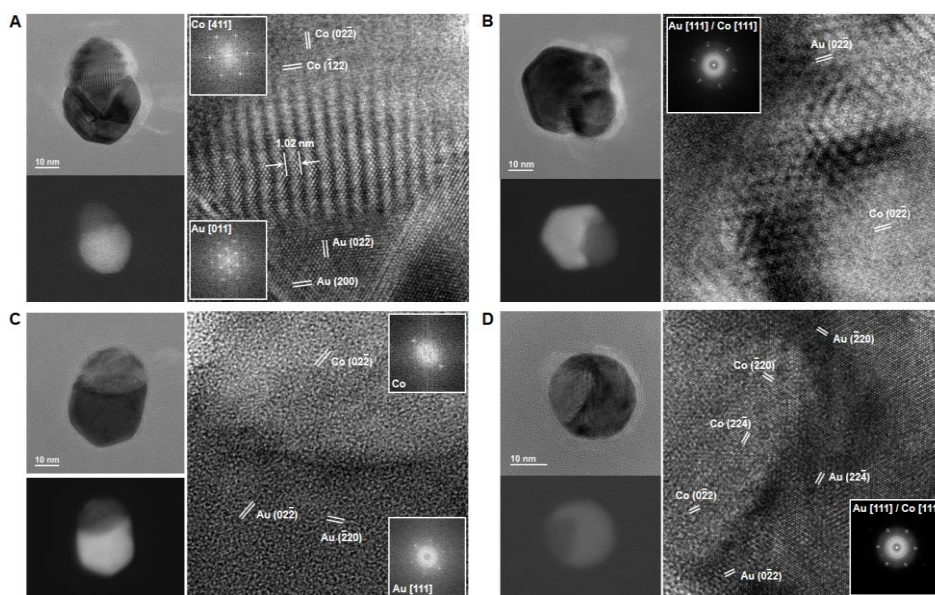


**Figure 4.10** (A-D) HRTEM and ADF-STEM characterization of Au-Co heterodimers synthesized in polymer nanoreactors. In each panel, the left column shows TEM and STEM images of entire particles; the right column shows a zoomed-in HRTEM image of the interface region between the Au and Co phases. Insets are FFTs of the Au domain or Co domain. (A) Au is oriented along the [011] zone axis. Co is along the [411] zone axis. The Moiré pattern ( $D = 1.02$  nm) at the interface is attributed to periodical lattice matching between the Co {220} and Au {220} planes. (B) Au and

Co are epitaxial, both oriented along the [111] zone axis. The two phases share {220} planes at the interface. (C) Au is oriented along the [111] zone axis while Co only shows lattice fringes in one direction that corresponds to one set of {220} planes. (D) Au and Co are epitaxial, both oriented along the [111] zone axis. The two phases share {422} and {220} planes at the interface.

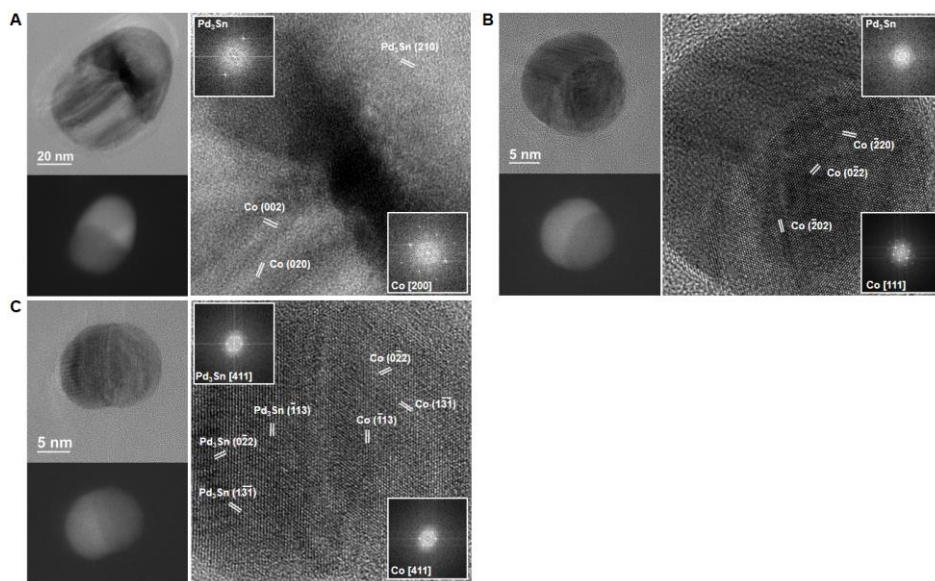


**Figure 4.11** (A-C) HRTEM and ADF-STEM characterization of Co-Pd<sub>3</sub>Sn heterodimers synthesized in polymer nanoreactors. In each panel, the left column shows TEM and STEM images of entire particles; the right column shows a zoomed-in HRTEM image of the interface region between the Co and Pd<sub>3</sub>Sn phases. Insets are FFTs of the Pd<sub>3</sub>Sn domain or Co domain. (A) The FFT of Co domain indicates that Co is on the [200] zone axis. The FFT of Pd<sub>3</sub>Sn domain only show one pair of reflections corresponding to Pd<sub>3</sub>Sn (210) planes. (B) Co is oriented along the [111] zone axis while no lattice plane is observable at the same direction in the Pd<sub>3</sub>Sn domain. (C) Co and Pd<sub>3</sub>Sn are on the [411] zone axis. The two phases share {311} planes at the interface.

Though the crystal structure of the interfaces within a Au-Co-PdSn NPs differs from one particle to another, all of the domains in the NPs are in a pie-shaped configuration (Figure 4.13 and 4.14). In contrast, the Ag-Cu-Co tri-phase system adopts a striped domain architecture, with a central Cu domain capped by Ag and Co domains (Figure 4.15). Within the Au-Co-PdSn and Ag-Cu-Co systems, although all three bi-phase NPs are structurally characterized as heterodimers, they are two very different classes of structure, demonstrating that the behavior of bi-phase architectures cannot be used to predict the architecture of tri-phase NPs (Figure 4.1B).

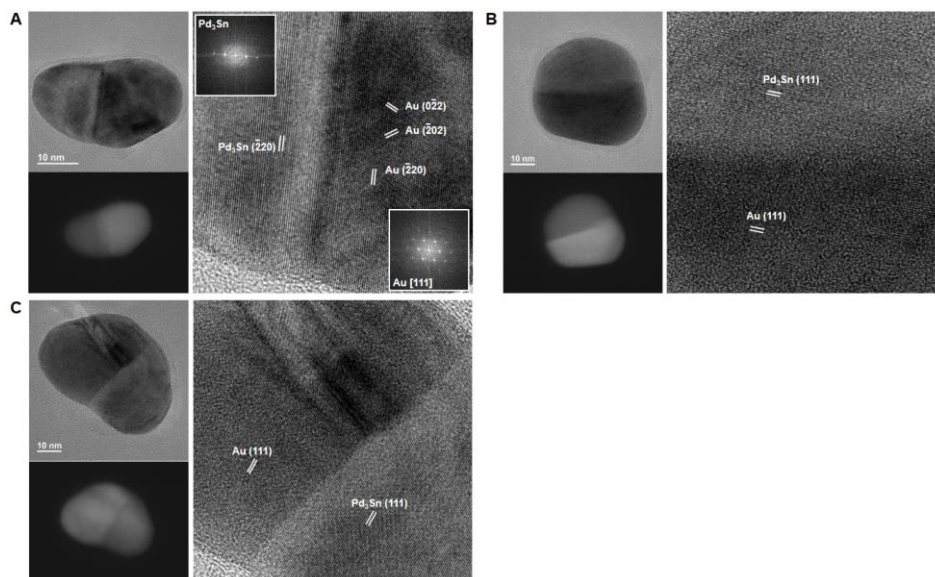


**Figure 4.12** (A-C) HRTEM and ADF-STEM characterization of Au-Pd<sub>3</sub>Sn heterodimers synthesized in polymer nanoreactors. In each panel, the left column shows TEM and STEM images of entire particles; the right column shows a zoomed-in HRTEM image of the interface region between the Au and Pd<sub>3</sub>Sn phases. Insets are FFTs of the Pd<sub>3</sub>Sn domain or Au domain. (A) Au is oriented along the [111] zone axis. Pd<sub>3</sub>Sn shows lattice fringes that can be attributed to {220} planes. The two phases share {220} planes at the interface. (B) Au and Pd<sub>3</sub>Sn share {111} planes at the interface. (C) Au and Pd<sub>3</sub>Sn share {111} planes at part of the interface. Stacking faults are present in the Au domain.

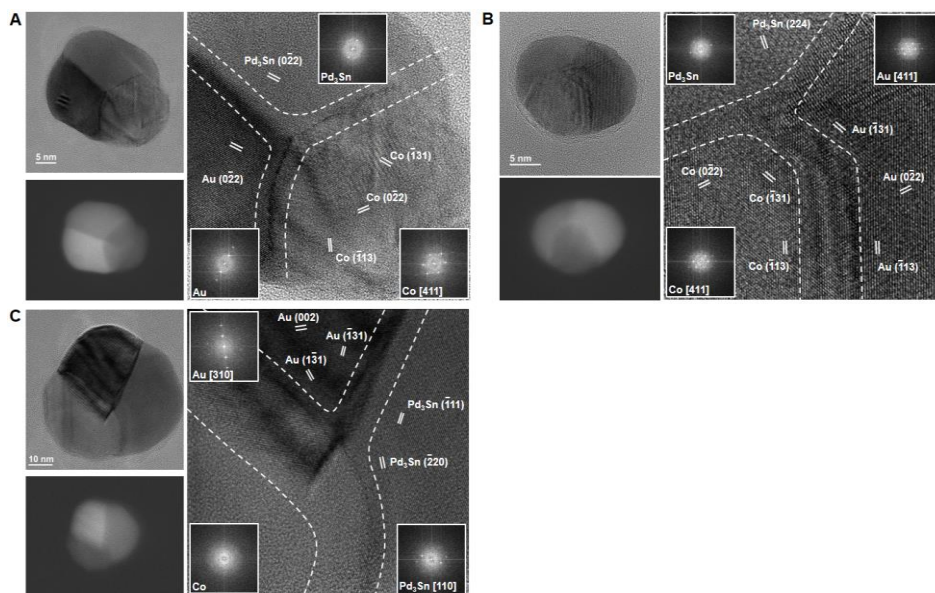


**Figure 4.13** HRTEM and ADF-STEM characterization of Au-Co-Pd<sub>3</sub>Sn heterotrimers synthesized in polymer nanoreactors. In each panel, the left column shows TEM and ADF-STEM images of entire particles. The right column shows a zoomed-in HRTEM image of the tri-phase junction

between the Co, Au, and Pd<sub>3</sub>Sn domains. Insets are FFTs of the Co, Pd<sub>3</sub>Sn or Au domains. Dashed lines highlight the position of the three phase boundaries. (A) The FFT of Co is indicative of Co along the [411] zone axis. The FFT of Au and Pd<sub>3</sub>Sn show reflections in the same direction that correspond to {220} planes. (B) Au and Co are both oriented along the [411] zone axis. The two phases share {311} planes at the interface. Pd<sub>3</sub>Sn domain only shows (224) crystallographic planes. (C) Au is along the [310] zone axis. Pd<sub>3</sub>Sn is along the [110] zone axis. Meanwhile, no lattice plane is observed in the Co domain. The HRTEM images of all the Au-Co-Pd<sub>3</sub>Sn nanoparticles confirm the formation of three solid-state interfaces in one particle. Despite the same domains (Au, Co, and Pd<sub>3</sub>Sn) constituting the nanoparticles in (A-C), the interfacial lattice structure differs between each individual nanoparticle.

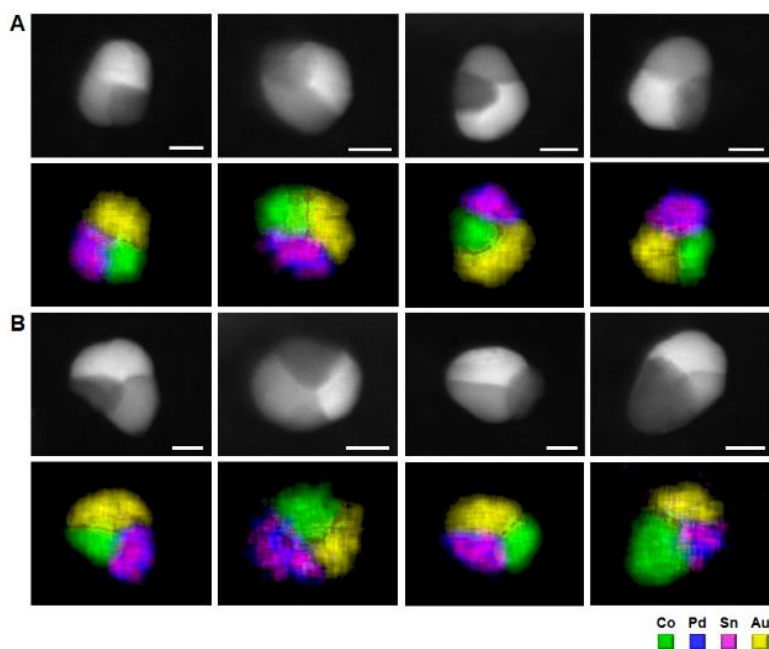


**Figure 4.14** (A) ADF-STEM images and EDS elemental mapping of Au-Co-PdSn tri-phase nanoparticles (Pd:Sn = 1:1) with different angles between the three phase boundaries. (B) ADF-STEM images and EDS elemental mapping of Au-Co-PdSn tri-phase nanoparticles (Pd:Sn = 2:1) with different angles between the three phase boundaries. Scale bars, 15 nm. While the nanoparticles in (A) or (B) are composed of the same material phases, the angles between the three phase boundaries are different in each particle. This suggests that the interfacial lattice structures in these nanoparticles are different. The nanoparticles all have a pie-shaped architecture.

*Observation 3: Thermodynamic architectures are a consequence of the balance between surface and interfacial energies (e.g. for a three-phase structure, dictating the likelihood of a pie-shaped or striped architecture).*

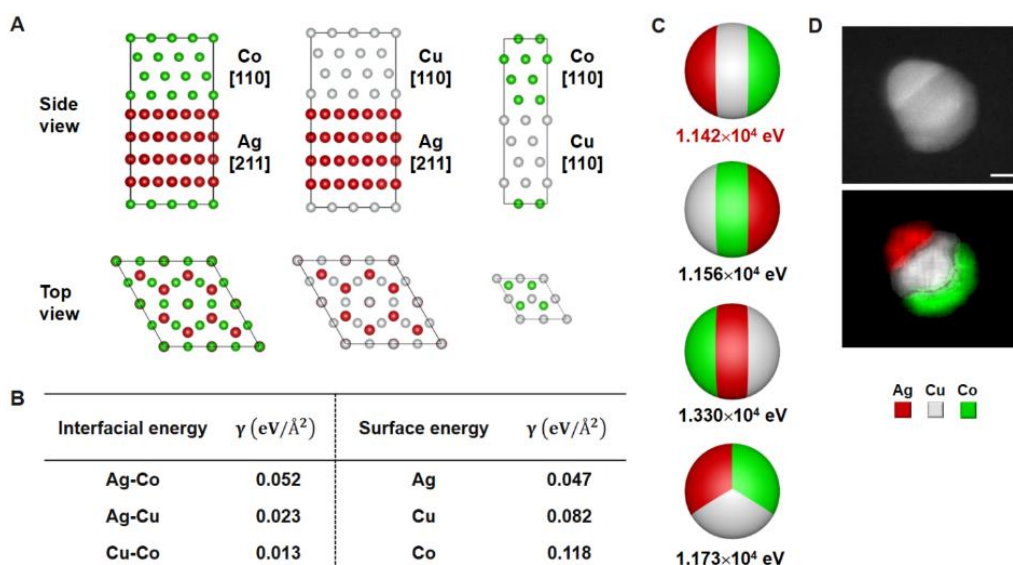


**Figure 4.15** (A) DFT-simulated relaxed structures of the (111) interfacial planes between Ag, Cu, and Co. (B) The surface energies of Ag, Cu, and Co (111) planes and the interfacial energies between Ag, Cu, and Co (111) planes. (C) Calculated total surface and interfacial energies of Ag-Cu-Co nanoparticles (diameter 20 nm) with equal volume of each phase. (D) ADF-STEM image and EDS mapping of a Ag-Cu-Co nanoparticle ( $\text{Ag}_{0.23}\text{Cu}_{0.47}\text{Co}_{0.30}$ ). Scale bar: 15 nm.

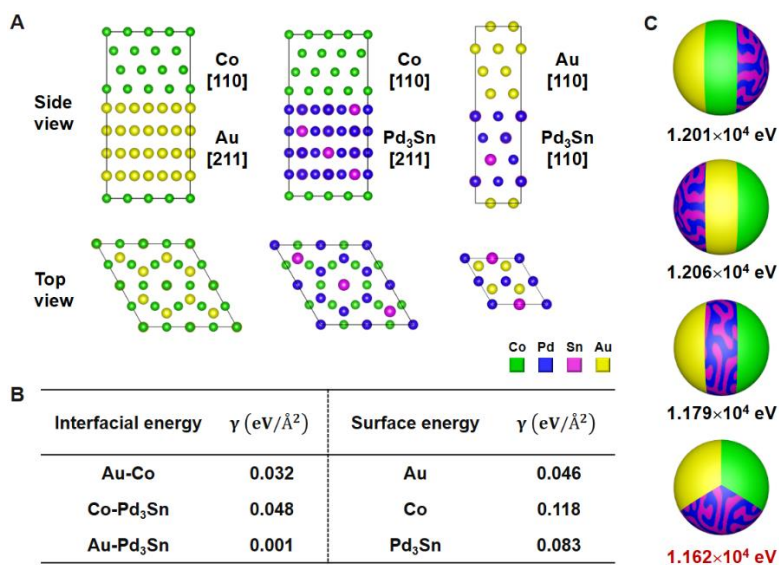


**Figure 4.16** DFT simulation of the architecture of Au-Co-Pd<sub>3</sub>Sn tri-phase nanoparticles. (A) DFT-simulated relaxed structures of the (111) interfacial planes between Au, Co, and Pd<sub>3</sub>Sn. (B) The Surface energies of Au, Co, and Pd<sub>3</sub>Sn (111) planes and the interfacial energies between Au, Co, and Pd<sub>3</sub>Sn (111) planes. (C) Calculated total surface and interfacial energies of Au-Co-Pd<sub>3</sub>Sn nanoparticles with equal volume of each phase (diameter 20 nm).

To understand why different architectures form in tri-phase NPs, we performed DFT calculations to determine the total surface/interfacial energy of Au-Co-Pd<sub>3</sub>Sn and Ag-Cu-Co tri-phase NPs for all possible structures. For the Au-Co-Pd<sub>3</sub>Sn tri-phase system, interface models were set up with each material domain composed of (111) atom planes (Figure 4.16A and Table 4.3). To minimize the interfacial energy, all interfacial supercells were fully relaxed with respect to volume as well as all cell-internal and cell-external degrees of freedom. The three calculated interfacial energies along with three calculated surface energies were combined to evaluate the total energy of NPs using spherical models that have equal volumes of each phase (Figure 4.16B, 4.17, and Table 4.4).

System	Lattice Strain	System	Lattice Strain
Au-Pd <sub>3</sub> Sn	1.02%	Ag-Cu	0.12%
Co-Pd <sub>3</sub> Sn	0.17%	Co-Ag	0.77%
Au-Co	0.85%	Co-Cu	0.89%

**Table 4.3** Mean absolute strain for different interface systems.

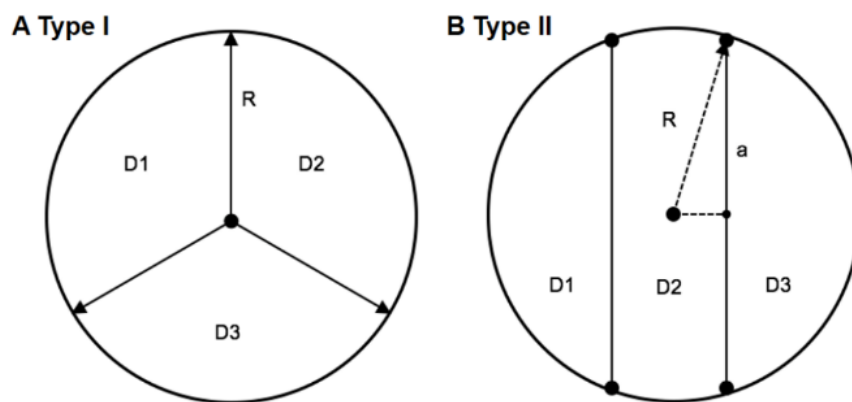


**Figure 4.17** 2D projections of spherical nanoparticle models with either (A) three or (B) two interfaces. Both sphere models consist of three different domains (denoted as D1, D2, and D3). The three domains in Type I nanoparticles are interconnected and have identical shape and size. The three domains in Type II nanoparticles form two interfaces where D1 and D3 are not connected. The volume of the three domains in each model are equal, i.e.,  $V(D1) = V(D2) = V(D3)$ .

Interface/Surface	Type I nanoparticle	Type II nanoparticle
$A_{12}$	$1.571 R^2$	$2.981 R^2$
$A_{23}$	$1.571 R^2$	$2.981 R^2$
$A_{31}$	$1.571 R^2$	0
$S_1$	$4.189 R^2$	$4.863 R^2$
$S_2$	$4.189 R^2$	$2.841 R^2$
$S_3$	$4.189 R^2$	$4.863 R^2$

**Table 4.4** The area of the interfaces and surfaces in each NP model.  $A_{ij}$  denotes the area of the interface between domain  $D_i$  and  $D_j$ .  $S_i$  denotes the surface area of domain  $D_i$ . The radius of the models is  $R$ .

As shown in Figure 4.16C, Au-Co-Pd<sub>3</sub>Sn NPs with pie-shaped architectures were found to possess the lowest total energy. In contrast, DFT energetics of the Ag-Cu-Co tri-phase system revealed that striped architectures with Cu as the central domain possess the lowest total energy (Figure 4.15). Thus, the preferential architecture of each tri-phase NP minimizes the combined surface and interfacial energies.

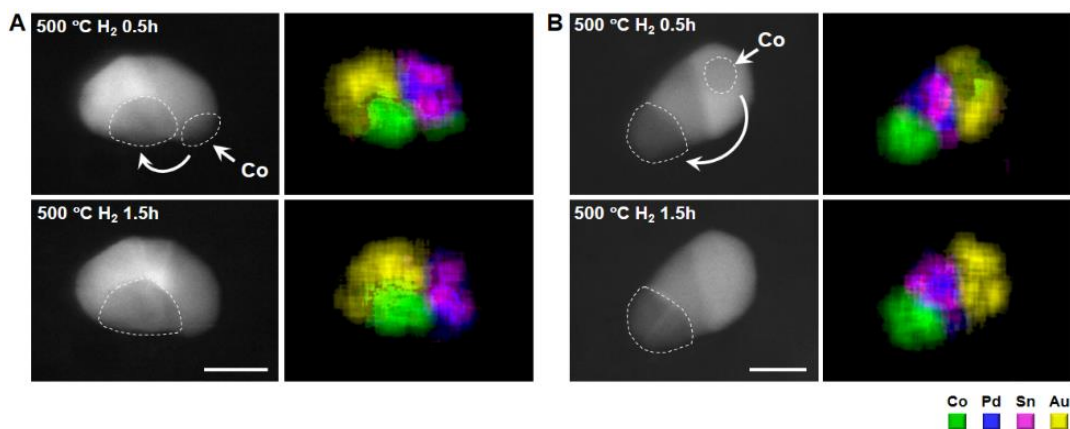


**Figure 4.18** (A,B) ADF-STEM images and EDS mapping of representative Au-Co-PdSn kinetic structures synthesized in polymer nanoreactors. Dashed circles in the ADF-STEM images outline the position of the Co phase as guides for the eye. Scale bars, 20 nm. During the final annealing step of particle synthesis (500 °C, H<sub>2</sub>), kinetic particles were trapped after 0.5 h, which results in particles containing more than three metal domains. In (A) Au<sub>0.32</sub>Co<sub>0.31</sub>Pd<sub>0.23</sub>Sn<sub>0.14</sub> and (B) Au<sub>0.27</sub>Co<sub>0.34</sub>Pd<sub>0.27</sub>Sn<sub>0.12</sub> nanoparticles, the Co phases are not fully aggregated to form one integral metal domain. Continuous annealing for another 1 h effectively triggers intraparticle coarsening between the discrete Co domains.

Although the DFT calculations were performed on lattice models with idealized interfacial structures that do not perfectly match the actual NPs (Figure 4.13 and 4.14), the architectures of tri-phase NPs synthesized by SPBCL match the predictions of the lowest-energy morphologies. We hypothesized that the high temperature long-term annealing process provides sufficient time and energy for the NPs to reconfigure their architectures to the energy-minimized state. To evaluate this hypothesis, we kinetically arrested the annealing process for the Au-Co-PdSn tri-phase NPs after 0.5 and 1.5 h at 500 °C, respectively (Figure 4.18). From this data, one can clearly see that the kinetics are complex, with intraparticle coarsening leading to particles with three distinct metal domains.

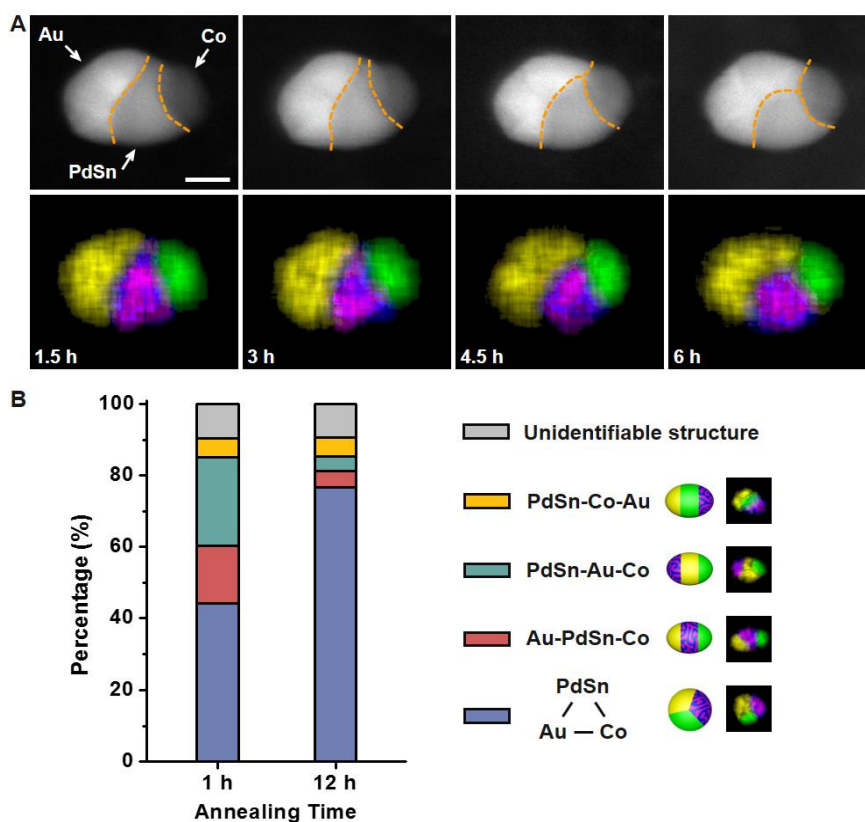


**Figure 4.19** Structural evolution of Au-Co-PdSn tri-phase nanoparticles during thermal annealing. (A) ADF-STEM images (top row) and corresponding EDS mapping (bottom row) of a Au-Co-PdSn NP ( $\text{Au}_{0.33}\text{Co}_{0.24}\text{Pd}_{0.26}\text{Sn}_{0.17}$ ) annealed under flowing  $\text{H}_2$  at 500 °C over time. Dashed yellow

lines outline the position of phase boundaries. Scale bar, 15 nm. (B) Statistical distributions of NPs ( $n = 150$ ) with different architectures.

Due to the randomness of the metal element aggregation within the polymer nanoreactors, the element distribution is different within such architectures. Specifically, for the Au-Co-PdSn NP system, striped tri-phase NPs containing only two interfaces are observed as kinetic products (where any of the three domains consisting of Au, Co, or PdSn form the central domain, Figure 4.19B). The interchangeability of the central domain provides further evidence that all three phases interact comparably well with each other. Importantly, upon continued annealing at 500 °C, the Au-Co-PdSn NPs transform into pie-shaped architectures (Figure 4.19A). Since the annealing temperature is higher than the Tamman temperature of bulk Au (395 °C)<sup>211</sup> and melting temperature of bulk Sn (232 °C), the transformation presumably proceeds through the motion of surface atoms on the NP. Experimentally, the majority of Au-Co-PdSn NPs were converted into a pie-shaped architecture (architectural yield: ~75%, sample size: 150, Figure 4.19B), consistent with the conclusion that the pie-shaped architecture is the thermodynamic product, due to a balance between surface and interfacial energies.

#### **4.4 Interface Engineering in Tetra-Phase Nanoparticles**

*Observation 4: Interfaces not observed in tri-phase nanoparticles do not exist in higher-order multi-phase (4 or more) nanoparticles.*

Predicting the architecture of tetra-phase heterostructured NPs with four distinct metal phases using DFT simulations is challenging because such particles will have four distinct types of surfaces, defined by the different phases that comprise them (Figure 4.1A, bottom row). In addition, they can have up to six interfaces (Figure 4.1A, bottom row, far right). Such a simulation requires one to compare the surface energy of four phases and the interfacial energy of six

interfaces, a situation that becomes even more convoluted when accounting for defects present near interfaces. Because a tetra-phase NP can always be broken down into four constituent tri-phase NPs (Figure 4.1B), experimentally the architecture of the four tri-phase NPs (either striped or pie-shaped) will be predictive of the thermodynamic architecture of the tetra-phase NP. For instance, Figure 4.1B shows six non-duplicated tri-phase NP combination types that, in theory, lead to tetra-phase NPs with either three-, four-, four-, five-, five-, or six- interfaces, respectively. Using SPBCL, one can quickly construct a combinatorial library of NPs by changing the formulation of the polymer nanoreactors. With PdSn as the basic building block, we synthesized and characterized all thirty-one types of multi-phase NPs consisting of Au, Ag, Cu, Co, Ni, and PdSn (Figure 4.20-4.24).

In addition to Au and Co, we found that Ag, Cu, and Ni phase-segregate with PdSn, forming Ag-PdSn,  $\text{Cu}_{0.92}\text{Pd}_{0.08}\text{-Cu}_{0.2}(\text{PdSn})_{0.8}$ , and  $\text{Ni}_{0.6}\text{Sn}_{0.4}\text{-Ni}_{0.08}(\text{PdSn})_{0.92}$  heterodimers, respectively. The phase segregation in these particles can be explained by the thermodynamically stable phases evaluated with the GCLP method (Table 4.2). When higher-order structures are synthesized, the library of PdSn-based NPs contains tri-phase NP combinations that can be used to synthesize tetra-phase architectures with up to six interfaces (Figure 4.1B). To confirm that tri-phase NP architectures could be used to predict tetra-phase NP architectures, we synthesized tetra-phase NPs by selecting tri-phase NP combinations that would yield increasingly complex architectures.

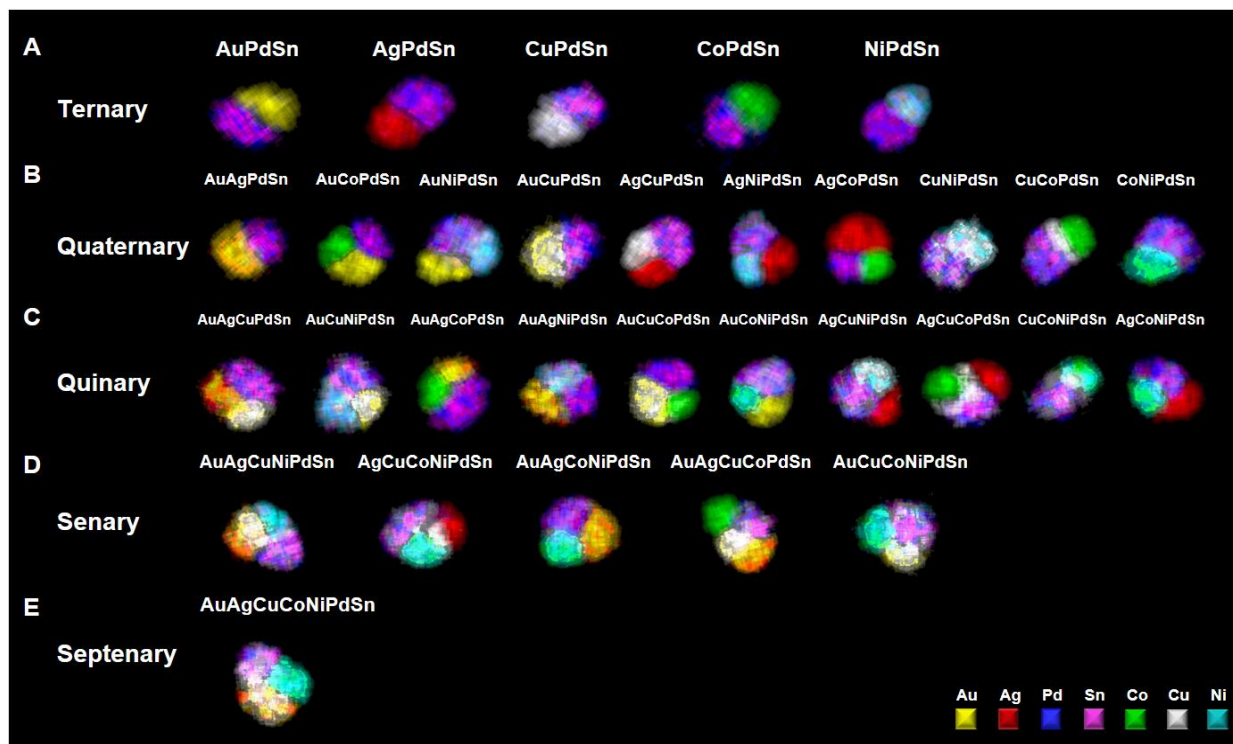


**Figure 4.20** A seven-element library of multi-phase heterostructured nanoparticles that utilize PdSn as the basic building block. Here one specific composition for each combination of metals is shown. (A) Heterodimers can be synthesized by combining PdSn with any of the other five metals, which lead to Au-PdSn, Ag-PdSn,  $\text{Cu}_{0.92}\text{Pd}_{0.08}\text{-Cu}_{0.2}(\text{PdSn})_{0.8}$ , Co-PdSn, and  $\text{Ni}_{0.6}\text{Sn}_{0.4}\text{-Ni}_{0.08}(\text{PdSn})_{0.92}$ . (B) AuAg-PdSn, AuCu-PdSn, CuNi-PdSn, and CoNi-PdSn are heterodimers. AuCo-PdSn, AuNiSn-PdSn, AgCu-PdSn, AgNiSn-PdSn, and AgCo-PdSn are heterotrimers with three interconnected interfaces. CoCu-PdSn is a heterotrimer with two disconnected interfaces. (C) AuAg-AuCu-PdSn, AuCu-CuNi-PdSn, AuAg-Co-PdSn, AuAg-NiSn-PdSn, AuCu-Co-PdSn, AuCoNi-PdSn, AgCuNi-PdSn, AgCoNi-PdSn are heterotrimers with three interconnected interfaces. CoNi-CuNi-PdSn is a heterotrimer with two disconnected interfaces. AgCuCo-PdSn is a heterotetramer with four interfaces. (D) AuAg-CoNi-PdSn and AuCu-CoNi-PdSn are heterotrimers with three interfaces. AuAg-AuCu-NiSn-PdSn and AuAg-AuCu-Co-PdSn are heterotetramers with five interfaces. AgCuCoNi-PdSn is a heterotetramer with four interfaces. (E) AuAgCuCoNi-PdSn is a heterotrimer with three interfaces. The number of phases in one particle is highly dependent on particle composition. For example, CoNiPdSn NPs with two different compositions show either a bi-phase structure (Figure 4.20B) or a tri-phase structure (Figure 4.31B), respectively. Detailed information about the nanoparticles shown in this figure can be found in Figure 4.21-4.24.

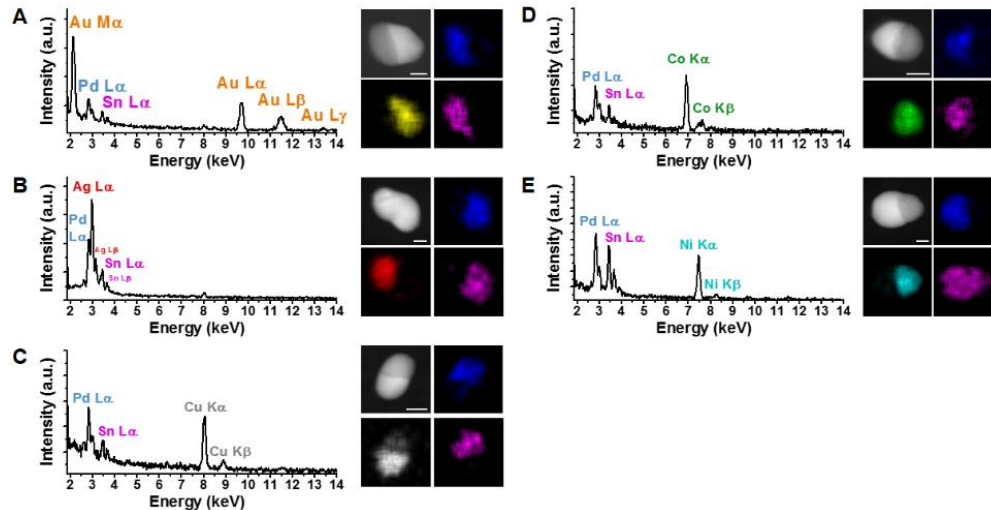


**Figure 4.21** ADF-STEM images, EDS spectra, and detailed EDS mapping of the ternary nanoparticles in Figure 4.20A. (A)  $\text{Au}_{0.57}\text{Pd}_{0.27}\text{Sn}_{0.16}$ , (B)  $\text{Ag}_{0.55}\text{Pd}_{0.26}\text{Sn}_{0.19}$ , (C)  $\text{Cu}_{0.46}\text{Pd}_{0.39}\text{Sn}_{0.15}$ , (D)  $\text{Co}_{0.50}\text{Pd}_{0.32}\text{Sn}_{0.18}$ , and (E)  $\text{Ni}_{0.32}\text{Pd}_{0.37}\text{Sn}_{0.31}$ . Scale bars, 15 nm.

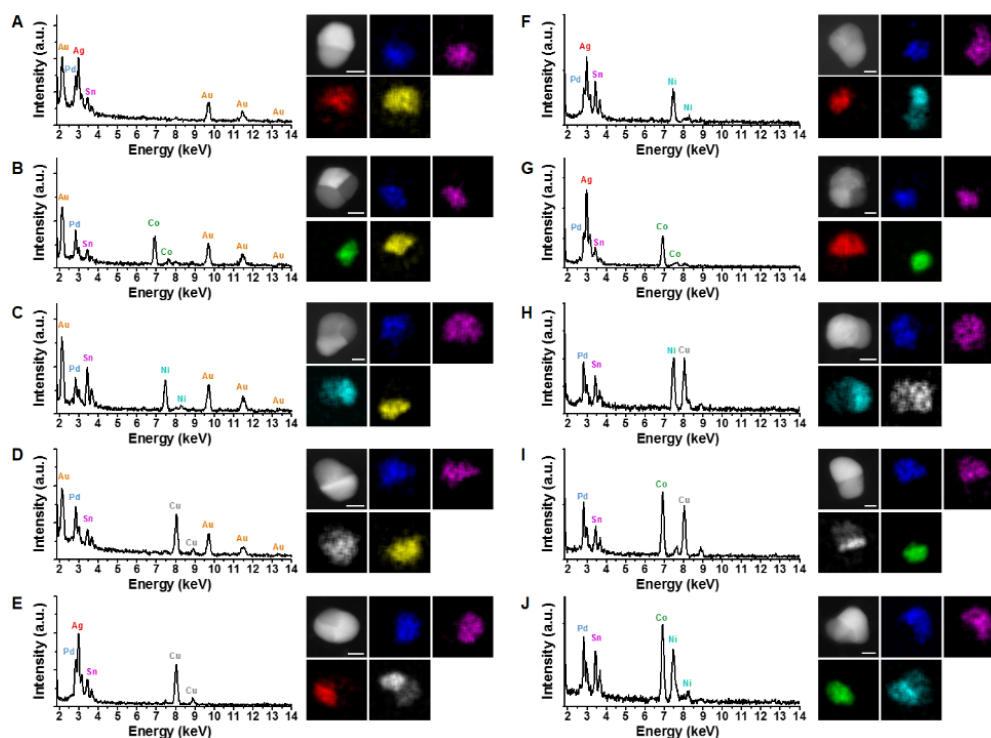


**Figure 4.22** ADF-STEM images, EDS spectra, and detailed EDS mapping of the quaternary nanoparticles in Figure 4.20B. (A)  $\text{Au}_{0.21}\text{Ag}_{0.32}\text{Pd}_{0.32}\text{Sn}_{0.15}$ , (B)  $\text{Au}_{0.31}\text{Co}_{0.34}\text{Pd}_{0.21}\text{Sn}_{0.14}$ , (C)  $\text{Au}_{0.25}\text{Ni}_{0.24}\text{Pd}_{0.20}\text{Sn}_{0.31}$ , (D)  $\text{Au}_{0.24}\text{Cu}_{0.38}\text{Pd}_{0.25}\text{Sn}_{0.13}$ , (E)  $\text{Ag}_{0.30}\text{Cu}_{0.30}\text{Pd}_{0.27}\text{Sn}_{0.13}$ , (F)  $\text{Ag}_{0.22}\text{Ni}_{0.24}\text{Pd}_{0.21}\text{Sn}_{0.33}$ , (G)  $\text{Ag}_{0.43}\text{Co}_{0.23}\text{Pd}_{0.23}\text{Sn}_{0.11}$ , (H)  $\text{Cu}_{0.33}\text{Ni}_{0.32}\text{Pd}_{0.16}\text{Sn}_{0.19}$ , (I)  $\text{Cu}_{0.29}\text{Co}_{0.34}\text{Pd}_{0.21}\text{Sn}_{0.16}$ , and (J)  $\text{Co}_{0.38}\text{Ni}_{0.23}\text{Pd}_{0.18}\text{Sn}_{0.21}$ . Scale bars, 15 nm.



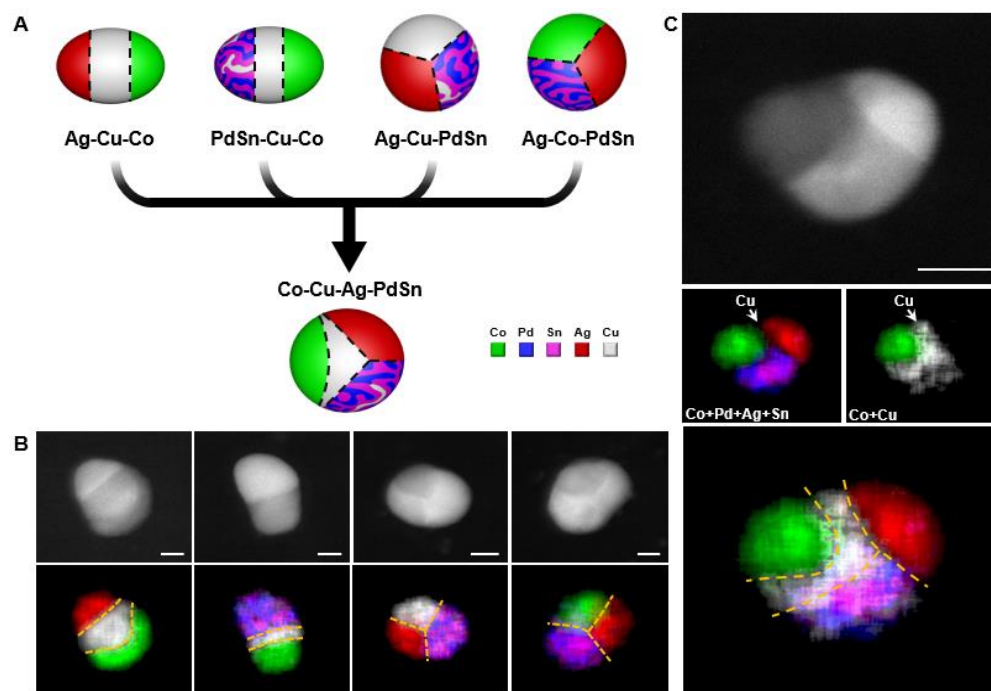


**Figure 4.25** Tetra-phase heterostructured nanoparticles with four interfaces. (A) Schematic illustration depicting the architectures of tri- and tetra-phase NPs composed of Ag, Cu, Co, and PdSn phases. Dashed lines outline the position of the phase boundaries. (B) ADF-STEM images (top row) and EDS mapping (bottom row) of representative tri-phase NPs for all phase combinations. The compositions of the four tri-phase NPs are  $\text{Ag}_{0.23}\text{Cu}_{0.47}\text{Co}_{0.30}$ ,  $\text{Co}_{0.34}\text{Cu}_{0.29}\text{Pd}_{0.21}\text{Sn}_{0.16}$ ,  $\text{Ag}_{0.30}\text{Cu}_{0.30}\text{Pd}_{0.27}\text{Sn}_{0.13}$ , and  $\text{Ag}_{0.33}\text{Co}_{0.23}\text{Pd}_{0.27}\text{Sn}_{0.17}$ . (C) ADF-STEM image (top row) and EDS mapping (bottom row) of a representative tetra-phase NP composed of Ag, Cu, Co, and PdSn phases ( $\text{Ag}_{0.32}\text{Cu}_{0.20}\text{Co}_{0.21}\text{Pd}_{0.15}\text{Sn}_{0.12}$ ). Overlay of selected element maps (middle row) reveals the relative position of the four phases in the NP. Scale bars, 15nm.

The first NP combination we explored included two striped tri-phase NPs and two pie-shaped tri-phase NPs (Figure 4.1B and 4.25A). A system consisting of Ag, Cu, Co, and PdSn matches this scenario, where Ag-Cu-Co and PdSn-Cu-Co are striped heterotrimers, and Ag-Cu-PdSn and Ag-Co-PdSn are pie-shaped heterotrimers, as observed in the ADF-STEM images and EDS elemental mapping of every tri-phase NP (Figure 4.25B and 4.26). The architectures of the four tri-phase NPs suggest that the interfaces between Ag/Co and between PdSn/Co are energetically unfavorable compared to the other four interfaces and four surfaces, which should prevent formation of such interfaces when the tetra-phase NP reaches a thermodynamic

configuration. To test this prediction, we synthesized Ag-Cu-Co-PdSn NPs and investigated their structures by ADF-STEM and EDS. Interestingly, the majority (architectural yield: ~70%, sample size: 30) of Ag-Cu-Co-PdSn NPs have architectures as predicted (Figure 4.25C and 4.27). The Cu domain in the center of the NP separates the Co domain from the Ag and PdSn domains, thus avoiding the formation of Ag-Co and PdSn-Co interfaces. On the other hand, the three interfaces between Cu, Ag, and PdSn domains connect with each other, forming a tri-phase junction. Tetra-phase NPs with this combination of tri-phase architectures adopt an architecture with four interfaces and one tri-phase junction.

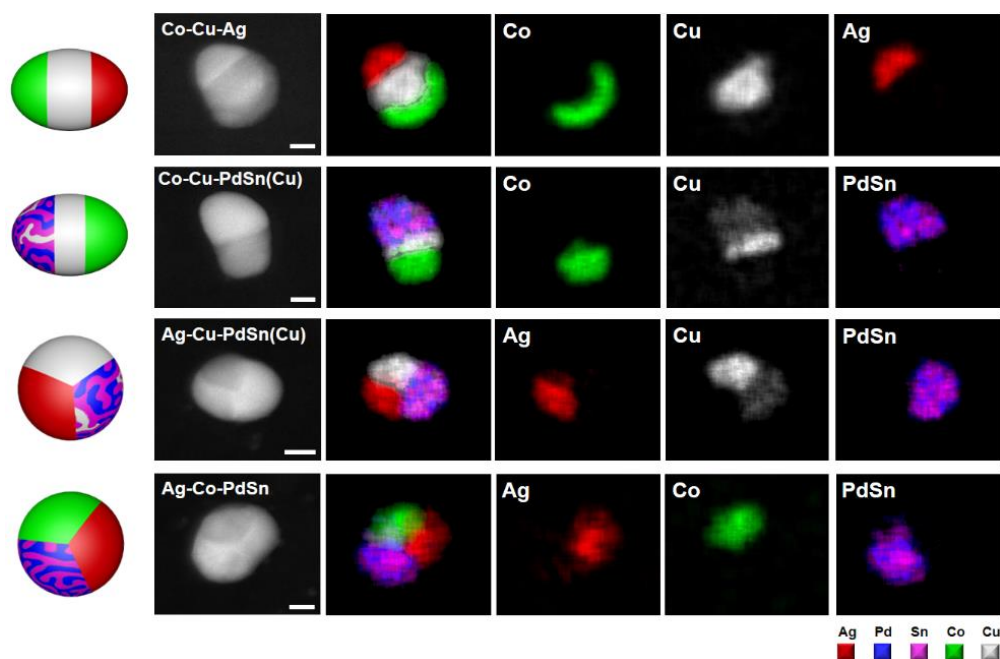


**Figure 4.26** ADF-STEM images and detailed EDS elemental mapping of the tri-phase nanoparticles in Figure 4.25B ( $\text{Ag}_{0.23}\text{Cu}_{0.47}\text{Co}_{0.30}$ ,  $\text{Co}_{0.34}\text{Cu}_{0.29}\text{Pd}_{0.21}\text{Sn}_{0.16}$ ,  $\text{Ag}_{0.30}\text{Cu}_{0.30}\text{Pd}_{0.27}\text{Sn}_{0.13}$ , and  $\text{Ag}_{0.33}\text{Co}_{0.23}\text{Pd}_{0.27}\text{Sn}_{0.17}$ ). Scale bars, 15 nm. Overlay of all element maps (second column) and selected element maps (third to fifth columns) show the relative position of the three phases in each particle.

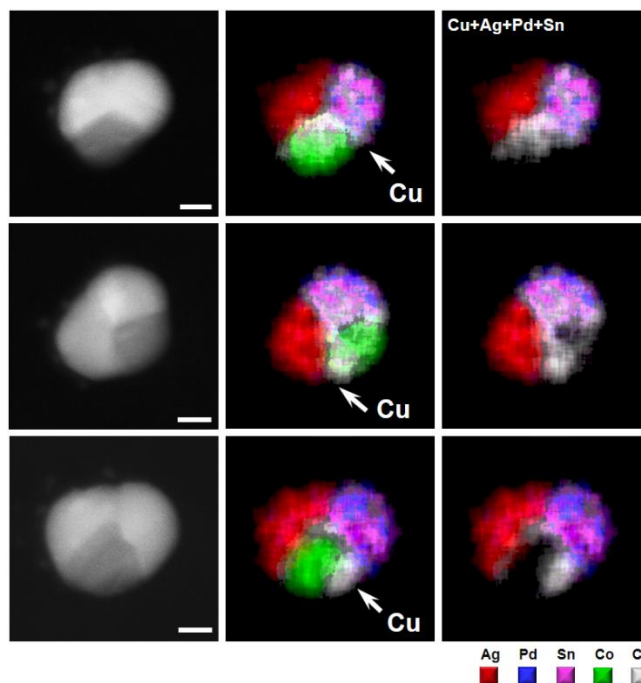


**Figure 4.27** ADF-STEM images and EDS elemental mapping of three representative Ag-Cu-Co-PdSn tetra-phase nanoparticles ( $\text{Ag}_{0.28}\text{Cu}_{0.23}\text{Co}_{0.23}\text{Pd}_{0.16}\text{Sn}_{0.10}$ ,  $\text{Ag}_{0.31}\text{Cu}_{0.19}\text{Co}_{0.21}\text{Pd}_{0.17}\text{Sn}_{0.12}$ , and  $\text{Ag}_{0.29}\text{Cu}_{0.21}\text{Co}_{0.22}\text{Pd}_{0.17}\text{Sn}_{0.11}$ ). Scale bars, 15 nm. Overlay of all element maps (middle column) and selected element maps (right column) reveal the configuration of the four phases in Ag-Cu-Co-PdSn particles.

The second NP combination consists of one tri-phase NP with two interfaces while the other three tri-phase NPs have three interfaces (Figure 4.1B and 4.28). The tri-phase combinations of AuAg, AuCu, Co, and PdSn satisfy this category, where AuAg-AuCu-Co is a striped heterotrimer, and AuAg-AuCu-PdSn, AuAg-PdSn-Co, and AuCu-PdSn-Co are pie-shaped heterotrimers. The architecture of every tri-phase NP was verified by ADF-STEM characterization and EDS elemental mapping (Figure 4.28B and 4.29). The only striped NP (AuAg-AgCu-Co) in this combination type suggests that only one interface is energetically unfavored when forming a tetra-phase NP.

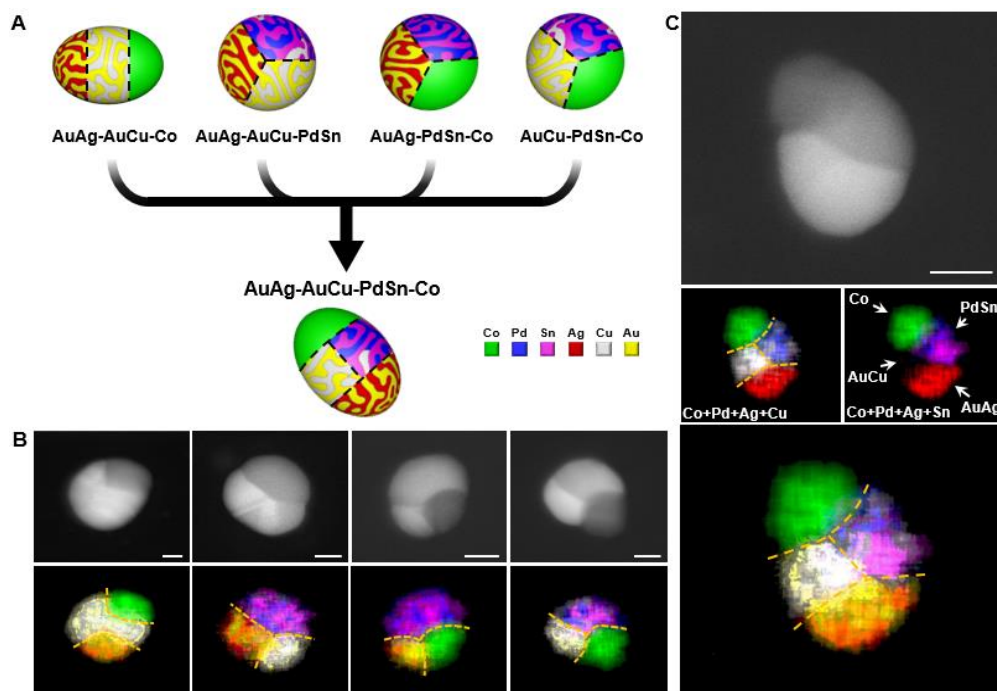


**Figure 4.28** Tetra-phase heterostructured nanoparticles with five interfaces. (A) Schematic illustration depicting the architectures of tri- and tetra-phase NPs composed of AuAg, AuCu, Co, and PdSn phases. Dashed lines outline the position of phase boundaries. (B) ADF-STEM images (top row) and EDS mapping (bottom row) of representative tri-phase NPs for all phase combinations. The compositions of the four tri-phase NPs are  $\text{Au}_{0.30}\text{Ag}_{0.19}\text{Cu}_{0.29}\text{Co}_{0.22}$ ,  $\text{Au}_{0.12}\text{Ag}_{0.30}\text{Cu}_{0.28}\text{Pd}_{0.20}\text{Sn}_{0.10}$ ,  $\text{Au}_{0.06}\text{Ag}_{0.10}\text{Co}_{0.24}\text{Pd}_{0.39}\text{Sn}_{0.21}$ , and  $\text{Au}_{0.13}\text{Cu}_{0.27}\text{Co}_{0.30}\text{Pd}_{0.15}\text{Sn}_{0.15}$ . (C) ADF-STEM image (top row) and EDS mapping (bottom row) of a representative tetra-phase NP composed of AuAg, AuCu, Co, and PdSn phases ( $\text{Au}_{0.18}\text{Ag}_{0.16}\text{Cu}_{0.20}\text{Co}_{0.23}\text{Pd}_{0.13}\text{Sn}_{0.10}$ ). Overlay of selected element maps (middle row) shows the relative configuration of the four phases in the NP. Dashed lines highlight the position of the five phase boundaries. Scale bars, 15 nm.

AuAg-AuCu-PdSn-Co NPs were synthesized to confirm the prediction. As shown in Figure 4.28C and 4.30, AuCu and PdSn domains are in the center of the particle with AuAg and Co domains capped on each end (architectural yield: ~70%, sample size: 30). One tri-phase junction forms between AuAg/AuCu/PdSn phases. The other tri-phase junction forms between AuCu/PdSn/Co phases. Tetra-phase NPs with this combination of tri-phase particle types have an architecture with five interfaces and two tri-phase junctions.

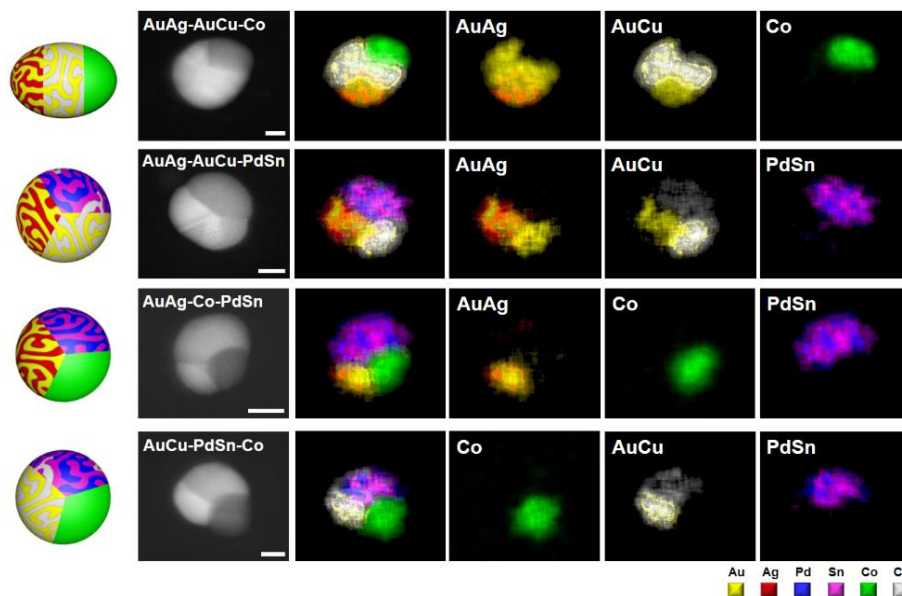


**Figure 4.29** ADF-STEM images and detailed EDS elemental mapping information of the tri-phase nanoparticles in Figure 4.28B ( $\text{Au}_{0.30}\text{Ag}_{0.19}\text{Cu}_{0.29}\text{Co}_{0.22}$ ,  $\text{Au}_{0.12}\text{Ag}_{0.30}\text{Cu}_{0.28}\text{Pd}_{0.20}\text{Sn}_{0.10}$ ,  $\text{Au}_{0.06}\text{Ag}_{0.10}\text{Co}_{0.24}\text{Pd}_{0.39}\text{Sn}_{0.21}$ , and  $\text{Au}_{0.13}\text{Cu}_{0.27}\text{Co}_{0.30}\text{Pd}_{0.15}\text{Sn}_{0.15}$ ). Scale bars, 15 nm. Overlays of all element maps (second column) and selected element maps (third to fifth columns) show the relative position of the three phases in each particle.

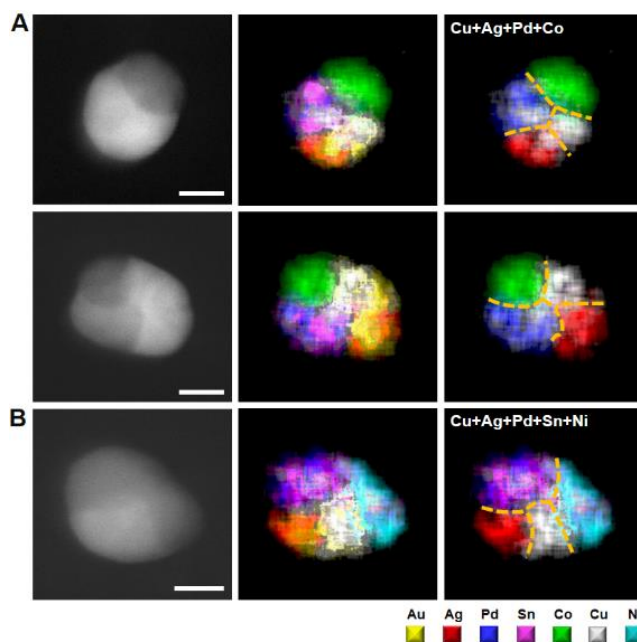


**Figure 4.30** ADF-STEM images and EDS elemental mapping of representative (A) AuAg-AuCu-Co-PdSn ( $\text{Au}_{0.11}\text{Ag}_{0.15}\text{Cu}_{0.17}\text{Co}_{0.28}\text{Pd}_{0.19}\text{Sn}_{0.10}$  and  $\text{Au}_{0.17}\text{Ag}_{0.15}\text{Cu}_{0.17}\text{Co}_{0.23}\text{Pd}_{0.18}\text{Sn}_{0.10}$ ) and (B) AuAg-AuCu-NiSn-PdSn ( $\text{Au}_{0.17}\text{Ag}_{0.12}\text{Cu}_{0.22}\text{Ni}_{0.14}\text{Pd}_{0.19}\text{Sn}_{0.16}$ ) tetra-phase nanoparticles. Scale bars, 15 nm. Overlays of all element maps (middle column) and selected element maps (right

column) reveal the configuration of the four phases in the nanoparticles. Dashed yellow lines indicate the position of the five phase boundaries in each nanoparticle.

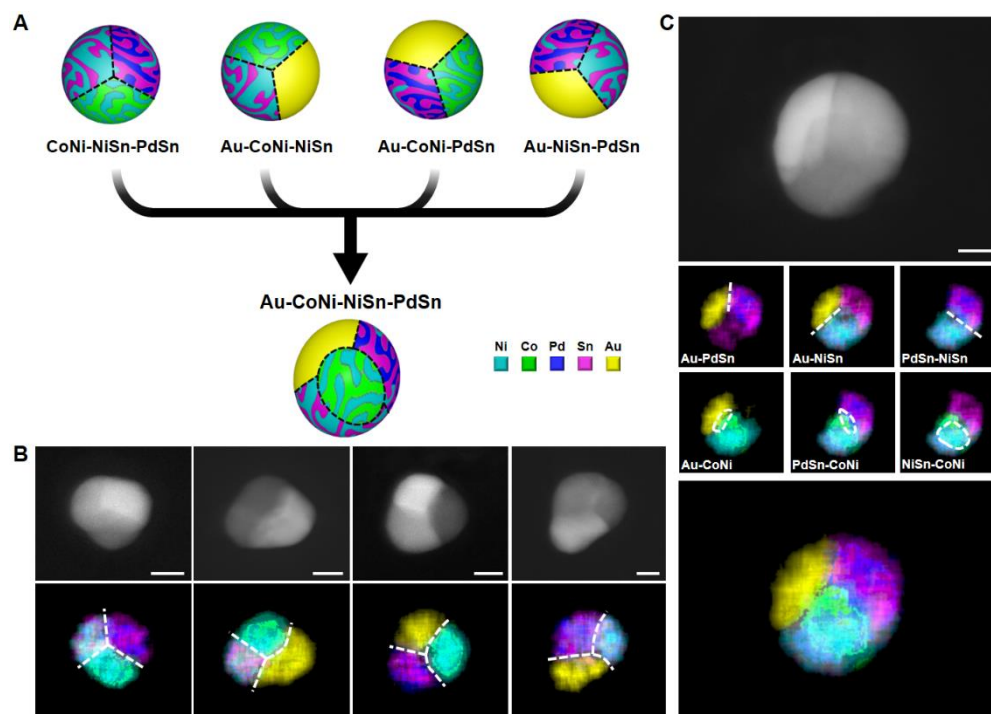


**Figure 4.31** Tetra-phase heterostructured nanoparticles with six interfaces. (A) Schematic illustration depicting the architectures of tri- and tetra-phase NPs composed of Au, CoNi, NiSn, and PdSn phases. Dashed lines outline the position of the phase boundaries. (B) ADF-STEM images (top row) and EDS mapping (bottom row) of representative tri-phase NPs for all phase combinations. The compositions of the four tri-phase NPs are  $\text{Co}_{0.13}\text{Ni}_{0.35}\text{Pd}_{0.26}\text{Sn}_{0.26}$ ,  $\text{Au}_{0.37}\text{Co}_{0.18}\text{Ni}_{0.36}\text{Sn}_{0.09}$ ,  $\text{Au}_{0.29}\text{Co}_{0.17}\text{Ni}_{0.19}\text{Pd}_{0.20}\text{Sn}_{0.15}$ , and  $\text{Au}_{0.25}\text{Ni}_{0.24}\text{Pd}_{0.20}\text{Sn}_{0.31}$ . (C) ADF-STEM image (top row) and EDS mapping (bottom row) of a representative tetra-phase NP composed of Au, CoNi, NiSn, and PdSn phases ( $\text{Au}_{0.20}\text{Co}_{0.11}\text{Ni}_{0.30}\text{Pd}_{0.21}\text{Sn}_{0.18}$ ). Overlay of selected elemental maps (two middle rows) show the relative position of any two of the four phases. Dashed lines/circles outline the position of the six phase boundaries in the NP. Scale bars, 15 nm.

As a final demonstration of interface engineering in polyelemental NPs, we utilized a system where all four tri-phase NPs share the same configurational feature, *i.e.*, a pie-shaped architecture (Figure 4.1B and 4.31A). The architecture of the four tri-phase NPs suggests that all six interfaces and four surfaces are energetically compatible with each other. The structures of tri-phase NPs containing Au, CoNi, NiSn, and PdSn phases provide a guide for predicting the thermodynamic structure of the single tetra-phase structure, which could have as many as six

interfaces (Figure 4.31B and 4.32).

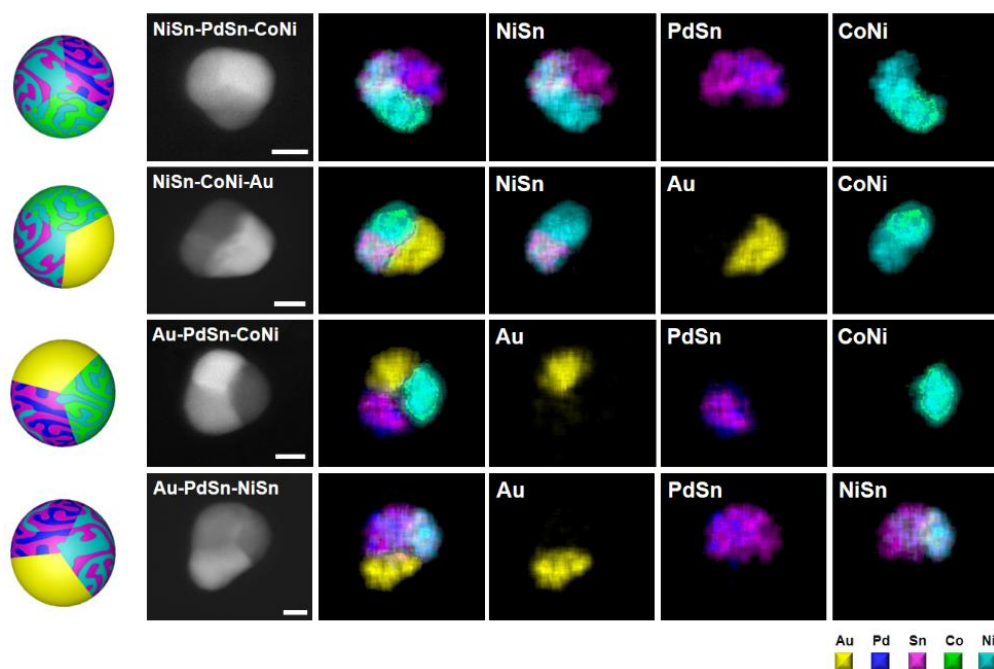


**Figure 4.32** ADF-STEM images and detailed EDS elemental mapping information of the tri-phase nanoparticles in Figure 4.31B ( $\text{Co}_{0.13}\text{Ni}_{0.35}\text{Pd}_{0.26}\text{Sn}_{0.26}$ ,  $\text{Au}_{0.37}\text{Co}_{0.18}\text{Ni}_{0.36}\text{Sn}_{0.09}$ ,  $\text{Au}_{0.29}\text{Co}_{0.17}\text{Ni}_{0.19}\text{Pd}_{0.20}\text{Sn}_{0.15}$ , and  $\text{Au}_{0.25}\text{Ni}_{0.24}\text{Pd}_{0.20}\text{Sn}_{0.31}$ ). Overlays of all element maps (second column) and selected element maps (third to fifth columns) show the relative position of the three phases in each particle. Scale bars, 15 nm.

Indeed, the incorporation of these four phases into one NP leads to an unprecedented nanostructure with four constituent domains interfaced with each other (architectural yield: ~65%, sample size: 30, Figure 4.31C and 4.33-4.36). The overlay of EDS element maps revealed the identity and distribution of the four phases and their spatial relationship in one typical NP. The Au, PdSn, and NiSn domains interconnect with each other while the CoNi domain sits on top of the other three domains, forming six phase boundaries in one particle (Figure 4.31C and 4.33). Tetra-phase NPs composed of a subset of four pie-shaped tri-phase NPs have an architecture with six interfaces, four tri-phase junctions, and one tetra-phase junction point that is embedded in a single NP. This study validates that NP phase hierarchy can be utilized for engineering the configuration

of phase boundaries in higher order structures.

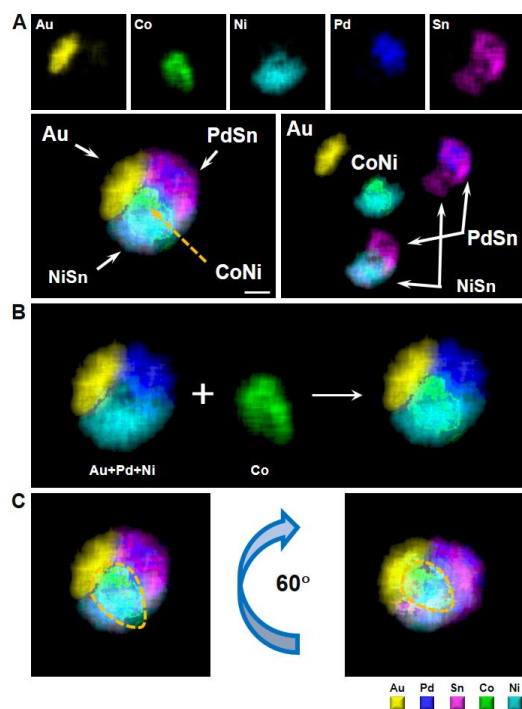


**Figure 4.33** (A,B) Additional EDS mapping information of the Au-CoNi-NiSn-PdSn tetra-phase nanoparticle in Figure 4.30C. The overlay of selected element maps clearly indicates that the particle consists of four phases with six phase boundaries. (C) EDS mapping of the same particle after rotating the particle  $60^\circ$ . Dashed circles in the images outline the position of CoNi phase as guides for the eye. The CoNi phase moves from the bottom of the image to the center of the image, indicating that the CoNi domain is on top of the particle. Scale bar, 15 nm.

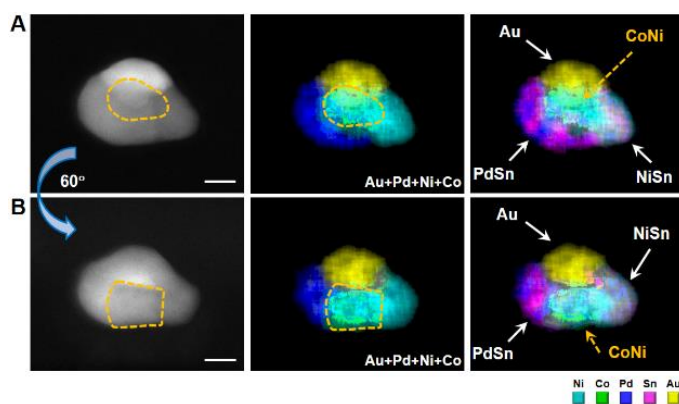


**Figure 4.34** (A) ADF-STEM image and EDS mapping of a Au-CoNi-NiSn-PdSn tetra-phase nanoparticle with six phase boundaries ( $\text{Au}_{0.18}\text{Co}_{0.14}\text{Ni}_{0.33}\text{Pd}_{0.18}\text{Sn}_{0.17}$ ). (B) ADF-STEM image and EDS mapping of the same particle after rotating the particle  $60^\circ$ . Scale bars, 20 nm. Dashed circles in first and second columns of the images outline the position of the CoNi phase as guides for the eye. After rotating the nanoparticle, the CoNi phase moves from the center of the image to the

bottom of the image, indicating that the CoNi domain is on top of the particle.

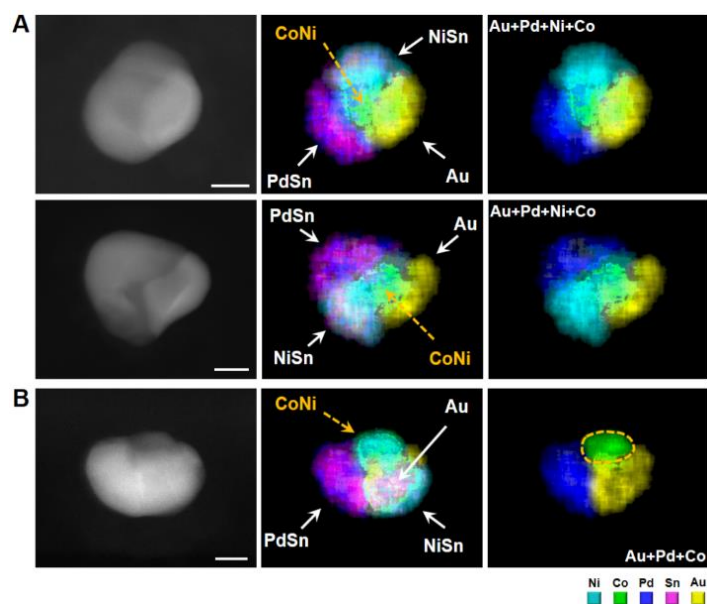


**Figure 4.35** (A) ADF-STEM images and EDS elemental mapping of two representative Au-CoNi-NiSn-PdSn tetra-phase nanoparticles ( $\text{Au}_{0.17}\text{Co}_{0.11}\text{Ni}_{0.33}\text{Pd}_{0.24}\text{Sn}_{0.15}$  and  $\text{Au}_{0.18}\text{Co}_{0.09}\text{Ni}_{0.33}\text{Pd}_{0.25}\text{Sn}_{0.15}$ ). Overlays of all element maps (middle column) and selected element maps (right column) indicates that the CoNi phases are either on top of the particle or at the bottom the of particle. (B) ADF-STEM images and EDS elemental mapping of a Au-CoNi-NiSn-PdSn tetra-phase nanoparticle ( $\text{Au}_{0.20}\text{Co}_{0.12}\text{Ni}_{0.32}\text{Pd}_{0.20}\text{Sn}_{0.16}$ ) with the CoNi phase located on the edge. Dashed circle outlines the position of the CoNi phase as a guide. Scale bars, 20 nm.

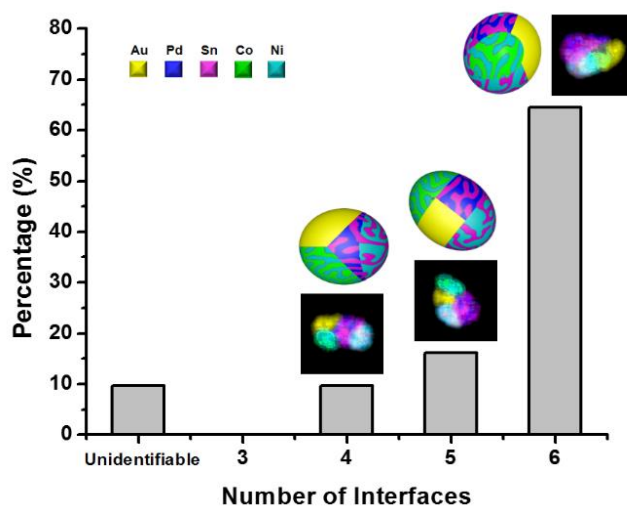


**Figure 4.36** Distributions of Au-CoNi-PdSn-NiSn heterotetramers with different architectures (calculated based on 30 particles).

## 4.5 Materials and Methods

### 4.5.1 Materials

Poly(ethylene oxide)-*b*-poly(2-vinyl pyridine) (PEO-*b*-P2VP,  $M_n = 2.8\text{-}1.5$  kg/mol, polydispersity index = 1.11) was purchased from Polymer Source, Inc. The polymer was purified by dialysis (ThermoFisher dialysis cassettes, 2K MWCO) with deionized water for 5 days before use. Metal compounds (>99.9% trace metal basis),  $\text{HAuCl}_4 \cdot 3\text{H}_2\text{O}$ ,  $\text{AgNO}_3$ ,  $\text{Cu}(\text{NO}_3)_2 \cdot x\text{H}_2\text{O}$ ,  $\text{Co}(\text{NO}_3)_2 \cdot 6\text{H}_2\text{O}$ ,  $\text{Ni}(\text{NO}_3)_2 \cdot 6\text{H}_2\text{O}$ ,  $(\text{NH}_4)_2\text{PdCl}_6$ , and  $\text{SnCl}_4$  were purchased from Sigma-Aldrich, Inc. and used without further purification. Atomic force microscopy (AFM) multi-contact 1D probes (type M, no gold coating) were purchased from Advanced Creative Solutions Technology, Inc. Hexamethyldisilazane (HMDS) was purchased from Sigma-Aldrich, Inc. TEM grids with 15 or 50 nm silicon nitride support films were purchased from Ted Pella, Inc.

### 4.5.2 Preparation of Block Copolymer Solution

Polymer ink solution was prepared by dissolving PEO-*b*-P2VP and different metal compounds in de-ionized water in predetermined molar ratios. The ink solution had a polymer concentration of 5 mg/mL. The molar ratio of pyridyl group to total metal precursors varied between 48:1 and 256:1 to control the size of NPs. To reduce the hydrolysis of  $\text{SnCl}_4$ , the pH of the ink solution was adjusted to 1 by the addition of HCl. The ink solution was stirred for 1 h at room temperature prior to use.

### 4.5.3 Nanoparticle (NP) Synthesis

Nanoparticles were synthesized on TEM grids by scanning probe block copolymer lithography (SPBCL) (23). In a typical experiment, hydrophobic TEM grids were obtained by vapor coating the grids with HMDS for 24 h in a desiccator that contained a vial of a HMDS and

hexane mixture (1:1, v/v). AFM 1D probes were mounted onto a Park XE-150 AFM. The probes were dip-coated with polymer ink solution and then brought into contact with the hydrophobic TEM grids to deposit arrays of polymer nanoreactors. The patterning process was performed in a chamber at a controlled temperature of 25 °C and relative humidity of 85%. To synthesize NPs in the polymer nanoreactors, the TEM grids were thermally annealed in a tube furnace. Typical annealing conditions were as follows: ramp to 160 °C under H<sub>2</sub> in 10 min, hold at 160 °C for 6 h, ramp to 300 °C in 10 min, hold at 300 °C for 6 h, ramp to 500 °C in 10 min, thermally anneal the grids at 500 °C for 12 h, and finally cool down to room temperature in 0.5 h.

#### *4.5.4 Density Functional Theory (DFT) Calculations*

All DFT calculations were carried out using the Vienna Ab-initio Simulation Package (VASP) with the projected augmented wave (PAW) potentials, and Perdew-Burke-Ernzerhof (PBE) formulation of the generalized gradient approximation (GGA) (43-45). To compute interfacial energies, we generated interfacial supercells containing two domains, where each domain consists of four (111) atomic planes. The interface structures are created using Virtual NanoLab (VNL) package and the final strain of each interface structure is less than 1.5%. All of these structures were fully relaxed and  $\Gamma$ -centered k-point meshes were constructed to achieve at least 4000 k-points per reciprocal atom. For each surface energy calculation, we used a crystal slab model and a vacuum region, which are periodically arranged along the direction perpendicular to the surface. Each surface contains seven (111) atomic layers of with (2×2) unit cell and a vacuum region of 15 Å in thickness. The middle three layers are fixed and the other layers are allowed to relax. Brillouin-zone integrations are sampled using  $\Gamma$ -centered k-point meshes corresponding to a 9×9×1 grid. For both interface and surface calculations, an energy cutoff of 400 eV is used for

the plane wave basis set used to represent the electronic wave functions and an energy tolerance of  $1 \times 10^{-5}$  eV for the relaxation of all the structure. Spin polarization is included for all DFT calculations in this work. The surface energies are calculated by  $\gamma = (E_{slab} - \sum n_i \mu_i) / 2A_{surface}$ , where  $E_{slab}$  is the total energy of the surface slab,  $n_i$  is number of  $i$  atoms in the systems,  $\mu_i$  is the chemical potential of the element  $i$  and  $A_{surface}$  is the surface area. The interfacial energy between phase  $A$  and  $B$  is calculated by  $\sigma = (E_{AB} - E_A^{strained} - E_B^{strained}) / 2A_{interface}$ , where  $E_{AB}$  is the total energy of the interfacial structure,  $E_A^{strained}$  and  $E_B^{strained}$  are the strained bulk energies for phase  $A$  and  $B$ , and  $A_{interface}$  is the interface area. The strained bulk energies of phase  $A$  and  $B$  represent the energy penalty associated with coherent, epitaxial lattice matching across the interface (46). To calculate the strained energies of  $A$  and  $B$ , they are both fixed to a common lattice constant (in two dimensions) in the interfacial plane, and the energy of each phase is relaxed to an energy minimum with respect to the lattice constant perpendicular to the interface plane. Then, the sum of these two epitaxial energies is minimized with respect to lattice parameter of the interfacial plane.

#### 4.5.5 Characterization

Scanning transmission electron microscopy (STEM) characterization of the NPs was performed on an in-house designed dual-energy dispersive X-ray spectroscopy (EDS) detector equipped Hitachi HD-2300 dedicated STEM. The dark-field images were taken with an annular dark-field (ADF) detector at an electron acceleration voltage of 200 kV. NP composition was studied using the equipped dual EDS detectors (Thermo Scientific) on the HD-2300 STEM with a 200 kV acceleration voltage. The  $L\alpha$  peaks of Pd, Ag, Sn, and Au, and the  $K\alpha$  peaks of Co, Ni, and Cu in the EDS spectra were used for elemental mapping and for composition quantification

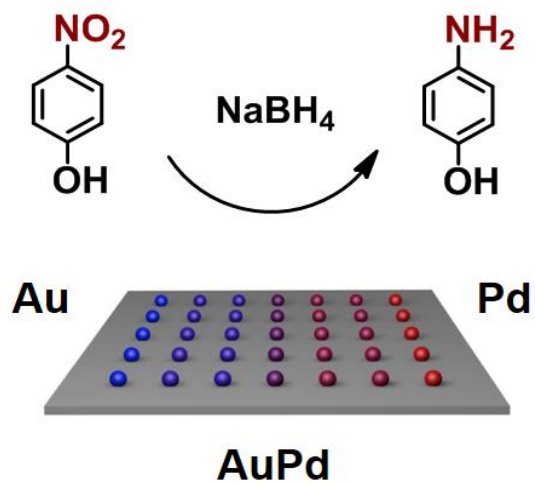
with standardless Cliff-Lorimer correction method. The atomic composition measured by EDS has an inherent error of less than 5% due to X-ray absorption and fluorescence. Each EDS map is built based on 30 frames with pixel dwell time of 203  $\mu$ s. Thermo Scientific NSS software was used for EDS data processing. High-resolution transmission electron microscopy (HRTEM) characterization were performed on a JEOL ARM300 transmission electron microscope at an acceleration voltage of 300 kV using NPs prepared on TEM grids with 15 nm SiN<sub>x</sub> support films.

#### **4.6 Conclusions and Outlook**

In this chapter, we have presented a set of four rules for engineering the arrangement of interfaces in multi-phase polyelemental NPs using PdSn-based multi-phase NPs as a proof-of-concept system. For interface engineering, the balancing of surface and interfacial energies is critical in determining the thermodynamically preferred structures for multi-phase NPs, as demonstrated by the extraordinary tetra-phase polyelemental NPs, reported herein, with four, five, and six phase boundaries. Looking forward, these guidelines will be particularly useful in elucidating the complex architectures of NPs containing more than four phases, where the NPs may have ten or more different interfaces. Interface engineering in polyelemental nanomaterials will be essential for optimizing their use in catalysis, plasmonics, nanoelectronics, and energy harvesting, and challenges moving forward are to establish high-throughput ways for characterizing their properties, as a function of composition, size, phase, and architecture, and the development of methods for their scalable syntheses.<sup>32,48,126,133,164</sup>

## CHAPTER FIVE

Catalytic Application of Nanoparticles Synthesized on a Substrate



Portions of this chapter have been published in: *J. Am. Chem. Soc.*, **2015**, *137*, 9167-9173.

## 5.1 Introduction

Multimetallic nanoparticles (NPs) are emerging as an important frontier of heterogeneous catalysts due to their remarkable catalytic performance through the combination of the high surface area to volume ratio inherent to NPs and the ability to tune the catalytic activity of NPs mandated by the Sabatier principle.<sup>1,8,9</sup> Compared with monometallic NPs, recent research regarding multimetallic NPs has focused on improving catalyst performance by engineering their electronic structures to enhance their activity and stability,<sup>5,7,80</sup> and reducing their cost by integrating non-precious metals.<sup>40</sup> While wet chemical approaches have been used to realize an enormous library of polyelemental NPs, control of particle size and compositional homogeneity over a wide range of stoichiometric ratios is difficult due to fundamental differences in growth kinetics inherent to the metal precursors.<sup>4,103</sup> Consequently, identification of optimal catalysts remains prohibitively difficult due to the vast numbers of compositional and structural parameters that would need to be synthesized and examined separately.

One potential way to overcome these drawbacks is to integrate arrays of multimetallic NPs on targeted surfaces while controlling their size and composition. The surface-immobilization of isolated nanocatalysts, in custom arrangements across large scales, could provide a unique platform for systematic catalyst screening.<sup>164</sup> Currently, several approaches such as block copolymer lithography,<sup>158,162</sup> vacuum deposition,<sup>169,170</sup> electrochemical deposition,<sup>149</sup> microdroplet dewetting,<sup>154,155</sup> NP sliding,<sup>156,157</sup> combinatorial metal sputtering,<sup>167</sup> and direct writing<sup>157,177-179</sup> have been developed to prepare mono- or multi-metallic NPs on surfaces. However, none of these methods can both control the particle size and composition while guaranteeing the presence of a single NP at a precise location, leaving the on-site synthesis of

arbitrarily chosen nanoalloys an open challenge.

In Chapter Three, Four, and Five, we utilize scanning probe block copolymer lithography (SPBCL), that integrates polymer-mediated particle synthesis and molecular printing techniques, to synthesize single NPs on surfaces with systematic control over particle size, composition, and structure. These characteristics make SPBCL a promising tool for integrating tremendous types of NPs on a single substrate, which is directly amenable to high-throughput screening. Through parallel screening of the vast compositional and structural space, novel NP catalysts can be discovered in a systematic way, thus avoiding the inefficient process of serially making and characterizing NPs (Figure 5.1).

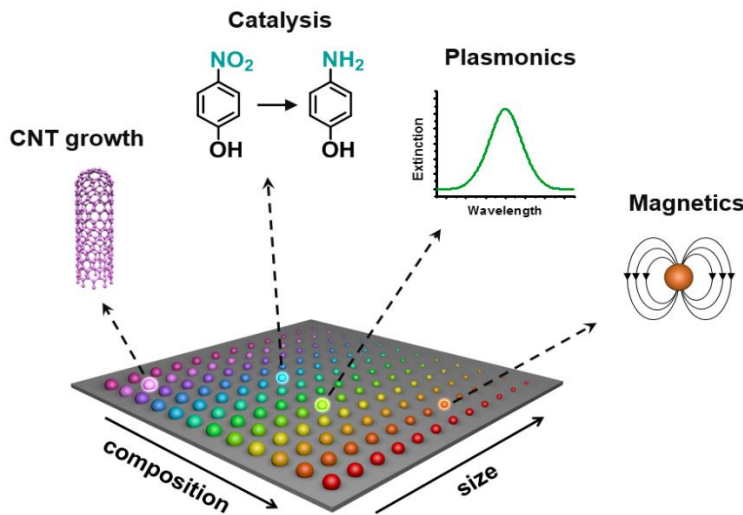


**Figure 5.1** Schematic illustration of the screening of nanostructures for a wide variety of properties with a substrate containing particles spatially-encoded with respect to size and composition.

In this chapter, we present systematic studies on the scale-up synthesis of multimetallic NPs with polymer pen lithography (PPL) and on NP catalytic activity. Specifically, we show that millions of NPs can be made on a single Si substrate at a centimeter scale. Importantly, the synthesized NPs are proven to be catalytically active for the reduction of 4-nitrophenol and the hydrogenation of cinnamaldehyde. As a proof-of-concept experiment, NP arrays were used to

perform a catalyst screening to elucidate the relationship between the size of AuPd NPs and their catalytic activity.

## 5.2 Scale-up Synthesis of Polyelemental Nanoparticles

While we have shown in Chapter Two and Four that polyelemental NPs with unprecedented level of control over composition and structure can be achieved by SPBCL, the particles are all generated with individual atomic force microscopy (AFM) probes, which limits the number of particles that can be obtained at a reasonable time scale. In order to obtain a sufficiently large quantity of particles for catalysis study, a large-scale cantilever-free scanning probe technique (*i.e.*, polymer pen lithography (PPL)) was used to synthesize NPs over centimeter areas. As shown in Figure 5.2, polymer pen lithography utilizes a massively parallel pen array, that are made by PDMS elastomers, to transport molecules directly on a centimeter area.<sup>186</sup> The PPL pen array consists of up to 11 million pyramidal pens with tip diameter of  $80 \pm 10$  nm, which allows for simultaneous deposition of molecules to accelerate the printing process. In a typical PPL experiment, the pen array was mounted on an AFM scanner and brought into contact with a substrate to transport ink molecules. The size of the printed features is facilely controlled by the diffusion time of ink molecules, *i.e.*, the pen-substrate dwell time. Besides the time dependence of feature size, when pressing the pen array harder on a substrate with larger z-piezo extension, the pen will deform more severely due to its elastomeric property and allow the generation of larger features, showing z-piezo dependence of feature size.<sup>214</sup>

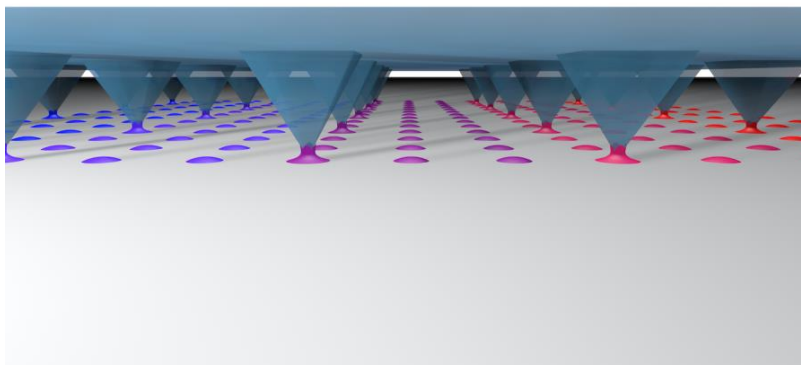


**Figure 5.2** Schematic illustration of polymer pen lithography (PPL) for centimeter area molecular printing.

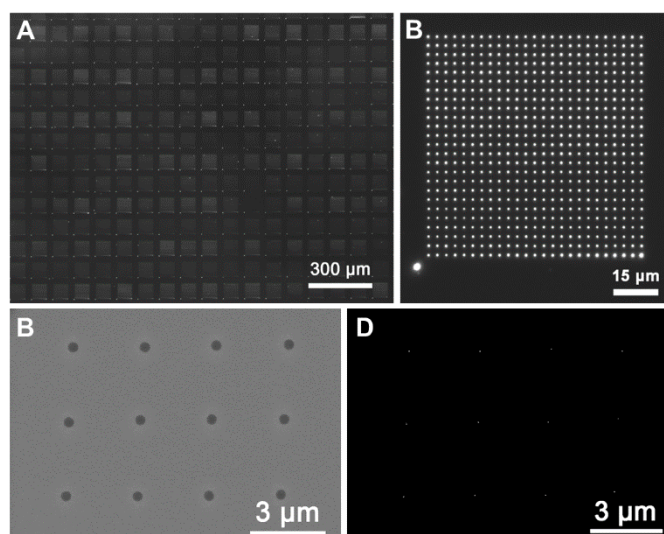


**Figure 5.3** PPL patterning of centimeter-scale AuPd nanoparticle arrays. (A) Dark-field optical microscopy image of a large-scale pattern of polymer dots. (B) Magnified dark-field image shows a 25-by-25 dot array with 3  $\mu\text{m}$  dot spacing. (C) SEM image of the polymer dot arrays printed by PPL. (D) SEM image of corresponding AuPd alloy nanoparticles formed after thermally annealing the polymer dots.

Experimentally, we combined SPBCL and PPL to simultaneously synthesize millions of polyelemental NPs on a 1  $\text{cm}^2$  area Si substrate (*e.g.*, AuPd and AuAgNi, Figure 5.3 and 5.4). In addition to Si, AuPd NPs were also successfully generated on oxide substrates such as  $\text{TiO}_2$  (Figure 5.5), which is a common support for catalysts. With the development of high throughput inking strategies<sup>216</sup> and increased polymer dome deposition densities, this technique will eventually allow

for simultaneous generation of billion types of particles over large areas (Figure 5.1).

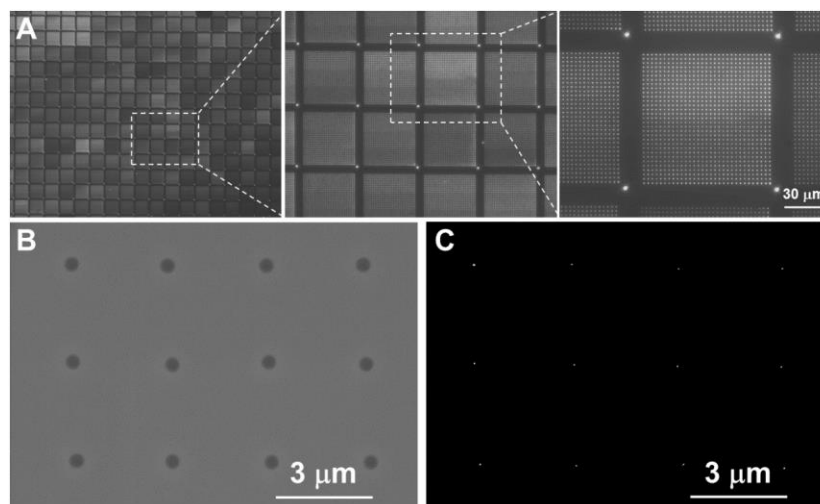


**Figure 5.4** Centimeter-scale AuAgNi nanoparticle arrays generated by a combination of SPBCL and Polymer Pen Lithography (PPL). (A) Dark-field optical microscopy image of a section of the centimeter-scale pattern of polymer features. (B) SEM image of the polymer features printed by PPL. (C) SEM image of the arrays of AuAgNi nanoparticles synthesized from the polymer nanoreactors that were printed by PPL.

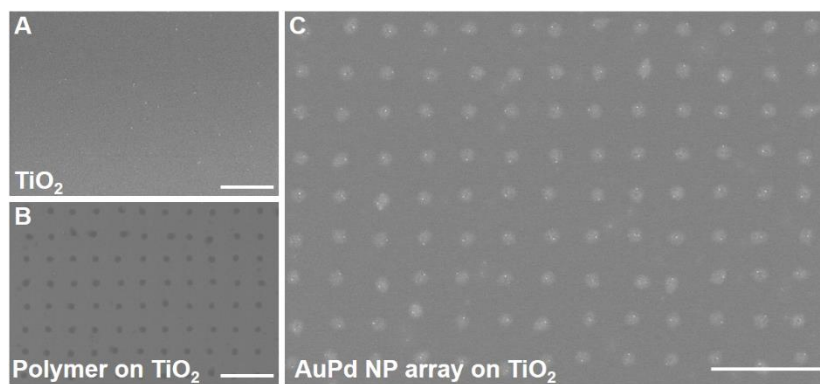


**Figure 5.5** Centimeter-scale AuPd nanoparticle arrays generated on  $\text{TiO}_2$  support. (A-C) SEM images of (A) a pristine  $\text{TiO}_2$  substrate, (B) polymer features printed on  $\text{TiO}_2$ , (C) an array of AuPd nanoparticles synthesized from the printed polymer features. Scale bars, 5  $\mu\text{m}$ .

### 5.3 Catalytic Reduction of 4-Nitrophenol

Multimetallic NPs have been widely studied for applications in catalysis.<sup>1,8,164</sup> For example, it has been demonstrated that AuPd alloy NPs exhibit superior activity as compared with NPs composed of Au or Pd alone for many chemical reactions including the reduction of 4-nitrophenol.<sup>212,213</sup> While we have shown that alloy NPs of this kind can be synthesized by SPBCL,

it remains to be seen whether or not these particles are catalytically active and possess the predicted enhanced activity. In particular, one could expect that the annealing process could leave a carbon-rich residue that blocks active sites and prevents activity. To examine the catalytic activity of NPs formed by SPBCL, arrays of Au, Pd, and AuPd NPs were used to catalyze the reduction of 4-nitrophenol with  $\text{NaBH}_4$  (Figure 5.6). While all samples with NPs exhibited significantly higher activity than the control samples prepared with inks containing just PEO-*b*-P2VP and no metal precursor, the AuPd alloy NPs showed the highest turnover number (Figure 5.6C and 5.6D), consistent with literature reports of how activity changes with composition.<sup>77,212,213</sup> Importantly, this result confirms that SPBCL is a viable method for integrating NP catalysts on a targeted surface.

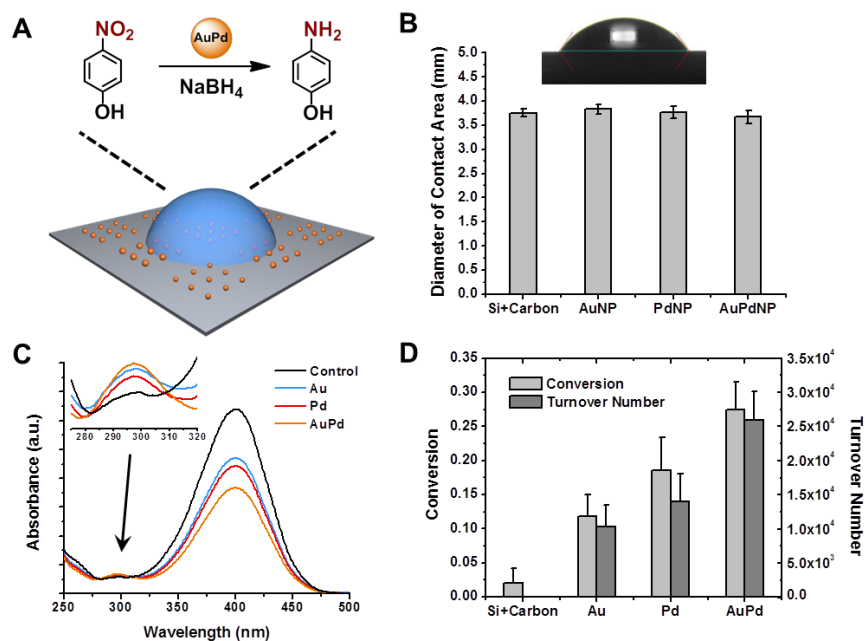


**Figure 5.6** Reduction of 4-nitrophenol catalyzed by a PPL-patterned nanoparticle array. (A) Scheme of the catalysis process. A 10  $\mu\text{L}$  aqueous droplet containing 4-nitrophenol and  $\text{NaBH}_4$  was dispensed onto a nanoparticle array. In the presence of nanoparticles, 4-nitrophenol was converted into 4-aminophenol. (B) The diameters of the contact area between droplets and various substrates were determined by a contact angle goniometer. About 0.7 million nanoparticles were covered by each droplet. Inset is a typical photograph of reactant droplet on PPL-patterned

nanoparticle array. (C) UV-Vis absorption spectra of the droplet solution after running catalysis on different substrates with product and reactant peaks at 296 nm and 400 nm, respectively. (D) Conversion percentage and turnover number of the reaction catalyzed by control sample (no particles), AuNP ( $16 \pm 2$  nm diameter) arrays, PdNP ( $16 \pm 3$  nm diameter) arrays, and AuPdNP ( $16 \pm 2$  nm diameter) arrays.

#### 5.4 Hydrogenation of Trans-Cinnamaldehyde

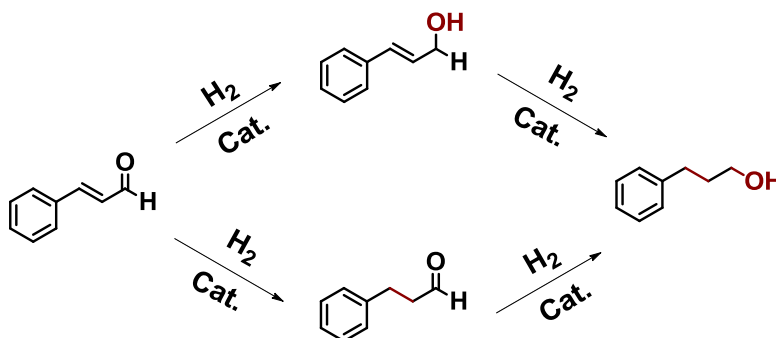


**Figure 5.7** General pathways for the hydrogenation of trans-cinnamaldehyde.

In addition to reduction reactions, we also examined the catalytic application of SPBCL NPs for hydrogenation reaction. An  $\alpha,\beta$ -unsaturated aldehyde, trans-cinnamaldehyde, that contains vinyl and carbonyl functional groups was chosen as the model reactant to evaluate whether or not PPL can afford sufficient number of NPs to catalyze hydrogenation (Figure 5.7). As depicted in Figure 5.8 (red line), Pd NPs, that are made by spin-coating a polymer film with subsequent thermal annealing, are active for the hydrogenation of cinnamaldehyde with high selectivity for hydrocinnamaldehyde. Only trace amounts of 3-phenyl-propanol could be detected under these reaction conditions. In contrast, patterned Pd NPs exhibited trace conversion of cinnamaldehyde into hydrocinnamaldehyde (Figure 5.8, blue line) while a Si substrate alone showed no activity in this reaction (Figure 5.8, black line). Since the NPs are synthesized through thermal decomposition of metal precursors and polymers, one could expect that carbon residue would be formed (Figure 5.9) and may partially block the active sites of NPs. To evaluate this influence, we thermally treated Pd NPs in  $O_2$  and  $H_2$  successively at  $400\text{ }^\circ\text{C}$ , then examined their

activity for cinnamaldehyde hydrogenation. After removing the carbon residue on patterned Pd NPs, the reaction conversion for cinnamaldehyde increased slightly (Figure 5.10). Therefore, the low reaction conversion on patterned Pd NPs can be attributed to the low particle density, since there is a 100-fold difference between the NP density of spin-coated and patterned samples. To apply SPBCL-synthesized NPs for hydrogenation reactions, either higher particle density on substrates or more sensitive product-detecting methods need to be developed.

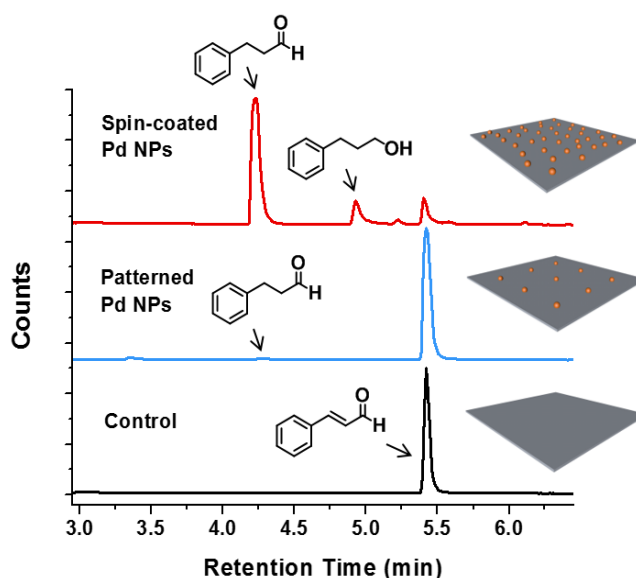


**Figure 5.8** Gas chromatograms of the catalytic hydrogenation of cinnamaldehyde mediated by Si (control, black line), PPL-patterned Pd nanoparticles with 1.5  $\mu\text{m}$  pitch (blue line, particle density 0.44  $\text{NP}/\mu\text{m}^2$ ), and spin-coated Pd nanoparticles (red line, particle density 40  $\text{NP}/\mu\text{m}^2$ ). Reaction conditions: 120  $\mu\text{L}$  0.5 mM cinnamaldehyde, 0.3  $\text{cm}^2$  samples, 1 MPa  $\text{H}_2$ , R.T., 24 h.

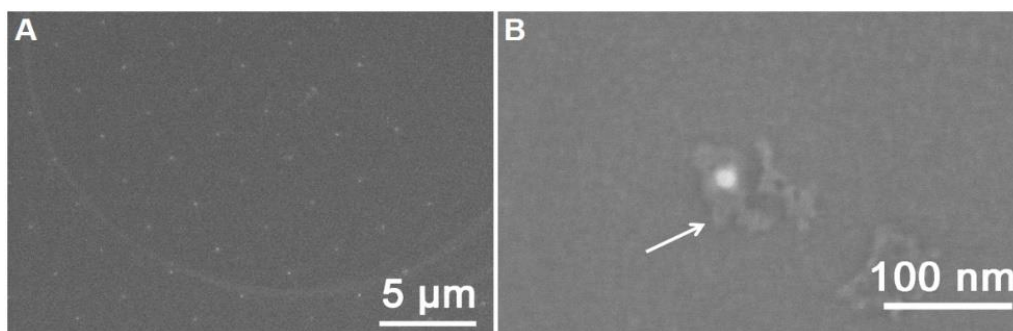


**Figure 5.9** (A) SEM image of PPL-patterned Pd nanoparticles with 2.5  $\mu\text{m}$  pitch on a Si substrate.

(B) Zoom-in SEM image of a single nanoparticle showing carbon residue around the particle.

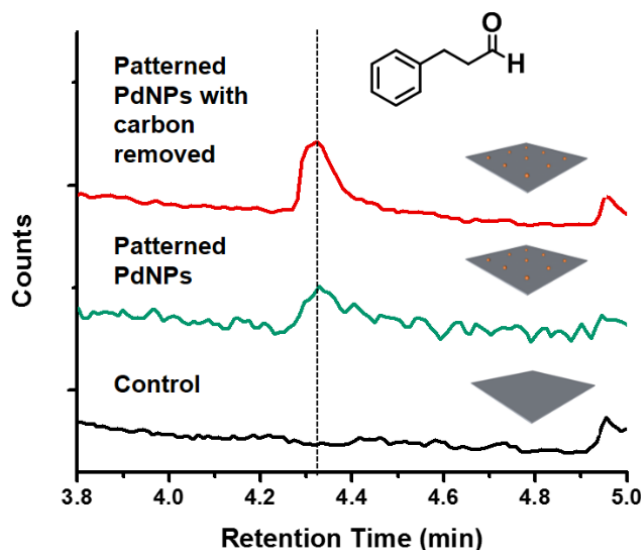


**Figure 5.10** Gas chromatograms of the catalytic hydrogenation of cinnamaldehyde mediated by Si (control, black line), PPL-patterned Pd nanoparticles with 1.5  $\mu\text{m}$  pitch (green line), and PPL-patterned Pd nanoparticles (1.5  $\mu\text{m}$  pitch, red line) annealed at 400  $^{\circ}\text{C}$  in  $\text{O}_2$  and  $\text{H}_2$  successively to remove carbon residue. Reaction conditions: 120  $\mu\text{L}$  0.5 mM cinnamaldehyde, 0.3  $\text{cm}^{-2}$  samples, 1 MPa  $\text{H}_2$ , R.T., 24 h.

### 5.5 Size Screening of AuPd Nanoparticle Catalysts

There are few systematic studies of the size-dependent catalytic activity of AuPd alloy NPs for the reduction of 4-nitrophenol. This deficiency can be understood by considering that in the conventional solution-based synthetic scheme, each unique size NP requires a distinct synthetic protocol. Thus, SBPCL potentially has a huge advantage here as one merely needs to tune lithographic parameters and the synthesis is performed locally. Thus, in order to demonstrate the application of SBPCL for screening NP catalysts, we synthesized an array of AuPd nanoalloys with a size gradient to perform a size screening experiment (Figure 5.11). To accomplish this, a tilted PPL patterning was carried out (Figure 5.11A) in which the contact area between the PPL pen array and the substrates decreases gradually along the tilting axis,<sup>214</sup> which led to a polymer array with dot size decreasing along this axis (Figure 5.11B and 5.11C). After thermal treatment,

an array of AuPd NPs was obtained that had a consistent spacing and a size gradient (Figure 5.11C and 5.11D). By performing the 4-nitrophenol-based catalytic assay on three regions with NP diameters ranging from 9 to 20 nm, we found that, while the total activity did not change appreciably with NP size, the catalyst-specific turnover number increased dramatically as NP size decreased (Figure 5.11E). We attribute this to the higher portion of under-coordinated atoms at the edges and corners of smaller NPs, which are more active than atoms on flat surfaces.<sup>4,8</sup> Alternatively, the difference in reactivity is probably owing to different electronic structure of NPs.<sup>9,213</sup>

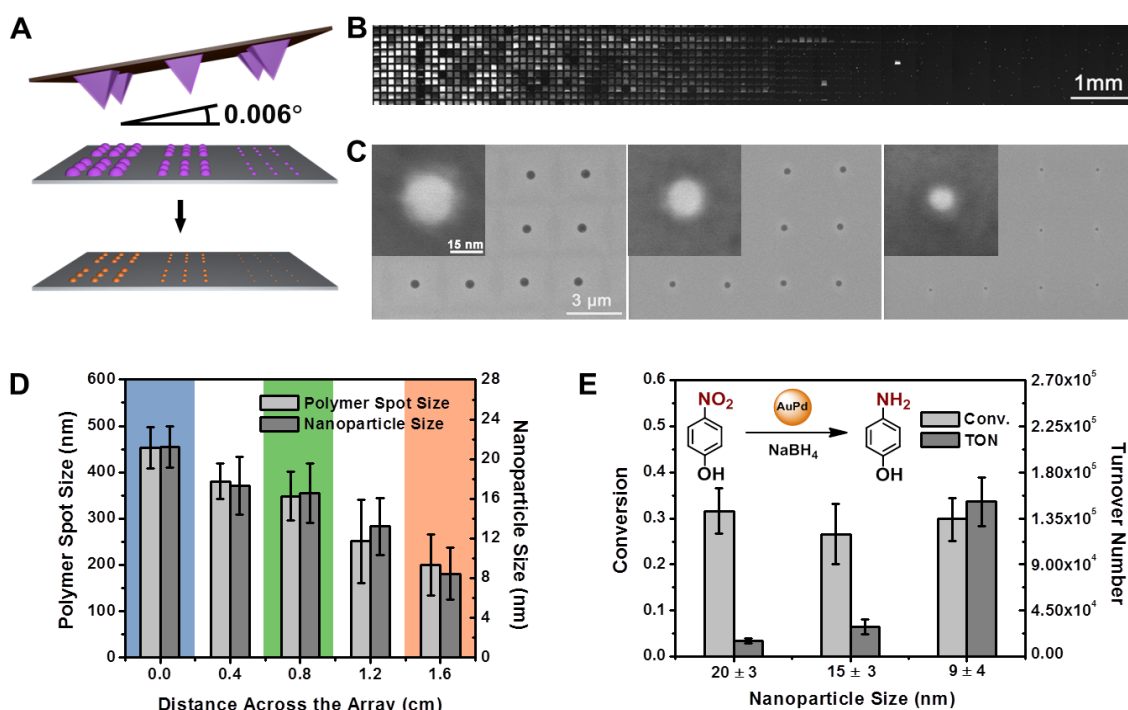


**Figure 5.11** Particle size effect on the activity of AuPd catalysts for the reduction of 4-nitrophenol. (A) Scheme of using a tilted polymer pen array to generate polymer dot array and corresponding AuPd nanoalloy array with size gradient. (B) Dark-field optical image of the gradient polymer dot array. (C) SEM images of the polymer dots on left, middle, and right sites of the gradient sample. Insets are SEM images of the resulting AuPd nanoalloys. The scale bars apply to all panels and insets. (D) The dependence of polymer dot size and corresponding alloy nanoparticle size on the distance from the one side of the gradient sample. (E) Conversion and turnover number of the reaction catalyzed by AuPd nanoalloy with various size. To study the size effect, three regions of

the gradient sample are used, namely the left side, middle, and right side (corresponding to the blue, green, and orange sections shown in (D)). The nanoparticle sizes in three regions are  $20 \pm 3$  nm,  $15 \pm 3$  nm, and  $9 \pm 4$  nm, respectively. The activity increases in the sequence of 20, 15, and 9 nm nanoparticles.

## 5.6 Materials and Methods

### 5.6.1 Materials

Poly(ethylene oxide)-*b*-poly(2-vinyl pyridine) (PEO-*b*-P2VP,  $M_n = 2.8$ - $1.5$  kg/mol, polydispersity index = 1.11) was purchased from Polymer Source, Inc. Metal compounds,  $\text{HAuCl}_4 \cdot 3\text{H}_2\text{O}$ ,  $\text{AgNO}_3$ ,  $\text{Cu}(\text{NO}_3)_2 \cdot x\text{H}_2\text{O}$ ,  $\text{Co}(\text{NO}_3)_2 \cdot 6\text{H}_2\text{O}$ ,  $\text{Ni}(\text{NO}_3)_2 \cdot 6\text{H}_2\text{O}$ ,  $\text{Na}_2\text{PdCl}_4$ , and  $\text{H}_2\text{PtCl}_6 \cdot 6\text{H}_2\text{O}$  were purchased from Sigma-Aldrich, Inc. and used without further purification. Hexamethyldisilazane (HMDS), sodium borohydride ( $\text{NaBH}_4$ ), 4-nitrophenol, *trans*-cinnamaldehyde, hydrocinnamaldehyde, cinnamyl alcohol, and 3-phenyl-propanol were purchased from Sigma-Aldrich, Inc. and used without further purification. Silicon wafers were purchased from Nova Electronic Materials.

### 5.6.2 Preparation of Block Copolymer Inks

Polymer inks were prepared by dissolving PEO-*b*-P2VP and different metal compounds in de-ionized water in predetermined molar ratios to achieve inks with specified molar ratios of metal precursors. The ink solution had a polymer concentration of 5 mg/mL and the molar ratio of pyridyl group to total metal precursors was 64:1. We expect that the use of an excess of pyridyl group will lead to a complete complexation of metal ions from the metal precursor salt onto PEO-*b*-P2VP. The pH of the ink solution was adjusted to between 3-4 by addition of  $\text{HNO}_3$ . The ink solution was stirred for 24 h at room temperature prior to use.

### 5.6.3 Polymer Pen Lithography (PPL) Patterning Process

Polymer pen arrays that are made of PDMS were used to perform SPBCL in a massively

parallel fashion.<sup>186</sup> The pen array was first treated with oxygen plasma (60 W, 4 min) to improve the conformity of ink coating. Following this step, the pen array was spin-coated with the ink solution (1000 rpm, 1 min), allowed to dry in air, and mounted onto an AFM (XE-150, Park Systems) to deposit polymer features on a Si substrate. The Si substrate was pre-treated with hexamethyldisilazane to make it hydrophobic. The patterning was carried out at a controlled temperature of 25 °C and relative humidity of 90%. For patterns with a size gradient along one axis, the pen arrays were tilted by approximately 0.006° with respect to the plane of substrate during patterning. The resulting polymer features were converted to NPs with thermal annealing. The heating process were programmed as follows: ramp to 120 °C under Ar in 1 h, hold at 120 °C for 48 h, cool back to room temperature in 4 h, switch the atmosphere into H<sub>2</sub>, ramp to 500 °C in 2 h, thermally anneal the substrate at 500 °C for 12 h, and cool down to room temperature in 6 h.

#### *5.6.4 Catalytic Reduction of 4-Nitrophenol*

To study the catalytic activity of patterned NPs, 5 µL of aqueous 4-nitrophenol solution (1.5 mmol/L) and 5 µL of freshly prepared aqueous NaBH<sub>4</sub> solution (750 mmol/L) were successively drop-cast onto a NP-patterned substrate. Then the substrate was stored in a 100% RH environment to minimize water evaporation. After allowing the reaction to proceed for 3 h at room temperature, both the substrate and the droplet were collected in an eppendorf tube. Another 140 µL of deionized water was added to rinse the substrate and dilute the droplet. The resulting solution was transferred into a quartz cuvette to collect UV-Vis adsorption spectra (Agilent Technologies, Cary 60). The difference in absorption at 400 and 525 nm, respectively, was used to quantify reaction conversion. A contact angle goniometer was used to measure the diameter of droplets in order to normalize the contact area between droplets and different substrates.

### 5.6.5 Hydrogenation of Cinnamaldehyde

To study the catalytic activity of NP-coated surfaces, a piece of spin-coated or NP-patterned substrate (about  $0.3 \text{ cm}^2$ ,  $1.5 \text{ }\mu\text{m}$  pitch for pattern substrate) and  $120 \text{ }\mu\text{L}$  of ethanolic solution of trans-cinnamaldehyde ( $0.5 \text{ mmol/L}$ ) were added into a  $2 \text{ mL}$  GC vial. A crimp cap was used to seal the vial and the septum was punched with a needle hole in order to allow gas transfer while minimizing solvent evaporation. The vial was then placed in a stainless-steel autoclave. The air content in the autoclave was minimized by pressurizing the autoclave with  $0.5 \text{ MPa}$  of Argon and then relieving the pressure for three cycles. Hydrogen was then introduced into the autoclave and hydrogenation reaction process was allowed to take place for  $24 \text{ h}$  under  $1 \text{ MPa H}_2$  at room temperature. In addition to reaction performed in GC vials, hydrogenation was also studied with well plate reactors. In a typical experiment, a piece of NP-patterned substrate ( $1 \text{ inch}$  by  $1 \text{ inch}$ , covering  $16$  wells) was put into a customized reactor and sealed by a PTFE gasket.  $120 \text{ }\mu\text{L}$  of an ethanolic solution of trans-cinnamaldehyde ( $0.5 \text{ mmol/L}$ ) were added into each well, followed by sealing the reactor with a PTFE/silicone septum. The septum was punched with  $16$  needle holes in order to allow gas transfer into wells while minimizing solvent evaporation. The reactor was then placed in a stainless-steel autoclave. The air content in the autoclave was minimized by pressurizing the autoclave with  $0.5 \text{ MPa}$  of argon and then relieving the pressure for three cycles. Hydrogen was then introduced into the autoclave and hydrogenation reaction process was allowed to take place for  $24 \text{ h}$  under  $1 \text{ MPa H}_2$  at room temperature.

### 5.6.6 Removal of Carbon Residue on Nanoparticles

To remove carbon residue and activate the catalysts, NP-patterned substrates were put into a tube furnace and heated in  $\text{O}_2$  and  $\text{H}_2$  successively. Typical heating conditions were as follows:

ramp to 400 °C under O<sub>2</sub> in 0.5 h, hold at 400 °C for 4 h, then cool back to room temperature, switch gas flow to H<sub>2</sub>, ramp to 400 °C in 0.5 h, hold the substrate at 400 °C for 4 h, and finally cool down to room temperature.

#### *5.6.7 Characterization*

SEM images of the NPs synthesized on Si or TiO<sub>2</sub> wafers were taken with a Hitachi S-8030 field-emission scanning electron microscope at an acceleration voltage of 5 kV and a current of 20 μA. For hydrogenation studies, the reaction mixtures were analyzed using a Waters Micromass GCT premier gas chromatograph time-of-flight mass spectrometer (GC-TOF-MS) equipped with a DB5 30-meter column. The column oven temperature was programmed from 100 °C to 235 °C at a ramp rate of 17 °C/min and then held at 235 °C for 3 minutes.

### **5.7 Conclusions and outlook**

In this chapter, we report that the combination of PPL and SPBCL can be used to scale up the synthesis of polyelemental NPs for catalysis study. In particular, this method is capable of synthesizing positionally encoded NPs wherein the size and composition of each NP in a centimeter-scale array is well known. Such arrays have enormous potential for catalyst discovery and optimization, as suggested by the initial studies presented here wherein we explored how AuPd NP size affects catalytic activity in the case of the reduction of 4-nitrophenol. Importantly, as this method relies upon an array of spatially separated polymer nanoreactors to synthesize individual NPs, it frees the experimentalist from synthesizing numerous batches of uniform NPs because each NP is locally defined by unique synthetic conditions. Given the diverse array of materials that can be used, this method could be applied to a number of important systems. Thus, one critical challenge going forward is to establish the degree to which polymer features can be independently

patterned through advances in individual pen actuation<sup>215</sup> and inking pens with distinct materials.<sup>216</sup> Another challenge is to establish high-throughput ways for characterizing the catalytic activities of polyelemental NPs, as a function of composition, size, phase, and architecture.

## **CHAPTER SIX**

Conclusions and Outlook

Despite the significance of polyelemental nanoparticles (NPs) in catalysis and many other fields, existing synthetic methods have limited access to the vast NP library, which bars the realization of the potential of polyelemental NPs. Since the inception of scanning probe block copolymer lithography (SPBCL), key concepts that will revolutionize the way people synthesize and study polyelemental NPs have been gradually developed. Specifically in this work, significant breakthroughs have been made to set SPBCL into a methodology capable of generating combinatorial libraries of NPs with unparalleled control over particle composition and structures. In this chapter, we summarize the results of Chapters Two-Five with an emphasis on research opportunities that have been made possible through our work, as well as propose potential future directions for SPBCL.

### **6.1 Tip-Directed Synthesis of Polyelemental Nanoparticle Libraries**

The limitation in synthesizing multimetallic NPs that contain three or more metals lies in the difficulties of balancing the reduction potentials of metal precursors, controlling the nucleation sites between metals, and understanding phase separation at the nanoscale. SPBCL stands to be a revolutionizing methodology that allows one to generate a nanoscale reactor consisting of a polymer feature with a predetermined metal ion content for the synthesis of a single NP. Chapter Two presents systematic studies on SPBCL-synthesized polyelemental NP systems where NP composition and size can be independently controlled, and where structure formation (alloy versus phase-separated state) can be understood. We have made libraries of NPs consisting of every combination of chosen elements (Au, Ag, Cu, Co, and Ni) through polymer nanoreactor-mediated synthesis. Important insight into the factors that lead to alloy formation and phase segregation at the nanoscale were obtained, and routes to libraries of nanostructures that cannot be made by

conventional methods were developed.

While Au, Ag, Co, Cu, and Ni were chosen as the model system to demonstrate the synthetic capability of SPBCL, the method has also been extended to NPs composed of other metals including Fe, Zn, Ru, Rh, Pd, Cd, Ir, Pt, Sn, and Se (Figure 6.1). Nevertheless, elements such as Ti, Si, and Zr have not been investigated because their available precursors (TiCl<sub>4</sub>, SiCl<sub>4</sub>, and ZrCl<sub>4</sub>) are hydrolyzable in water, which will increase the difficulty of making a uniform aqueous ink solution. To broaden the applicability of SPBCL to these metals, it is worth to seek water-soluble and non-hydrolyzable precursors in the future. Besides, the record of elements systematically examined thus far stands at seven. It remains unclear about the maximum number of elements that can be incorporated into a single NP. Future efforts can be put on extending SPBCL to more combinations of elements. These studies will provide insight into the synthetic limits of SPBCL and the formation processes of specific metal combinations, which may require variations in thermal treatment.

H																				He
Li	Be											B	C	N	O	F				Ne
Na	Mg											Al	Si	P	S	Cl				Ar
K	Ca	Sc	Ti	V	Cr	Mn	Fe	Co	Ni	Cu	Zn	Ga	Ge	As	Se	Br				Kr
Rb	Sr	Y	Zr	Nb	Mo	Tc	Ru	Rh	Pd	Ag	Cd	In	Sn	Sb	Te	I				Xe
Cs	Ba	L	Hf	Ta	W	Re	Os	Ir	Pt	Au	Hg	Tl	Pb	Bi	Po	At				Rn
Fr	Ra	A																		n

Legend:

- SPBCL synthesized (Green)
- Hydrolyzable precursor (Pink)
- Not tested (Yellow)
- No available precursor (White)

**Figure 6.1** Elements that potentially can be used to synthesize nanoparticles by SPBCL.

## 6.2 Structural Evolution of Polyelemental Nanoparticles in Polymer Nanoreactors

To reveal the process by which multimetallic NPs form in SPBCL-patterned nanoreactors.

In Chapter Three, we utilize the combination of PEO-*b*-P2VP and Au, Ag, and Cu salts as a model

three-component system to investigate this process. The results suggest that the formation of single-component NPs (Au, Ag, or Cu) within polymer nanoreactors consists of two stages: I) nucleation, growth, and coarsening of the particles to yield a single NP in each reactor; II) the NP continues to grow by depleting the remaining precursor in the reactor until it reaches a stable size. Also, different aggregation rates were observed for single-component NP formation (Au>Ag>Cu). With multimetallic systems, the different aggregation rates lead to the formation of kinetically trapped structures. High temperature treatment ultimately facilitates the structural evolution of the kinetic NP into a NP with a fixed structure. Therefore, a three-stage process that involves elemental redistribution within the particle is used to describe the synthetic process of multimetallic NPs. As such, the work in Chapter Three not only provides a glimpse at the mechanism underlying multimetallic NP formation in SPBCL but also illustrates, for the first time, the potential of using SPBCL as a platform to study the architectural evolution of multimetallic NPs.

Since metal aggregation mainly occurs after precursor salts being chemically reduced or thermally decomposed, the rates of metal aggregation are highly dictated by the chemical/thermal stability of precursors. Therefore, a combination of different precursors will in theory allow for the tuning of metal aggregation rates, thus enabling richer types of kinetic NPs with architectures that may have enhanced properties of interest. In addition, one key factor that has yet to be investigated is the fundamental role that the polymer plays during NP synthesis. In particular, insight into the chemical forces that drive the formation of a single NP in the polymer reactor need to be understood. Such studies will inform which polymers best facilitate NP formation and how to control the SPBCL process for refined structural control. Taken together Chapter Two and Three, the interplay of metal miscibility, particle composition, polymer type, precursor type, and thermal

treatment condition will provide rich avenues to control polyelemental NP structures.

### **6.3 Heterostructure Engineering in Polyelemental Nanoparticles**

For polyelemental nanomaterials, there is still a poor understanding of how phases form in such structures and how specific classes of interfaces can be designed and synthesized. In Chapter Four, SPBCL is used to explore how PdSn alloys form mixed composition phases with metals with known but complex miscibilities. NPs with up to seven elements are synthesized, and many form unique tri-phase heterostructures consisting of either pie-shaped or striped architectures. Density functional theory simulation and experimental work have been used together to show that NP architectures are a consequence of the balance between surface and interfacial energies. From these observations, design rules have been established for making polyelemental systems with specific heterostructures, as demonstrated by the synthesis of tetra-phase NPs with six junctions.

While the maximum numbers of phases and interfaces in a NP we have explored stand at four and six, respectively, the combination of Au, Ag, Cu, Co, Ni, Sn, and Pd in theory can lead to NPs with as many as five phases (AuAg-AuCu-CoNi-NiSn-PdSn) if the particle composition is finely tuned. In this case, the NPs may have up to ten types of interfaces, the architectures of which are challenging to anticipate by any conventional means. The guidelines developed in our work will be particularly useful in elucidating such complex NPs containing more than four phases. The ability to predict and control interface configuration is important for developing polyelemental nanomaterials featuring functional interfaces by design. This chapter stands to impact the development of heterostructured nanomaterials spanning many fields.

### **6.4 Combinatorial Synthesis of Polyelemental Nanoparticles for Catalyst Screening**

Combinatorial NP arrays integrated on a single substrate could become a promising

platform for high-efficiency catalyst screening. Building on the broad synthetic capabilities of SPBCL, in Chapter Five, we have combined SPBCL with large-area cantilever-free scanning probe techniques to scale up the synthesis of polyelemental NPs over centimeter-scale regions. It is found that polymer pen lithography can afford the ability to synthesize a sufficiently large number of NPs to enable the study of catalytic reduction of 4-nitrophenol. In addition, using tilted polymer pen lithography patterning, we have made arrays of AuPd NPs with varying size continuously across a centimeter-scale. Such arrays are employed to explore the size-dependent activity of AuPd NPs, which shows the potential of SPBCL for combinatorial catalyst screening. While the size gradient of NPs only accounts for one dimension of variables in the NP array, future study can be focused on finding more effective strategies in constructing NP arrays with several dimensions of variables (*e.g.*, composition, size, phase, and architecture), as well as establishing high-throughput ways for characterizing the properties of NPs on substrates.

## 6.5 Summary

The ultimate goal of SPBCL is to revolutionize the methodology of studying polyelemental NPs for target applications. It is anticipated that with the unparalleled synthetic capabilities of SPBCL established in this work, future study can continue along the direction toward high-efficiency combinatorial screening of polyelemental nanomaterials. While the goal may seem ambitious, the accomplishments demonstrated in this work have indicated its feasibility. With appropriate effort and innovation, following research will undoubtedly hold promise for discovering polyelemental nanomaterials that increase the sustainability and efficiency of chemical processes, as well as for finding materials that have potential to impact plasmonic, photonic, electronic, magnetic fields.

## REFERENCES

- (1) Ferrando, R.; Jellinek, J.; Johnston, R. L. Nanoalloys: From theory to applications of alloy clusters and nanoparticles. *Chem. Rev.* **2008**, *108*, 845-910.
- (2) Buck, M. R.; Schaak, R. E. Emerging Strategies for the Total Synthesis of Inorganic Nanostructures. *Angew. Chem. Int. Ed.* **2013**, *52*, 6154-6178.
- (3) Gilroy, K. D.; Ruditskiy, A.; Peng, H. C.; Qin, D.; Xia, Y. N. Bimetallic Nanocrystals: Syntheses, Properties, and Applications. *Chem. Rev.* **2016**, *116*, 10414-10472.
- (4) Sankar, M.; Dimitratos, N.; Miedziak, P. J.; Wells, P. P.; Kiely, C. J.; Hutchings, G. J. Designing bimetallic catalysts for a green and sustainable future. *Chem. Soc. Rev.* **2012**, *41*, 8099-8139.
- (5) Jiang, H. L.; Xu, Q. Recent progress in synergistic catalysis over heterometallic nanoparticles. *J. Mater. Chem.* **2011**, *21*, 13705-13725.
- (6) Alloyeau, D.; Mottet, C.; Ricolleau, C. Eds. *Nanoalloys Synthesis, Structure and Properties*; Springer: New York, NY, U.S.A., 2012.
- (7) Wang, D. S.; Li, Y. D. Bimetallic Nanocrystals: Liquid-Phase Synthesis and Catalytic Applications. *Adv. Mater.* **2011**, *23*, 1044-1060.
- (8) Chen, C.; Kang, Y.; Huo, Z.; Zhu, Z.; Huang, W.; Xin, H. L.; Snyder, J. D.; Li, D.; Herron, J. A.; Mavrikakis, M.; Chi, M.; More, K. L.; Li, Y.; Markovic, N. M.; Somorjai, G. A.; Yang, P.; Stamenkovic, V. R. Highly Crystalline Multimetallic Nanoframes with Three-Dimensional Electrocatalytic Surfaces. *Science* **2014**, *343*, 1339-1343.
- (9) Chen, G.; Zhao, Y.; Fu, G.; Duchesne, P. N.; Gu, L.; Zheng, Y.; Weng, X.; Chen, M.; Zhang, P.; Pao, C.-W.; Lee, J.-F.; Zheng, N. Interfacial Effects in Iron-Nickel Hydroxide-Platinum Nanoparticles Enhance Catalytic Oxidation. *Science* **2014**, *344*, 495-499.
- (10) Cortie, M. B.; McDonagh, A. M. Synthesis and Optical Properties of Hybrid and Alloy Plasmonic Nanoparticles. *Chem. Rev.* **2011**, *111*, 3713-3735.
- (11) Gordon, T. R.; Schaak, R. E. Synthesis of Hybrid Au-In<sub>2</sub>O<sub>3</sub> Nanoparticles Exhibiting Dual Plasmonic Resonance. *Chem. Mater.* **2014**, *26*, 5900-5904.
- (12) Hong, J. W.; Wi, D. H.; Lee, S. U.; Han, S. W. Metal-Semiconductor Heteronanocrystals with Desired Configurations for Plasmonic Photocatalysis. *J. Am. Chem. Soc.* **2016**, *138*, 15766-15773.
- (13) Lin, M.; Kim, G. H.; Kim, J. H.; Oh, J. W.; Nam, J. M. Transformative Heterointerface Evolution and Plasmonic Tuning of Anisotropic Trimetallic Nanoparticles. *J. Am. Chem. Soc.* **2017**, *139*, 10180-10183.
- (14) Mokari, T.; Rothenberg, E.; Popov, I.; Costi, R.; Banin, U. Selective growth of metal tips onto semiconductor quantum rods and tetrapods. *Science* **2004**, *304*, 1787-1790.
- (15) Oh, N. R.; Kim, B. H.; Cho, S. Y.; Nam, S.; Rogers, S. P.; Jiang, Y. R.; Flanagan, J. C.; Zhai, Y.; Kim, J. H.; Lee, J. Y.; Yu, Y. J.; Cho, Y. K.; Hur, G.; Zhang, J. Q.; Trefonas, P.; Rogers, J. A.; Shim, M. Double-heterojunction nanorod light-responsive LEDs for display applications. *Science* **2017**, *355*, 616-619.
- (16) Figuerola, A.; Fiore, A.; Di Corato, R.; Falqui, A.; Giannini, C.; Micotti, E.; Lascialfari, A.; Corti, M.; Cingolani, R.; Pellegrino, T.; Cozzoli, P. D.; Manna, L. One-pot synthesis and characterization of size-controlled bimagnetic FePt-iron oxide heterodimer nanocrystals. *J. Am. Chem. Soc.* **2008**, *130*, 1477-1487.
- (17) Antoniuk, C.; Gruner, M. E.; Spasova, M.; Trunova, A. V.; Romer, F. M.; Warland, A.; Krumme, B.; Fauth, K.; Sun, S. H.; Entel, P.; Farle, M.; Wende, H. A guideline for atomistic

- design and understanding of ultrahard nanomagnets. *Nat. Commun.* **2011**, *2*, 528.
- (18) Xu, C.; Wang, B.; Sun, S. Dumbbell-like Au-Fe<sub>3</sub>O<sub>4</sub> Nanoparticles for Target-Specific Platin Delivery. *J. Am. Chem. Soc.* **2009**, *131*, 4216-4217.
- (19) Jiang, J.; Gu, H. W.; Shao, H. L.; Devlin, E.; Papaefthymiou, G. C.; Ying, J. Y. Manipulation Bifunctional Fe<sub>3</sub>O<sub>4</sub>-Ag Heterodimer Nanoparticles for Two-Photon Fluorescence Imaging and Magnetic Manipulation. *Adv. Mater.* **2008**, *20*, 4403-4407.
- (20) Rodriguez-Fernandez, D.; Langer, J.; Henriksen-Lacey, M.; Liz-Marzan, L. M. Hybrid Au-SiO<sub>2</sub> Core-Satellite Colloids as Switchable SERS Tags. *Chem. Mater.* **2015**, *27*, 2540-2545.
- (21) Xie, J.; Zhang, F.; Aronova, M.; Zhu, L.; Lin, X.; Quan, Q. M.; Liu, G.; Zhang, G. F.; Choi, K. Y.; Kim, K.; Sun, X. L.; Lee, S.; Sun, S. H.; Leapman, R.; Chen, X. Y. Manipulating the Power of an Additional Phase: A Flower-like Au-Fe<sub>3</sub>O<sub>4</sub> Optical Nanosensor for Imaging Protease Expressions In vivo. *ACS Nano* **2011**, *5*, 3043-3051.
- (22) George, C.; Genovese, A.; Casu, A.; Prato, M.; Povia, M.; Manna, L.; Montanari, T. CO Oxidation on Colloidal Au<sub>0.80</sub>Pd<sub>0.20</sub>-Fe<sub>x</sub>O<sub>y</sub> Dumbbell Nanocrystals. *Nano Lett.* **2013**, *13*, 752-757.
- (23) Demortiere, A.; Schaller, R. D.; Li, T.; Chattopadhyay, S.; Krylova, G.; Shibata, T.; Claro, P. C. d. S.; Rowland, C. E.; Miller, J. T.; Cook, R.; Lee, B.; Shevchenko, E. V. In Situ Optical and Structural Studies on Photoluminescence Quenching in CdSe/CdS/Au Heterostructures. *J. Am. Chem. Soc.* **2014**, *136*, 2342-2350.
- (24) Li, L.; Chen, X.; Wu, Y.; Wang, D.; Peng, Q.; Zhou, G.; Li, Y. Pd-Cu<sub>2</sub>O and Ag-Cu<sub>2</sub>O Hybrid Concave Nanomaterials for an Effective Synergistic Catalyst. *Angew. Chem. Int. Ed.* **2013**, *52*, 11049-11053.
- (25) Wang, C.; Yin, H. F.; Dai, S.; Sun, S. H. A General Approach to Noble Metal-Metal Oxide Dumbbell Nanoparticles and Their Catalytic Application for CO Oxidation. *Chem. Mater.* **2010**, *22*, 3277-3282.
- (26) Li, P.; Wei, Z.; Wu, T.; Peng, Q.; Li, Y. Au-ZnO Hybrid Nanopyramids and Their Photocatalytic Properties. *J. Am. Chem. Soc.* **2011**, *133*, 5660-5663.
- (27) Ye, X. C.; Hickey, D. R.; Fei, J. Y.; Diroll, B. T.; Paik, T.; Chen, J.; Murray, C. B. Seeded Growth of Metal-Doped Plasmonic Oxide Heterodimer Nanocrystals and Their Chemical Transformation. *J. Am. Chem. Soc.* **2014**, *136*, 5106-5115.
- (28) Yu, X.; Shavel, A.; An, X.; Luo, Z.; Ibanez, M.; Cabot, A. Cu<sub>2</sub>ZnSnS<sub>4</sub>-Pt and Cu<sub>2</sub>ZnSnS<sub>4</sub>-Au Heterostructured Nanoparticles for Photocatalytic Water Splitting and Pollutant Degradation. *J. Am. Chem. Soc.* **2014**, *136*, 9236-9239.
- (29) Najafshirvari, S.; Guardia, P.; Scarpellini, A.; Prato, M.; Marras, S.; Manna, L.; Colombo, M. The effect of Au domain size on the CO oxidation catalytic activity of colloidal Au-FeOx dumbbell-like heterodimers. *J. Catal.* **2016**, *338*, 115-123.
- (30) Serpell, C. J.; Cookson, J.; Ozkaya, D.; Beer, P. D. Core@shell bimetallic nanoparticle synthesis via anion coordination. *Nat. Chem.* **2011**, *3*, 478-483.
- (31) Campbell, C. T. CATALYST-SUPPORT INTERACTIONS Electronic perturbations. *Nat. Chem.* **2012**, *4*, 597-598.
- (32) Weng, L.; Zhang, H.; Govorov, A. O.; Ouyang, M. Hierarchical synthesis of non-centrosymmetric hybrid nanostructures and enabled plasmon-driven photocatalysis. *Nat. Commun.* **2014**, *5*, 4792.
- (33) Sun, Y. G.; Foley, J. J.; Peng, S.; Li, Z.; Gray, S. K. Interfaced Metal Heterodimers in the

- Quantum Size Regime. *Nano Lett.* **2013**, *13*, 3958-3964.
- (34) Ge, H. B.; Zhang, B.; Gu, X. M.; Liang, H. J.; Yang, H. M.; Gao, Z.; Wang, J. G.; Qin, Y. A Tandem Catalyst with Multiple Metal Oxide Interfaces Produced by Atomic Layer Deposition. *Angew. Chem. Int. Ed.* **2016**, *55*, 7081-7085.
- (35) Zhao, M. T.; Deng, K.; He, L. C.; Liu, Y.; Li, G. D.; Zhao, H. J.; Tang, Z. Y. Core-Shell Palladium Nanoparticle@Metal-Organic Frameworks as Multifunctional Catalysts for Cascade Reactions. *J. Am. Chem. Soc.* **2014**, *136*, 1738-1741.
- (36) Schick, I.; Lorenz, S.; Gehrig, D.; Schilman, A. M.; Bauer, H.; Panthofer, M.; Fischer, K.; Strand, D.; Laquai, F.; Tremel, W. Multifunctional Two-Photon Active Silica-Coated Au@MnO Janus Particles for Selective Dual Functionalization and Imaging. *J. Am. Chem. Soc.* **2014**, *136*, 2473-2483.
- (37) Su, J.; Xie, C. L.; Chen, C.; Yu, Y.; Kennedy, G.; Somorjai, G. A.; Yang, P. D. Insights into the Mechanism of Tandem Alkene Hydroformylation over a Nanostructured Catalyst with Multiple Interfaces. *J. Am. Chem. Soc.* **2016**, *138*, 11568-11574.
- (38) Kamat, P. V. Manipulation of Charge Transfer Across Semiconductor Interface. A Criterion That Cannot Be Ignored in Photocatalyst Design. *J. Phys. Chem. Lett.* **2012**, *3*, 663-672.
- (39) Xie, C. L.; Chen, C.; Yu, Y.; Su, J.; Li, Y. F.; Somorjai, G. A.; Yang, P. D. Tandem Catalysis for CO<sub>2</sub> Hydrogenation to C<sub>2</sub>-C<sub>4</sub> Hydrocarbons. *Nano Lett.* **2017**, *17*, 3798-3802.
- (40) Choi, S. I.; Xie, S. F.; Shao, M. H.; Odell, J. H.; Lu, N.; Peng, H. C.; Protsailo, L.; Guerrero, S.; Park, J. H.; Xia, X. H.; Wang, J. G.; Kim, M. J.; Xia, Y. N. Synthesis and Characterization of 9 nm Pt-Ni Octahedra with a Record High Activity of 3.3 A/mg(Pt) for the Oxygen Reduction Reaction. *Nano Lett.* **2013**, *13*, 3420-3425.
- (41) Climent, M. J.; Corma, A.; Iborra, S.; Sabater, M. J. Heterogeneous Catalysis for Tandem Reactions. *ACS Catal.* **2014**, *4*, 870-891.
- (42) Sankar, M.; He, Q.; Dawson, S.; Nowicka, E.; Lu, L.; Bruijninx, P. C. A.; Beale, A. M.; Kiely, C. J.; Weckhuysen, B. M. Supported bimetallic nano-alloys as highly active catalysts for the one-pot tandem synthesis of imines and secondary amines from nitrobenzene and alcohols. *Catal. Sci. Technol.* **2016**, *6*, 5473-5482.
- (43) Parlett, C. M. A.; Isaacs, M. A.; Beaumont, S. K.; Bingham, L. M.; Hondow, N. S.; Wilson, K.; Lee, A. F. Spatially orthogonal chemical functionalization of a hierarchical pore network for catalytic cascade reactions. *Nat. Mater.* **2016**, *15*, 178-182.
- (44) Shaabani, A.; Hezarkhani, Z.; Nejad, M. K. AuCu and AgCu bimetallic nanoparticles supported on guanidine-modified reduced graphene oxide nanosheets as catalysts in the reduction of nitroarenes: tandem synthesis of benzo b 1,4 diazepine derivatives. *RSC Adv.* **2016**, *6*, 30247-30257.
- (45) Min, Y.; Kwak, J.; Soon, A.; Jeong, U. Nonstoichiometric Nucleation and Growth of Multicomponent Nanocrystals in Solution. *Acc. Chem. Res.* **2014**, *47*, 2887-2893.
- (46) Hodges, J. M.; Morse, J. R.; Williams, M. E.; Schaak, R. E. Microscopic Investigation of Chemoselectivity in Ag-Pt-Fe<sub>3</sub>O<sub>4</sub> Heterotrimer Formation: Mechanistic Insights and Implications for Controlling High-Order Hybrid Nanoparticle Morphology. *J. Am. Chem. Soc.* **2015**, *137*, 15493-15500.
- (47) Read, C. G.; Gordon, T. R.; Hodges, J. M.; Schaak, R. E. Colloidal Hybrid Nanoparticle Insertion Reaction for Transforming Heterodimers into Heterotrimers. *J. Am. Chem. Soc.* **2015**, *137*, 12514-12517.

- (48) Buck, M. R.; Bondi, J. F.; Schaak, R. E. A total-synthesis framework for the construction of high-order colloidal hybrid nanoparticles. *Nat. Chem.* **2012**, *4*, 37-44.
- (49) Kwon, S. G.; Krylova, G.; Phillips, P. J.; Klie, R. F.; Chattopadhyay, S.; Shibata, T.; Bunel, E. E.; Liu, Y. Z.; Prakapenka, V. B.; Lee, B.; Shevchenko, E. V. Heterogeneous nucleation and shape transformation of multicomponent metallic nanostructures. *Nat. Mater.* **2015**, *14*, 215-223.
- (50) McKeown, J. T.; Wu, Y. Y.; Fowlkes, J. D.; Rack, P. D.; Campbell, G. H. Simultaneous In-Situ Synthesis and Characterization of Co@Cu Core-Shell Nanoparticle Arrays. *Adv. Mater.* **2015**, *27*, 1060-1065.
- (51) Zhou, S. H.; Yin, H. F.; Schwartz, V.; Wu, Z. L.; Mullins, D.; Eichhorn, B.; Overbury, S. H.; Dai, S. In Situ Phase Separation of NiAu Alloy Nanoparticles for Preparing Highly Active Au/NiO CO Oxidation Catalysts. *ChemPhysChem* **2008**, *9*, 2475-2479.
- (52) Mbenkum, B. N.; Diaz-Ortiz, A.; Gu, L.; van Aken, P. A.; Schutz, G. Expanding Micelle Nanolithography to the Self-Assembly of Multicomponent Core Shell Nanoparticles. *J. Am. Chem. Soc.* **2010**, *132*, 10671-10673.
- (53) Sneed, B. T.; Brodsky, C. N.; Kuo, C. H.; Lamontagne, L. K.; Jiang, Y.; Wang, Y.; Tao, F.; Huang, W. X.; Tsung, C. K. Nanoscale-Phase-Separated Pd-Rh Boxes Synthesized via Metal Migration: An Archetype for Studying Lattice Strain and Composition Effects in Electrocatalysis. *J. Am. Chem. Soc.* **2013**, *135*, 14691-14700.
- (54) Uemura, Y.; Inada, Y.; Bando, K. K.; Sasaki, T.; Kamiuchi, N.; Eguchi, K.; Yagishita, A.; Nomura, M.; Tada, M.; Iwasawa, Y. Core-Shell Phase Separation and Structural Transformation of Pt<sub>3</sub>Sn Alloy Nanoparticles Supported on gamma-Al<sub>2</sub>O<sub>3</sub> in the Reduction and Oxidation Processes Characterized by In Situ Time-Resolved XAFS. *J. Phys. Chem. C* **2011**, *115*, 5823-5833.
- (55) Liu, M. H.; Zeng, H. C. General Synthetic Approach to Heterostructured Nanocrystals Based on Noble Metals and I-VI, II-VI, and I-III-VI Metal Chalcogenides. *Langmuir* **2014**, *30*, 9838-9849.
- (56) Guisbiers, G.; Khanal, S.; Ruiz-Zepeda, F.; de la Puente, J. R.; Jose-Yacaman, M. Cu-Ni nano-alloy: mixed, core-shell or Janus nano-particle? *Nanoscale* **2014**, *6*, 14630-14635.
- (57) Shirinyan, A. S.; Wautelet, M. Phase separation in nanoparticles. *Nanotechnology* **2004**, *15*, 1720-1731.
- (58) Calvo, F. Thermodynamics of nanoalloys. *Phys. Chem. Chem. Phys.* **2015**, *17*, 27922-27939.
- (59) Akbarzadeh, H.; Abbaspour, M.; Mehrjouei, E. Investigation of thermal, structural and dynamical properties of (Au-x-Cu-y-Ni-y)(N=32,108,256) ternary nanosystems: effect of Au addition to Cu-Ni bimetallic nanoclusters via MD simulation. *RSC Adv.* **2016**, *6*, 67619-67629.
- (60) Ertl, G.; Knozinger, H.; Shuth, F.; Weikamp, J. Eds. *Handbook of Heterogeneous Catalysis*; Wiley-VCH: Weinheim, Germany, 2008; Vol.1.
- (61) Spivey, J. J.; Han, Y.-F.; Dooley, K. M. Eds. *Catalysis*; RSC Publishing: Cambridge, UK, 2013; Vol.25.
- (62) Norskov, J. K.; Studt, F.; Abild-Pedersen, F.; Bligaard, T. *Fundamental Concepts in Heterogeneous Catalysis*; Wiley-VCH: Weinheim, Germany, 2014.
- (63) Heiz, U.; Landman, U. Eds. *Nanocatalysis*; Springer: New York, NY, U.S.A., 2007.
- (64) Cai, S. F.; Wang, D. S.; Niu, Z. Q.; Li, Y. D. Progress in organic reactions catalyzed by

- bimetallic nanomaterials. *Chin. J. Catal.* **2013**, *34*, 1964-1974.
- (65) Wang, A. Q.; Liu, X. Y.; Mou, C. Y.; Zhang, T. Understanding the synergistic effects of gold bimetallic catalysts. *J. Catal.* **2013**, *308*, 258-271.
- (66) Tsang, S. C.; Cailuo, N.; Oduro, W.; Kong, A. T. S.; Clifton, L.; Yu, K. M. K.; Thiebaut, B.; Cookson, J.; Bishop, P. Engineering Preformed Cobalt-Doped Platinum Nanocatalysts For Ultrasensitive Hydrogenation. *ACS Nano* **2008**, *2*, 2547-2553.
- (67) Ide, M. S.; Hao, B.; Neurock, M.; Davis, R. J. Mechanistic Insights on the Hydrogenation of alpha,beta-Unsaturated Ketones and Aldehydes to Unsaturated Alcohols over Metal Catalysts. *ACS Catal.* **2012**, *2*, 671-683.
- (68) Zhang, L.; Wang, A.; Miller, J. T.; Liu, X.; Yang, X.; Wang, W.; Li, L.; Huang, Y.; Mou, C. Y.; Zhang, T. Efficient and Durable Au Alloyed Pd Single-Atom Catalyst for the Ullmann Reaction of Aryl Chlorides in Water. *ACS Catal.* **2014**, *4*, 1546-1553.
- (69) Holgado, J. P.; Ternero, F.; Gonzalez-delaCruz, V. M.; Caballero, A. Promotional Effect of the Base Metal on Bimetallic Au-Ni/CeO<sub>2</sub> Catalysts Prepared from Core-Shell Nanoparticles. *ACS Catal.* **2013**, *3*, 2169-2180.
- (70) Joo, S. H.; Park, J. Y.; Tsung, C.-K.; Yamada, Y.; Yang, P.; Somorjai, G. A. Thermally stable Pt/mesoporous silica core-shell nanocatalysts for high-temperature reactions. *Nat. Mater.* **2009**, *8*, 126-131.
- (71) Green, I. X.; Tang, W. J.; Neurock, M.; Yates, J. T. Spectroscopic Observation of Dual Catalytic Sites During Oxidation of CO on a Au/TiO<sub>2</sub> Catalyst. *Science* **2011**, *333*, 736-739.
- (72) Saavedra, J.; Doan, H. A.; Pursell, C. J.; Grabow, L. C.; Chandler, B. D. The critical role of water at the gold-titania interface in catalytic CO oxidation. *Science* **2014**, *345*, 1599-1602.
- (73) Xie, S. H.; Tsunoyama, H.; Kurashige, W.; Negishi, Y.; Tsukuda, T. Enhancement in Aerobic Alcohol Oxidation Catalysis of Au-25 Clusters by Single Pd Atom Doping. *ACS Catal.* **2012**, *2*, 1519-1523.
- (74) Zhang, H. J.; Lu, L. L.; Kawashima, K.; Okumura, M.; Haruta, M.; Toshima, N. Synthesis and Catalytic Activity of Crown Jewel-Structured (IrPd)/Au Trimetallic Nanoclusters. *Adv. Mater.* **2015**, *27*, 1383-1388.
- (75) Cui, W. J.; Xiao, Q.; Sarina, S.; Ao, W. L.; Xie, M. X.; Zhu, H. Y.; Bao, Z. Au-Pd alloy nanoparticle catalyzed selective oxidation of benzyl alcohol and tandem synthesis of imines at ambient conditions. *Catal. Today* **2014**, *235*, 152-159.
- (76) Xiao, Q.; Liu, Z.; Bo, A.; Zavahir, S.; Sarina, S.; Bottle, S.; Riches, J. D.; Zhu, H. Y. Catalytic Transformation of Aliphatic Alcohols to Corresponding Esters in O<sub>2</sub> under Neutral Conditions Using Visible-Light Irradiation. *J. Am. Chem. Soc.* **2015**, *137*, 1956-1966.
- (77) Shi, L. H.; Wang, A. Q.; Zhang, T.; Zhang, B. S.; Su, D. S.; Li, H. Q.; Song, Y. J. One-Step Synthesis of Au-Pd Alloy Nanodendrites and Their Catalytic Activity. *J. Phys. Chem. C* **2013**, *117*, 12526-12536.
- (78) Kattel, S.; Liu, P.; Chen, J. G. G. Tuning Selectivity of CO<sub>2</sub> Hydrogenation Reactions at the Metal/Oxide Interface. *J. Am. Chem. Soc.* **2017**, *139*, 9739-9754.
- (79) Kattel, S.; Ramirez, P. J.; Chen, J. G.; Rodriguez, J. A.; Liu, P. CATALYSIS Active sites for CO<sub>2</sub> hydrogenation to methanol on Cu/ZnO catalysts. *Science* **2017**, *355*, 1296-1299.
- (80) Wang, Z. L.; Yan, J. M.; Ping, Y.; Wang, H. L.; Zheng, W. T.; Jiang, Q. An Efficient CoAuPd/C Catalyst for Hydrogen Generation from Formic Acid at Room Temperature.

- Angew. Chem. Int. Ed.* **2013**, *52*, 4406-4409.
- (81) Tedsree, K.; Li, T.; Jones, S.; Chan, C. W. A.; Yu, K. M. K.; Bagot, P. A. J.; Marquis, E. A.; Smith, G. D. W.; Tsang, S. C. E. Hydrogen production from formic acid decomposition at room temperature using a Ag-Pd core-shell nanocatalyst. *Nat. Nanotechnol.* **2011**, *6*, 302-307.
- (82) Huang, X.; Zhao, Z.; Cao, L.; Chen, Y.; Zhu, E.; Lin, Z.; Li, M.; Yan, A.; Zettl, A.; Wang, Y. M.; Duan, X.; Mueller, T.; Huang, Y. High-performance transition metal-doped Pt<sub>3</sub>Ni octahedra for oxygen reduction reaction. *Science* **2015**, *348*, 1230-1234.
- (83) Zhang, S. C.; Hu, Y.; Wu, J. X.; Liu, D.; Kang, L. X.; Zhao, Q. C.; Zhang, J. Selective Scission of C-O and C-C Bonds in Ethanol Using Bimetal Catalysts for the Preferential Growth of Semiconducting SWNT Arrays. *J. Am. Chem. Soc.* **2015**, *137*, 1012-1015.
- (84) Stratakis, M.; Garcia, H. Catalysis by Supported Gold Nanoparticles: Beyond Aerobic Oxidative Processes. *Chem. Rev.* **2012**, *112*, 4469-4506.
- (85) Sun, D. H.; Mazumder, V.; Metin, O.; Sun, S. H. Methanolysis of Ammonia Borane by CoPd Nanoparticles. *ACS Catal.* **2012**, *2*, 1290-1295.
- (86) Suib, S. L. Ed. *Catalysis by Nanoparticles*; Elsevier: Amsterdam, The Netherlands, 2013.
- (87) Horiuti, I.; Polanyi, M. Exchange reactions of hydrogen on metallic catalysts. *Trans. Faraday Soc.* **1934**, *30*, 1164-1172.
- (88) Bailie, J. E.; Hutchings, G. J. Promotion by sulfur of gold catalysts for crotyl alcohol formation from crotonaldehyde hydrogenation. *Chem. Commun.* **1999**, 2151-2152.
- (89) Milone, C.; Tropeano, M. L.; Gulino, G.; Neri, G.; Ingoglia, R.; Galvagno, S. Selective liquid phase hydrogenation of citral on Au/Fe<sub>2</sub>O<sub>3</sub> catalysts. *Chem. Commun.* **2002**, 868-869.
- (90) Mitsudome, T.; Kaneda, K. Gold nanoparticle catalysts for selective hydrogenations. *Green Chem.* **2013**, *15*, 2636-2654.
- (91) Mohr, C.; Hofmeister, H.; Claus, P. The influence of real structure of gold catalysts in the partial hydrogenation of acrolein. *J. Catal.* **2003**, *213*, 86-94.
- (92) Bratlie, K. M.; Lee, H.; Komvopoulos, K.; Yang, P.; Somorjai, G. A. Platinum nanoparticle shape effects on benzene hydrogenation selectivity. *Nano Lett.* **2007**, *7*, 3097-3101.
- (93) Telkar, M. M.; Rode, C. V.; Chaudhari, R. V.; Joshi, S. S.; Nalawade, A. M. Shape-controlled preparation and catalytic activity of metal nanoparticles for hydrogenation of 2-butyne-1,4-diol and styrene oxide. *Appl. Catal., A* **2004**, *273*, 11-19.
- (94) Studt, F.; Abild-Pedersen, F.; Bligaard, T.; Sorensen, R. Z.; Christensen, C. H.; Norskov, J. K. Identification of non-precious metal alloy catalysts for selective hydrogenation of acetylene. *Science* **2008**, *320*, 1320-1322.
- (95) Zhao, M. T.; Yuan, K.; Wang, Y.; Li, G. D.; Guo, J.; Gu, L.; Hu, W. P.; Zhao, H. J.; Tang, Z. Y. Metal-organic frameworks as selectivity regulators for hydrogenation reactions. *Nature* **2016**, *539*, 76-80.
- (96) Hungria, A. B.; Raja, R.; Adams, R. D.; Captain, B.; Thomas, J. M.; Midgley, P. A.; Golovko, V.; Johnson, B. F. G. Single-step conversion of dimethyl terephthalate into cyclohexanedimethanol with Ru<sub>5</sub>PtSn, a trimetallic nanoparticle catalyst. *Angew. Chem. Int. Ed.* **2006**, *45*, 4782-4785.
- (97) Toshima, N.; Ito, R.; Matsushita, T.; Shiraishi, Y. Trimetallic nanoparticles having a Au-core structure. *Catal. Today* **2007**, *122*, 239-244.

- (98) Faraday, M. Experimental relations of gold (and other metals) to light. *Phil. Trans. R. Soc. Lond.* **1857**, *147*, 145-181.
- (99) Astruc, D. Ed. *Nanoparticles and Catalysis*; Wiley-VCH: Weinheim, Germany, 2008.
- (100) Lee, H.; Habas, S. E.; Kweskin, S.; Butcher, D.; Somorjai, G. A.; Yang, P. Morphological control of catalytically active platinum nanocrystals. *Angew. Chem. Int. Ed.* **2006**, *45*, 7824-7828.
- (101) Li, Y. D.; Li, L. Q.; Liao, H. W.; Wang, H. R. Preparation of pure nickel, cobalt, nickel-cobalt and nickel-copper alloys by hydrothermal reduction. *J. Mater. Chem.* **1999**, *9*, 2675-2677.
- (102) Hou, P. F.; Liu, H.; Li, J. L.; Yang, J. One-pot synthesis of noble metal nanoparticles with a core-shell construction. *CrystEngComm* **2015**, *17*, 1826-1832.
- (103) Wang, D. S.; Li, Y. D. One-Pot Protocol for Au-Based Hybrid Magnetic Nanostructures via a Noble-Metal-Induced Reduction Process. *J. Am. Chem. Soc.* **2010**, *132*, 6280-6281.
- (104) Wu, Y. E.; Cai, S. F.; Wang, D. S.; He, W.; Li, Y. D. Syntheses of Water-Soluble Octahedral, Truncated Octahedral, and Cubic Pt-Ni Nanocrystals and Their Structure-Activity Study in Model Hydrogenation Reactions. *J. Am. Chem. Soc.* **2012**, *134*, 8975-8981.
- (105) Sang, W.; Zheng, T. T.; Wang, Y. C.; Li, X.; Zhao, X.; Zeng, J.; Hou, J. G. One-Step Synthesis of Hybrid Nanocrystals with Rational Tuning of the Morphology. *Nano Lett.* **2014**, *14*, 6666-6671.
- (106) Liu, X. W.; Wang, W. Y.; Li, H.; Li, L. S.; Zhou, G. B.; Yu, R.; Wang, D. S.; Li, Y. D. One-Pot Protocol for Bimetallic Pt/Cu Hexapod Concave Nanocrystals with Enhanced Electrocatalytic Activity. *Sci. Rep.* **2013**, *3*, 1404.
- (107) Wu, J.; Zhang, J.; Peng, Z.; Yang, S.; Wagner, F. T.; Yang, H. Truncated Octahedral Pt<sub>3</sub>Ni Oxygen Reduction Reaction Electrocatalysts. *J. Am. Chem. Soc.* **2010**, *132*, 4984-4985.
- (108) Guo, H. Z.; Chen, Y. Z.; Ping, H. M.; Wang, L. S.; Peng, D. L. One-pot synthesis of hexagonal and triangular nickel-copper alloy nanoplates and their magnetic and catalytic properties. *J. Mater. Chem.* **2012**, *22*, 8336-8344.
- (109) Dong, H.; Chen, Y. C.; Feldmann, C. Polyol synthesis of nanoparticles: status and options regarding metals, oxides, chalcogenides, and non-metal elements. *Green Chem.* **2015**, *17*, 4107-4132.
- (110) Mazumder, V.; Chi, M.; More, K. L.; Sun, S. Synthesis and Characterization of Multimetallic Pd/Au and Pd/Au/FePt Core/Shell Nanoparticles. *Angew. Chem. Int. Ed.* **2010**, *49*, 9368-9372.
- (111) Kirkemide, A.; Spurlin, S.; Draxler-Sixta, L.; Cooper, J.; Ren, S. Q. Metal Redox Processes for the Controlled Synthesis of Metal Alloy Nanoparticles. *Angew. Chem. Int. Ed.* **2015**, *54*, 4203-4207.
- (112) Zhang, Q.; Lee, I.; Joo, J. B.; Zaera, F.; Yin, Y. Core-Shell Nanostructured Catalysts. *Acc. Chem. Res.* **2013**, *46*, 1816-1824.
- (113) Chaudhuri, R. G.; Paria, S. Core/Shell Nanoparticles: Classes, Properties, Synthesis Mechanisms, Characterization, and Applications. *Chem. Rev.* **2012**, *112*, 2373-2433.
- (114) Hodges, J. M.; Schaak, R. E. Controlling Configurational Isomerism in Three-Component Colloidal Hybrid Nanoparticles. *Acc. Chem. Res.* **2017**, *50*, 1433-1440.
- (115) Hodges, J. M.; Biacchi, A. J.; Schaak, R. E. Ternary Hybrid Nanoparticle Isomers: Directing the Nucleation of Ag on Pt-Fe<sub>3</sub>O<sub>4</sub> Using a Solid-State Protecting Group. *ACS Nano* **2014**,

- 8, 1047-1055.
- (116) Hodges, J. M.; Morse, J. R.; Fenton, J. L.; Ackerman, J. D.; Alameda, L. T.; Schaak, R. E. Insights into the Seeded-Growth Synthesis of Colloidal Hybrid Nanoparticles. *Chem. Mater.* **2017**, *29*, 106-119.
- (117) Zhang, H. T.; Ding, J.; Chow, G. M.; Dong, Z. L. Engineering Inorganic Hybrid Nanoparticles: Tuning Combination Fashions of Gold, Platinum, and Iron Oxide. *Langmuir* **2008**, *24*, 13197-13202.
- (118) Yu, H.; Chen, M.; Rice, P. M.; Wang, S. X.; White, R. L.; Sun, S. H. Dumbbell-like bifunctional Au-Fe<sub>3</sub>O<sub>4</sub> nanoparticles. *Nano Lett.* **2005**, *5*, 379-382.
- (119) Shi, W. L.; Zeng, H.; Sahoo, Y.; Ohulchanskyy, T. Y.; Ding, Y.; Wang, Z. L.; Swihart, M.; Prasad, P. N. A general approach to binary and ternary hybrid nanocrystals. *Nano Lett.* **2006**, *6*, 875-881.
- (120) Costi, R.; Saunders, A. E.; Banin, U. Colloidal Hybrid Nanostructures: A New Type of Functional Materials. *Angew. Chem. Int. Ed.* **2010**, *49*, 4878-4897.
- (121) Chen, W.; Yu, R.; Li, L. L.; Wang, A. N.; Peng, Q.; Li, Y. D. A Seed-Based Diffusion Route to Monodisperse Intermetallic CuAu Nanocrystals. *Angew. Chem. Int. Ed.* **2010**, *49*, 2917-2921.
- (122) Zhang, L.; Roling, L. T.; Wang, X.; Vara, M.; Chi, M. F.; Liu, J. Y.; Choi, S. I.; Park, J.; Herron, J. A.; Xie, Z. X.; Mavrikakis, M.; Xia, Y. N. Platinum-based nanocages with subnanometer-thick walls and well-defined, controllable facets. *Science* **2015**, *349*, 412-416.
- (123) Bu, L. Z.; Zhang, N.; Guo, S. J.; Zhang, X.; Li, J.; Yao, J. L.; Wu, T.; Lu, G.; Ma, J. Y.; Su, D.; Huang, X. Q. Biaxially strained PtPb/Pt core/shell nanoplate boosts oxygen reduction catalysis. *Science* **2016**, *354*, 1410-1414.
- (124) Hodges, J. M.; Kletetschka, K.; Fenton, J. L.; Read, C. G.; Schaak, R. E. Sequential Anion and Cation Exchange Reactions for Complete Material Transformations of Nanoparticles with Morphological Retention. *Angew. Chem. Int. Ed.* **2015**, *54*, 8669-8672.
- (125) Sciacca, B.; Yalcin, A. O.; Garnett, E. C. Transformation of Ag Nanowires into Semiconducting AgFeS<sub>2</sub> Nanowires. *J. Am. Chem. Soc.* **2015**, *137*, 4340-4343.
- (126) Fenton, J. L.; Steimle, B. C.; Schaak, R. E. Tunable intraparticle frameworks for creating complex heterostructured nanoparticle libraries. *Science* **2018**, *360*, 513-517.
- (127) Benedetti, T. M.; Andronescu, C.; Cheong, S.; Wilde, P.; Wordsworth, J.; Kientz, M.; Tilley, R. D.; Schuhmann, W.; Gooding, J. J. Electrocatalytic Nanoparticles That Mimic the Three-Dimensional Geometric Architecture of Enzymes: Nanozymes. *J. Am. Chem. Soc.* **2018**, *140*, 13449-13455.
- (128) Sun, S. H.; Murray, C. B.; Weller, D.; Folks, L.; Moser, A. Monodisperse FePt nanoparticles and ferromagnetic FePt nanocrystal superlattices. *Science* **2000**, *287*, 1989-1992.
- (129) Bonnemann, H.; Brand, R. A.; Brijoux, W.; Hofstadt, H. W.; Frerichs, M.; Kempter, V.; Maus-Friedrichs, W.; Matoussevitch, N.; Nagabhushana, K. S.; Voigts, F.; Caps, V. Air stable Fe and Fe-Co magnetic fluids - synthesis and characterization. *Appl. Organomet. Chem.* **2005**, *19*, 790-796.
- (130) Robinson, I.; Zacchini, S.; Tung, L. D.; Maenosono, S.; Thanh, N. T. K. Synthesis and Characterization of Magnetic Nanoalloys from Bimetallic Carbonyl Clusters. *Chem. Mater.* **2009**, *21*, 3021-3026.
- (131) Ortiz-Soto, L.; Monnier, J.; Amiridis, M. Structure-sensitivity of propylene hydrogenation

- over cluster-derived bimetallic Pt-Au catalysts. *Catal. Lett.* **2006**, *107*, 13-17.
- (132) Thomas, J. M.; Johnson, B. F. G.; Raja, R.; Sankar, G.; Midgley, P. A. High-performance nanocatalysts for single-step hydrogenations. *Acc. Chem. Res.* **2003**, *36*, 20-30.
- (133) Yao, Y. G.; Huang, Z. N.; Xie, P. F.; Lacey, S. D.; Jacob, R. J.; Xie, H.; Chen, F. J.; Nie, A. M.; Pu, T. C.; Rehwoldt, M.; Yu, D. W.; Zachariah, M. R.; Wang, C.; Shahbazian-Yassar, R.; Li, J.; Hu, L. B. Carbothermal shock synthesis of high-entropy-alloy nanoparticles. *Science* **2018**, *359*, 1489-1494.
- (134) Yang, H.; Bradley, S. J.; Wu, X.; Chan, A.; Waterhouse, G. I. N.; Nann, T.; Zhang, J.; Kruger, P. E.; Ma, S. Q.; Telfer, S. G. General Synthetic Strategy for Libraries of Supported Multicomponent Metal Nanoparticles. *ACS Nano* **2018**, *12*, 4594-4604.
- (135) Radmilovic, V.; Ophus, C.; Marquis, E. A.; Rossell, M. D.; Tolley, A.; Gautam, A.; Asta, M.; Dahmen, U. Highly monodisperse core-shell particles created by solid-state reactions. *Nat. Mater.* **2011**, *10*, 710-715.
- (136) Zhou, B.; Han, S.; Raja, R.; Somorjai, G. A. Eds. *Nanotechnology in Catalysis*; Springer: New York, NY, U.S.A., 2007; Vol.3.
- (137) Pang, X. C.; Zhao, L.; Han, W.; Xin, X. K.; Lin, Z. Q. A general and robust strategy for the synthesis of nearly monodisperse colloidal nanocrystals. *Nat. Nanotechnol.* **2013**, *8*, 426-431.
- (138) Pang, X. C.; He, Y. J.; Jung, J. H.; Lin, Z. Q. 1D nanocrystals with precisely controlled dimensions, compositions, and architectures. *Science* **2016**, *353*, 1268-1272.
- (139) Scott, R. W. J.; Datye, A. K.; Crooks, R. M. Bimetallic palladium-platinum dendrimer-encapsulated catalysts. *J. Am. Chem. Soc.* **2003**, *125*, 3708-3709.
- (140) Yancey, D. F.; Carino, E. V.; Crooks, R. M. Electrochemical Synthesis and Electrocatalytic Properties of Au@Pt Dendrimer-Encapsulated Nanoparticles. *J. Am. Chem. Soc.* **2010**, *132*, 10988-10989.
- (141) Iyyamperumal, R.; Zhang, L.; Henkelman, G.; Crooks, R. M. Efficient Electrocatalytic Oxidation of Formic Acid Using Au@Pt Dendrimer-Encapsulated Nanoparticles. *J. Am. Chem. Soc.* **2013**, *135*, 5521-5524.
- (142) ten Hove, J. B.; Wang, J.; van Leeuwen, F. W. B.; Velders, A. H. Dendrimer-encapsulated nanoparticle-core micelles as a modular strategy for particle-in-a-box-in-a-box nanostructures. *Nanoscale* **2017**, *9*, 18619-18623.
- (143) Tsukamoto, T.; Kambe, T.; Nakao, A.; Imaoka, T.; Yamamoto, K. Atom-hybridization for synthesis of polymetallic clusters. *Nat. Commun.* **2018**, *9*, 3873.
- (144) Ganguli, A. K.; Ganguly, A.; Vaidya, S. Microemulsion-based synthesis of nanocrystalline materials. *Chem. Soc. Rev.* **2010**, *39*, 474-485.
- (145) Buceta, D.; Tojo, C.; Vukmirovic, M. B.; Deepak, F. L.; Lopez-Quintela, M. A. Controlling Bimetallic Nanostructures by the Microemulsion Method with Subnanometer Resolution Using a Prediction Model. *Langmuir* **2015**, *31*, 7435-7439.
- (146) Pileni, M. P. The role of soft colloidal templates in controlling the size and shape of inorganic nanocrystals. *Nat. Mater.* **2003**, *2*, 145-150.
- (147) McCaffrey, R.; Long, H.; Jin, Y. H.; Sanders, A.; Park, W.; Zhang, W. Template Synthesis of Gold Nanoparticles with an Organic Molecular Cage. *J. Am. Chem. Soc.* **2014**, *136*, 1782-1785.
- (148) Jiang, B. B.; Pang, X. C.; Li, B.; Lin, Z. Q. Organic-Inorganic Nanocomposites via Placing

- Monodisperse Ferroelectric Nanocrystals in Direct and Permanent Contact with Ferroelectric Polymers. *J. Am. Chem. Soc.* **2015**, *137*, 11760-11767.
- (149) Tanabe, I.; Tatsuma, T. Size- and Shape-Controlled Electrochemical Deposition of Metal Nanoparticles by Tapping Mode Atomic Force Microscopy. *J. Phys. Chem. C* **2012**, *116*, 3995-3999.
- (150) Doudna, C. M.; Bertino, M. F.; Blum, F. D.; Tokuhira, A. T.; Lahiri-Dey, D.; Chattopadhyay, S.; Terry, J. Radiolytic synthesis of bimetallic Ag-Pt nanoparticles with a high aspect ratio. *J. Phys. Chem. B* **2003**, *107*, 2966-2970.
- (151) Anandan, S.; Grieser, F.; Ashokkumar, M. Sonochemical synthesis of Au-Ag core-shell bimetallic nanoparticles. *J. Phys. Chem. C* **2008**, *112*, 15102-15105.
- (152) Luo, R. C.; Li, C.; Du, X. W.; Yang, J. Direct Conversion of Bulk Metals to Size-Tailored, Monodisperse Spherical Non-Coinage-Metal Nanocrystals. *Angew. Chem. Int. Ed.* **2015**, *54*, 4787-4791.
- (153) von Bojnicic-Kninski, C.; Popov, R.; Dorsam, E.; Loeffler, F. F.; Breitling, F.; Nesterov-Mueller, A. Combinatorial Particle Patterning. *Adv. Funct. Mater.* **2017**, *27*, 1703511.
- (154) Cheng, W. L.; Park, N. Y.; Walter, M. T.; Hartman, M. R.; Luo, D. Nanopatterning self-assembled nanoparticle superlattices by moulding microdroplets. *Nat. Nanotechnol.* **2008**, *3*, 682-690.
- (155) Kraus, T.; Malaquin, L.; Schmid, H.; Riess, W.; Spencer, N. D.; Wolf, H. Nanoparticle printing with single-particle resolution. *Nat. Nanotechnol.* **2007**, *2*, 570-576.
- (156) Flauraud, V.; Mastrangeli, M.; Bernasconi, G. D.; Butet, J.; Alexander, D. T. L.; Shahrabi, E.; Martin, O. J. F.; Brugger, J. Nanoscale topographical control of capillary assembly of nanoparticles. *Nat. Nanotechnol.* **2017**, *12*, 73-80.
- (157) Guo, Q. J.; Teng, X. W.; Rahman, S.; Yang, H. Patterned Langmuir-Blodgett films of monodisperse nanoparticles of iron oxide using soft lithography. *J. Am. Chem. Soc.* **2003**, *125*, 630-631.
- (158) Mun, J. H.; Chang, Y. H.; Shin, D. O.; Yoon, J. M.; Choi, D. S.; Lee, K. M.; Kim, J. Y.; Cha, S. K.; Lee, J. Y.; Jeong, J. R.; Kim, Y. H.; Kim, S. O. Monodisperse Pattern Nanoalloying for Synergistic Intermetallic Catalysis. *Nano Lett.* **2013**, *13*, 5720-5726.
- (159) Lohmuller, T.; Aydin, D.; Schwieder, M.; Morhard, C.; Louban, I.; Pacholski, C.; Spatz, J. P. Nanopatterning by block copolymer micelle nanolithography and bioinspired applications. *Biointerphases* **2011**, *6*, MR1-MR12.
- (160) Spatz, J. P.; Roescher, A.; Moller, M. Gold nanoparticles in micellar poly(styrene)-b-poly(ethylene oxide) films-size and interparticle distance control in monodisperse films. *Adv. Mater.* **1996**, *8*, 337-340.
- (161) Menezes, W. G.; Zielasek, V.; Thiel, K.; Hartwig, A.; Baumer, M. Effects of particle size, composition, and support on catalytic activity of AuAg nanoparticles prepared in reverse block copolymer micelles as nanoreactors. *J. Catal.* **2013**, *299*, 222-231.
- (162) Ethirajan, A.; Wiedwald, U.; Boyen, H. G.; Kern, B.; Han, L. Y.; Klimmer, A.; Weigl, F.; Kastle, G.; Ziemann, P.; Fauth, K.; Cai, J.; Behm, R. J.; Romanyuk, A.; Oelhafen, P.; Walther, P.; Biskupek, J.; Kaiser, U. A micellar approach to magnetic ultrahigh-density data-storage media: Extending the limits of current colloidal methods. *Adv. Mater.* **2007**, *19*, 406-410.
- (163) Mark, A. G.; Gibbs, J. G.; Lee, T. C.; Fischer, P. Hybrid nanocolloids with programmed three-dimensional shape and material composition. *Nat. Mater.* **2013**, *12*, 802-807.

- (164) Liu, X. N.; Shen, Y.; Yang, R. T.; Zou, S. H.; Ji, X. L.; Shi, L.; Zhang, Y. C.; Liu, D. Y.; Xiao, L. P.; Zheng, X. M.; Li, S.; Fan, J.; Stucky, G. D. Inkjet Printing Assisted Synthesis of Multicomponent Mesoporous Metal Oxides for Ultrafast Catalyst Exploration. *Nano Lett.* **2012**, *12*, 5733-5739.
- (165) Schneider, J.; Rohner, P.; Galliker, P.; Raja, S. N.; Pan, Y.; Tiwari, M. K.; Poulidakos, D. Site-specific deposition of single gold nanoparticles by individual growth in electrohydrodynamically-printed attoliter droplet reactors. *Nanoscale* **2015**, *7*, 9510-9519.
- (166) Neretina, S.; Hughes, R. A.; Gilroy, K. D.; Hajfathalian, M. Noble Metal Nanostructure Synthesis at the Liquid-Substrate Interface: New Structures, New Insights, and New Possibilities. *Acc. Chem. Res.* **2016**, *49*, 2243-2250.
- (167) Konig, D.; Richter, K.; Siegel, A.; Mudring, A. V.; Ludwig, A. High-Throughput Fabrication of Au-Cu Nanoparticle Libraries by Combinatorial Sputtering in Ionic Liquids. *Adv. Funct. Mater.* **2014**, *24*, 2049-2056.
- (168) Palmer, R. E.; Cai, R. S.; Vernieres, J. Synthesis without Solvents: The Cluster (Nanoparticle) Beam Route to Catalysts and Sensors. *Acc. Chem. Res.* **2018**, *51*, 2296-2304.
- (169) Grunes, J.; Zhu, J.; Anderson, E. A.; Somorjai, G. A. Ethylene hydrogenation over platinum nanoparticle array model catalysts fabricated by electron beam lithography: Determination of active metal surface area. *J. Phys. Chem. B* **2002**, *106*, 11463-11468.
- (170) Javey, A.; Dai, H. J. Regular arrays of 2 nm metal nanoparticles for deterministic synthesis of nanomaterials. *J. Am. Chem. Soc.* **2005**, *127*, 11942-11943.
- (171) Palankar, R.; Medvedev, N.; Rong, A.; Delcea, M. Fabrication of Quantum Dot Microarrays Using Electron Beam Lithography for Applications in Analyte Sensing and Cellular Dynamics. *ACS Nano* **2013**, *7*, 4617-4628.
- (172) Piner, R. D.; Zhu, J.; Xu, F.; Hong, S. H.; Mirkin, C. A. "Dip-pen" nanolithography. *Science* **1999**, *283*, 661-663.
- (173) Hernandez-Santana, A.; Irvine, E.; Faulds, K.; Graham, D. Rapid prototyping of poly(dimethoxysiloxane) dot arrays by dip-pen nanolithography. *Chem. Sci.* **2011**, *2*, 211-215.
- (174) Ielasi, F. S.; Hirtz, M.; Sekula-Neuner, S.; Laue, T.; Fuchs, H.; Willaert, R. G. Dip-Pen Nanolithography-Assisted Protein Crystallization. *J. Am. Chem. Soc.* **2015**, *137*, 154-157.
- (175) O'Connell, C. D.; Higgins, M. J.; Marusic, D.; Moulton, S. E.; Wallace, G. G. Liquid Ink Deposition from an Atomic Force Microscope Tip: Deposition Monitoring and Control of Feature Size. *Langmuir* **2014**, *30*, 2712-2721.
- (176) Zhong, J.; Sun, G.; He, D. N. Classic, liquid, and matrix-assisted dip-pen nanolithography for materials research. *Nanoscale* **2014**, *6*, 12217-12228.
- (177) Wang, W. C. M.; Stoltenberg, R. M.; Liu, S. H.; Bao, Z. N. Direct Patterning of Gold Nanoparticles Using Dip-Pen Nanolithography. *ACS Nano* **2008**, *2*, 2135-2142.
- (178) Gilles, S.; Tuchscherer, A.; Lang, H.; Simon, U. Dip-pen-based direct writing of conducting silver dots. *J. Colloid Interface Sci.* **2013**, *406*, 256-262.
- (179) Hung, S. C.; Nafday, O. A.; Haaheim, J. R.; Ren, F.; Chi, G. C.; Pearton, S. J. Dip Pen Nanolithography of Conductive Silver Traces. *J. Phys. Chem. C* **2010**, *114*, 9672-9677.
- (180) Chai, J. A.; Huo, F. W.; Zheng, Z. J.; Giam, L. R.; Shim, W.; Mirkin, C. A. Scanning probe block copolymer lithography. *Proc. Natl. Acad. Sci. U. S. A.* **2010**, *107*, 20202-20206.
- (181) Liu, G. L.; Eichelsdoerfer, D. J.; Rasin, B.; Zhou, Y.; Brown, K. A.; Liao, X.; Mirkin, C. A.

- Delineating the pathways for the site-directed synthesis of individual nanoparticles on surfaces. *Proc. Natl. Acad. Sci. U. S. A.* **2013**, *110*, 887-891.
- (182) Giam, L. R.; He, S.; Horwitz, N. E.; Eichelsdoerfer, D. J.; Chai, J. N.; Zheng, Z. J.; Kim, D.; Shim, W.; Mirkin, C. A. Positionally Defined, Binary Semiconductor Nanoparticles Synthesized by Scanning Probe Block Copolymer Lithography. *Nano Lett.* **2012**, *12*, 1022-1025.
- (183) Gan, L.; Cui, C. H.; Heggen, M.; Dionigi, F.; Rudi, S.; Strasser, P. Element-specific anisotropic growth of shaped platinum alloy nanocrystals. *Science* **2014**, *346*, 1502-1506.
- (184) Nie, Z. H.; Li, W.; Seo, M.; Xu, S. Q.; Kumacheva, E. Janus and ternary particles generated by microfluidic synthesis: Design, synthesis, and self-assembly. *J. Am. Chem. Soc.* **2006**, *128*, 9408-9412.
- (185) Chai, J. A.; Wong, L. S.; Giam, L.; Mirkin, C. A. Single-molecule protein arrays enabled by scanning probe block copolymer lithography. *Proc. Natl. Acad. Sci. U. S. A.* **2011**, *108*, 19521-19525.
- (186) Huo, F. W.; Zheng, Z. J.; Zheng, G. F.; Giam, L. R.; Zhang, H.; Mirkin, C. A. Polymer pen lithography. *Science* **2008**, *321*, 1658-1660.
- (187) Wu, J.; Zan, X. L.; Li, S. Z.; Liu, Y. Y.; Cui, C. L.; Zou, B. H.; Zhang, W. N.; Xu, H. B.; Duan, H. W.; Tian, D. B.; Huang, W.; Huo, F. W. In situ synthesis of large-area single sub-10 nm nanoparticle arrays by polymer pen lithography. *Nanoscale* **2014**, *6*, 749-752.
- (188) Chai, J.; Liao, X.; Giam, L. R.; Mirkin, C. A. Nanoreactors for Studying Single Nanoparticle Coarsening. *J. Am. Chem. Soc.* **2012**, *134*, 158-161.
- (189) Hoyt, J. J. *Phase Transformations*; McMaster Innovation Press: Hamilton, Canada, 2011.
- (190) Villars, P.; Okamoto, H.; Cenzual, K. Eds. *ASM Alloy Phase Diagrams Database* (<http://www1.asminternational.org/AsmEnterprise/APD>, ASM International, Materials Park, OH, 2006).
- (191) Liao, H. G.; Cui, L. K.; Whitlam, S.; Zheng, H. M. Real-Time Imaging of Pt<sub>3</sub>Fe Nanorod Growth in Solution. *Science* **2012**, *336*, 1011-1014.
- (192) Jungjohann, K. L.; Bliznakov, S.; Sutter, P. W.; Stach, E. A.; Sutter, E. A. In Situ Liquid Cell Electron Microscopy of the Solution Growth of Au-Pd Core-Shell Nanostructures. *Nano Lett.* **2013**, *13*, 2964-2970.
- (193) Tan, S. F.; Chee, S. W.; Lin, G. H.; Bosman, M.; Lin, M.; Mirsaidov, U.; Nijhuis, C. A. Real-Time Imaging of the Formation of Au-Ag Core-Shell Nanoparticles. *J. Am. Chem. Soc.* **2016**, *138*, 5190-5193.
- (194) De Clercq, A.; Dachraoui, W.; Margeat, O.; Pelzer, K.; Henry, C. R.; Giorgio, S. Growth of Pt-Pd Nanoparticles Studied In Situ by HRTEM in a Liquid Cell. *J. Phys. Chem. Lett.* **2014**, *5*, 2126-2130.
- (195) Loh, N. D.; Sen, S.; Bosman, M.; Tan, S. F.; Zhong, J.; Nijhuis, C. A.; Kral, P.; Matsudaira, P.; Mirsaidov, U. Multistep nucleation of nanocrystals in aqueous solution. *Nat. Chem.* **2017**, *9*, 77-82.
- (196) Niu, Z. Q.; Becknell, N.; Yu, Y.; Kim, D.; Chen, C.; Kornienko, N.; Somorjai, G. A.; Yang, P. D. Anisotropic phase segregation and migration of Pt in nanocrystals en route to nanoframe catalysts. *Nat. Mater.* **2016**, *15*, 1188-1194.
- (197) Morozov, I. V.; Znamenkov, K. O.; Korenev, Y. M.; Shlyakhtin, O. A. Thermal decomposition of Cu(NO<sub>3</sub>)<sub>2</sub>·3H<sub>2</sub>O at reduced pressures. *Thermochimica Acta*

- 2003**, *403*, 173-179.
- (198) Wang, D. S.; Li, Y. D. Effective Octadecylamine System for Nanocrystal Synthesis. *Inorg. Chem.* **2011**, *50*, 5196-5202.
- (199) De Yoreo, J. J.; Gilbert, P.; Sommerdijk, N.; Penn, R. L.; Whitelam, S.; Joester, D.; Zhang, H. Z.; Rimer, J. D.; Navrotsky, A.; Banfield, J. F.; Wallace, A. F.; Michel, F. M.; Meldrum, F. C.; Colfen, H.; Dove, P. M. Crystallization by particle attachment in synthetic, biogenic, and geologic environments. *Science* **2015**, *349*, aaa6760.
- (200) Peng, S.; Lei, C. H.; Ren, Y.; Cook, R. E.; Sun, Y. G. Plasmonic/Magnetic Bifunctional Nanoparticles. *Angew. Chem. Int. Ed.* **2011**, *50*, 3158-3163.
- (201) Wu, H. M.; Chen, O.; Zhuang, J. Q.; Lynch, J.; LaMontagne, D.; Nagaoka, Y.; Cao, Y. C. Formation of Heterodimer Nanocrystals: UO<sub>2</sub>/In<sub>2</sub>O<sub>3</sub> and FePt/In<sub>2</sub>O<sub>3</sub>. *J. Am. Chem. Soc.* **2011**, *133*, 14327-14337.
- (202) Zhang, Z. C.; Xu, B.; Wang, X. Engineering nanointerfaces for nanocatalysis. *Chem. Soc. Rev.* **2014**, *43*, 7870-7886.
- (203) Fu, Q.; Wagner, T. Interaction of nanostructured metal overlayers with oxide surfaces. *Surf. Sci. Rep.* **2007**, *62*, 431-498.
- (204) Wang, H. T.; Xu, S. C.; Tsai, C.; Li, Y. Z.; Liu, C.; Zhao, J.; Liu, Y. Y.; Yuan, H. Y.; Abild-Pedersen, F.; Prinz, F. B.; Norskov, J. K.; Cui, Y. Direct and continuous strain control of catalysts with tunable battery electrode materials. *Science* **2016**, *354*, 1031-1036.
- (205) Li, C. W.; Ciston, J.; Kanan, M. W. Electroreduction of carbon monoxide to liquid fuel on oxide-derived nanocrystalline copper. *Nature* **2014**, *508*, 504-507.
- (206) Li, X. F.; Schaak, R. E. Reactive AgAuS and Ag<sub>3</sub>AuS<sub>2</sub> Synthons Enable the Sequential Transformation of Spherical Nanocrystals into Asymmetric Multicomponent Hybrid Nanoparticles. *Chem. Mater.* **2017**, *29*, 4153-4160.
- (207) Casavola, M.; Falqui, A.; Garcia, M. A.; Garcia-Hernandez, M.; Giannini, C.; Cingolani, R.; Cozzoli, P. D. Exchange-Coupled Bimagnetic Cobalt/Iron Oxide Branched Nanocrystal Heterostructures. *Nano Lett.* **2009**, *9*, 366-376.
- (208) Saal, J. E.; Kirklin, S.; Aykol, M.; Meredig, B.; Wolverton, C. Materials Design and Discovery with High-Throughput Density Functional Theory: The Open Quantum Materials Database (OQMD). *JOM* **2013**, *65*, 1501-1509.
- (209) Kirklin, S.; Saal, J. E.; Meredig, B.; Thompson, A.; Doak, J. W.; Aykol, M.; Ruhl, S.; Wolverton, C. The Open Quantum Materials Database (OQMD): assessing the accuracy of DFT formation energies. *NPJ Computational Materials* **2015**, *1*, 15010.
- (210) Kirklin, S.; Meredig, B.; Wolverton, C. High-Throughput Computational Screening of New Li-Ion Battery Anode Materials. *Adv. Energy Mater.* **2013**, *3*, 252-262.
- (211) Zhang, Y. L.; Cattrall, R. W.; McKelvie, I. D.; Kolev, S. D. Gold, an alternative to platinum group metals in automobile catalytic converters. *Gold Bull.* **2011**, *44*, 145-153.
- (212) Ma, A. J.; Xu, J.; Zhang, X. H.; Zhang, B.; Wang, D. Y.; Xu, H. L. Interfacial nanodroplets guided construction of hierarchical Au, Au-Pt, and Au-Pd particles as excellent catalysts. *Sci. Rep.* **2014**, *4*, 4819.
- (213) Kaiser, J.; Leppert, L.; Welz, H.; Polzer, F.; Wunder, S.; Wanderka, N.; Albrecht, M.; Lunkenbein, T.; Brey, J.; Kummel, S.; Lu, Y.; Ballauff, M. Catalytic activity of nanoalloys from gold and palladium. *Phys. Chem. Chem. Phys.* **2012**, *14*, 6487-6495.
- (214) Giam, L. R.; Massich, M. D.; Hao, L. L.; Wong, L. S.; Mader, C. C.; Mirkin, C. A. Scanning

- probe-enabled nanocombinatorics define the relationship between fibronectin feature size and stem cell fate. *Proc. Natl. Acad. Sci. U. S. A.* **2012**, *109*, 4377-4382.
- (215) Brown, K. A.; Eichelsdoerfer, D. J.; Shim, W.; Rasin, B.; Radha, B.; Liao, X.; Schmucker, A. L.; Liu, G. L.; Mirkin, C. A. A cantilever-free approach to dot-matrix nanoprinting. *Proc. Natl. Acad. Sci. U. S. A.* **2013**, *110*, 12921-12924.
- (216) Zheng, Z. J.; Daniel, W. L.; Giam, L. R.; Huo, F. W.; Senesi, A. J.; Zheng, G. F.; Mirkin, C. A. Multiplexed Protein Arrays Enabled by Polymer Pen Lithography: Addressing the Inking Challenge. *Angew. Chem. Int. Ed.* **2009**, *48*, 7626-7629.

**CURRICULUM VITAE**

## Pengcheng Chen

Department of Materials Science and Engineering E-mail: [cpc@u.northwestern.edu](mailto:cpc@u.northwestern.edu)  
Northwestern University, Ryan Hall, Room 2027, Evanston, IL 60208

### **EDUCATION**

---

<b>Ph.D., Northwestern University</b>	<b>(expected) 12/2018</b>
Materials Science and Engineering (Advisor: Prof. Chad A. Mirkin)	
<b>M.S., Zhejiang University, China</b>	<b>03/2013</b>
Polymer Chemistry and Physics (Advisor: Prof. Zhi-Kang Xu)	
<b>B.S., Zhejiang University, China</b>	<b>06/2010</b>
Polymer Materials and Engineering	

### **HONORS AND AWARDS**

---

ACS Inorganic Chemistry Young Investigator Award, American Chemical Society	<b>2018</b>
Hilliard Scholarship, Northwestern University	<b>2018</b>
Cabell Terminal Year Fellowship, Northwestern University	<b>2018</b>
Chinese Government Award for Outstanding Self-Financed Students Abroad	<b>2017</b>
MRS Graduate Student Gold Award, Materials Research Society	<b>2017</b>
Park AFM Scholarship	<b>2017</b>
IIN Outstanding Researcher Award, Northwestern University	<b>2016</b>
IPMI Student Award, International Precious Metal Institute	<b>2016</b>
Grand Prize of NUANCE Scientific Image Contest, Northwestern University	<b>2015</b>
Ryan Fellowship, Northwestern University	<b>2015</b>
Excellent Graduate Student Awards, Zhejiang University	<b>2013</b>
National Scholarship, China	<b>2012</b>
Kingfa Science and Technology Scholarship	<b>2012</b>
First-Class Award of Honor for Graduates, Zhejiang University	<b>2012</b>
GE Foundation Tech Award	<b>2011</b>
Outstanding Graduate of Zhejiang University	<b>2010</b>
Top 100 Outstanding Undergraduate Thesis, Zhejiang University	<b>2010</b>
Weichai-Power Scholarship	<b>2009</b>
National Scholarship, China	<b>2008</b>
First-Class Scholarship for Outstanding Students, Zhejiang University	<b>2007/2008/2009</b>
Excellent Student Awards, Zhejiang University	<b>2007/2008/2009</b>

### **PUBLICATIONS**

---

†equal contribution  
at Northwestern University

- (1) **P. C. Chen**, J. S. Du, B. Meckes, L. Huang, Z. Xie, J. L. Hedrick, V. P. Dravid and C. A. Mirkin, Structural Evolution of Three-Component Nanoparticles in Polymer Nanoreactors, *Journal of the American Chemical Society* 2017, *139*, 9876-9884.
- (2) **P. C. Chen**, X. Liu, J. L. Hedrick, Z. Xie, S. Wang, Q. Y. Lin, M. C. Hersam, V. P. Dravid and C. A. Mirkin, Polyelemental Nanoparticle Libraries, *Science* 2016, *352*, 1565-1569.
- (3) **P. C. Chen**, G. Liu, Y. Zhou, K. A. Brown, N. Chernyak, J. L. Hedrick, S. He, Z. Xie, Q. Y. Lin, V. P. Dravid and C. A. Mirkin, Tip-Directed Synthesis of Multimetallic Nanoparticles, *Journal of the American Chemical Society* 2015, *137*, 9167-9173.
- (4) J. S. Du<sup>†</sup>, **P. C. Chen**<sup>†</sup>, B. Meckes, Z. Xie, J. Zhu, Y. Liu, V. P. Dravid and C. A. Mirkin, The Structural Fate of Individual Multicomponent Metal-Oxide Nanoparticles in Polymer Nanoreactors, *Angewandte Chemie International Edition* 2017, *56*, 7625-7629.
- (5) L. Huang<sup>†</sup>, **P. C. Chen**<sup>†</sup>, M. Liu, X. Fu, P. Gordiichuk, Y. Yu, C. Wolverton, Y. Kang and C. A. Mirin, Catalyst Design by DFT and Scanning Probe Block Copolymer Lithography, *Proceedings of the National Academy of Sciences of the United States of America* 2018, *115*, 3764-3769.
- (6) J. S. Du, **P. C. Chen**, B. Meckes, E. J. Kluender, Z. Xie, V. P. Dravid and C. A. Mirkin, Windowless Observation of Evaporation-Induced Coarsening of Au-Pt Nanoparticles in Polymer Nanoreactors, *Journal of the American Chemical Society* 2018, *140*, 7213-7221.
- (7) Z. Xie, Y. Zhou, J. L. Hedrick, **P. C. Chen**, M. M. Shahjamali, S. He, S. Wang, Z. Zheng and C. A. Mirkin, On-Tip Photo-Modulated Molecular Printing, *Angewandte Chemie International Edition* 2015, *54*, 12894-12899.
- (8) S. Wang, C. M. McGuirk, M. B. Ross, S. Wang, **P. C. Chen**, H. Xing, Y. Liu and C. A. Mirkin, General and Direct Method for Preparing Oligonucleotide-Functionalized Metal-Organic Framework Nanoparticles, *Journal of the American Chemical Society* 2017, *139*, 9827-9830.
- (9) Z. Xie, P. Gordiichuk, Q. Y. Lin, B. Meckes, **P. C. Chen**, L. Sun, J. S. Du, J. Zhu, Y. Liu, V. P. Dravid and C. A. Mirkin, Solution-Phase Photochemical Nanopatterning Enabled by High-Refractive-Index Beam Pen Arrays, *ACS Nano* 2017, *11*, 8231-8241.
- (10) J. L. Hedrick, K. A. Brown, E. J. Kluender, M. D. Cabezas, **P. C. Chen** and C. A. Mirkin, Hard Transparent Arrays for Polymer Pen Lithography, *ACS Nano* 2016, *10*, 3144-3148.
- (11) S. He, D. J. Park, X. Liao, Z. Xie, K. A. Brown, **P. C. Chen**, Y. Zhou, G. C. Schatz and C. A. Mirkin, Liquid Phase Beam Pen Lithography, *Small* 2016, *12*, 988-993.
- (12) Y. Zhou, Z. Xie, K. A. Brown, D. J. Park, X. Zhou, **P. C. Chen**, M. Hirtz, Q. Y. Lin, V. P. Dravid, G. C. Schatz, Z. Zheng and C. A. Mirkin, Apertureless Cantilever-Free Pen Arrays for Scanning Photochemical Printing, *Small* 2015, *11*, 913-918.
- (13) Q. Y. Lin, E. Palacios, W. Zhou, Z. Li, J. A. Mason, Z. Liu, H. Lin, **P. C. Chen**, V. P. Dravid, K. Aydin and C. A. Mirkin, DNA-Mediated Size-Selective Nanoparticle Assembly for Multiplexed Surface Encoding, *Nano Letters* 2018, *18*, 2645-2649.
- (14) Q. Y. Lin, Z. Li, K. A. Brown, M. N. O'Brien, M. B. Ross, Y. Zhou, S. Butun, **P. C. Chen**, G. C. Schatz, V. P. Dravid, K. Aydin and C. A. Mirkin, Strong Coupling between Plasmonic Gap Modes and Photonic Lattice Modes in DNA-Assembled Gold Nanocube Arrays, *Nano Letters* 2015, *15*, 4699-4703.

at Zhejiang University

- (15) **P. C. Chen** and Z. K. Xu, Mineral-Coated Polymer Membranes with Superhydrophilicity and Underwater Superoleophobicity for Effective Oil/Water Separation, *Scientific Reports* 2013, *3*, 2776.
- (16) **P. C. Chen**, L. S. Wan and Z. K. Xu, Bio-inspired CaCO<sub>3</sub> coating for superhydrophilic hybrid membranes with high water permeability, *Journal of Materials Chemistry* 2012, *22*, 22727-22733.
- (17) **P. C. Chen**, L. S. Wan, B. B. Ke, and Z. K. Xu, Honeycomb-Patterned Film Segregated with Phenylboronic Acid for Glucose Sensing, *Langmuir* 2011, *27*, 12597-12605.

- (18) L. S. Wan, Q. L. Li, **P. C. Chen** and Z. K. Xu, Patterned biocatalytic films via one-step self-assembly, *Chemical Communications* 2012, 48, 4417–4419. [Back Cover]
- (19) B. B. Ke, L. S. Wan, **P. C. Chen**, L. Y. Zhang, and Z. K. Xu, Tunable Assembly of Nanoparticles on Patterned Porous Film, *Langmuir* 2010, 26, 15982–15988.
- (20) M. Cao, J. Q. Wang, **P. C. Chen**, J. T. Xu and Z. Q. Fan, Cleavage of Polystyrene-*b*-Poly(ethylene oxide) Block Copolymers with a Trithiocarbonate Linkage in Solutions, *Journal of Polymer Science, Part A: Polymer Chemistry* 2010, 48, 3834-3840.
- (21) W. X. Zhang, L. S. Wan, X. L. Meng, J. W. Li, B. B. Ke, **P. C. Chen** and Z. K. Xu, Macroporous, protein-containing films cast from water-in-oil emulsions featuring a block-copolymer, *Soft Matter* 2011, 7, 4221-4227.

## **PRESENTATIONS**

---

### Oral

- (1) "Combinatorial Synthesis of Multimetallic Heterostructured Nanoparticles in Polymer Nanoreactors", *ACS Fall Meeting*, Boston, USA, 2018.
- (2) "Combinatorial Synthesis of Multicomponent Nanostructures", *John E. Hilliard Symposium*, Northwestern University, Evanston, USA, 2018.
- (3) "Combinatorial Synthesis of Multimetallic Nanoparticles", *ACS Spring Meeting*, New Orleans, USA, 2018.
- (4) "Polymer Approaches to Synthesize Complex Multicomponent Nanostructures", *SPIE-MRSEC Student Seminar*, Northwestern University, Evanston, USA, 2018.
- (5) "Combinatorial Synthesis of Multimetallic Nanoparticles", *MRS Spring Meeting*, Phoenix, USA, 2017.
- (6) "Developing a Combinatorial Library of Multimetallic Nanoparticles for Catalyst Screening", *International Precious Metal Institute 40<sup>th</sup> Annual Conference*, Phoenix, USA, 2016.

### Poster

- (1) "Tip-Directed Synthesis of Multimetallic Nanoparticles", *MRS Fall Meeting*, Boston, USA, 2015.
- (2) "Fabrication of phenylboronic acid modified honeycomb-patterned films and its application in glucose sensor", *National Meeting of Chinese Chemical Society-Polymer Division*, Dalian, China, 2011.
- (3) "Functional Honeycomb-Patterned Films for Biosensing", *Unilever-RSC International Symposium on Functional Materials Science*, Hangzhou, China, 2010.

## **TEACHING EXPERIENCE**

---

Teaching Assistant, Course "Principles of the Properties of Materials", Northwestern University, 2017 Fall  
 Teaching Assistant, Course "Imperfection in Materials", Northwestern University, 2015 Winter  
 Teaching Assistant, Course "Polymer Chemistry", Zhejiang University, 2010 Fall

## **PATENTS**

---

- (1) "Polyelemental Heterostructure Nanoparticles and methods of Making the Same", C. A. Mirkin and **P. C. Chen**, provisional patent, August 2018.

## **OTHER ACTIVITIES**

---

Dip-Pen Nanolithography Subgroup Leader (Mirkin Group), Northwestern University 06/2015-08/2018